NONLINEAR DYNAMIC ANALYSIS OF HYBRID FRAMES

by

DOBRINKA RADULOVA

Presented to the Faculty of the Graduate School of

The University of Texas at Arlington in Partial Fulfillment

of the Requirements

for the Degree of

MASTER OF SCIENCE IN CIVIL ENGINEERING

THE UNIVERSITY OF TEXAS AT ARLINGTON

December 2009

Copyright © by Dobrinka Radulova 2009

All Rights Reserved

ACKNOWLEDGEMENTS

My sincere appreciation and great respect goes to my advisor Dr. Ali Abolmaali for his guidance and support that has inspired me to pursue this research and higher education. I am very thankful for his patience and understanding through difficult times and for his continuous encouragement. Working with Dr. Abolmaali has made me not only a better researcher, but also a better person. Special thanks also goes to Dr. Matthys, Dr. Ramirez and Dr. Chao for providing helpful suggestions and taking the time to serve on my thesis committee.

I am very grateful to my fiancé Richard Nichols for his endless support and encouragement. His love has helped me overcome many obstacles, and I cannot wait to spend the rest of my life with him. Also, the help of Marcus Allen, Ardavan Motahari, Tri Le and all my friends and colleagues is greatly appreciated.

Last but not least, my deepest thanks go to my family for their ever-lasting love that has made me who I am today. Their encouragement and unconditional support mean so much. I love you.

Finally, thanks to God for giving these people to me.

November 17, 2009

ABSTRACT

NONLINEAR DYNAMIC ANALYSIS OF HYBRID FRAMES

Dobrinka Radulova, M.S.

The University of Texas at Arlington, 2009

Supervising Professor: Ali Abolmaali

This study proposes a hybrid frame system consisting of rigid and semi-rigid connections subjected to a dynamic loading. Two building geometries are chosen to represent low-rise and high-rise buildings. Multiple locations for placement of semi-rigid connections are proposed, and the hybrid systems with the most efficient energy dissipation are identified. During this analysis, five earthquake records are used to provide a spectrum of frequencies. Five practical semi-rigid connection types and one connection with analytical parameters are also modeled into the selected hybrid combinations by applying zero-length springs at the ends of beams, in which their nonlinear constitutive relation is defined by bilinear moment-rotation curves. Incremental transient dynamic analysis including P-Δ effects is conducted.

The results of the research indicated that the proposed placement of partially restrained connections significantly decreases moment and shear force

demands on structural members in the studied tall building during high-frequency earthquakes. In contrast, earthquakes with low frequency acceleration records adversely affect the deflections and member forces in the selected hybrid buildings compared to their rigid equivalents.

TABLE OF CONTENTS

LIST OF ILLUSTRATIONS

Figure Page

LIST OF TABLES

CHAPTER 1

INTRODUCTION

1.1. Introduction

Design of buildings, especially high-rise buildings, for seismic loads has always been among the most challenging for the structural engineering community. The high degree of uncertainty associated with earthquake loads is the main barrier to overcome for researchers and professionals who strive to establish generalized design guidelines. Some of the variables that make the structural seismic response so unpredictable are the unknown distance from epicenter, magnitude of ground shaking, underground depth of origin, type of ground-shaking waves, period of the earthquake, on-site soil properties, building geometry and dynamic characteristics, quality of used materials and construction procedures as well as maintenance of the building. Incorporating all these parameters by the designer alone is largely unpractical. Instead, researchers and professionals across the world continue to look for patterns that would group the behavior of certain types of buildings into a separate design category.

In the past, seismic design of buildings was falsely over-simplified. In the 1960s, welded steel-moment frames were believed to effectively dissipated earthquake induced energy due to ductile behavior in their members and connections (FEMA-355F). Ductility, which is critical for performance under

dynamic loads, is the ability of a member to significantly deform without loss of strength. As a result of the misconception, welded steel-moment frames were the dominant design choice in seismic prone regions. Hundreds of such structures were built in California, a highly seismic region. Many of these buildings were affected by the Northridge earthquake in 1994, when the beam-to-column connections failed in a brittle matter (FEMA-355F). Damage was spread over large distances from the epicenter and appeared to be independent of the buildings' age or geometric properties. Although a majority of the buildings did not collapse, the economic losses surpassed $20 billion (FEMA-355F). The structural engineering community was largely puzzled and concerned. Soon after the earthquake, the SAC Joint Venture was formed to investigate structural seismic response. The venture is a partnership between Structural Engineers Association of California (SEAOC), Applied Technology Council (ATC), California Universities for Research in Earthquake Engineering (CUREe), Federal Emergency Management Association (FEMA), American Institute of Steel Construction (AISC), American Welding Society (AWS) and others. Their mutual efforts concentrated on producing altered guidelines for design of new buildings and for retrofitting existing buildings. Current design philosophies, namely equivalent static design and performance-based design, were closely reviewed.

The equivalent static design method replaces dynamic loads, which are difficult to process for a designer on a daily basis, with static loads amplified by

dynamic factors. The dynamic factors are a product of the global stiffness matrix and the displacement vector at a certain time of peak displacement. The result is an amplified static load at a particular time that generates identical displacement vector. The same procedure is repeated for different times of peak responses to simulate seismic loads. However, finding the exact solution for the dynamic factors is mathematically involved and expensive. Therefore, approximate methods have been developed, where the number of "significant" degrees-of-freedom, n, is less than the actual degrees-of-freedom, N (Choi et al. 2005). Whether a degree-of-freedom is significant or not is determined based on engineering judgment and the final results might be significantly altered, if the assumptions are not supported.

One approximate solution of solving the equivalent static load is displacement based, and it produces dynamic displacements of equal or greater value than those determined from the exact solution. However, this method fails to comply with the stress and strain energy fields, which do not necessarily reach their maximum values at the times of peak displacement. As a result, the direction of the dynamic response is ignored and some constraints are not fully satisfied. The equivalent static load design based on this approximate method which violates some constrains is not always conservative.

Another method is based on the stress fields. In this case, the results are always conservative, but it usually provides over-designed solutions. Overall, the equivalent static design procedure is more suitable for relatively

small frames, because large frames have a considerable number of significant degrees-of-freedom, and applying this method becomes impractical (Choi et al. 2005). Also, the previously discussed mathematical procedure yields results for a particular moment in time, and several calculations at various peak displacements are needed to effectively represent a dynamic load. For this reason, the method may become involved even for relatively small frames. While this procedure is still in use, many code provisions have implemented the performance-based design philosophy instead.

The large economic losses from Northridge and other moderate earthquakes showed a need for new performance criteria. Previously, the seismic design of buildings was governed by a collapse prevention philosophy without consideration of monetary damage. However, in September 2000, the SAC Joint Venture published FEMA-355F which explicitly defined the governing design factors – performance levels and seismic hazards.

The four performance levels are operational, immediate occupancy, life safety and collapse prevention. To meet the immediate occupational level, a building has minimal to no structural and non-structural damage, and utilities remain unaffected. The immediate occupancy level implies that minor non-structural and even structural damage may be observed, but is repairable while the building remains occupied. This means the utilities and equipment may need repair, but no permanent drift is recorded. Under the life safety level, damage is extensive and repair may be economically unfeasible. The building

will remain stable; however, permanent drifts of 2.5 percent or larger are observed. Life loss is not expected. Finally, the collapse prevention level precludes gross loss of life, but implies hazard to life safety. Permanent drifts exceed 5 percent, and the building is severely damaged.

These criteria classify the building performance, but they give little information about the ground shaking characteristics. The statistical probability of occurrence of earthquakes with different magnitudes is covered in the definitions for seismic hazard. For example, according to SAC Joint Venture a major earthquake is described as the one with 2 percent probability of occurrence in 50 years, denoted as 2/50. A minor earthquake has 50 percent probability of occurrence in 50 years, or 50/50. The performance-based design uses confidence levels to satisfy performance objectives. For instance, a 95 percent confidence that a building will meet the collapse prevention performance level for the 2/50 hazard is adequate.

These guidelines are used to estimate seismic demands on a building, but how the loads are carried out is decided by the designer. In practice, intentionally weakened elements called “fuses” control the local failure mechanism. These could be connections, sections of beams with reduced strength and/or shear walls. In all cases, properly designed fuses are the first to fail during an earthquake. Thus, failure is controlled and easily repaired. However, weak elements, used to control failure location, generally increase the

overall cost of the building as the remaining elements have to be designed to behave elastically (AISC Seismic Provisions 2005).

In this research, the hybrid systems of rigid and semi-rigid connections will be incorporated into different steel moment frames in efforts to optimize seismic performance. The semi-rigid connections will act as fuses and will confine damage to connections; thus, enabling potential rehabilitation of the buildings, while undamaged columns support gravity loads. A pattern for semi-rigid connection placement is sought as this might impose a building natural damper that would decouple the building lateral drift from the ground motion acceleration. Such behavior is highly desirable, since it would optimize the building design with minimal material and construction cost.

When semi-rigid connections are applied at various locations, moment redistribution occurs. This phenomenon is monitored closely in search of similarities. Several earthquake records are applied, and the redistribution patterns are compared. Finally, the properties of multiple commonly used semi-rigid connections are incorporated to determine the effect of connection properties on the global frame performance.

1.2. Background

1.2.1. Pre-Northridge Design

Seismic design of buildings has evolved over the years to establish the current design philosophies. As in other fields, research promotes new knowledge, which is incorporated into the appropriate code procedures. While

often this is a gradual process, a single day stands out in the history of design of structures for seismic response. In January 17, 1994 an earthquake with a magnitude of 6.7 shook a small town in California. The Northridge earthquake severely damaged some concrete structures, while steel buildings performed seemingly well. However, a closer inspection discovered many beam-to-column connections in steel frames had failed in a brittle matter. The economic losses were substantial. The alerted engineering and construction communities quickly started evaluating seismic provisions. Since structures built as early as the 1960s were still in public use, the design provisions from prior applicable codes were also reviewed. The specifications were divided into three separate groups, which combined the most significant changes that developed over the years.

The earliest group of Uniform Building Code (UBC) provisions covered the period from 1958 to 1973. These codes had no limitations on lateral drift for seismic design. They did provide a limit for wind load drifts of 0.0025, and engineers nowadays assume this restriction was also used for earthquake induced response. However, this assumption cannot be justified with guidance from the then current code. Moreover, ductility was assumed to develop in the beam ends only, and no consideration was given to the panel zone. Recent research has shown that this is a highly unrealistic expectation, and unless the panel zone strength is significantly increased, it may reach its ultimate capacity before the beam has yielded (FEMA- 355C). Other design concepts that

adversely affect the performance of buildings from this time period include the low design base shear and the absence of restrictions for weak column formation. The effects of on-site soil conditions were also neglected.

In the years between 1976 and 1985 the UBC integrated few improvements. A maximum seismic drift of 0.005 rad was introduced. The code began to consider the building location and occupancy by incorporating the design spectral acceleration, S and the importance factor, I. In 1978, the Applied Technology Council published ATC 3-06, where it defined seismic hazard exposure groups and acknowledged the importance of the soil-structure interaction. It also published national maps for seismic hazard and introduced the response reduction factor, R.

The time period from 1988 to 1994 provided additional development in the UBC provisions. The ductility of the lateral load resistant system and the shear base were accounted by the response modification factor, Rw. In addition, the seismic zone factor, Z, accounted for the peak ground acceleration for the 10/50 hazard. Panel zone strength requirements and special loading conditions for columns were also established. As a result of these efforts, the National Earthquake Hazard Reduction Program (NEHRP) was developed.

Despite the year at which a building was designed, a structure was always assumed to behave in a ductile matter if subjected to an earthquake (FEMA-355C). This expected ductile behavior allowed designers to account only for a portion of the strength required if the building were to stay in its elastic

range. For this reason, the structural engineering community was largely troubled when the Northridge earthquake caused a brittle failure in beam-to-column connections. The earthquake triggered research efforts around the globe to determine the cause for this unexpected behavior.

1.2.2.. Post-Northridge Design

Since 1994 more information is available about the seismic performance of buildings. Researchers have found multiple flaws that influence the building capacity, and their combined effects explain the unsatisfactory performance of steel structures. The five factors identified as the primary reasons for the brittle failure of connections are ground shaking characteristics, design philosophies and detailing, material properties, workmanship and inspection (Miller 1998).

1.1.1.1. Ground Shaking Characteristics

The ground shaking characteristics are largely unpredictable and often beyond the scope of design procedures. Yet, attempts are made to provide confidence levels that the building will sustain an earthquake with anticipated fundamental period and peak accelerations (FEMA-355F). On-site soil properties are also targeted for better global performance. However, other factors such as design for near-fault ground shaking are considered uneconomical and thus, they are neglected. Any design of buildings should be considered accurate in the context of these and other broad uncertainties associated with earthquakes.

1.1.1.2.. Design Philosophies and Detailing

Many design and detailing assumptions prior to the Northridge earthquake were later proven erroneous. For example, disregarding the contribution of the shear panel zone between the beam and the column was a major flaw with the pre-Northridge design procedures (Mao et al). In some cases, the strength of the panel zone was small enough that it failed before the beams could reach its yield capacity. Chi et al. (2000) argues this behavior is dictated by the large stress and strain demands on the beam flanges in the proximity of the connection compared to potential plastic hinges forming along the beam length. Assuming the plastic deformation will occur only in the beam, the design assumption prior to 1994, is possible if the panel zone is significantly stiffer; however, such design is not economical (FEMA-355C). Instead, providing stiffness that allows both the beam end and the panel zone to develop plastic hinges at the same time will optimize the design. The challenge to current designers is to find this balance.

The absence of the “strong column” concept in earlier editions of the design codes also effected buildings from this time period. If the beam is not deliberately failed first, damaged columns may form a soft-story mechanism, where localized story failure replaces global collapse. This mechanism is highly undesirable as it may result in some loss of life and large fiscal damage.

Structural redundancy and member sizes also affect building performance (Lee and Foutch 2002). In earlier code provisions the lateral load

moment-resisting frames usually involved plethora of members. Thus, the member sizes were relatively small, and the overall design had considerable redundancy. However, over time engineers began to use heavier members in order to minimize the construction cost of the now smaller lateral load moment-resisting fames. As a result, not only did the redundancy of the structure reduce, but also the demand on the connections increased. Meanwhile, the connections' detailing remained similar as a ductile behavior of pre-Northridge connections was assumed. The Northridge earthquake proved this design assumption was not scientifically backed, and the connection details before 1994 have been widely studied since then. Multiple problems were discovered as a result of this intensive research.

A design assumption that may have contributed to the brittle fracture of connections during the Northridge earthquake is the high demand imposed on them. The details for Pre-Northridge connections specify that the beam web is bolted to a steel plate, which in turn is connected to the column. Therefore, the beam web is perforated to accommodate placement of bolts, and the cross-sectional area, A, and the moment of inertia, I, are decreased. As a result, the section of the beam experiencing the highest demands has reduced sectional properties (FEMA-355C).

In theory, pre-Northridge connections were to transfer shear from the beam to the column through the beam web, while moment and axial forces were carried by the beam flanges. However, the boundary conditions of the

connection forced much of the shear demand to the flanges with development of triaxial stresses (Miller 1998). While steel elements maintain much desirable ductility under a uniaxial stress, no yielding and decking develops if they are subjected to multi-axial stresses. Instead, the material fractures in a brittle matter, which explains the sudden failure of beam flanges and their corresponding welds during the Northridge earthquake.

Other connection details also contributed to the poor performance of the pre-Northridge connections. A backing bar is commonly used in welding practices, and leaving it in place after fulfilling its function was believed to have no consequences on the connection strength. According to Popov et al. (1998), however, leaving the weld backing bar in place created an artificial crack in the flange welds. Inspections of many damaged connections confirmed fracture began in the weld notch created by the backing bar (Chi et al. 2000). The failure usually initiated in the bottom flange, where the backing bar obstructed proper welding procedures and inspections (Popov et al. 1998).

Another performance factor was the size of access holes, which provide access for welders to deliver weld continuity across the thickness of the beam web (Lu et al. 2000). Small access holes obstruct weld installation and may cause dubious weld performance. Large access holes on the other hand, increase stress concentrations in the beam flange. Lu et al. (2000) have tested different shapes and sizes of access holes and have outlined recommended access hole configurations for future applications.

According to Barsom and Pellegrino (2002) having the bottom surface of the bottom beam flange perpendicular to the column face develops large stress concentrations in the welds. As previously discussed, weld quality in pre-Northridge connections often cannot be guaranteed, which poses a risk to the building. Research has shown that the angle between the bottom surface of the bottom beam flange and the column face should be limited to 20 degrees or less (Barsom and Pellegrino, 2002).

1.1.1.3. Material Properties

Material properties proved to be influential in structural performance as well. As previously addressed, large stress concentrations developed in the connection welds; thus the weld stiffness is crucial for adequate seismic performance. However, a typical welded metal used in pre-Northridge connections is E70T-4, which has a Charpy V-notch toughness of only 7-14 J at 70℃ (158℉) (Chi et al 2000). To compare the requi red range of Charpy V-notch toughness in current provisions is 27-54 J at -28℃ (-18℉) (Mao et al. 2001). This lack of weld stiffness contributed to the widespread brittle failure of Pre-Northridge connections.

In addition, the member yield strength is significantly modified due to alloys added in the rolling mills. Therefore, the average yield strength of the widely used A36 steel is increased to 48 ksi (331 MPa) and the average ultimate stress is 70 ksi (483 MPa) (Popov et al. 1998). Since the UBC provisions prior to the Northridge earthquake provided only minimum limits and

no maximum strengths were cited, the designers were forced to use the minimum yield strength of 36 ksi (248 MPa) as the strength at which plastic hinges would develop in the beam. However, in reality the plastic hinges will not form until the actual yield strength of the steel is reached, and plastic hinges appear in the weaker beam-to-column connections instead.

1.1.1.4. Workmanship

The capacity of welds is also dependant on the work of the individual welder. As previously mentioned, leaving the backing bar in place often made the job of construction workers difficult, which may have resulted in lower weld quality. According to Miller (1998) other workmanship deficiencies include slag influsions, deficient penetration, absence of fusion, poor “tie-ins” and less-than-perfect access holes. Miller also points out the unfavorable consequences of using weld tabs other than those specified by the applicable code.

1.1.1.5. Inspection

A popular evaluation method for on-site beam-to-column connections is ultrasonic inspection. While this method provides important information about some connection properties, it is unable to detect others such as voltage, travel speed, electrode extension, polarity, bead sequence, preheat and interpass temperatures and welding amperage (Miller 1998). Therefore, visual inspection is highly advisable; yet, it is not common.

It should be noted that leaving the weld backing bar in place after construction is complete would affect the visibility and therefore the proper on-

site evaluation of connections. As a result, a connection might pass both the ultrasonic and visual inspections and still not perform as expected. Current code provisions aim to minimize this possibility.

1.1.1.6. Rehabilitation and Design of New Buildings

The brittle fracture of connections observed after the Northridge earthquake is rarely a result of any one of the pointed weaknesses. Instead, a combination of several of these factors produced this unexpected structural performance. Following the earthquake, the engineering community began modifying design requirements and retrofitting buildings designed based on previous UBC editions. One method to improve the performance of existing buildings is to increase the beam capacity at the column face by supplying cover plates. As a result, the panel zone is stiffer, and the beam is able to reach inelastic behavior before failure occurs. FEMA-355C suggests placing haunches or ribs as an alternative to the cover plates. The major disadvantage to this approach is the uncertainty associated with plastic hinge location. A seismic load could force an inelastic behavior in the beam, the connection or preferably in both, which would provide optimal structural response (FEMA-355C). However, not knowing the exact plastic hinge locations prior to the earthquake may impose larger replacement cost of the damaged elements.

Another method is to decrease the beam flanges at the locations where plastic hinges were initially assumed to develop. This approach is termed the Reduced Beam Section (RBS) method, and it successfully shifts the seismic

demand from the connection to the beam, where damage can be controlled (FEAM-355C). However, reducing the beam section at the location of anticipated plastic deformations implies that the remaining portion of the beam as well as all other structural elements must be designed to carry seismic loads elastically. Therefore, the RBS method has shown to be predictable, thus safe, but rather costly.

Overall, current provisions are based on lessons learned from the Northridge earthquake. Among the many changes instigated since 1994 are the removal of weld backing bar at the bottom beam flange, closely monitored workmanship and regulation of the weld stiffness. Moreover, the panel zone capacity is now given significant attention. Also, FEMA 1997 restricted plastic rotation to a minimum of 0.003 rad. While these regulations are believed to provide for adequate seismic structural response, the seismic design of buildings has yet to offer an economic solution. Recent research results indicate that the use of semi-rigid connections in moment-resisting frames may address this problem while meeting all other design objectives of the current codes (Abolmaali et al. 2008).

1.2.3. Semi-Rigid Connections

The potential benefits of using semi-rigid connections cannot be fully evaluated without proper modeling. FEMA-355C provides several methods for simulation of semi-rigid connection behavior. One model uses multiple springs placed between the beam and column end nodes. Each spring is assigned pre-

determined stiffness properties that correspond to a particular characteristic of the connection behavior. Therefore, the combined action of all springs mimics the response of the semi-rigid connection.

Another model uses a single spring instead; however, the stiffness relationship is non-linear. The complexity in the modeling the connection stiffness properties is proportional to the expected accuracy of the results, and it is based on the researcher's judgment. A bi-linear relationship is frequently used because of its simplicity and relative veracity.

A different method uses four rigid members linked together to represent a realistic geometric model of the panel zone. Inner springs duplicate the rotational capacity of the panel zone, while outer springs join the rigid assembly and end nodes of adjacent beams and columns (FEMA-355F). While this composition provides a realistic representation of semi-rigid connection behavior, it is rather complex.

These and other models are used by researchers who explore the unknown benefits of partially restrained buildings. Despite, the limited knowledge about the effects of semi-rigid connections on building performance during an earthquake has pushed them into a secondary role in seismic design. FEMA-355C calls partially restrained buildings "comparable" to fully restrained structures, yet it recommends that they are only used in low seismic regions. The report points out that the weaker connections localize damage and may cause a soft-story collapse. However, precisely this behavior may, if properly

controlled, provide some certainty to the otherwise ambiguous plastic hinge formation. Moreover, FEMA-355C recognizes semi-rigid connections affect the structural period; consequently, they alter the seismic response of the building, but little is known about the triggered changes. Additional evaluation is required to determine secondary effects such as higher structural modes and moment redistribution. The state-of-the-art report summarizes major design philosophies concerning semi-rigid constructions in the following paragraph:

> "Present seismic codes have essentially eliminated partially restrained connections in highly seismic regions. One can argue that more frame bays with relatively stiff partially restrained connections can provide the same stiffness as fewer frame bays with fully restrained connections, and that seismic behavior could be improved by increasing the redundancy through the use of many moment-resisting connections." (FEMA-355C)

This conclusion, while complete in the context of current knowledge, invites many questions. Kasai et al. (1999) and Maison et al. (2000) are among the researchers, who have studied buildings with all connections being semi-rigid; however, the knowledge on hybrid structures, which combines the use of both fully and partially restrained connections, is sparse. An insight to the seismic behavior of hybrid systems may prove to be beneficent to future design practices.

The history of seismic provision testifies that design can always be improved, and comprehension of structural behavior is the key to adequate

building performance. With this in mind, the perpetual race between human knowledge and natural forces is only possible because of new discoveries.

1.3. Objectives

The objective of this research is to explore the seismic response of steel frames by replacing selected fully restrained connections with semi-rigid connections. The goal is to find a pattern in placing partially restrained connections that would optimize seismic response. This is done by monitoring moment redistribution in frames having different connection compositions and by searching for common load paths or a preeminent structural response. Earthquake records with different intensities and frequencies are applied to evaluate the effects of the proposed hybrid system on the modeled buildings. Once several favored hybrid frames are selected, the properties of multiple commonly used moment connections are inputted, and results are compared.

Overall, this research aims to expand knowledge about semi-rigid connections and their potential application in lateral load moment-resisting frames likely to experience seismic loads. The goal is to find a hybrid system that would optimize global seismic response and reduce material, construction and potentially rehabilitation costs. This study will also lay the grounds for even closer evaluation of buildings with mixed connection properties.

CHAPTER 2

BACKGROUND ON NONLINEAR FRAME ANALYSIS AND STEEL CONNECTIONS

2.1. First Order Linear Elastic Analysis

First order linear elastic analysis provides a basic linear relationship between the load applied on a structure and the displacement resulting from this load. This method assumes the displacement associated with the applied loads is small compared to the height of the building, and it could be neglected in the solution of the stiffness matrix. Therefore, second order effects due to geometric changes are ignored, and all members in a frame have constant stiffness independent of the axial force applied to the corresponding member. This constant stiffness is the slope of the line corresponding to the linear elastic model labeled in Figure 2.1. The initial slopes of all other types of analyses coincide with it, because they are essentially identical if the applied loads are insufficient to allow for the development of second order effects and/or inelastic behavior.

This analytical method is often selected because of its simplicity and favorable computational time. Superposition is also feasible, which allows the application of multiple independent loads that are superimposed at later time. However, the first order linear elastic analysis lacks accuracy compared to other

methods, because of its inability to consider material nonlinearity and geometric effects such as P-Δ and P-δ.

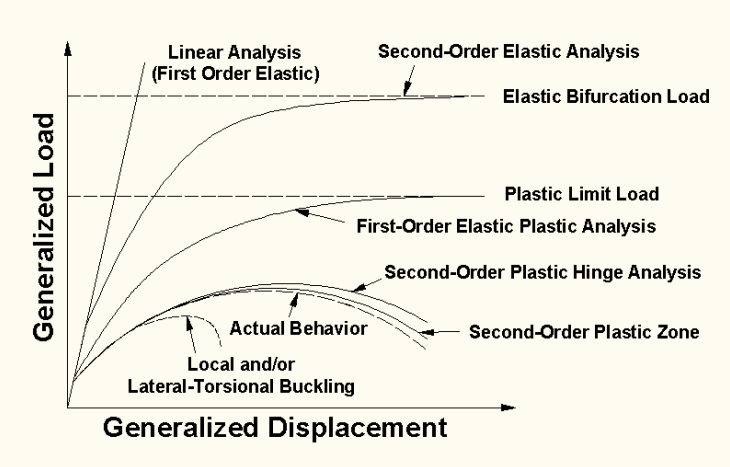

Figure 2.1 General Analysis Types for Frame Structures [2]

2.2. Second-Order Non-linear Elastic Analysis

Second-order non-linear elastic analysis improves the accuracy by considering element and structural geometric effects, P-δ and P-Δ respectively. The non-linear behavior developed as a result of geometric changes in the structure is conceptually presented in Figure 2.1. Figure 2.2 presents both element geometric nonlinearities, P-δ, and structural geometric nonlinearities, P-Δ. The deflections introduce a higher moment demand resulting from the axial load developed due to the frame self-weight. The stiffness matrix is adjusted to reflect these changes; however, this correction introduces additional deflections. This iterative process continues until equilibrium is reached. Unfortunately, superposition is not applicable for the second-order non-linear analysis, because the stiffness matrix is dependent on the deflected shape,

which is changed multiple times during the process of obtaining the final solution. In addition, this method is overly conservative because yielding of member material is not modeled as implied by the term “elastic.”

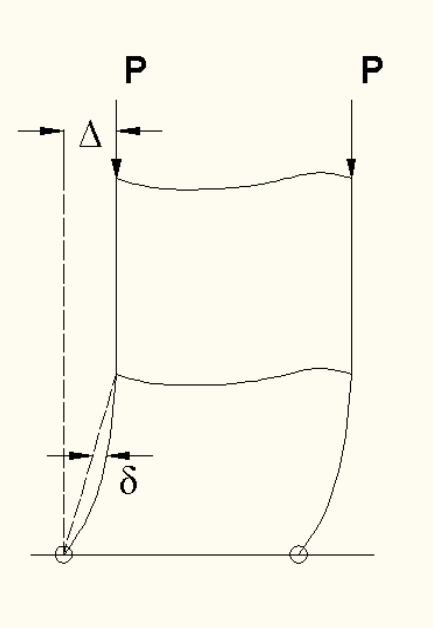

Figure 2.2 The P-δ and P-Δ effect [2]

2.2.1. The P-δ Effect

It is recognized that when a member deforms, the axial load applied to it will reduce its stiffness as a result of the additional moment developed in the member. This phenomenon is known as the P-δ effect. Its magnitude is related to the axial load applied to the structural member. The P-δ effect is modeled using *stability stiffness functions* if beam-column formulation is employed and *geometrical stiffness*, also known as *initial stress*, if finite element analysis is applied.

2.2.2. The P-Δ Effect

The P-Δ effect reflects changes in the structural geometry. The transformation matrix, used to derive the stiffness matrix, requires updates to reflect changes to frame coordinates. This is done by modifying the Lagrangian transformation at each iterative step by adding the horizontal and vertical displacement to the corresponding proceeding coordinates. The updated transformation matrix is used to include effects from global displacements.

2.3. Second-Order Non-linear Inelastic Analysis

Elastic analysis assumes sudden loss of member strength. However, in practice structural elements experience gradual strength reduction as a result of material properties. This modeling oversight may become significant for structural steel shapes like I-shapes, H-shapes and tubes and employing elastic analysis becomes uneconomical. Therefore, researchers implement inelastic analysis to include material nonlinearities such as steel yielding.

Yielding starts when the outer fiber of a member cross section is loaded up to the material yield moment, My. As additional load is applied, yielding spread across the section towards the plastic neutral axis. The cross section begins to lose its strength caring capacity as fibers start reaching the ultimate moment, Mu. This gradual loss of strength across the cross section of a member is termed “plastification.” Yielding also spreads along the element length, in which case a plastic zone is formed. Both outcomes can be modeled based on the expected degree of accuracy. In the first case, plastic hinges are

assumed to form at the ends of a member; therefore, all material non-linearities are lumped into two nodes and the remaining section of the element stays elastic. This is known as the *concentrated plasticity approach*. The more accurate method is to model the plastic zone by dividing the element into elastic and inelastic sections. This approach is termed *distributed plasticity.* Third, more accurate method also exists and models the combined effects of axial force and flexure in I-shapes and H-shapes. It is referred to as the *section assemblage approach.* More details for each method are provided in the proceeding sections.

2.3.1. Concentrated Plasticity Approach

Yielding of steel develops along the length of a member and across its cross-section, starting from the outer fiber and progressing towards the plastic neutral axis. Plastification, a term used to describe yielding across the member cross section, occurs at a given point and causes the formation of a plastic hinge. In computer modeling, this hinge is denoted by a zero-length spring, while the structural element remains elastic. Therefore, the concentrated plasticity approach lumps the effects of material non-linearities into the member end nodes. This assumption simplifies the actual behavior of the member, but allows for significant savings in computational time. The concentrated plasticity approach has proven to be satisfactory in producing a good approximation of the real behavior of beams and columns. Popular methods to model plastic hinges are elastic-plastic hinge method, column tangent modulus method,

beam-column stiffness degradation method, beam-column strength degradation method, and end-spring method.

2.3.2. Distributed Plasticity Approach

A more accurate approach to model material non-linearities is by accounting for the plastic zone region, a segment of an element that experiences a demand larger than the yield moment. In this case, the structural element is divided into sections containing either elastic or plastic characteristics. This method is known as the distributed plasticity approach. The plastic zone model most effectively approximates real-world material non-linear behavior, while providing the means to account for other factors, which influence member performance such as residual stresses and fabrication imperfections. However, this method requires a considerable amount of computational time, and it becomes exponentially impractical as the complexity of tested frames increases. The plastic zone region can be modeled by either the traditional plastic zone method or the simplified plastic zone method.

2.3.3. Section Assemblage Approach

A commonly used approach to finding the section capacity of a member subjected to a combination of compressive and flexural loading is using an empirically derived linear relationship between the axial and moment strengths. This relationship is derived from the stress equation for elastic analysis, yet it is used to provide an approximation for plastic analysis. Therefore, a conceptual error is introduces, and its magnitude depends on the degree of plastification.

Chen and Lui (1991) have proposed the subsequent linear equations to obtain an estimate of the section capacity, and this relationship is implemented by the American Institute of Steel Construction (AISC 2005):

$$\frac{P}{P_y}+\frac{8}{9}\frac{M}{M_p}=1.0 \text{ for } \frac{P}{P_y}\geq 0.2$$

$$\frac{P}{2P_y}+\frac{M}{M_p}=1.0 \text{ for } \frac{P}{P_y}< 0.2 \qquad (2.1)$$

Each term in the above equations is defined as follows:

$P_y=\sigma_y A$ is the squash load of the cross section,

$M_p=\sigma_y Z_p$ is the plastic moment capacity of member loaded by pure bending,

σ_y is the yield stress of material,

A is the cross-sectional area,

Z_p is the plastic modulus,

M, P are the bending moment and axial force at cross section.

This relationship provides a lower bound cross-sectional capacity for members subject to axial force and flexure. Therefore, it may become overly conservative for members experiencing plastic deformations, and analysis based on this approach can produce uneconomical estimates. Furthermore, this method develops a discontinuity or kink in the axial force – moment curve for $\frac{P}{P_y}=0.2$ as shown in Figure 2.3.

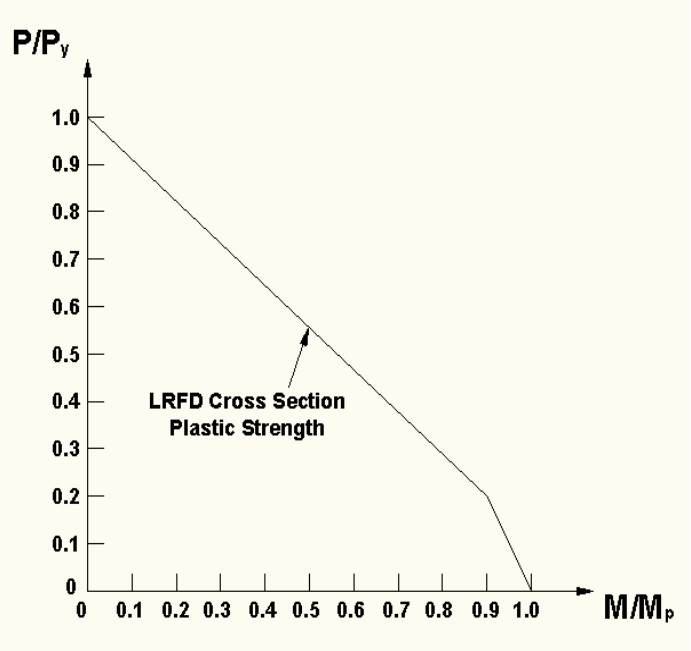

Figure 2.3 AISC-LRFD Bilinear Strength Curve (AISC-LRFD, 1986)

A more precise method is to divide the structural member into a large number of finite sections, and apply the initial stress to each of them. The initial stress is a combination of the axial stress experienced by the member and the residual stress developed during the fabrication and transportation of the element to the construction site. Then, the curvature is gradually increased until the final strain in the cross section is obtained. A mathematical function for the elasto-plastic analysis is developed based on the moment – curvature curves generated during this process. However, this approach is complicated for manual check and evaluation, which designates it as impractical in general design practice.

2.3.3.1. Formulation of Initial and Full Yield Surfaces

Chan and Chui (1997) use the section assemblage approach to develop a derivation for I and H structural steel shapes that aims to approximate the simplicity of the linear axial force - moment relationship and the accuracy of the mathematical function for elaso-plastic analysis discussed previously. The fundamental assumption they make is that the web of the member carries all axial force and the remaining non-yielded area of the cross section takes the applied moment. As a result, both the first yield and the fully plastic functions can be defined exclusively based on the geometric properties of the cross section. This method eliminates the need to apply empirical derivations such as the bilinear function suggested in AISC (2005).

The plastic zone for annealed sections that resists the axial force can be determined using the following equations:

$$\eta = \frac{P}{2\sigma_y t} \qquad \text{for } \eta \le \frac{d}{2}$$

$$\eta = \frac{(P - \sigma_y t d)}{2B\sigma_y} + \frac{d}{2} \qquad \text{for } \frac{d}{2} \le \eta \le \frac{d}{2} + T \tag{2.2}$$

Where P is the axial load,

η is the half-depth of yielded area for axial load,

σ_y is the yield stress,

B is the flange width,

t is the web thickness,

T is the flange thickness

d is the depth of web.

Figure 2.4 illustrates this concept for I and H structural steel shapes.

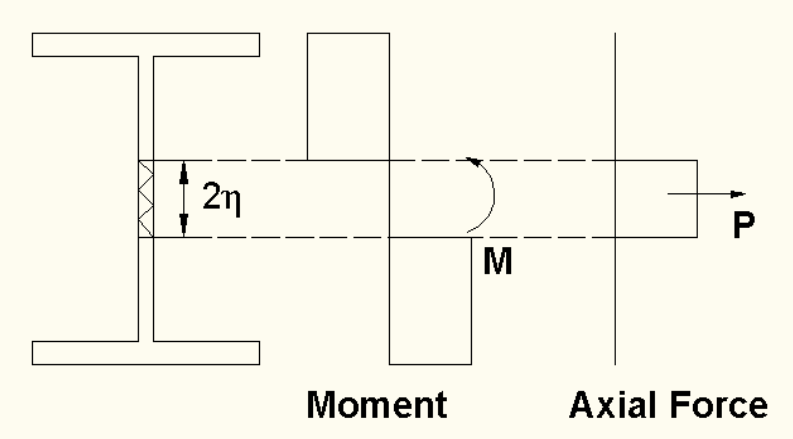

Figure 2.4 The Section Assemblage Concept [3]

Once the plastic zone region is established, the portion of the cross section that has not yielded is calculated. It is used to determine the section moment resistance, since it is assumed to carry the full flexural load imposed on the cross section. The following equations are applicable:

$$M_{pr} = \left[BT(D-T) + \left(\left(\frac{d}{2} \right)^2 - \eta^2 \right) t \right] \sigma_y \qquad \text{for } \eta \le \frac{d}{2}$$

$$M_{pr} = \left[\left(\frac{D}{2} \right)^2 - \eta^2 \right] B\sigma_y \qquad \text{for } \frac{d}{2} \le \eta \le \frac{d}{2} + T, \tag{2.3}$$

in which

M_{pr} is the reduced plastic moment capacity of section when axial load is applied, and

D is the total depth of the section.

Equation 1.3 is used to graph Figure 2.5, where envelopes for the initial yielding and full plastification of the cross section are presented. In the figure, if the moment-axial force coordinates for a section fall within the first yield envelope, the member remains elastic and no modification of the spring stiffness is required. On the other hand, if the coordinates fall outside the full yield surface, the spring has lost all of its stiffeness, and it is no longer capable of transferring any load. The moment capacity of the cross section has reached the ultimate value, Mu, and any additional flexural load is redistributed to other members of the building. Finally, if the moment-axial force coordinates fall in the area between the two envelopes, elasto-plastic analysis reflects gradual loss of strength in the spring.

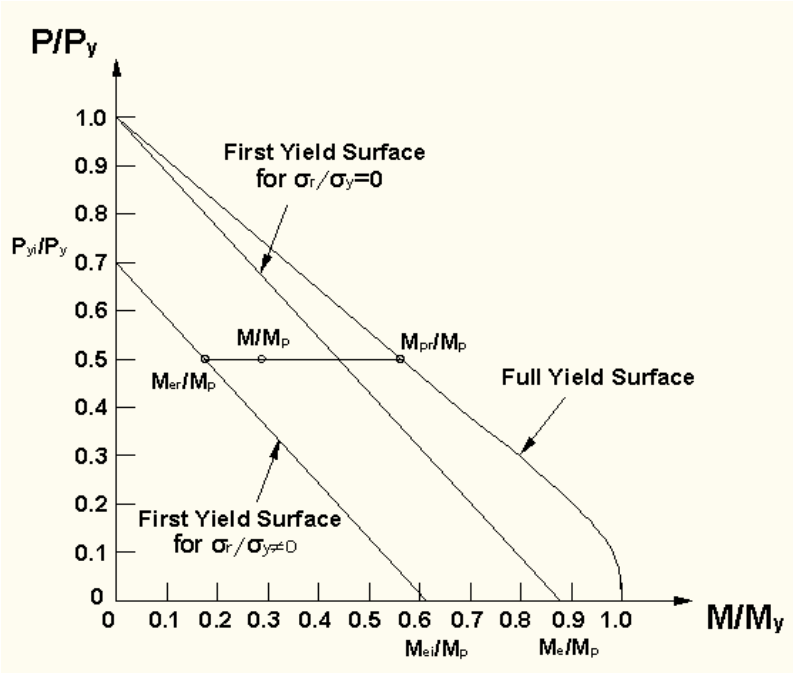

Figure 2.5 First Yield and Full Yield Surfaces of Section [3]

The first yield surface is produced based on the moment at which the section begins to experience inelastic deformations. This moment is known as the elastic moment, Me, and it is the product of the yield stress, σ_y, and the plastic modulus about the principle axis, Z_e. This moment is modified to reflect the effects of residual and axial force stress as shown in equation 1.4.

$$M_{er} = (\sigma_y - \sigma_r - \frac{P}{A})Z_e \qquad (2.4)$$

In this equation,

M_{er} is the reduced first yield moment,

σ_r is the residual stress, and

A is the cross-sectional area.

Equation 1.4 presents a linear relationship, because the stress is linearly proportional to the strain during the elastic behavior of the member. The first yield surface line in Figure 2.5 reflects this observation.

2.3.3.2. Refined Plastic Hinge Method

Once the reduced first yield moment, M_{er}, and the reduced plastic moment, M_{pr}, are known, the can be used to determine the section spring stiffness, S, as follow:

$$S = \frac{6EI}{L}\frac{|M_{pr} - M|}{|M - M_{er}|} \text{ for } M_{er} < M < M_{pr}, \quad (2.5)$$

where

EI is the member flexural rigidity,

L is the member length,

M_{er} is the reduced first yield moment calculated per equation 1.4, and

M_{pr} is the reduced plastic moment, calculated per equation 1.3.

According to equation 1.5, the section spring stiffness, S, is infinitely large when the applied moment is equal to the reduced first yield moment. This mathematical derivation is interpreted as allowing full moment continuity across the spring. On the other hand, if the applied moment matches the reduced plastic moment, the spring stiffness becomes equal to zero. Therefore, no moment is transferred across the spring. The constant $\frac{6EI}{L}$ is used to define

the transition curve between the two extremes, and it originates from the element stiffness.

2.3.3.3. The Elastic-Plastic Hinge Method

The elastic-plastic hinge method assumes the axial load-moment relationship is either elastic or plastic, and no transition period is modeled. Therefore, the first yield and fully plastic surfaces in Figure 2.5 coincide, and the cross section reaches its ultimate capacity as soon as yielding is initiated. According to this method, no degradation of spring stiffness occurs. Instead, the stiffness is assumed to be infinitely large until the yield moment is reached, at which point the spring loses any load transferring capacity. For computational purposes, large and small numerical values are given to the section stiffness for elastic and plastic behavior, respectively:

$$S = 10^{+10}\frac{EI}{L} \text{ for } M < M_{pr}$$

$$S = 10^{-10}\frac{EI}{L} \text{ for } M = M_{pr}. \qquad (2.6)$$

2.4. Solution Method Used for Non-Linear Analysis: Newton-Raphson Method

Since the cross sectional stiffness in non-linear analysis varies, finding the equilibrium path requires an iterative solution. Two methods are widely used for this purpose in computer software, namely the conventional Newton-Raphson method and the modified Newton-Raphson method. The first approach starts with the initial stiffness obtained during the elastic analysis and

extends this slope until the first load step is reached. The corresponding solution is calculated and the stiffness is modified to reflect any changes implemented at this point. This process continues until the solution for the first load step is reach, and the same process is applied to proceeding load steps until the entire equilibrium path is determined. This procedure is visually presented in Figure 2.6.

The modified Newton-Raphson method uses similar techniques except that it does not update the stiffness at each iterations step. Rather, the initial stiffness is used throughout the load cycle. This approach is shown in Figure 2.7. Either method can prove advantageous when computational time is evaluated depending on the initial conditions and equilibrium path.

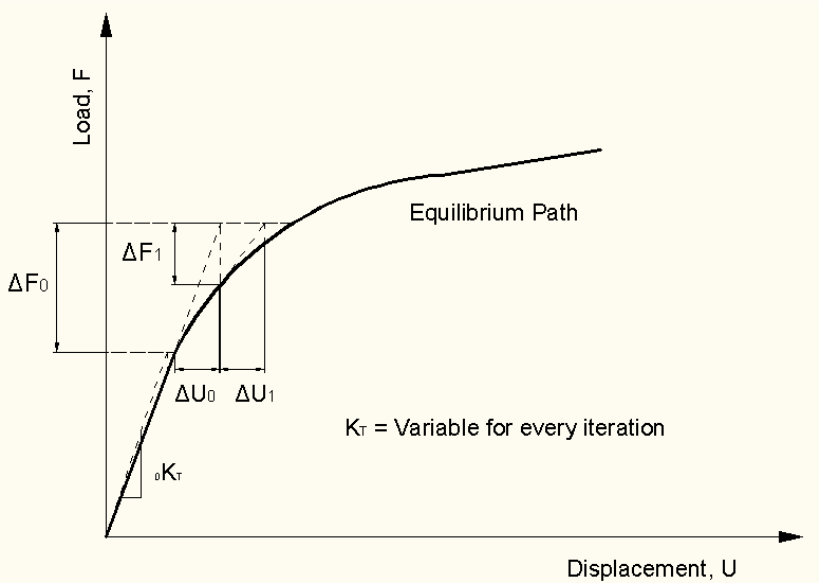

Figure 2.6 Conventional Newton-Raphson Method

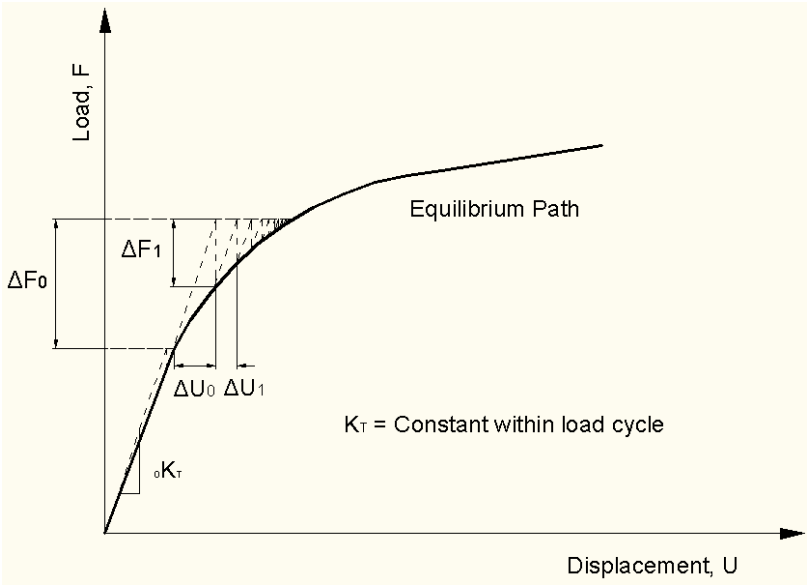

Figure 2.7 Modified Newton-Raphson Method

2.5. Techniques and Algorithms for Linear and Non-Linear Analysis

Linear and non-linear analyses require the solution of different equations. Modal analysis is used in linear frames, while transient analysis is applied when geometric and material non-linearities are considered.

2.5.1. Modal Analysis

The equation of motion for a linear single degree-of-freedom system subjected to a dynamic load is given as follows:

$$m\ddot{u} + c\dot{u} + ku = -m\ddot{u}_g(t) \tag{2.7}$$

where

m is the mass matrix,

$\ddot{u}$ is the mass acceleration matrix,

c is the viscous damping coefficient,

$\dot{u}$ is the mass velocity matrix,

k is the stiffness matrix,

u is the displacement matrix, and

$\ddot{u}_g(t)$ is the earthquake ground acceleration.

The mass matrix of the system, m, must be known for the equation of motion to be solved. Multiple methods are currently available to determine the mass matrix of a system. In this research, the lumped-mass approach is utilized to determine the mass matrixes for the studies frames. According to this method, dead load of the system is applied at the end nodes of beams, where the magnitude of the mass assigned to each node is calculated based on the node's tributary area. Therefore, a node in the middle of a frame has more mass assigned to it than an end node does. The lumped-mass approach is conceptually shown in Figure 2.8.

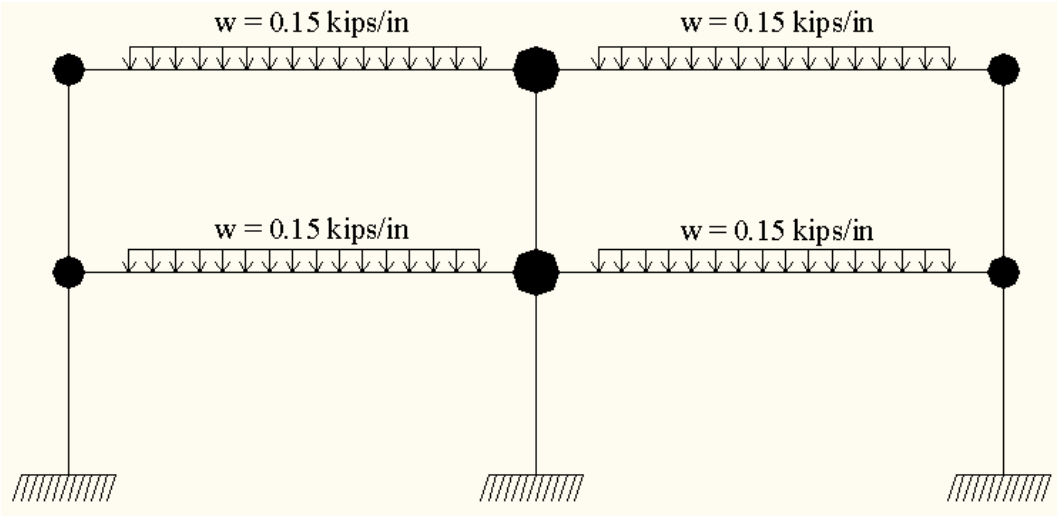

Figure 2.8 Mass Distribution Based on the Lumped-Mass Approach

If equation 2.7 is divided by the mass matrix, m, it can be re-written as follows:

$$\ddot{u} + 2\xi\omega_n\dot{u} + \omega_n{}^2 u = -\ddot{u}_g(t) \tag{2.8}$$

where

ω_n is the natural frequency of the system, and

ξ is the damping ratio of the system.

Since the natural frequency, ω_n, and the natural period, T_n, are inversely proportional, the displacement of an elastic structure for a given earthquake acceleration, $\ddot{u}_g$, is only dependent on the damping ratio, ξ, and the natural period, T_n.

Equation 1.7 can be solved for the first time step using the initial conditions for displacement and velocity, $u_0 = u(0)$ and $\dot{u}_0 = \dot{u}(0)$ respectively. Once a solution for the first time step is obtained, the results are used as initial conditions for the next iteration. This process continues until the end of the earthquake acceleration record is reached. However, the solution at each time step needs to meet three important criteria. First, it must converge meaning it is approaching the exact solution as more iteration steps are conducted. Secondly, the solution needs to be stable in the presence of numerical errors. Last but not least, the solution must be accurate and must give a close approximation of the exact answer. These criteria are addressed by OpenSees, the software package used in this study.

Different methods for solving the time-stepping procedure discussed above are available in literature. The three approaches discussed by Chopra (2007) are based on the interpolation of the excitation function, the finite difference expressions of velocity and acceleration and the assumed variation of acceleration. More information on each method is available in the mentioned reference.

2.5.2. Transient Analysis

The equation of motion for a non-linear single degree-of-freedom system subjected to a dynamic load is given as follows:

$$m\ddot{u} + c\dot{u} + f_s(u,\dot{u}) = -m\ddot{u}_g(t) \tag{2.9}$$

where

$f_s(u,\dot{u})$ is the resisting force. For linear elastic analysis $f_s(u,\dot{u}) = ku$ as seen in the previous section, but if geometric and material non-linearities are introduced, the resisting force becomes dependant on prior displacement history and velocity at each time step. Equation 1.9 can be solved for the first time step using the initial conditions for displacement and velocity, $u_0 = u(0)$ and $\dot{u}_0 = \dot{u}(0)$ respectively. Once a solution for the first time step is obtained, the results are used as initial conditions for the next iteration. This process continues until the end of the earthquake acceleration record is reached.

If equation 1.9 is divided by the mass matrix, m, equation 1.10 originates.

$$\ddot{u} + 2\xi\omega_n\dot{u} + \omega_n{}^2 u_y \widetilde{f}_s(u,\dot{u}) = -\ddot{u}_g(t) \qquad (2.10)$$

where

u_y is the deformation at which yielding occurs, and

$\widetilde{f}_s(u,\dot{u})$ is the function describing the force-deformation relationship. Therefore, for a given earthquake acceleration, $\ddot{u}_g$, the displacement of an inelastic structure is dependent on the damping ratio, ξ, and the natural period, T_n, which is inversely proportional to the natural frequency, ω_n, and the initial yield deformation, u_y. In addition, the ductility factor, μ, where $\mu(t) = \frac{u(t)}{u_y}$, depends in the following parameters: ω_n, ξ and the normalized yield strength of the elasto-plastic system, $\bar{f}_y$. As previously discussed, the methods covered by Chapra (2007) or any other alternative approach available in the literature can be used to solve the time-stepping process of this iterative method.

CHAPTER 3

HYBRID FRAMES

3.1. Introduction

Two steel frames are chosen for this research – a 2-story, 3-bay frame represents a typical low-rise building, while conclusions for performance of high-rise structures are drawn from a 20-story, 5-bay frame. Multiple hybrid combinations for each frame are introduced, in which semi-rigid connections' location differs. Appropriate building notation for each frame is incorporated. The analysis starts with a static pushover analysis, which gives an initial estimate of the expected dynamic response. Then, wind loads calculated as per the American Society of Civil Engineers (ASCE) provisions are applied in addition to gravity loads. A cyclic load pattern based on a displacement controlled solution is also applied to determine the energy dissipation capacity of the 20-story hybrid cases. Finally, several earthquake records from both the SAC Joint Venture database and the Pacific Earthquake Engineering Research (PEER) database are applied. The acceleration records chosen for this study reflect a variety of earthquake frequencies and intensities. The results for each hybrid case, which include member forces, lateral displacements, energy dissipation and moment-rotation development in the semi-rigid connections, are compared to evaluate the frames' performance.

3.2. Two-Story Frame

The 2-story, 3-bay frame used in this analysis to estimate the performance of low-rise buildings is similar to the second example presented in chapter 2 (Bhatti and Hingtgen 1995). Its elevation view and member sizes are shown in Figure 3.1. A total of fourteen hybrid models of this frame were developed, and the adopted building designation is $BL\_ST-B1,B2-S1,S2-LSR1,LSR2-L(K_i-K_f/K_i-M_y)-R(K_i-K_f/K_i-M_y)$, where

BL represents "building,"

ST is the total number of stories in the frame,

$B1$ is the bay where the first beam with semi-rigid connections is placed,

$B2$ is the bay where the second beam with semi-rigid connections is placed,

$S1$ is the story where the first beam with semi-rigid connections is placed,

$S2$ is the story where the second beam with semi-rigid connections is placed,

$LSR1$ is the location of semi-rigid connection(s) for the first beam, where valid entries are the left node (L), the right node (R) and both nodes (B),

$LSR2$ is the location of semi-rigid connection(s) for the second beam, where valid entries are the left node (L), the right node (R) and both nodes (B),

K_i is the initial connection stiffness in thousands for the left (L) and right (R) connections, respectively,

K_f/K_i is the ratio of post-yield to initial stiffness for the left (L) and right (R) connections, respectively, and

M_y is the yield moment for the left (L) and right (R) connections, respectively.

For instance, the frame in Figure 3.2 has semi-rigid connections placed on both side of the beams located at the first and second stories of the second bay, and the connections have an initial stiffness of 236,020 kips-in/rad (26,667 kN-m/rad), a post-yield stiffness of 2,360 kips-in/rad (267 kN-m/rad) and an yield moment of 1,000 kip-in (113 kN-m). Therefore, its abbreviated description is $BL\_2-2,2-1,2-B,B-L(236-0.01-1{,}000)-R(236-0.01-1{,}000)$. The remaining thirteen cases and their corresponding notations are presented in Figure 3.3 through Figure 3.15. It should be noted that a bi-linear model with no ultimate capacity is used to simulate the behavior of semi-rigid connections; thus, the three connection parameters used in the building notations are adequate to define the connection characteristics.

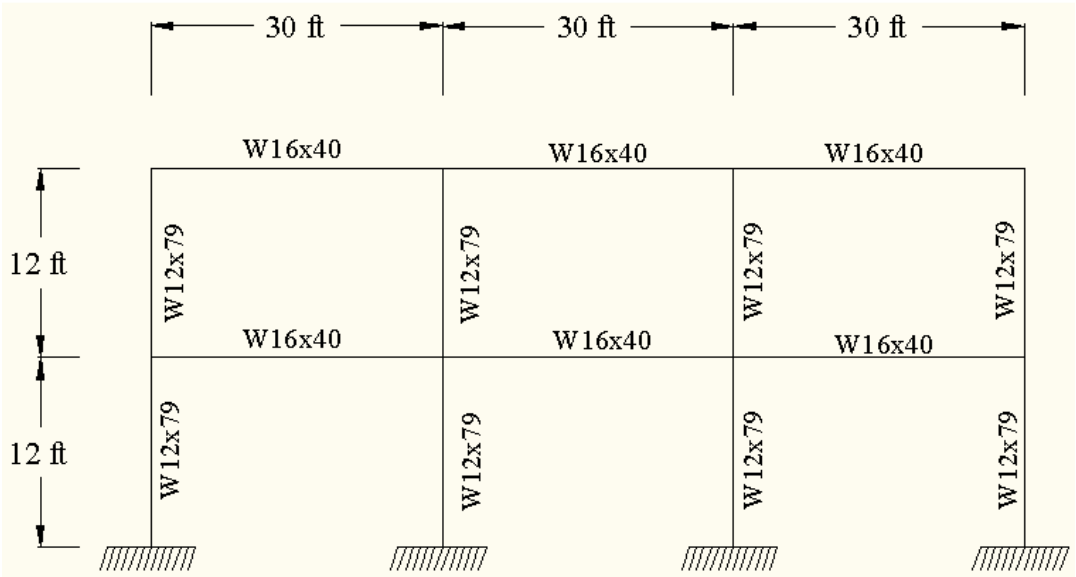

Figure 3.1 Two-Story Frame

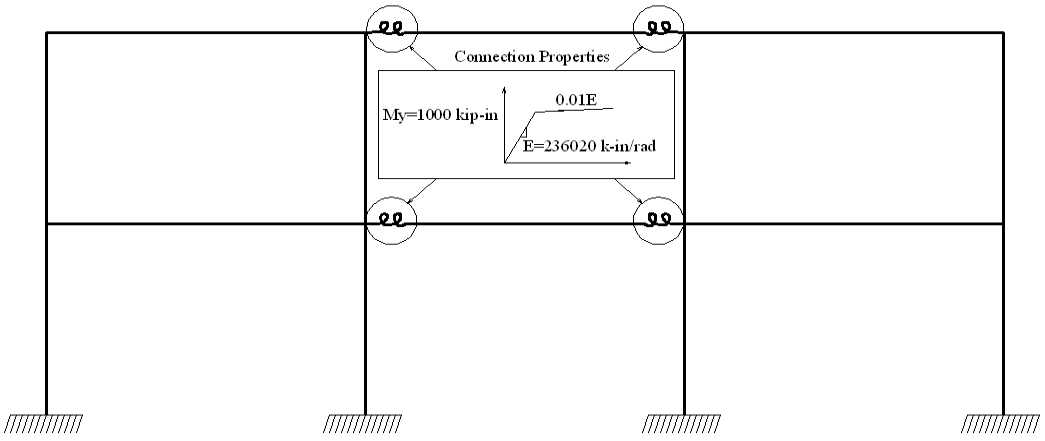

Figure 3.2 Connection Location and M-θ relation for
$BL\_2-2{,}2-1{,}2-B, B-L(236-0.01-1{,}000)-R(236-0.01-1{,}000)$

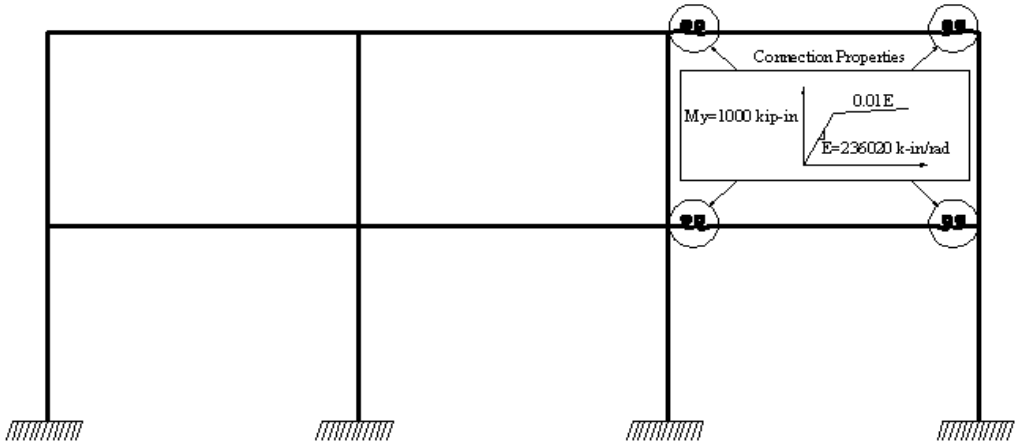

Figure 3.3 Connection Location and M-θ relation for
$BL\_2-3{,}3-1{,}2-B, B-L(236-0.01-1{,}000)-R(236-0.01-1{,}000)$

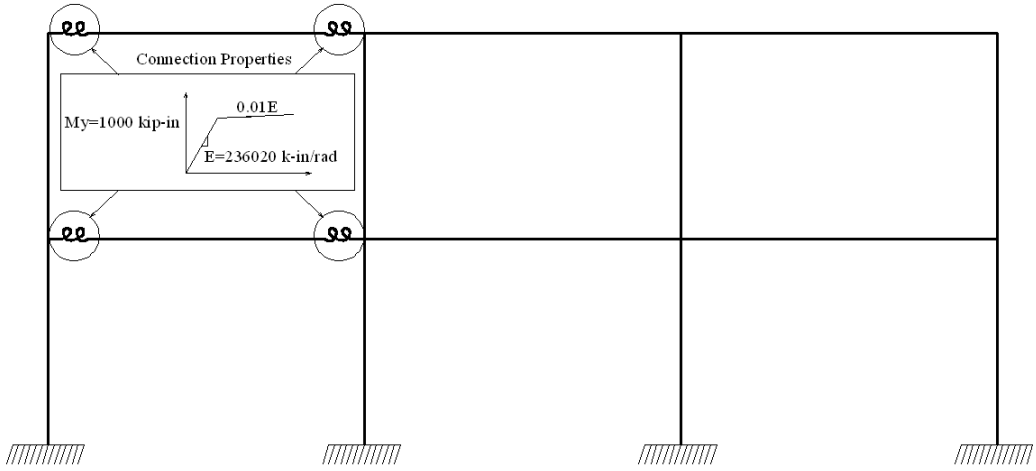

Figure 3.4 Connection Location and M-θ relation for
$BL\_2-1{,}1-1{,}2-B, B-L(236-0.01-1{,}000)-R(236-0.01-1{,}000)$

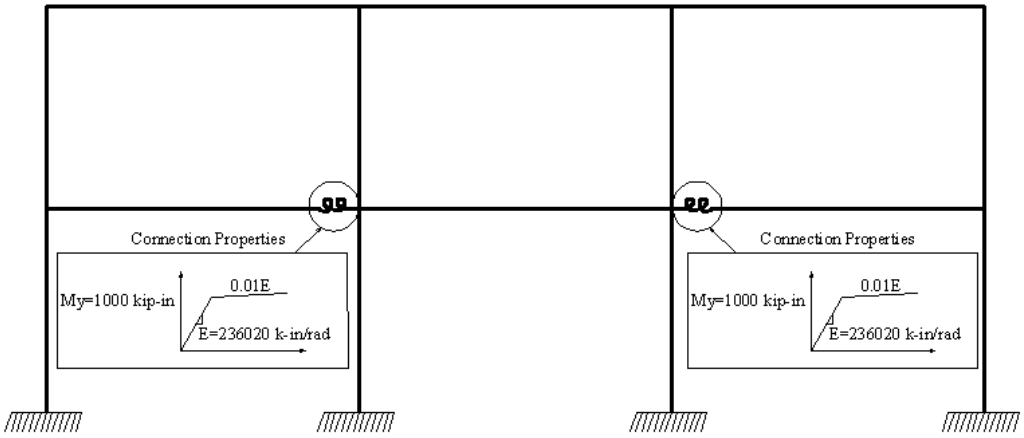

Figure 3.5 Connection Location and M-θ relation for
$BL\_2-1{,}3-1{,}1-R, L-L(236-0.01-1{,}000)-R(236-0.01-1{,}000)$

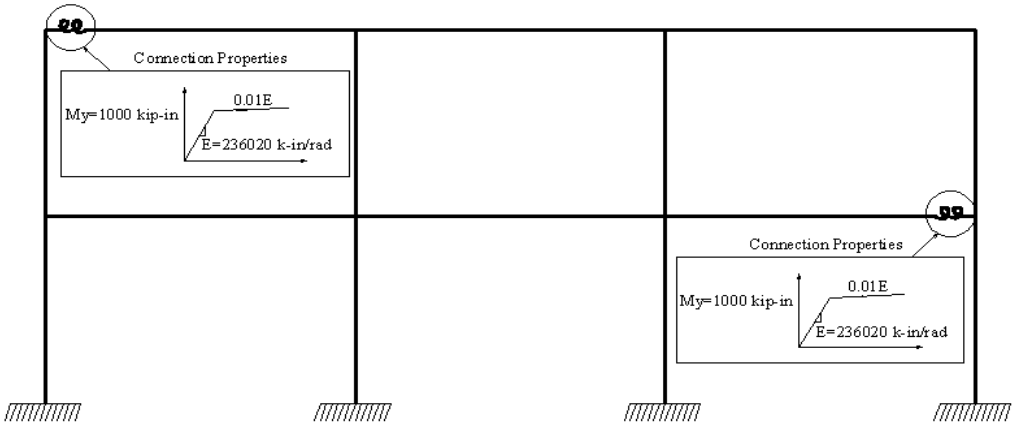

Figure 3.6 Connection Location and M-θ relation for
$BL\_2-1{,}3-2{,}1-L, R-L(236-0.01-1{,}000)-R(236-0.01-1{,}000)$

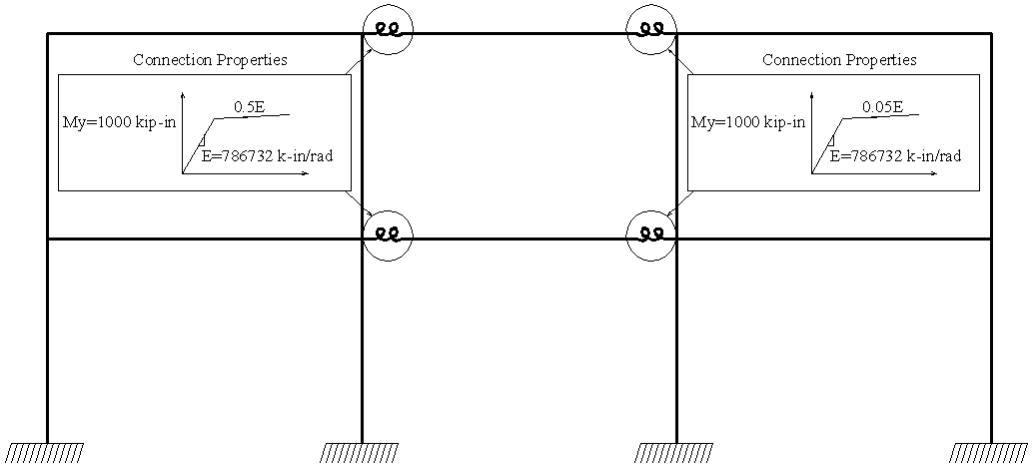

Figure 3.7 Connection Location and M-θ relation for
$BL\_2-2,2-1,2-B,B-L(787-0.5-1{,}000)-R(787-0.05-1{,}000)$

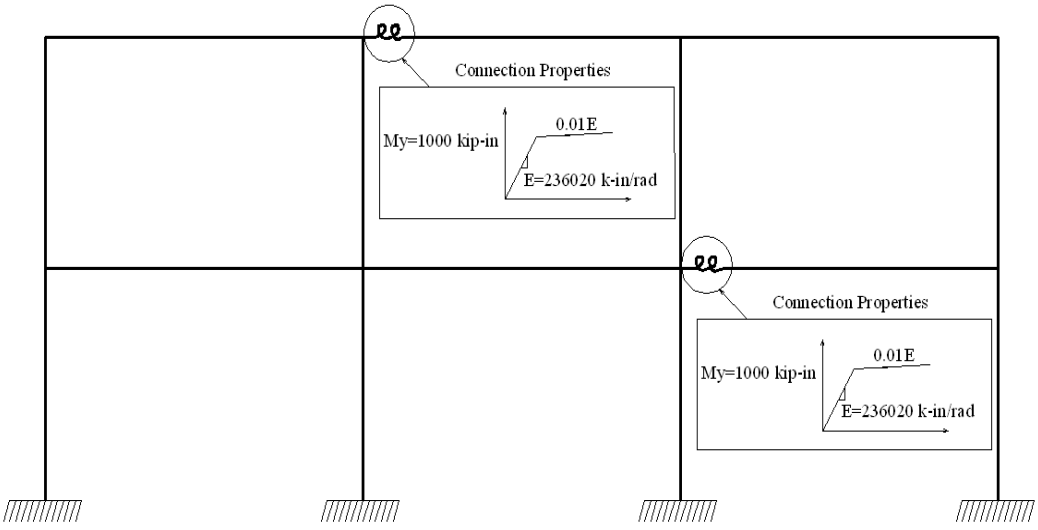

Figure 3.8 Connection Location and M-θ relation for
$BL\_2-2,3-2,1-L,L-L(236-0.01-1{,}000)$

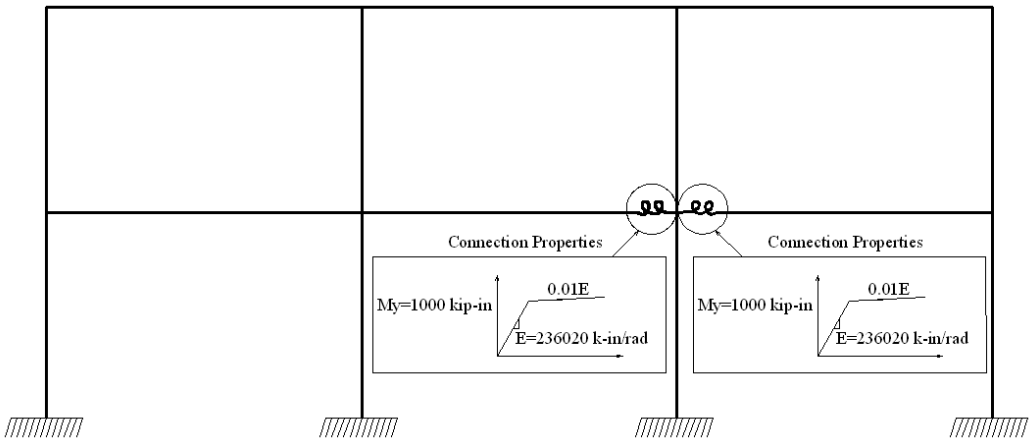

Figure 3.9 Connection Location and M-θ relation for
$BL\_2-2,3-1,1-R,L-L(236-0.01-1,000)-R(236-0.01-1,000)$

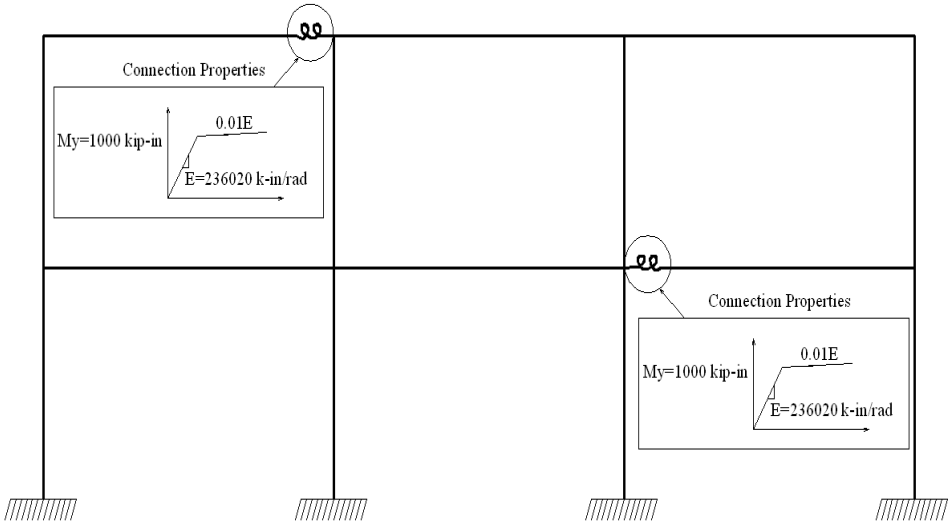

Figure 3.10 Connection Location and M-θ relation for
$BL\_2-1,3-2,1-R,L-L(236-0.01-1,000)-R(236-0.01-1,000)$

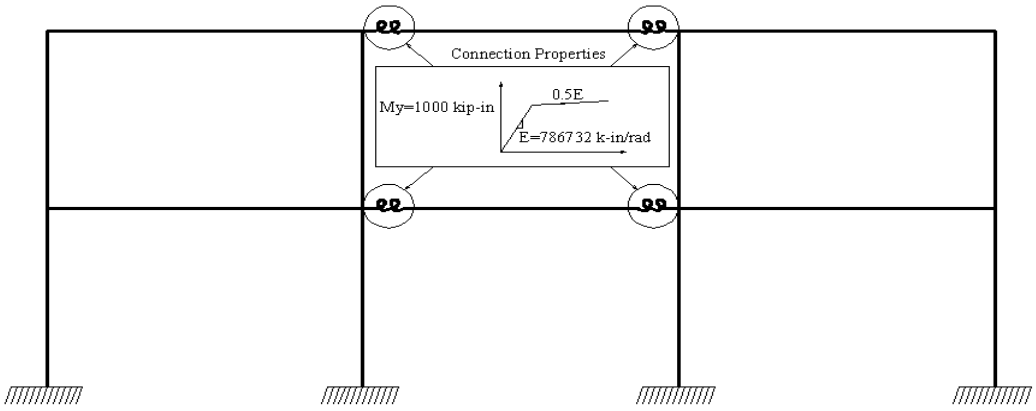

Figure 3.11 Connection Location and M-θ relation for
$BL\_2-2{,}2-1{,}2-B, B-L(787-0.5-1{,}000)-R(787-0.5-1{,}000)$

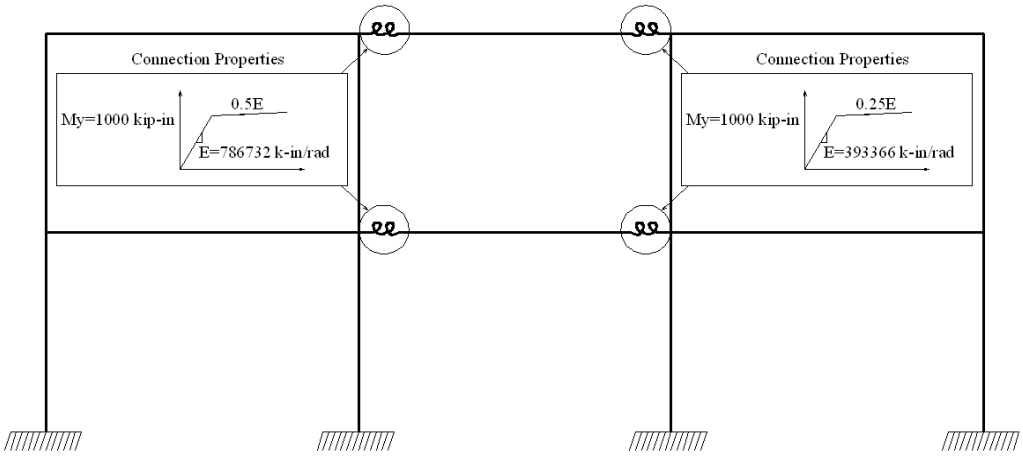

Figure 3.12 Connection Location and M-θ relation for
$BL\_2-2{,}2-1{,}2-B, B-L(787-0.5-1{,}000)-R(393-0.25-1{,}000)$

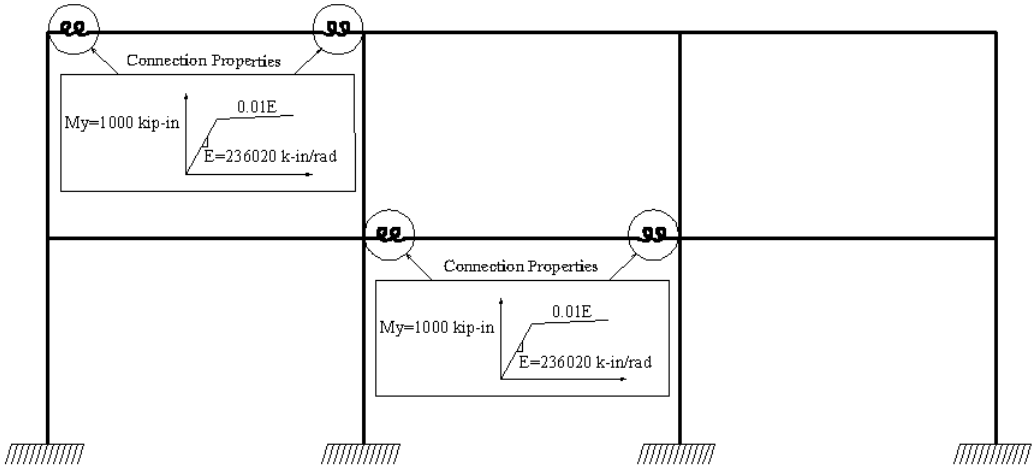

Figure 3.13 Connection Location and M-θ relation for
$BL\_2-1{,}2-2{,}1-B, B-L(236-0.01-1{,}000)-R(236-0.01-1{,}000)$

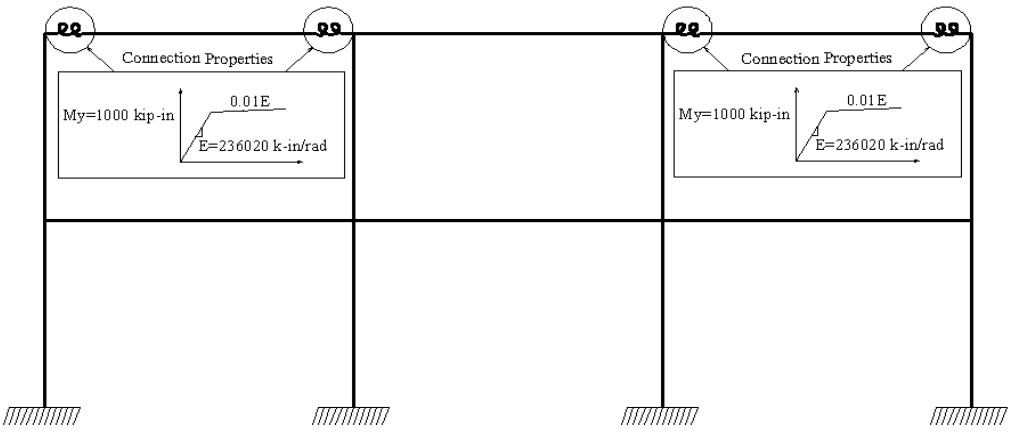

Figure 3.14 Connection Location and M-θ relation for
$BL\_2-1{,}3-2{,}2-B, B-L(236-0.01-1{,}000)-R(236-0.01-1{,}000)$

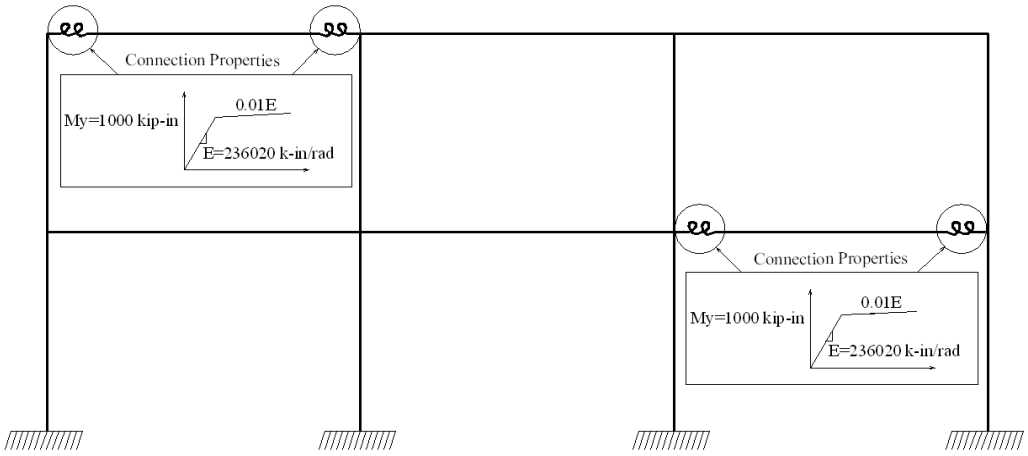

Figure 3.15 Connection Location and M-θ relation for
$BL\_2-1,3-2,1-B,B-L(236-0.01-1{,}000)-R(236-0.01-1{,}000)$

3.3. 20-Story Frame

The 20-story building used in this study is designed based on the 2000 International Building Code (IBC) provisions. The building geometry in plan and elevation views is shown in Figure 3.16. The geometry mimics a previously designed SAC building, which is a widely used model by researchers and professionals. The member sizes are adopted from Lee and Foutch (2006), where the response modification factor, R, has a value of 8, a number currently required for moment resisting frames by the National Earthquake Hazard Reduction Program (NEHRP) provisions. Information about the member sizes is summarized in Table 3.1.

Six hybrid models were presented for this 20-story frame. The standard building description is $BL\_ST-BS:ES-LSR-K_i-K_f/K_i-M_y$, where

BL represents "building,"

ST is the total number of stories in the frame,

BS is the beginning story in the range of stories where semi-rigid connections is placed,

ES is the end story for in range of stories where semi-rigid connections is placed,

LSR is the location of semi-rigid connections, where valid entries are the all nodes (A), nodes at the middle of a frame (M) and nodes at the ends of a frame (E). If partially restrained connections are placed at the middle of the frame, all nodes except beam-to-column connections in exterior columns are given semi-rigid properties. On the other hand, if partially restrained connections are placed at the ends of a frame, both nodes of beams connected to an exterior column are assigned semi-rigid connection properties.

K_i is the initial connection stiffness in thousands for the left (L) and right (R) connections, respectively,

K_f / K_i is the ratio of post-yield to initial stiffness for the left (L) and right (R) connections, respectively, and

M_y is the yield moment for the left (L) and right (R) connections, respectively.

For instance, the frame in Figure 3.17 has semi-rigid connections placed along the entire story starting from the basement, assigned a value of zero in the notation, through the fifth story, and the connections have an initial stiffness of 236,020 kips-in/rad (26,667 kN-m/rad), a post-yield stiffness of

2,360 kips-in/rad (267 kN-m/rad) and an yield moment of 1,000 kip-in (113 kN-m). Therefore, its abbreviated description is $BL\_20-0:5-A-236-0.01-1{,}000$. In Figure 3.18, semi-rigid connections in the ninth through the thirteenth stories are placed along the entire floor, and the connections have an initial stiffness of 236,020 kips-in/rad (26,667 kN-m/rad), a post-yield stiffness of 2,360 kips-in/rad (267 kN-m/rad) and a yield moment of 1,000 kip-in (113 kN-m). Therefore, its abbreviated description for this figure is $BL\_20-9:13-A-236-0.01-1{,}000$. The remaining four cases and their corresponding notations are presented in Figure 3.19 through Figure 3.22. It should be noted that a bi-linear model with no ultimate capacity is used to model the behavior of semi-rigid connections; thus, the three connection parameters used in the building notations are adequate to define the connection characteristics.

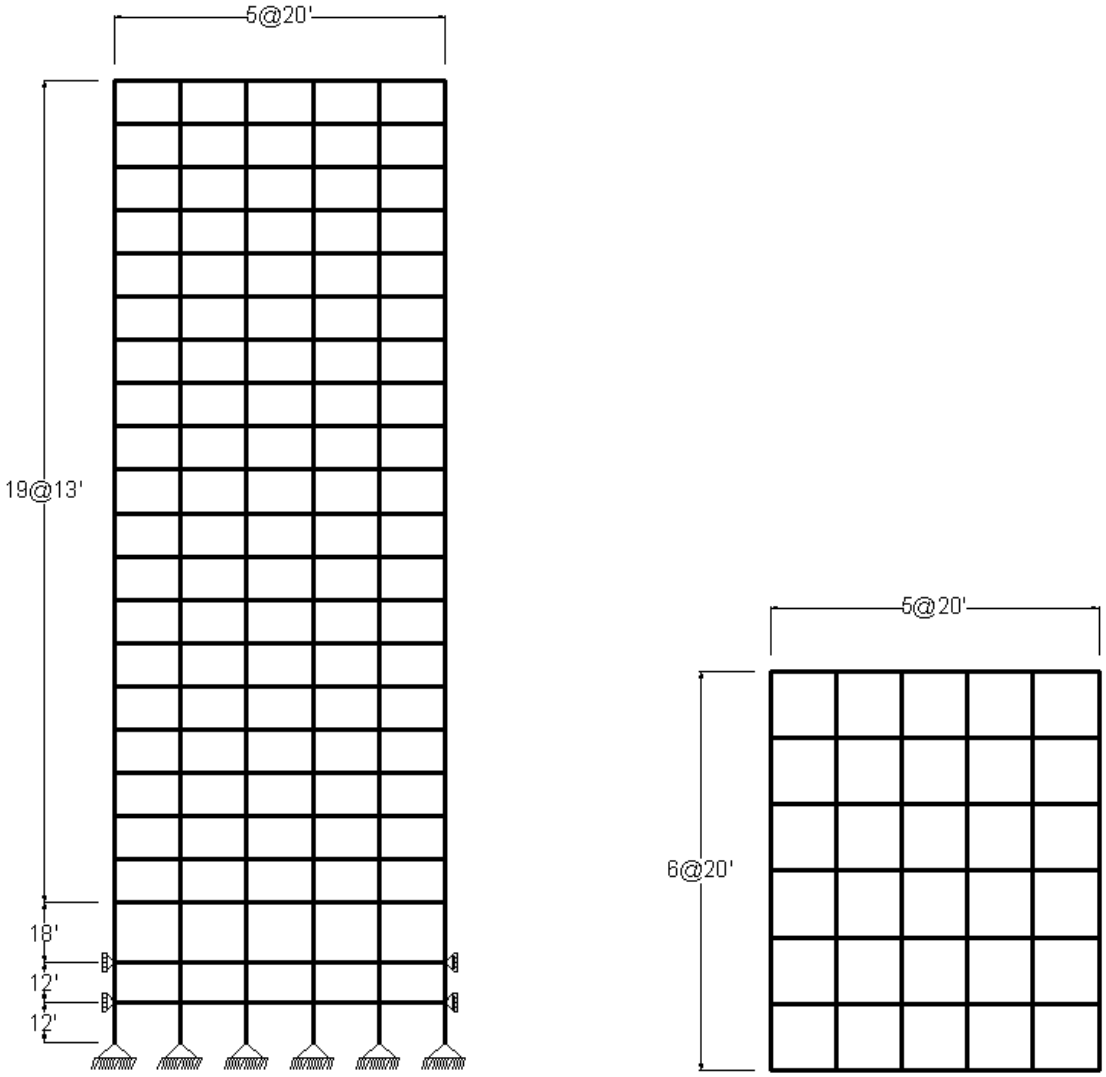

a) b)

Figure 3.16 20-Story SAC Frame: a) Elevation View, b) Plan View

Table 3.1 Member Sizes for 20-Story Frame

Story	Exterior Column	Interior Column	Beam
Basement	15x15x2.0	W24x279	W14x22
1	15x15x2.08	W24x279	W30x90
2	15x15x2.08	W24x279	W30x90
3	15x15x1.25	W24x250	W30x90
4	15x15x1.25	W24x250	W30x90
5	15x15x1.25	W24x250	W27x84
6	15x15x1.25	W24x250	W30x90
7	15x15x1.25	W24x250	W30x90
8	15x15x1.25	W24x250	W30x90
9	15x15x1.0	W24x229	W30x90
10	15x15x1.0	W24x229	W30x90
11	15x15x1.0	W24x229	W30x90
12	15x15x1.0	W24x229	W30x90
13	15x15x1.0	W24x229	W30x90
14	15x15x1.0	W24x229	W30x90
15	15x15x0.75	W24x192	W27x84
16	15x15x0.75	W24x192	W27x84
17	15x15x0.75	W24x192	W27x84
18	15x15x0.5	W24x146	W27x84
19	15x15x0.5	W24x146	W24x62
20	15x15x0.5	W24x131	W18x40
Roof	15x15x0.5	W24x131	W16x31

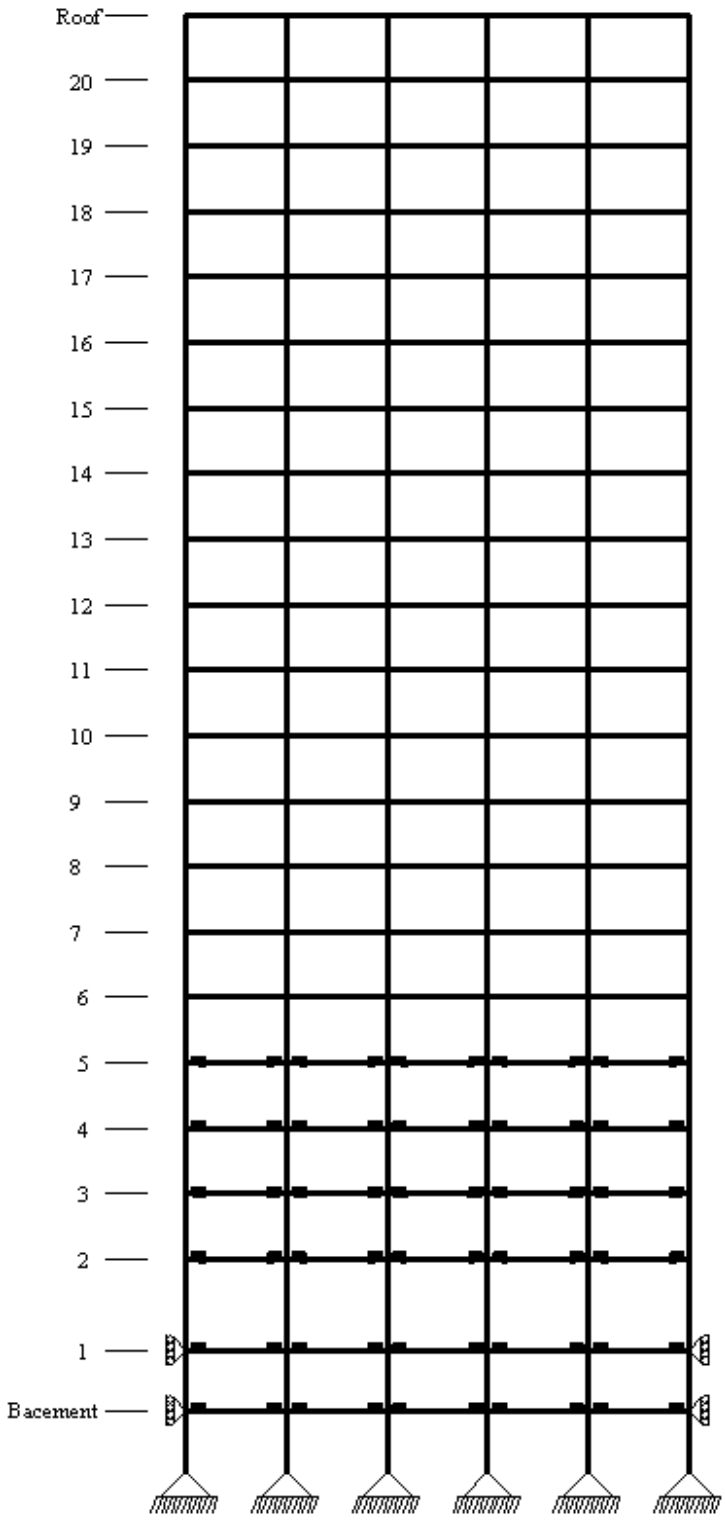

Figure 3.17 Hybrid SAC Frame: $BL\_20-0:5-A-236-0.01-1{,}000$

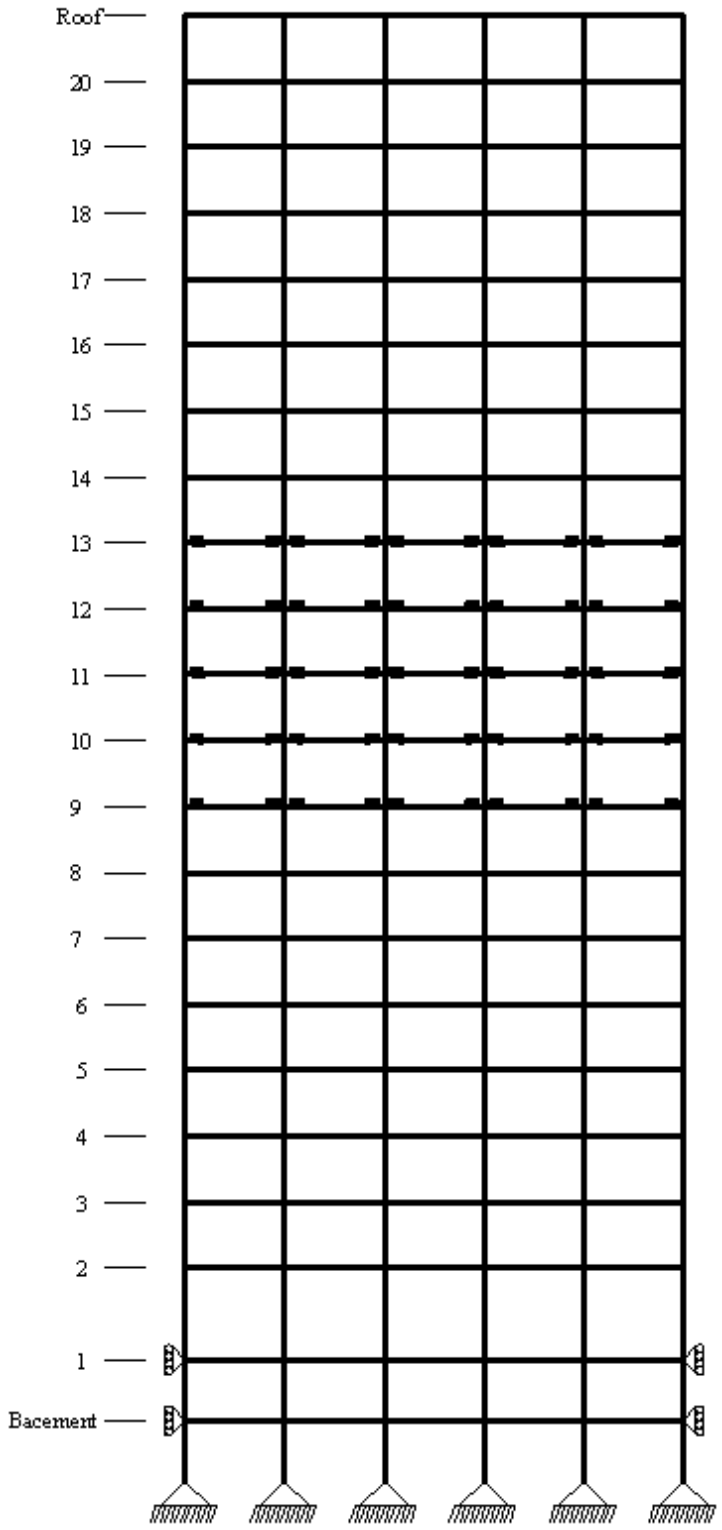

Figure 3.18 Hybrid SAC Frame: $BL\_20-9:13-A-236-0.01-1{,}000$

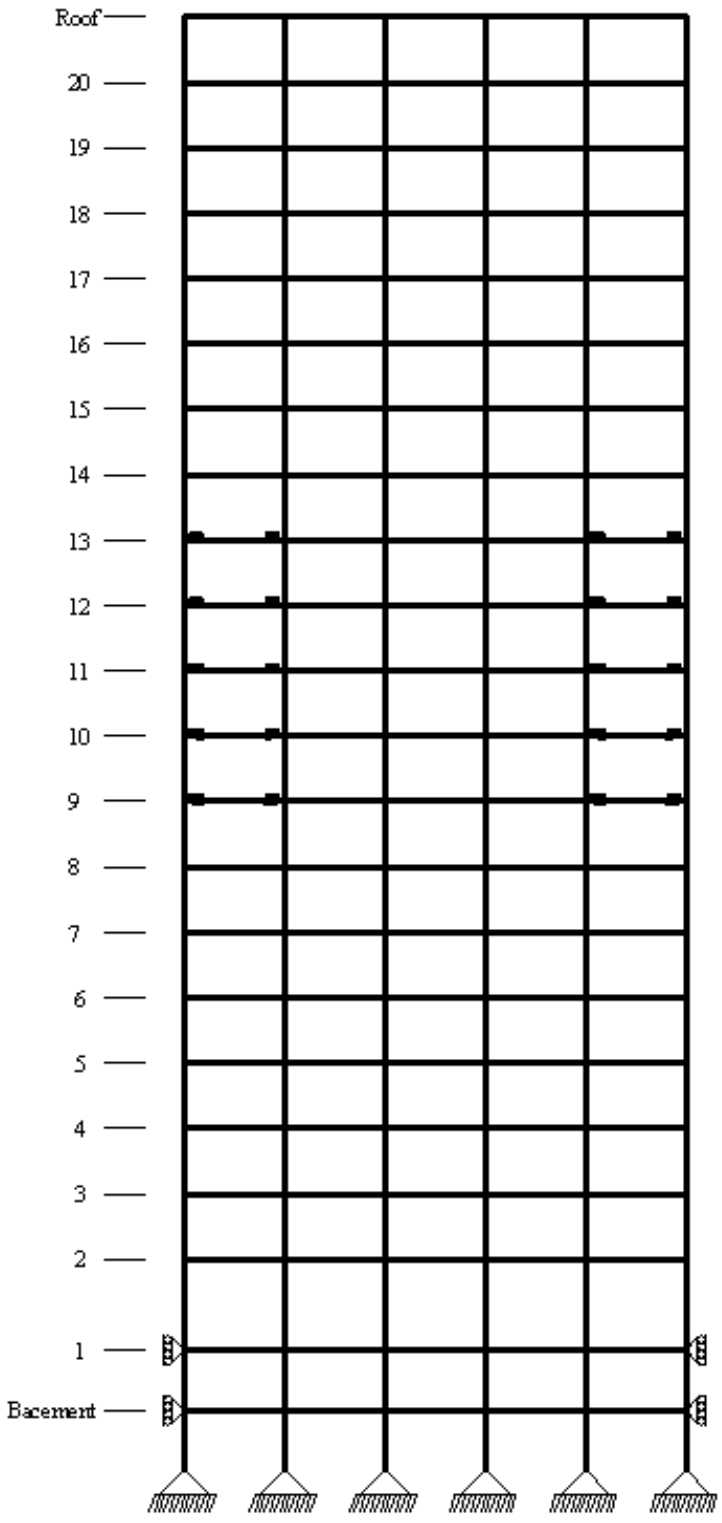

Figure 3.19 Hybrid SAC Frame: $BL\_20-9:13-E-236-0.01-1{,}000$

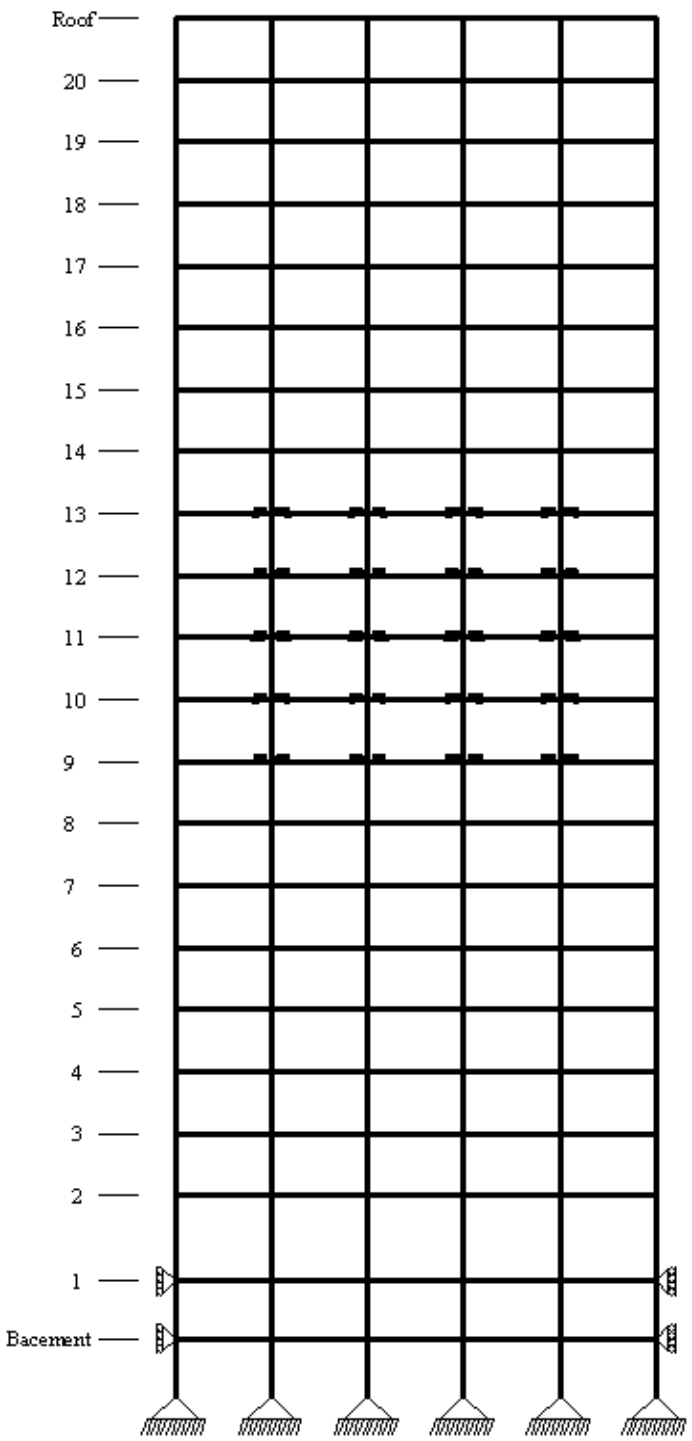

Figure 3.20 Hybrid SAC Frame: $BL\_20-9:13-M-236-0.01-1{,}000$

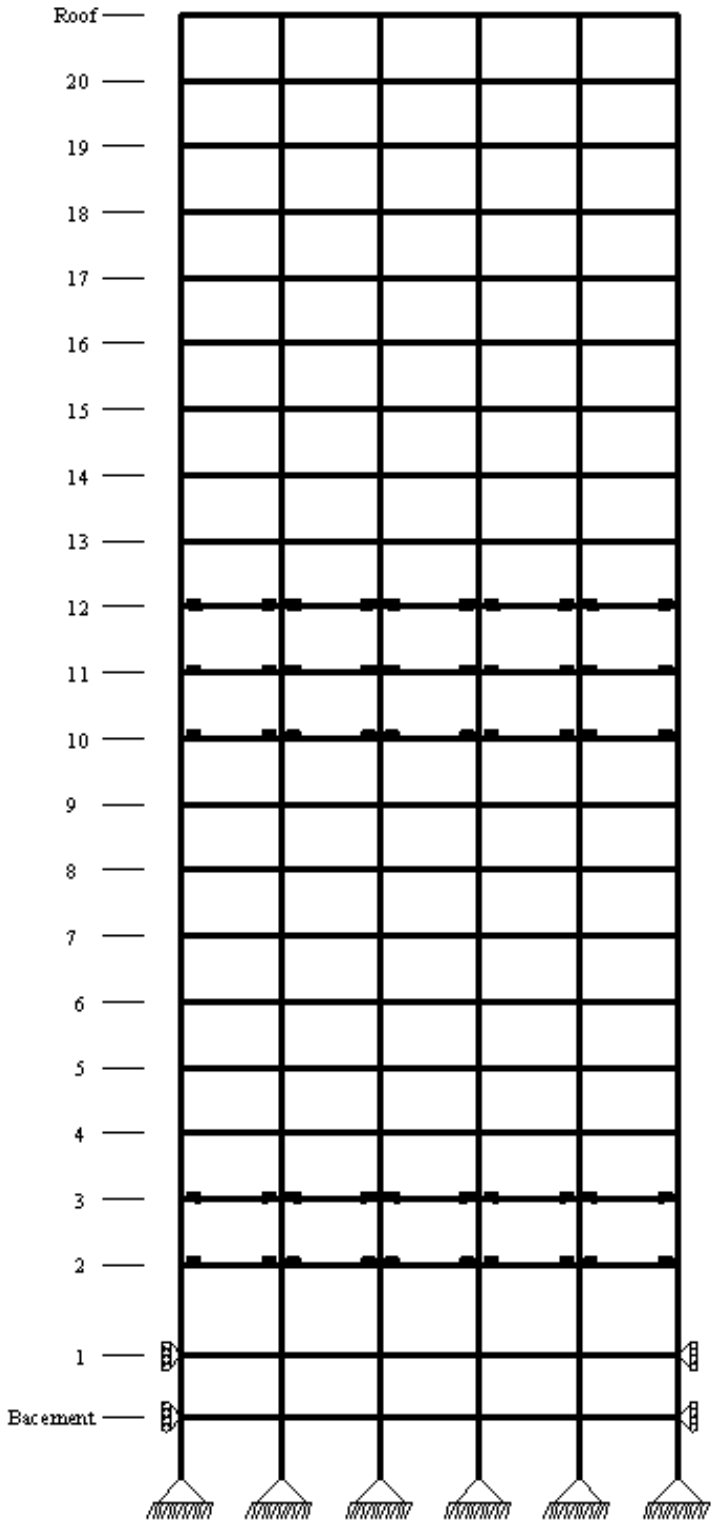

Figure 3.21 Hybrid SAC Frame: $BL\_20-2:3,10:12-A-236-0.01-1,000$

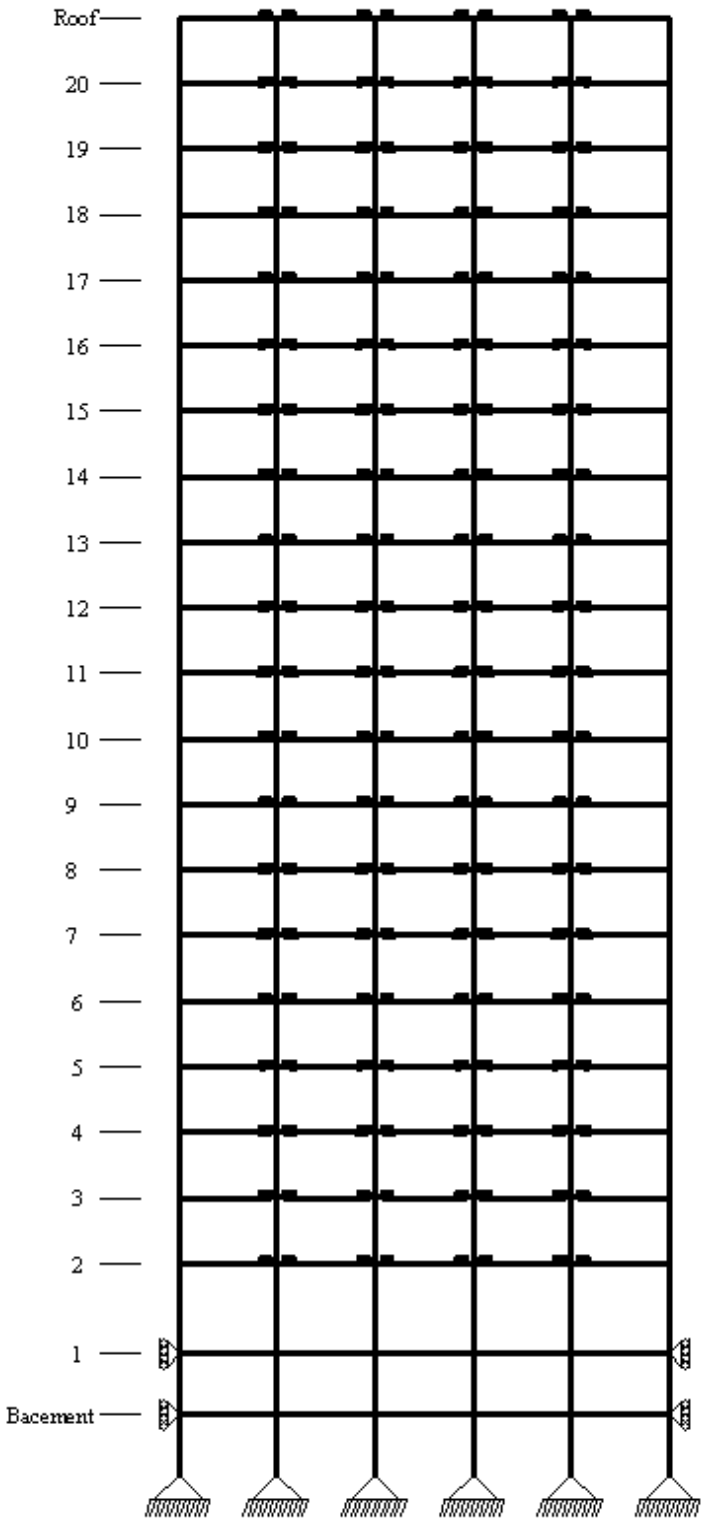

Figure 3.22 Hybrid SAC Frame: $BL\_20-2:21-M-236-0.01-1{,}000$

CHAPTER 4

ANALYSIS OF TWO-STORY FRAME

4.1. Introduction

The 2-story frame introduced in chapter 3 and its hybrid variations are analyzed. The effect of placement of semi-rigid connections is evaluated based on lateral drifts and member forces induced in the building. The moment-rotation diagrams of partially restrained connections and the variation of member forces are used to monitor moment redistribution in frames. The moment redistribution largely occurs due to the presence of semi-rigid connections placed on the selected regions.

Only static loads are applied to this model in efforts to reduce the complexity of moment redistribution and to seek common load paths among the proposed hybrid frames. First, a uniformly distributed gravity load of 150 lbs/in (26 kN/m) is applied along the length of each beam. This load originates from members' self-weight and weight of the concrete slab. The magnitude of the load is adopted from Bhatti and Hingtgen (1995) and was repeatedly used in Chapter 2. Moreover, a joint lateral load is applied at the top left-most node of each frame, and its magnitude is varied from 10 kips (44.5 kN) to 100 kips (445 kN). All loads are applied using load-controlled analysis.

In addition to the 2-story cases introduced in Chapter 3, another frame is also analyzed, where all beam-to-column connections are semi-rigid. The initial and post-yield connection stiffness and yield moment in this case are 236,020 kips-in/rad (26,667 kN-m/rad), 2,360 kips-in/rad (267 kN-m/rad) and 1000 kips-in (113 kN-m), respectively. This frame is compared to the rigid case, and it is used as a measure of performance for the hybrid frames.

While no seismic loads are introduced for the 2-story frame, the results obtained during the static pushover analysis are used to evaluate the expected earthquake performance of the building, which is a valid prediction method according to FEMA-355C. Moreover, the 2-story frame is used to introduce the concept of moment redistribution and its role in building seismic behavior. Results for lateral drifts, moment-rotation diagrams in partially restrained connections and member forces for each case are compared in separate sections and conclusions are drown.

All analyses developed in this study are performed using Open System for Earthquake Engineering Simulation (OpenSees), a software framework developed at the University of California at Berkeley to simulate structural dynamic behaviors during a seismic event. Additional information about the program is available in the Reference section of this document.

4.2. Analysis Verification

A simple structure, whose actual response is known, is needed to verify the software capabilities. Therefore, a 2-story, 1-bay frame and a 4-story, 2-bay

frame modeled by Bhatti and Hingtgen (1995) and King and Chen (1993) were used for verification purposes.

Figure 4.1 and Figure 4.2 present the geometries of the 2-story and the 4-story buildings, respectively. The compressive force, P, and the lateral load, H, for the first frame are 100 kips (445 kN) and 10 kips (44.5 kN), respectively. The uniformly distributed dead load, w, and the lateral force, H, applied to the frame in Figure 4.2 are 0.15 kips/in (26 kN/m) and 7 kips (31 kN), respectively. At the beginning, rigid joints with no P-Δ effects are analyzed and the results are compared to the data reported by the aforementioned articles. Next, structural geometric non-linearities are implemented, while the connections between members remained rigid. Finally, both P-Δ effects and connection non-linearities are modeled, where the semi-rigid connections are presented using zero-length springs. The 2-noded rotational spring elements have two translational and one rotational degrees of freedom at each node. Both nodes of each element have identical translational degrees of freedom, while their rotational degrees of freedom are different to simulate relative rotation during the analysis. Thus, the springs permit relative rotation, which is consistent with the behavior of semi-rigid connections.

Figure 4.3 presents the moment-rotation (M-θ) relationship used by King and Chen (1993) and Bhatti and Hingtgen (1995). The same M-θ relationship was also used in this study for overall model verification. The zero-length springs implemented by Bhatti and Hingtgen follow the elastic, perfectly

plastic loading model, shown by the dashed line in Figure 4.3; therefore, the same connection properties are imported into OpenSees. Results are presented for comparison in Table 4.1 though Table 4.4.

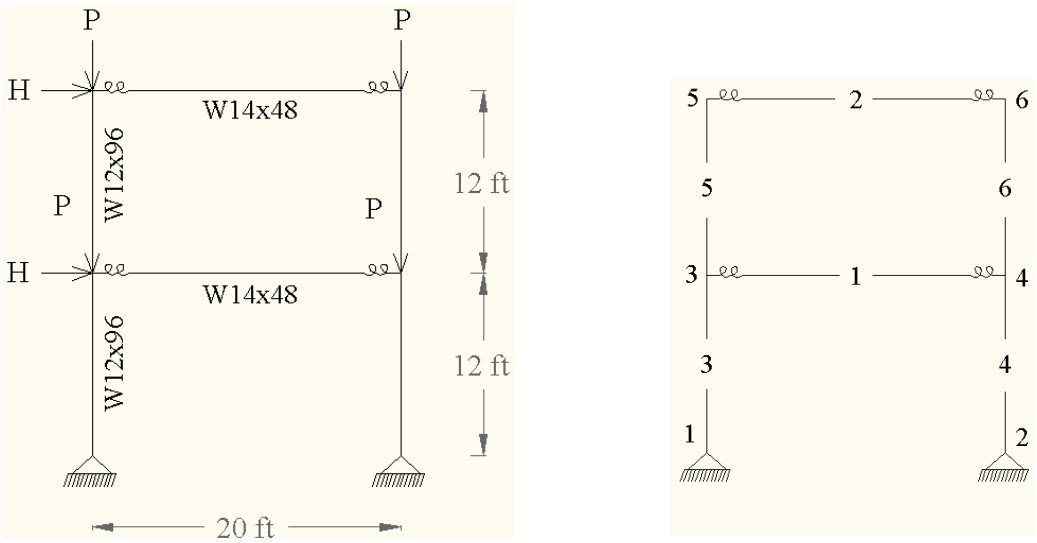

a) b)

Figure 4.1 Two-Story, One-Bay Frame by Bhatti and Hingtgen [1]: a) Geometry and Member Sizes , b) Node and Element Numbers

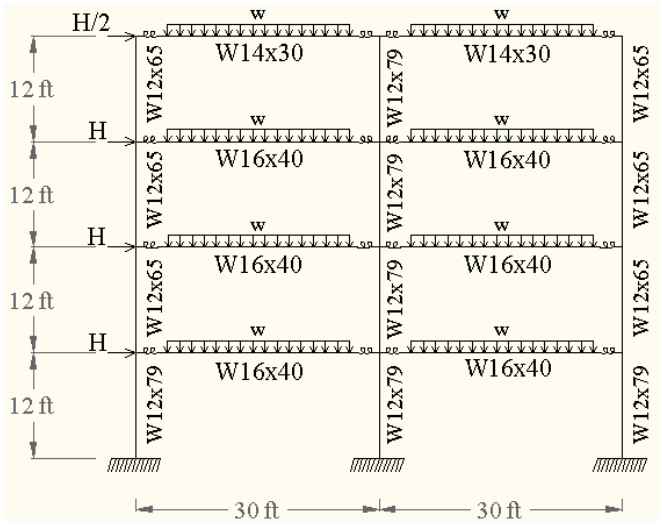

a)

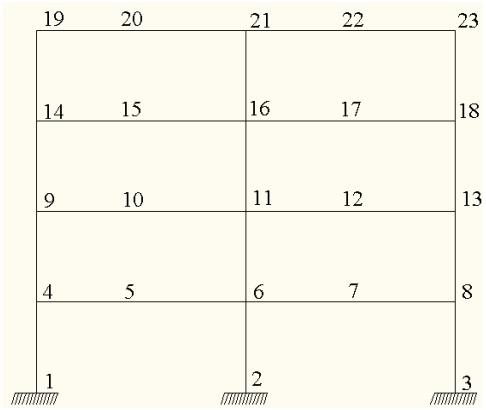

b)

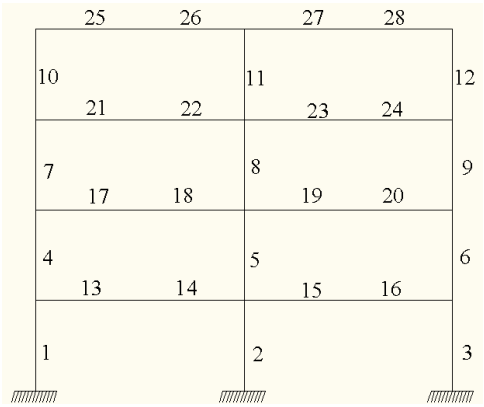

c)

Figure 4.2 Four-Story, Two-Bay Frame by Bhatti and Hingtgen [1]: a) Geometry and Member Sizes, b) Node Numbers, c) Element Numbers

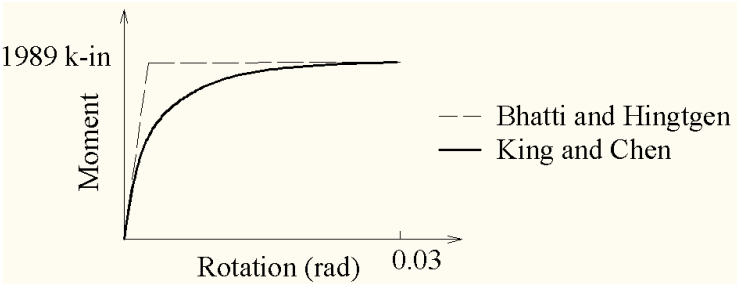

Figure 4.3 Connection Moment-Rotation Relationship [1]

Table 4.1 Lateral Displacement for Two-Story, One-Bay Frame

	Rigid No P-Delta		Rigid with P-Delta		Flexible with P-Delta	
	Node 3	Node 5	Node 3	Node 5	Node 3	Node 5
Bhatti & Hingtgen	1.011	1.509	1.168	1.731	1.477	2.292
King &Chen	-	-	1.16	1.82	2.02	3.26
This Study	1.012	1.511	1.162	1.725	1.471	2.285

Table 4.2 Absolute Maximum Bending Moments for Two-Story, One-Bay Frame

Element #		1	2	3	4	5	6
Rigid No P-Delta	Bhatti & Hingtgen	1450	711	1443	1437	711	711
	This Study	1448	711	1443	1437	711	711
Rigid with P-Delta	Bhatti & Hingtgen	1654	765	1677	1669	794	795
	King &Chen	1649	794	1670	1664	794	794
	This Study	1652	796	1675	1669	796	796
Flexible with P-Delta	Bhatti & Hingtgen	1634	902	1739	1731	902	902
	King &Chen	1560	1116	1837	1834	1116	1116
	This Study	1632	903	1736	1731	903	903

Table 4.3 Lateral Displacement for Four-Story, Two-Bay Frame

Node #	Rigid with P-Delta			Flexible with P-Delta		
	Bhatti & Hingtgen	King &Chen	This Study	Bhatti & Hingtgen	King &Chen	This Study
4	0.269	0.27	0.269	0.304	0.4	0.305
9	0.663	0.66	0.661	0.771	1.07	0.773
14	0.941	0.94	0.939	1.116	1.61	1.118
19	1.109	1.11	1.107	1.328	1.95	1.330

Table 4.4 Absolute Maximum Bending Moments for Four-Story, Two-Bay Frame

Element #	Rigid with P-Delta			Flexible with P-Delta		
	Bhatti & Hingtgen	King &Chen	This Study	Bhatti & Hingtgen	King &Chen	This Study
1	534	534	536	619	843	633
2	957	958	961	1016	1170	1022
3	1202	1202	1203	1254	1397	1252
4	455	455	455	404	291	387
5	657	656	657	649	596	650
6	1102	1101	1102	1064	1044	1049
7	615	615	615	591	559	573
8	474	473	474	496	542	497
9	1029	1029	1029	1005	996	987
10	704	702	703	687	705	672
11	200	200	200	225	313	225
12	820	818	820	812	846	801

The presented data verifies that the results obtained by OpenSees are comparable with those in the literature. The results for the 2-story and the 4-story frames are very close to those presented by Bhatti and Hingtgen (1995).

The difference between the results of this study and King and Chen (1993) is attributed to the M-θ relationship. This study uses bilinear M-θ curve, which is similar to these used by Bhatti and Hingtgen (1995), while King and Chen (1993) use a Ramberg-Osgood type function.

4.3. Analysis of 2-Story Hybrid Frame

The building lateral displacement, which quantifies serviceability design requirements, is compared first. A load-controlled analysis is used to obtain the lateral displacement at both sides of each floor, and the results for $BL\_2-2,2-1,2-B,B-L(236-0.01-1{,}000)-R(236-0.01-1{,}000)$ are presented in Figure 4.4. The difference in measured lateral drift between the left and right sides of a frame on a given floor is insignificant. Such variation is expected, and its range for all other hybrid frames remains similar to that illustrated in Figure 4.4. Therefore, the maximum displacement, which occurs at the point where the lateral load is applied, is selected to evaluate the serviceability performance of the 2-story hybrid frames introduced in chapter 3.

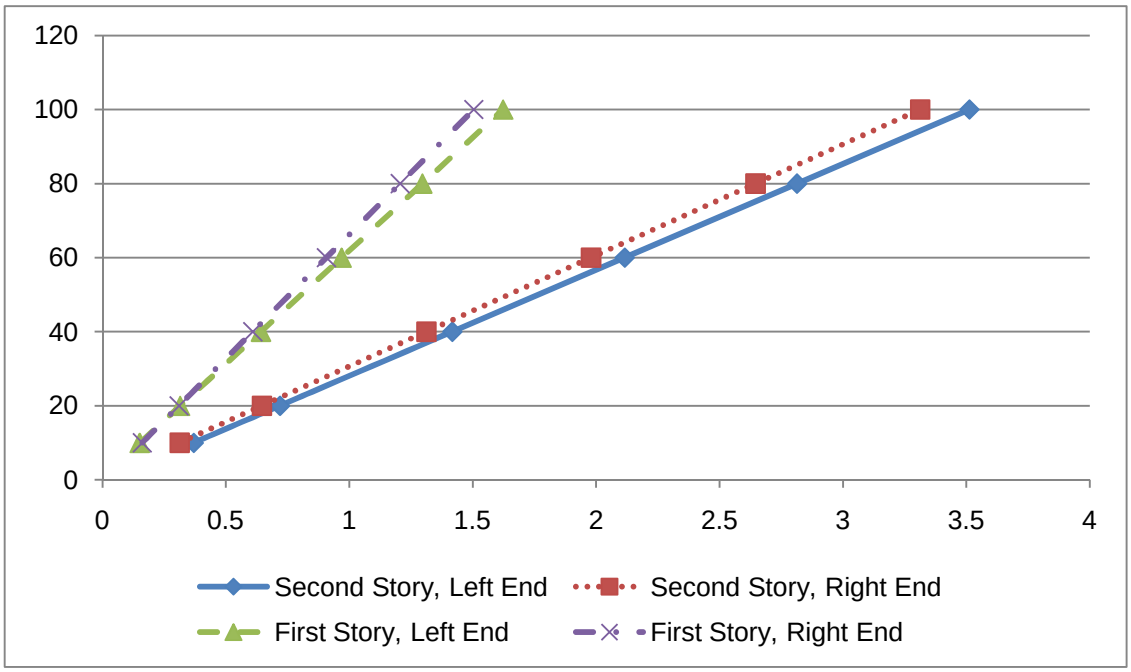

Figure 4.4 Lateral Drift in
$BL\_2-2,2-1,2-B, B-L(236-0.01-1{,}000)-R(236-0.01-1{,}000)$

Figure 4.5 shows a plot of the applied lateral load verses top story, left node lateral sway for different models. As expected, the frame with semi-rigid properties at every beam-to-column connection provides the most flexible results. The remaining models offer closer results with frames $BL\_2-1,1-1,2-B, B-L(236-0.01-1{,}000)-R(236-0.01-1{,}000)$ and $BL\_2-3,3-1,2-B, B-L(236-0.01-1{,}000)-R(236-0.01-1{,}000)$ deflecting the most within this group, while frame $BL\_2-2,3-2,1-L, L-L(236-0.01-1{,}000)-R(236-0.01-1{,}000)$ and the rigid case proved to be the stiffest among all analyzed buildings.

The validity of the results is justified by comparing the lateral displacements of frames $BL\_2-2,2-1,2-B,B-L(236-0.01-1{,}000)-R(236-0.01-1{,}000)$ and $BL\_2-2,2-1,2-B,B-L(787-0.5-1{,}000)-R(787-0.5-1{,}000)$. Both hybrid cases have the same geometry, but the second building has stiffer semi-rigid connections; therefore, their lateral displacements are similar, while the second frame performs slightly better than the first structure.

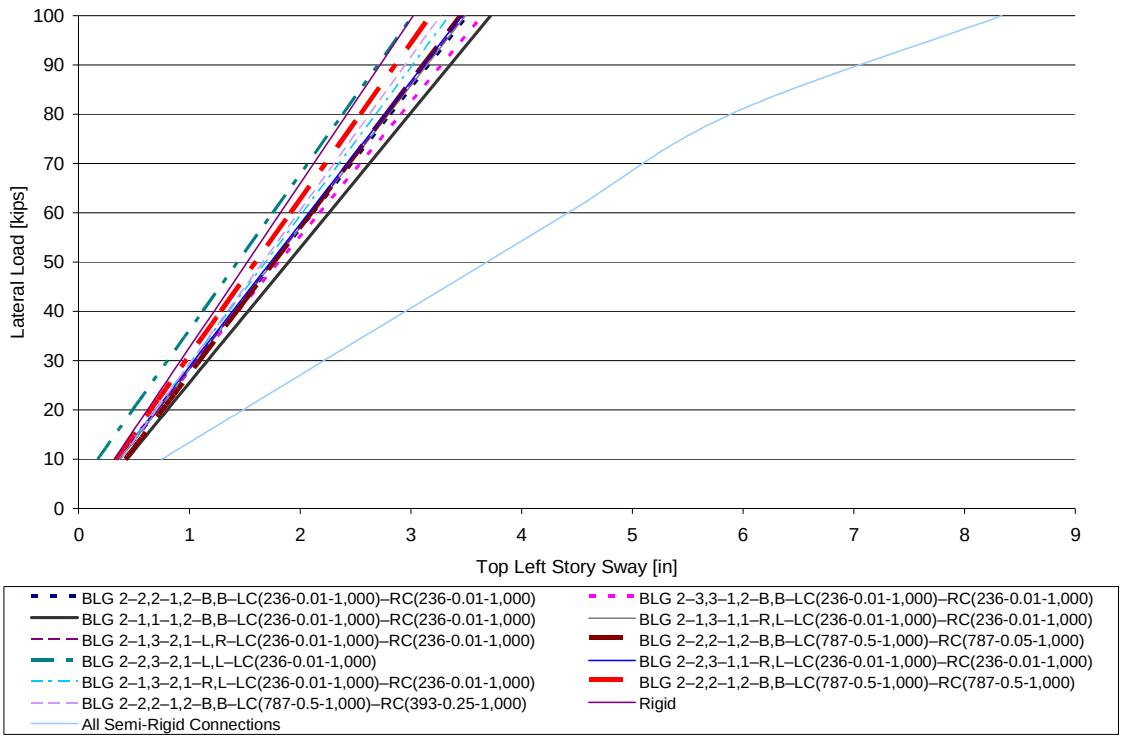

Figure 4.5 Comparison of Top Lateral Drift for Two-Story Hybrid Frames

Frame $BL\_2-2,3-2,1-L,L-L(236-0.01-1{,}000)$ results in less lateral deformation than the rigid case. This is due to placing all semi-rigid connections at the left ends of beams, where the combination of applied dead

and lateral loads results in connection unloading. Therefore, all semi-rigid connections increase their stiffness from the post-yield value to the initial connection stiffness, and the frame behaves similarly to the rigid frame. In Figure 4.5, frame $BL\_2-2{,}3-2{,}1-L, L-L(236-0.01-1{,}000)$ appears to be stiffer than the rigid frame, which is attributed to a numerical error in the approximate solution method used by the software program. Other results such as moment-rotation diagrams in semi-rigid connections and member forces in structural elements are presented in proceeding sections to aid the evaluation of this and other hybrid frames.

4.4. Moment-Rotation Diagrams

Moment-rotation diagrams, also known as M-θ graphs, are used to visualize the behavior of semi-rigid connections in a hybrid frame. They relate the moment transferred from the beam to the column to the relative rotation of the beam end and column end connection. The M-θ diagrams offer information about the load transferred through partially restrained connections, their expected damage and the overall response of the building.

Once a connection becomes inelastic, its stiffness is reduced from its initial value provided for the particular model to the post-yield capacity. Depending on the connection type a ductile semi-rigid connection experiences significant rotational increase, while the applied load may remain virtually unchanged. Thus, the connection may no longer be able to carry the imposed demands, and it provides minimal resistance to the applied load, which results

in moment redistribution. As a result, the connection may experience a reversed moment, which results in a connection unloading and the original initial stiffness, Ki, is restored. This behavior is important in earthquake design, since the overall building stiffness is improved and the structure is more likely to sustain the seismic loads depending on the building and earthquake frequencies. However, moment redistribution is complex and largely unpredictable due to its dependence on member and connection stiffnesses, semi-rigid connection locations, frame boundary conditions and direction and location of the applied load.

This phenomenon is monitored for the 2-story building in efforts to determine a general load pattern. In the analyses, a lateral load of 100 kips (445 kN) is applied at the left node of the top story in addition to the uniformly distributed gravity loads. All forces are applied at ten load-controlled incremental steps.

Figure 4.6 through Figure 4.17 present the moment versus relative rotation diagrams for all semi-rigid connections in the hybrid cases for the 2-story frame. These figures show that for a lateral load applied from left to right, unloading occurs in connections at the left nodes of beams, while connections at the right nodes are loaded unidirectionally and mostly remain in their inelastic region. The opposite observation can be made if the lateral load were applied on the reverse side of the frames. No ultimate moment is considered, which means the connection failure is not modeled. Thus, according to the analytical

results a connection will not fail even if excessive rotation develops. Therefore, this study only compares the frame behavior relative to connection loading and unloading. However, Figure 4.6 through Figure 4.17 reveals that the connection rotation values remain under 0.04 radians based on the applied load, which is a typical rotation that non-brittle semi-rigid connections can withstand before failure (Abolmaali 2008).

The uniformly distributed gravity loads of 150 lbs/in (26 kN/m), which during the analyses are applied first, result in clockwise moments and rotations at the left beam nodes and counterclockwise moments and rotations at the right beam nodes. Once the dead load is fully applied, lateral point loads of 100 kips (445 kN) are applied at the left corners for each story. They produce counterclockwise moments and rotations in all connections. Thus, only the connections on the left side of the beams experiences moment reversal, which increases their stiffness back to its initial value. As a result, these connections become stiffer compared to those on the right side of the beams. This behavior is true for all cases including that shown in Figure 4.12, where two semi-rigid connections are placed on the left nodes of beams. In this case, both connections unload and the frame behaves similarly to a rigid frame.

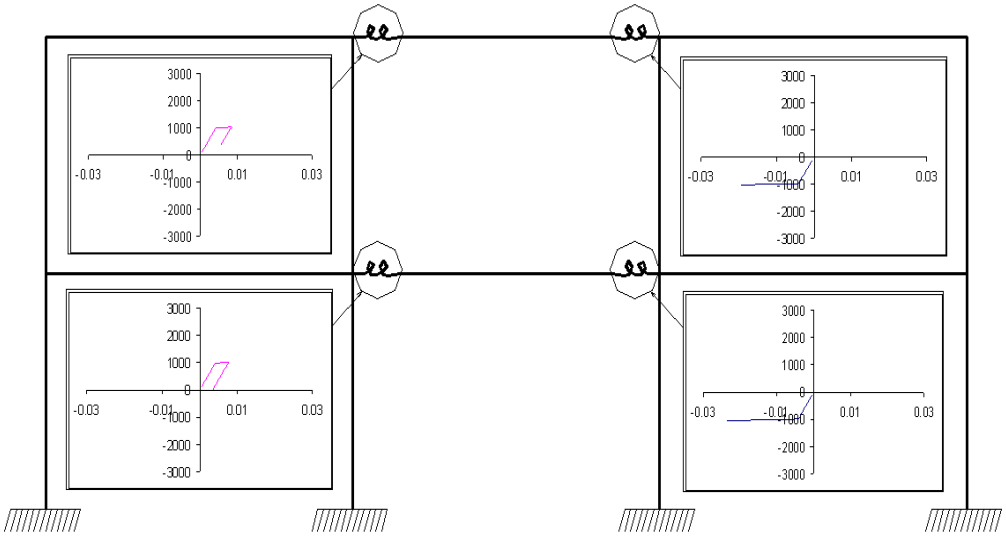

Figure 4.6 Connection Hysteresis Moment – Rotation for:
$BL\_2-2{,}2-1{,}2-B, B-L(236-0.01-1{,}000)-R(236-0.01-1{,}000)$

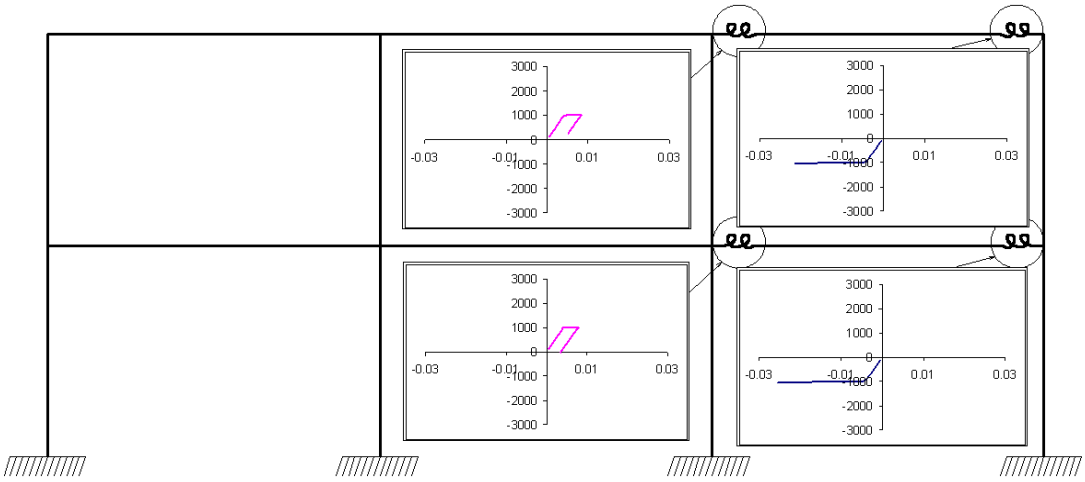

Figure 4.7 Connection Hysteresis Moment – Rotation for:
$BL\_2-3{,}3-1{,}2-B, B-L(236-0.01-1{,}000)-R(236-0.01-1{,}000)$

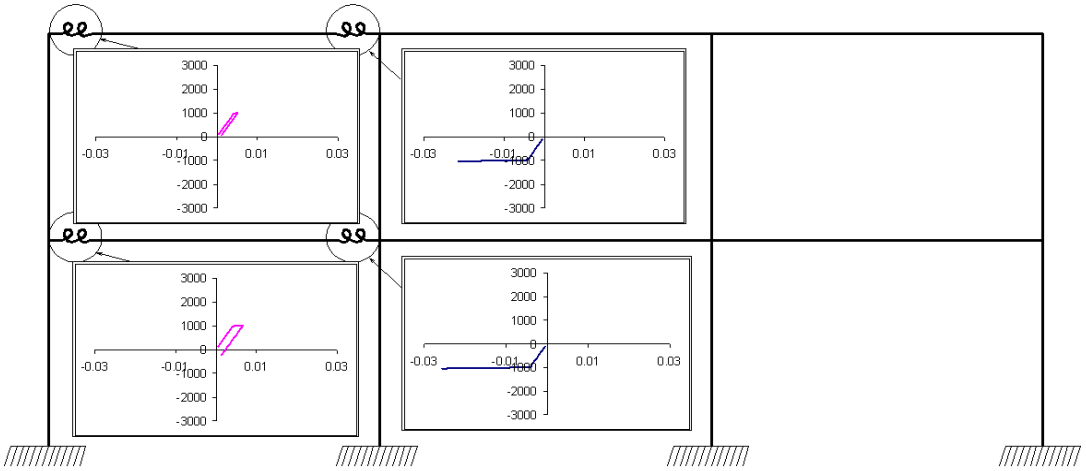

Figure 4.8 Connection Hysteresis Moment – Rotation for:
$BL\_2-1{,}1-1{,}2-B, B-L(236-0.01-1{,}000)-R(236-0.01-1{,}000)$

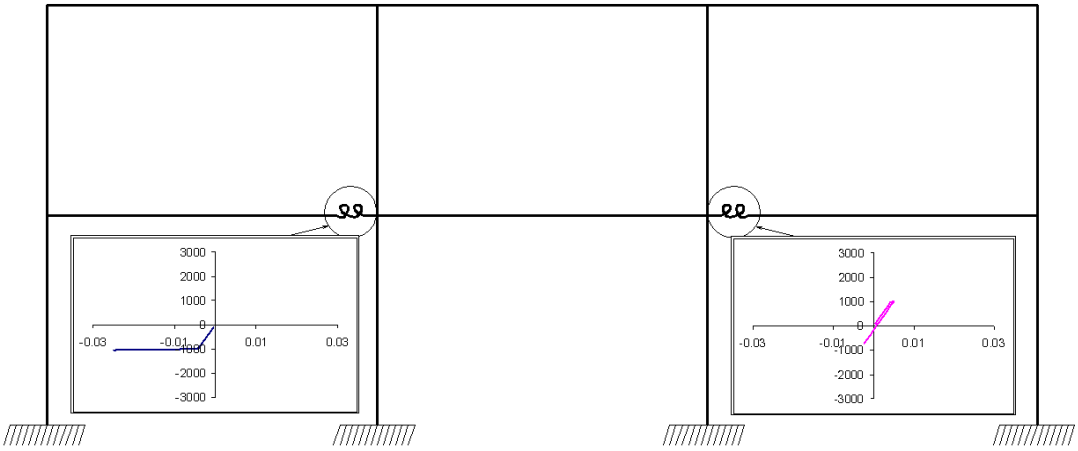

Figure 4.9 Connection Hysteresis Moment – Rotation for:
$BL\_2-1{,}3-1{,}1-R, L-L(236-0.01-1{,}000)-R(236-0.01-1{,}000)$

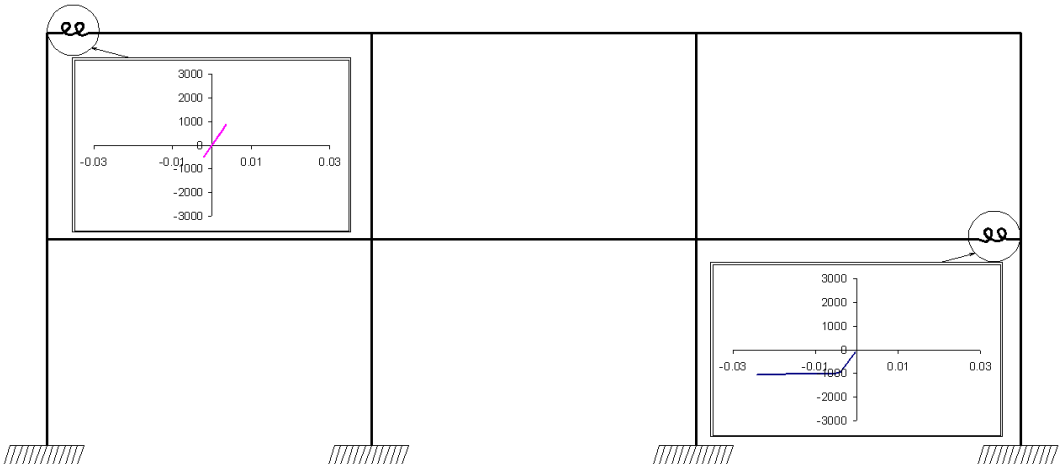

Figure 4.10 Connection Hysteresis Moment – Rotation for:
$BL\_2-1{,}3-2{,}1-L, R-L(236-0.01-1{,}000)-R(236-0.01-1{,}000)$

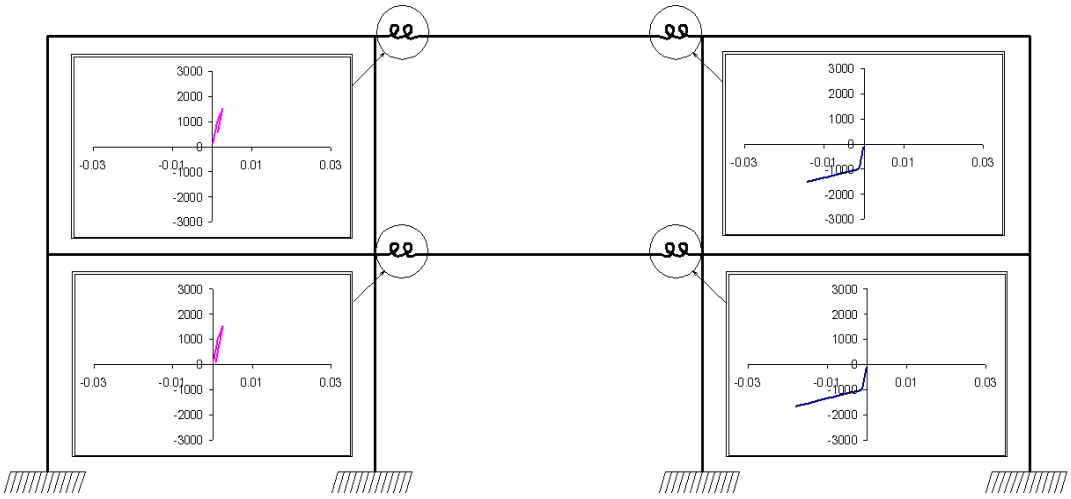

Figure 4.11 Connection Hysteresis Moment – Rotation for:
$BL\_2-2{,}2-1{,}2-B, B-L(787-0.5-1{,}000)-R(787-0.05-1{,}000)$

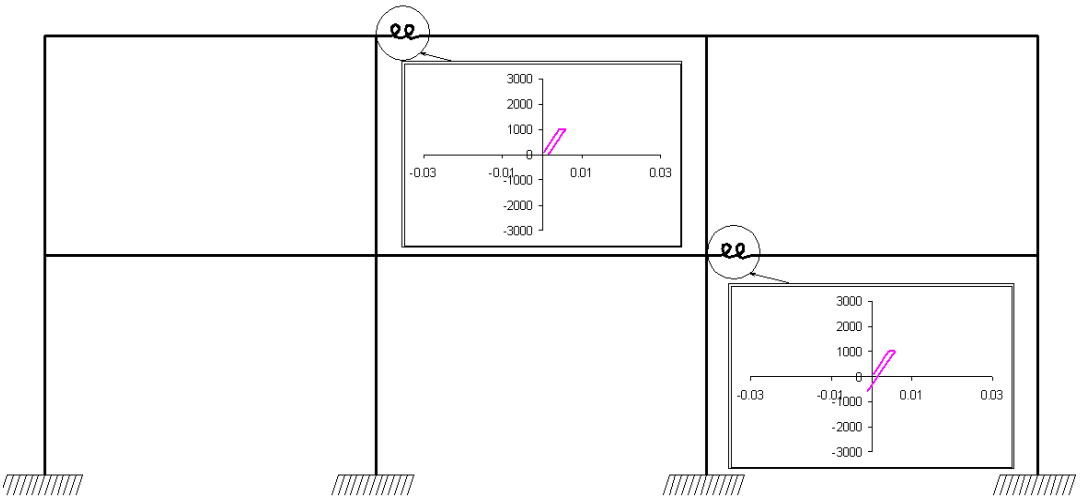

Figure 4.12 Connection Hysteresis Moment – Rotation for:
$BL\_2-2{,}3-1{,}2-L, L-L(236-0.01-1{,}000)$

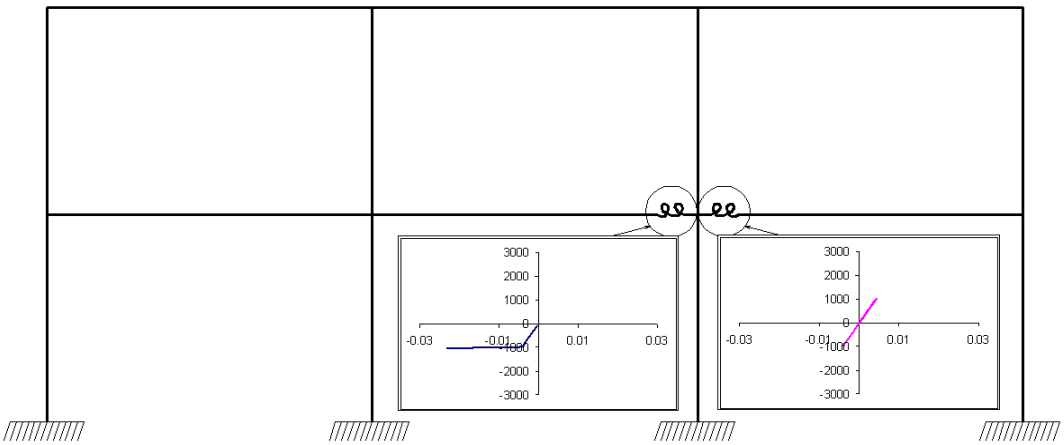

Figure 4.13 Connection Hysteresis Moment – Rotation for:
$BL\_2-2{,}3-1{,}1-R, L-L(236-0.01-1{,}000)-R(236-0.01-1{,}000)$

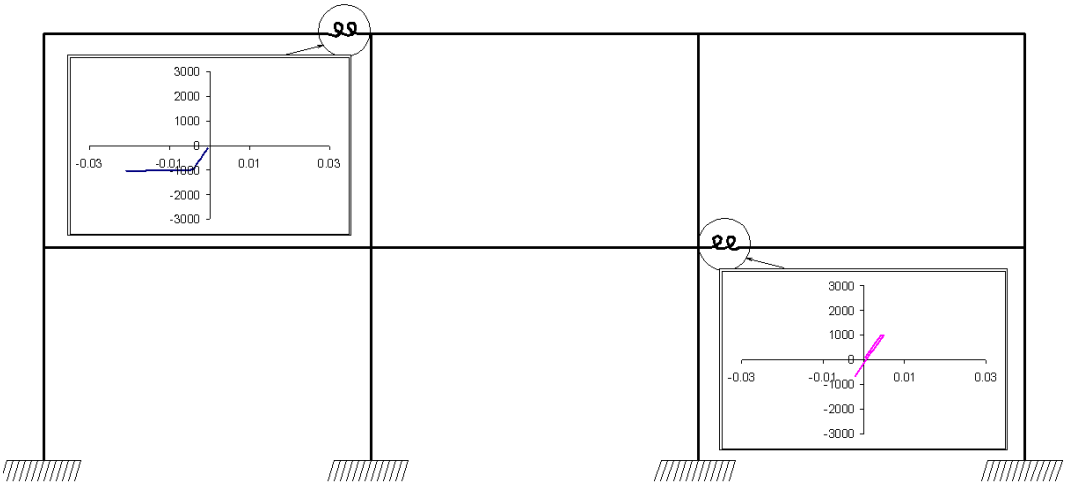

Figure 4.14 Connection Hysteresis Moment – Rotation for:
$BL\_2-1{,}3-2{,}1-R, L-L(236-0.01-1{,}000)-R(236-0.01-1{,}000)$

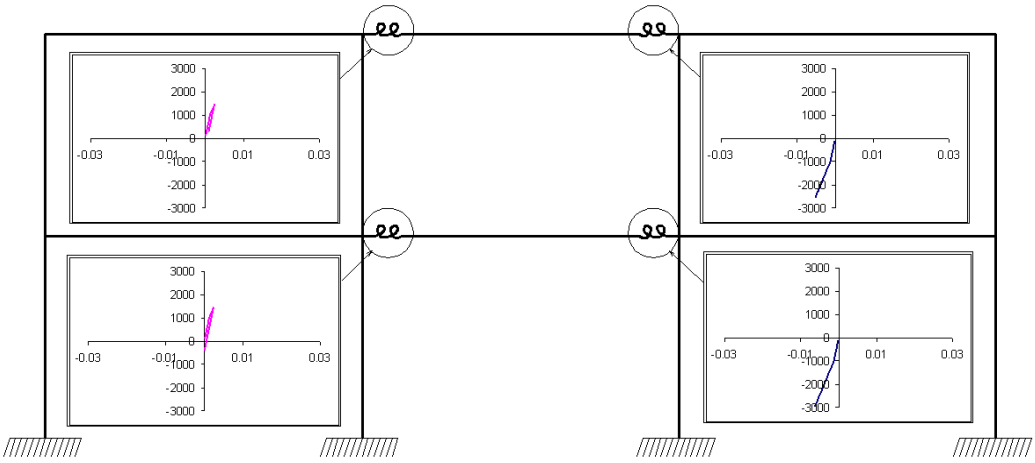

Figure 4.15 Connection Hysteresis Moment – Rotation for:
$BL\_2-2{,}2-1{,}2-B, B-L(787-0.5-1{,}000)-R(787-0.5-1{,}000)$

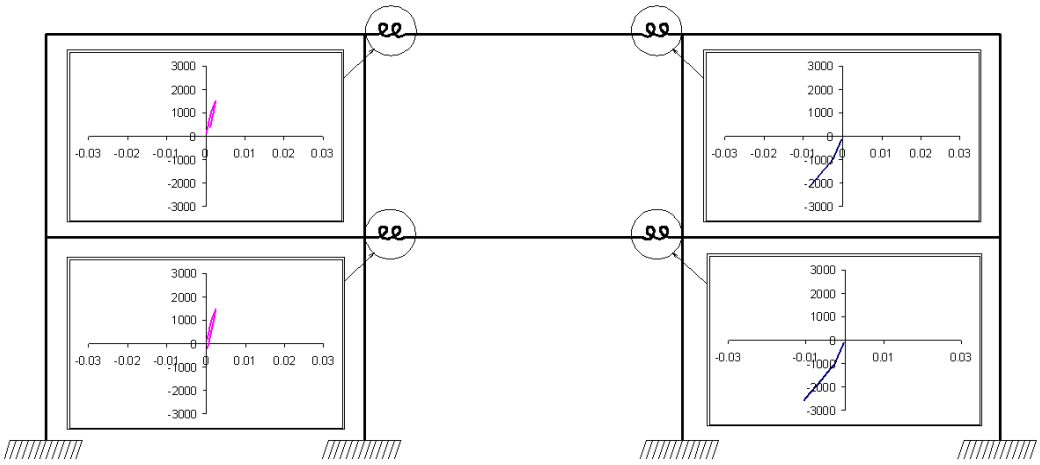

Figure 4.16 Connection Hysteresis Moment – Rotation for:
$BL\_2-2{,}2-1{,}2-B, B-L(787-0.5-1{,}000)-R(393-0.25-1{,}000)$

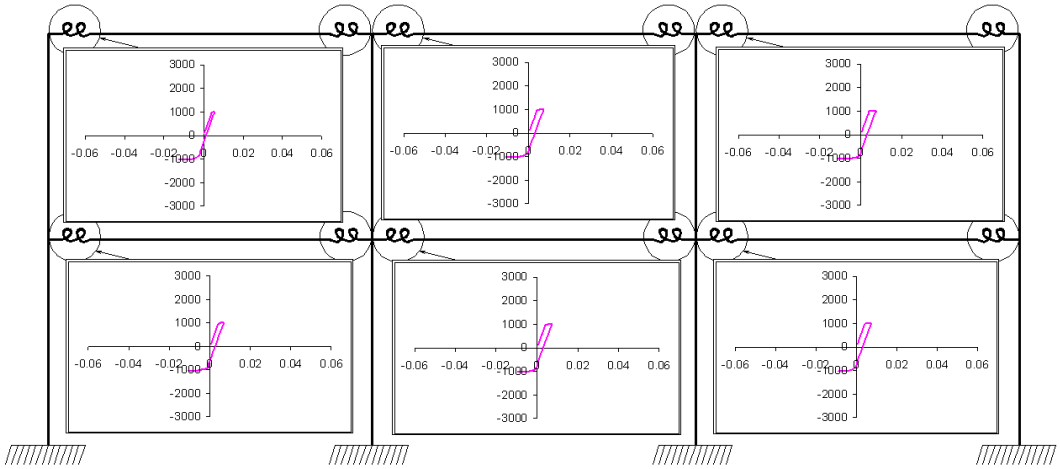

a)

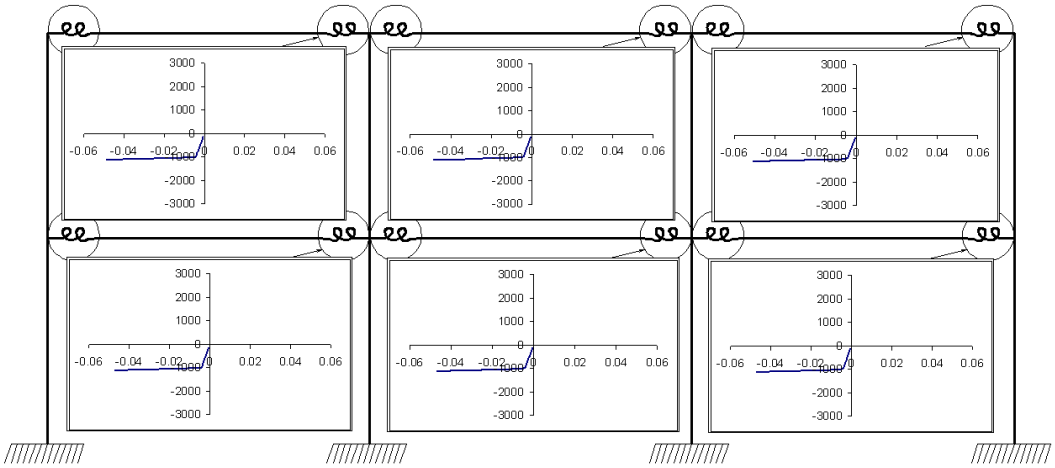

b)

Figure 4.17 Connection Hysteresis Moment – Rotation for All Semi-Rigid Connections Frame: a) Left Nodes of Beams, b) Right Nodes of Beams

The linear nature of the applied loads in this analysis reduces the complexity involved in moment redistribution during cyclic loads. This is done in order to introduce this important phenomenon in its simplest known format and to search for behavioral patterns that would be valid in more complex load combinations. However, any results presented thus far should be evaluated

with this lineal load nature in mind. More discussion on moment redistribution is presented in chapter 5.

4.5. Member Forces

Forces carried by members in a frame are important in structural design, because they affect element sizes and thus economy. Comparison of nodal moments between a hybrid building and its rigid counterpart also helps to evaluate moment redistribution and to determine the effects of semi-rigid connections on the structural behavior. Figure 4.18 through Figure 4.29 plot the ratios of the moments in elements in a hybrid structure to the moments in the rigid frame, where results are presented for each story. In these figures, M_1 is the end moment at the bottom and left nodes for columns and beams respectively, while M_2 is the end moment at the top and right nodes, respectively. The results for beams and columns are presented separately for clarity. A uniformly distributed gravity load and a lateral point load of 100 kips (445 kN) applied at the left nodes of the first and second stories are the only loads imposed to the 2-story frames.

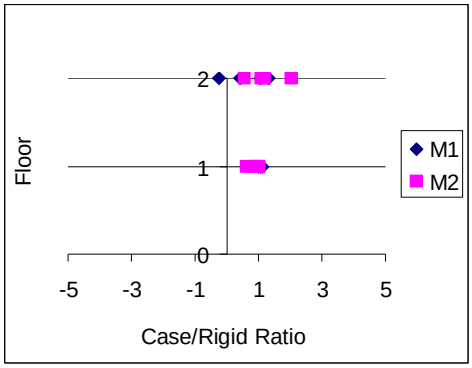

a)

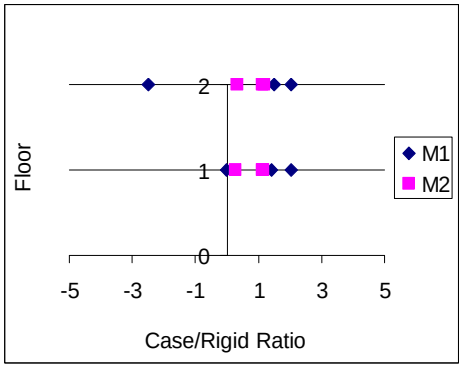

b)

Figure 4.18 End Moments Ratios for $BL\_2-2,2-1,2-B, B-L(236-0.01-1{,}000)-R(236-0.01-1{,}000)$: a) Ratios in Columns, b) Ratios in Beams

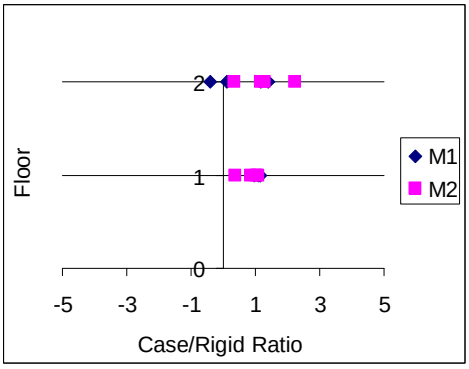

a)

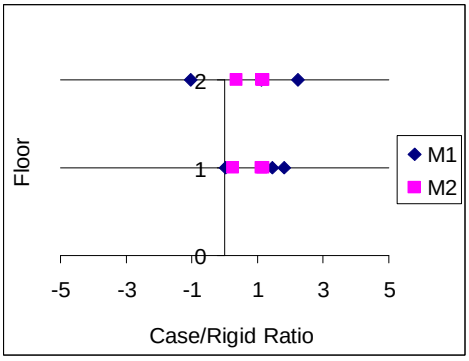

b)

Figure 4.19 End Moment Ratios for $BL\_2-3,3-1,2-B, B-L(236-0.01-1{,}000)-R(236-0.01-1{,}000)$: a) Ratios in Columns, b) Ratios in Beams

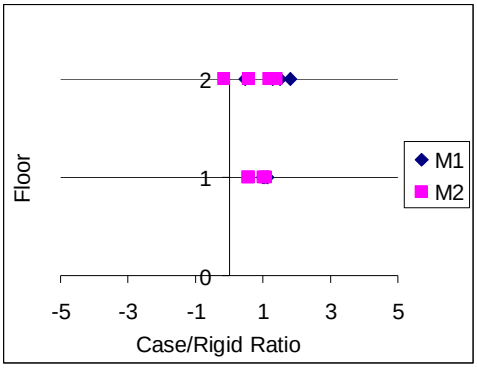

a)

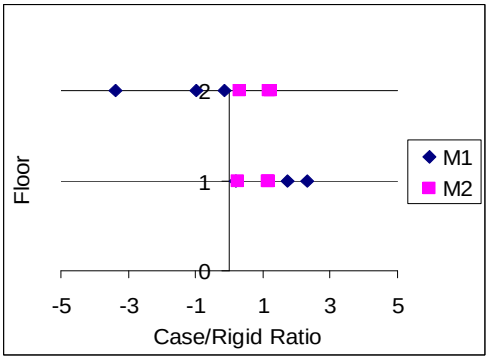

b)

Figure 4.20 End Moment Ratios for $BL\_2-1,1-1,2-B, B-L(236-0.01-1,000)-R(236-0.01-1,000)$: a) Ratios in Columns, b) Ratios in Beams

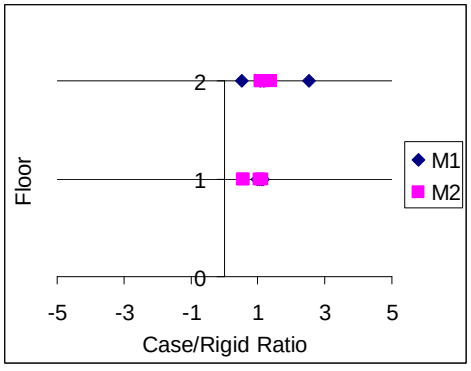

a)

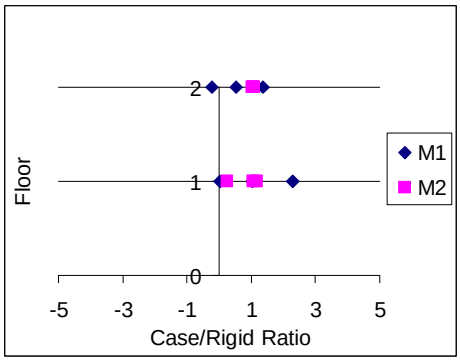

b)

Figure 4.21 End Moment Ratios for $BL\_2-1,3-1,1-R, L-L(236-0.01-1,000)-R(236-0.01-1,000)$: a) Ratios in Columns, b) Ratios in Beams

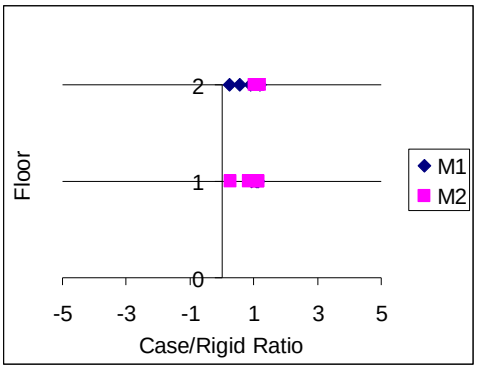

a)

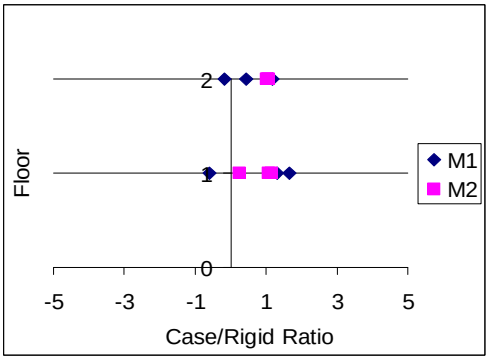

b)

Figure 4.22 End Moment Ratios for
$BL\_2-1{,}3-2{,}1-L, R-L(236-0.01-1{,}000)-R(236-0.01-1{,}000)$:
a) Ratios in Columns, b) Ratios in Beams

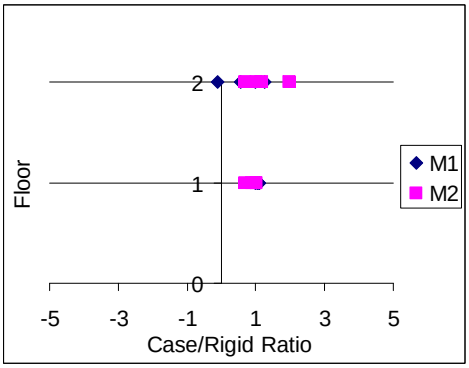

a)

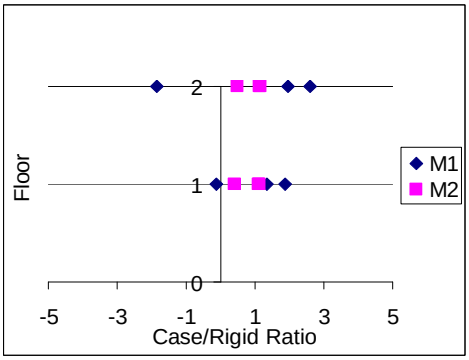

b)

Figure 4.23 End Moment Ratios for
$BL\_2-2{,}2-1{,}2-B, B-L(787-0.5-1{,}000)-R(787-0.05-1{,}000)$: a) Ratios in Columns, b) Ratios in Beams

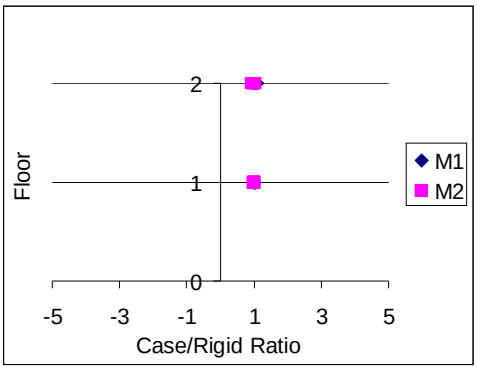

a)

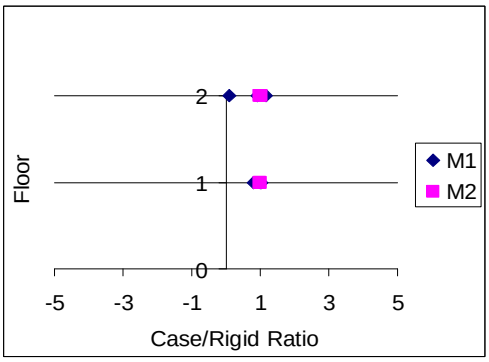

b)

Figure 4.24 End Moment Ratios for $BL\_2-2,3-2,1-L, L-L(236-0.01-1{,}000)$: a) Ratios in Columns, b) Ratios in Beams

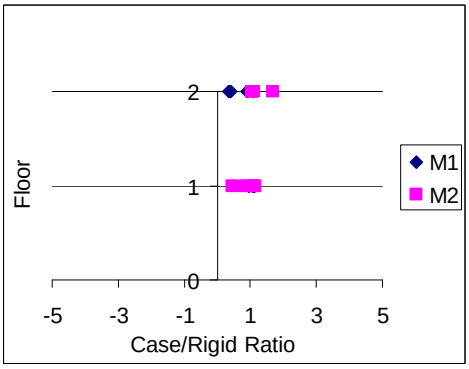

a)

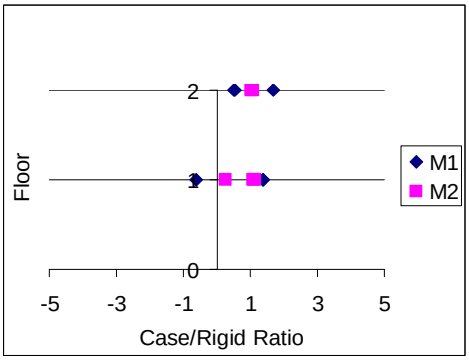

b)

Figure 4.25 End Moment Ratios for $BL\_2-2,3-1,1-R, L-L(236-0.01-1{,}000)-R(236-0.01-1{,}000)$: a) Ratios in Columns, b) Ratios in Beams

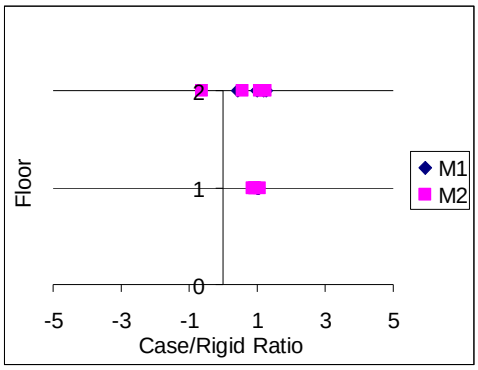

a)

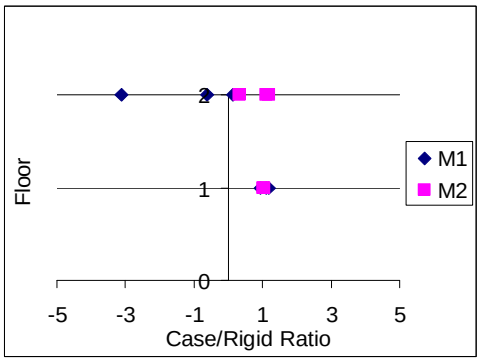

b)

Figure 4.26 End Moment Ratios for $BL\_2-1,3-2,1-R, L-L(236-0.01-1{,}000)-R(236-0.01-1{,}000)$: a) Ratios in Columns, b) Ratios in Beams

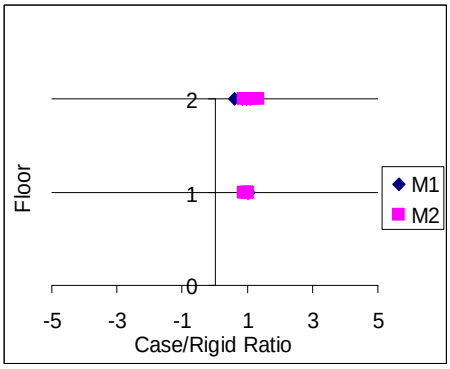

a)

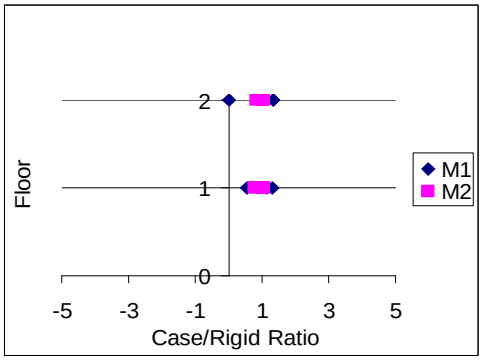

b)

Figure 4.27 End Moment Ratios for $BL\_2-2,2-1,2-B, B-L(78-0.5-1{,}000)-R(787-0.5-1{,}000)$: a) Ratios in Columns, b) Ratios in Beams

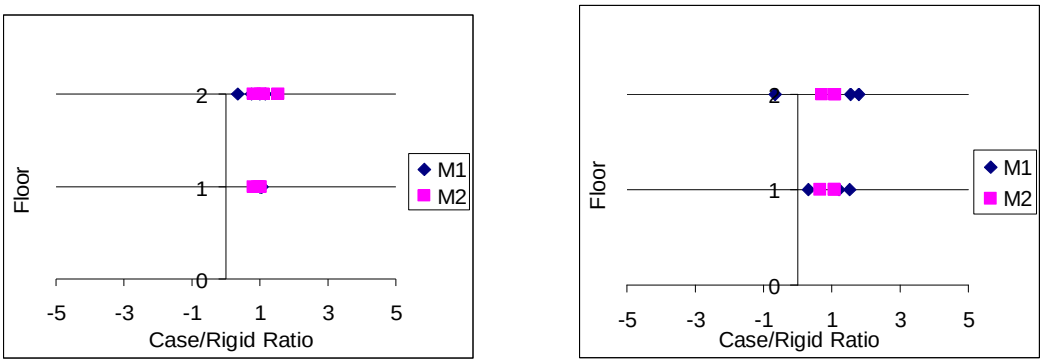

a) b)

Figure 4.28 End Moment Ratios for $BL\_2-2,2-1,2-B, B-L(787-0.5-1{,}000)-R(787-0.25-1{,}000)$: a) Ratios in Columns, b) Ratios in Beams

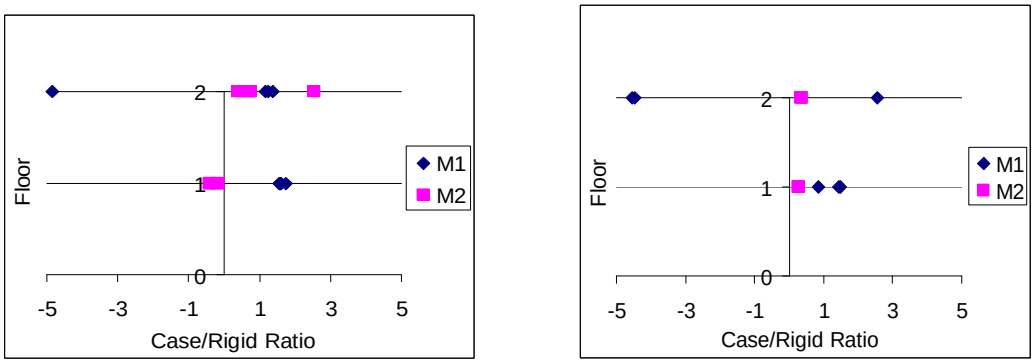

a) b)

Figure 4.29 End Moment Ratios for Fully Semi-Rigid Frame: a) Ratios in Columns, b) Ratios in Beams

In these figures, connections experiencing moment reversal due to the modified geometric properties of the frames have negative moment ratios. Also, members that experience lighter moment demands than the rigid frame have ratios smaller than 1, while connections with increased demands produce ratios of greater than 1. For example, the column ratios for $BL\_2-1,3-1,1-R, L-L(236-0.01-1{,}000)-R(236-0.01-1{,}000)$ presented in

Figure 4.21 indicate only one end moment at the second story increased its value compared to the results obtained during the analysis of the rigid frame. The rest of the moment ratios in this figure are either less than or equal to 1, which indicates that the demand on the rest of the columns has decreased or stayed the same.

Since the moment ratios for frame $BL\_2-2,3-2,1-L, L-L(236-0.01-1{,}000)$ are close to 1 as shown in Figure 4.24, this model experience almost the same member forces as the rigid case due to moment reversal in both semi-rigid connections. Meanwhile, the frame where all connections are semi-rigid gives moment ratios of significant variance, where some of its end moments are five times larger than those developed in the rigid frame as shown in Figure 4.29.

4.6. Conclusion

Lateral displacement, moment-rotation relationship in semi-rigid connections and member forces are useful tools to evaluate the performance of the proposed hybrid cases for the 2-story frame. Each hybrid combination was evaluated based on these criteria to determine the case/cases that demonstrate the largest improvement in performance compared to the rigid frame. Frame $BL\_2-2,2-1,2-B, B-L(236-0.01-1{,}000)-R(236-0.01-1{,}000)$ shows satisfactory results in all three disciplines and similar placement of semi-rigid connections will be implemented into the 20-story frame analysis.

CHAPTER 5

ANALYSIS OF SAC FRAME

5.1. Introduction

The 20-story frame adopted from the SAC Joint Venture research and introduced in Chapter 3 is analyzed next. Different hybrid combinations are developed in efforts to improve structural performance, which is evaluated based on lateral drifts, maximum member forces and energy dissipation of the building. Cyclic displacement-controlled analysis, static load-controlled analysis, wind and earthquake analyses are independently run to optimize knowledge of the structural response and to effectively determine the most desirable hybrid system for this high-rise model. In all cases, a uniformly distributed gravity load of 150 lbs/in (26 kN/m) is applied along the length of each beam. This load originates from members' self-weight and weight of the concrete slab. The load magnitude is adopted from Bhatti and Hingtgen (1995).

The following discussion references the building notation for the 20-story frame introduced in Chapter 3. Geometry and member sizes for this model are also presented. The remaining sections in Chapter 5, namely Static Analysis and Earthquake Analysis, present different load patterns and provide results for lateral drifts, maximum member forces and energy dissipation. Once all patterns are covered, conclusions are drown.

5.2. Static Analysis

The SAC frame is first subjected to static loads. This is done to provide transparency between the results obtained from the 2-story frame discussed in Chapter 4 and the high-rise SAC model. Applying static loads also allows the researchers to eliminate inadequate hybrid combinations at an early stage of the analysis and to have general performance expectations for the dynamic response of the remaining cases.

The results discussed in Chapter 4 imply that the hybrid building $BL\_2-2,2-1,2-B,B-L(236-0.01-1{,}000)-R(236-0.01-1{,}000)$ allows for the best structural performance for the 2-story frame. A parallel model is statically tested for the 20-story frame. It is referred to as $BL\_20-2,21-M\ -236-0.01-1{,}000$ based on the notation discussed in Chapter 3, where this case is shown in Figure 3.22. Other hybrid models for the high-rise building are derived based on this proposed configuration.

5.2.1. Static Load-Controlled Analysis

A static load-controlled analysis is used to compare the lateral displacements along the height of the hybrid buildings. This load pattern is chosen over the more commonly used displacement-controlled analysis, because it allows for better interpretation of the results obtained for the lateral displacement of the buildings. Following the uniformly distributed gravity load, a lateral point load of 350 kips (1557 kN) is incrementally applied at the top left corner of each building. The magnitude of this force is determined by imposing

a 15 in (38.1 cm) lateral displacement to the top of the 20-story rigid frame. Therefore, a lateral force of 350 kips (1557 kN) in the rigid frame allows for less than 0.5 percent variation in the ratio of lateral displacement to total height of the building. The results obtained at the end of this load pattern are presented in Figure 5.2. In the figure, the basement of the building is labeled as floor "0", and the roof is floor "21." Seven hybrid systems are compared to the rigid frame, which is the stiffest of all as anticipated. The hybrid frame with most semi-rigid connections, namely $BL\_20-2,21-M-236-0.01-1,000$, experiences the largest lateral deformation, which also complies with the researcher's expectations. Finally, frame $BL\_20-9:13-A-236-0.01-1,000$ deflects less than its pinned counterpart, which is compatible with the properties of the connections in each case.

Hybrid frames $BL\_20-0:5-A-236-0.01-1,000$ and $BL\_20-9:13-A-236-0.01-1,000$ proved to be most intriguing, because of their ability to localize lateral displacement almost entirely at the regions with semi-rigid connections. If the high-rise building is seen as a single cantilever beam, these regions simulate spring development within the beam as shown in Figure 5.1. This grossly simplified model explains why the two cases have a significant potential in earthquake design, where the newly formed springs may help to decouple the earthquake acceleration. Nonetheless, both cases experience relatively high top story deflections, which may become problematic in meeting serviceability requirements. Moreover, assigning semi-rigid

connections to additional floors has adverse effect to the overall lateral displacement as seen in Figure 5.2 for case $BL\_20-3:10-A-236-0.01-1{,}000$. Additional load patterns are applied to the discussed cases to further evaluate their performance, and the results are compared to other alternatives.

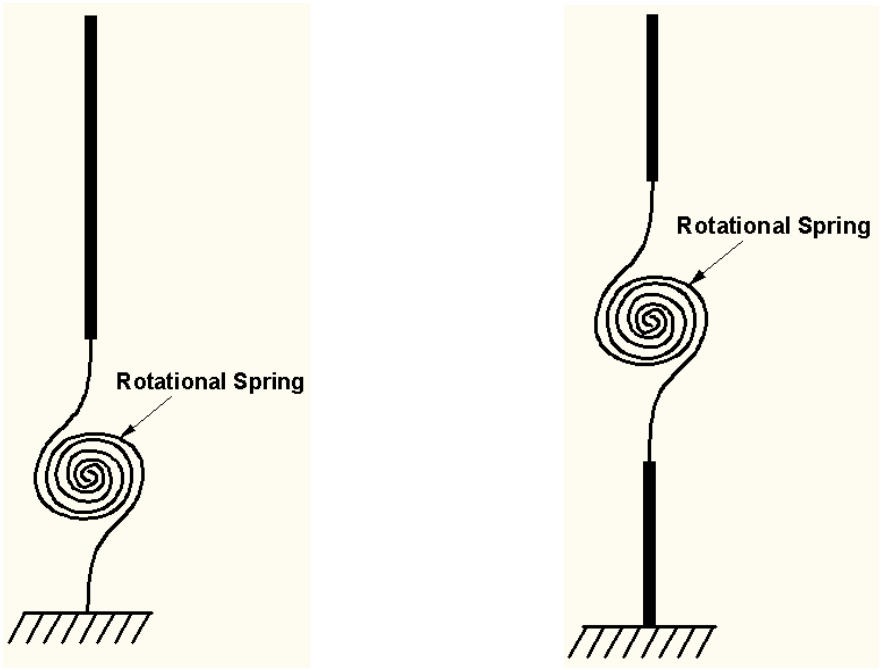

a) b)

Figure 5.1 Simplified Model for Hybrid Frames:
a) $BL\_20-0:5-A-236-0.01-1{,}000$, b) $BL\_20-9:13-A-236-0.01-1{,}000$

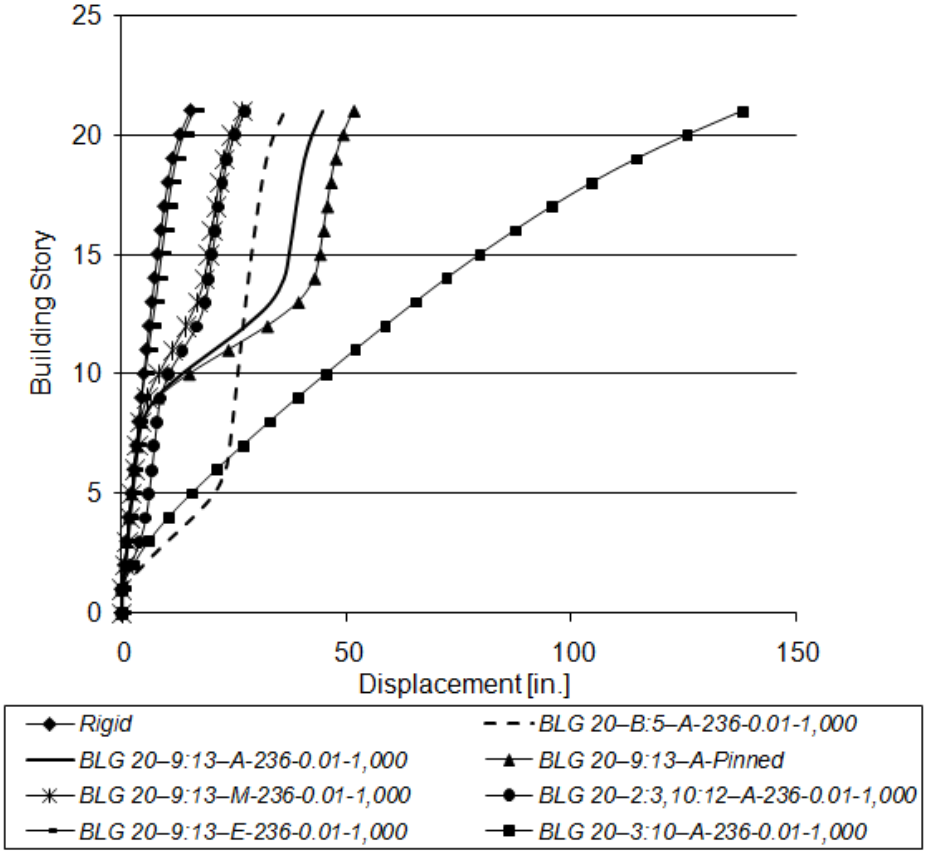

Figure 5.2 Lateral Displacement for Static Load-Controlled Analysis

5.2.2. Cyclic Displacement-Controlled Analysis

A customized cyclic displacement record is developed to evaluate building response with increasing cyclic displacement. The record begins at 0 in displacement and increasingly oscillates around this value at 0.1 in (0.25 cm) increments until a final displacement of 15 in is reached. Therefore, the displacements in inches at the beginning of the record are 0.1, -0.1, 0.2, -0.2, 0.3, -0.3, 0.4 etc., and the pattern continues until 15 in (38.1 cm) displacement

is imposed on the top left corner of the building. A general overview of this load is presented in Figure 5.3.

This loading is selected to better understand the buildings' response to cyclic loading, and it is not intended to simulate earthquake response.

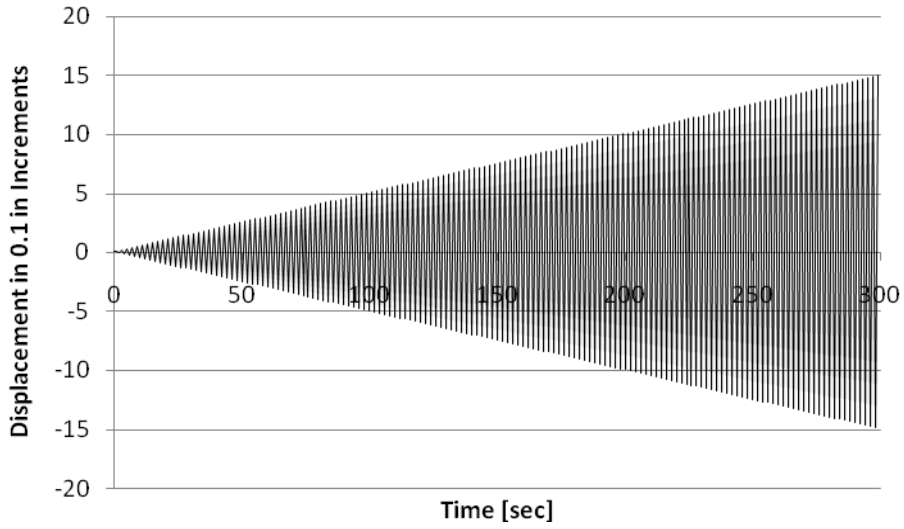

Figure 5.3 Displacement Record Used in Cyclic Displacement-Controlled Analysis

Earthquake ground shaking carries large amounts of energy. This energy is conveyed to buildings, where it causes structural damage. Scientists have developed multiple methods to provide reliable channels for earthquake induced energy and to minimize and control member failure. One approach is to add building dampers and another is to localize plastic hinge development in beams as to avoid soft story development. Such paths allow for minimum impact on the structural integrity. Therefore, a greater amount of dissipated energy is desirable, because it is directly proportional to the building's durability during an earthquake. This research aims to improve structural energy

dissipation by finding a pattern of partially restrained connections that optimizes the performance of the tested system. The importance of providing an economical solution to earthquake induced structural damage is recognized.

Energy dissipation is monitored by plotting lateral force verses horizontal sway. Since the cyclic displacement pattern discussed earlier is assigned to the top left corners of the experimental frames, the sway records at this location are used in the proceeding analysis. The lateral force records are obtained by summing the shear in the basement columns of each structure. Figure 5.4 graphs lateral force verses horizontal sway hysteresis loops at each time increment for six hybrid frames and compares their energy dissipation to that of the rigid building. The cases with largest area under their curves dissipate energy most efficiently. Therefore, frames $BL\_20-0:5-A-236-0.01-1{,}000$ and $BL\_20-9:13-A-236-0.01-1{,}000$ appear to provide the optimal combinations of rigid and partially restrained connections for this criterion. This observation and the conclusions drawn from the previous section stipulate the two cases may meet the objectives of this study. However, wind load analysis is performed to determine if the frames satisfy serviceability requirements as evoked by the results obtained from the static load-controlled analysis.

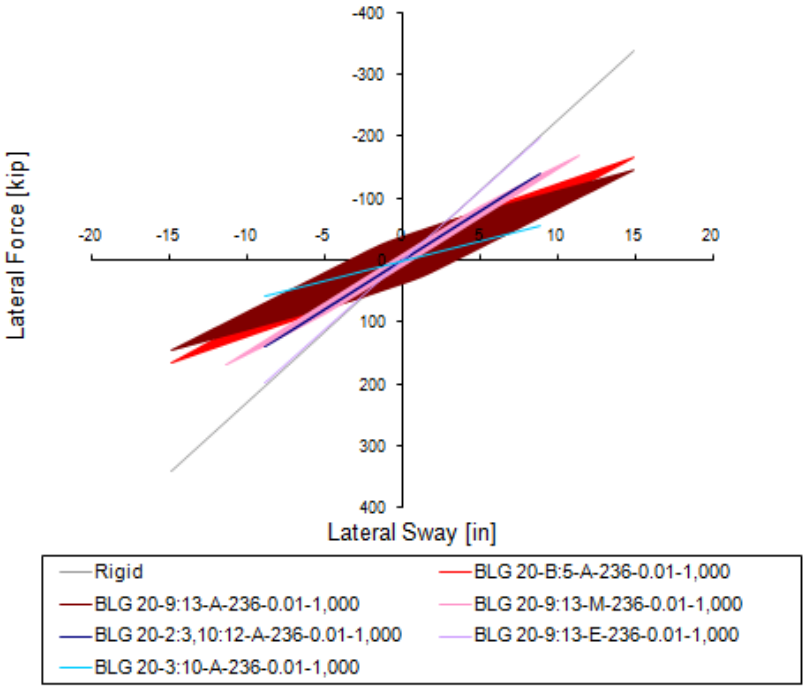

Figure 5.4 Energy Dissipation in Hybrid Frames

5.2.3. Wind Load

Uniformly distributed wind loads for the windward and the leeward sides of each structure are calculated per the applicable code, namely ASCE 7-05. The location of all buildings is assumed to be a typical site on the west coast, where the frames are likely to experience seismic loading. Therefore, the design wind velocity is 85 mph (153 km/h) as stated in Figure 6-1 of ASCE 7-05. All calculations performed while finding the wind load distributions are presented in detail in Appendix A. Figure 5.5 illustrates the lateral loads due to wind pressures simultaneously imposed on both sides of each building. For simplicity, they are applied as point loads at each story, which does not alter results significantly. In addition, two load combinations for partially enclosed

buildings are considered as per ASCE 7-05. They are obtained for -0.55 and 0.55 as values for the internal pressure coefficient, and calculations for both loading conditions are presented in Appendix A. However, the wind loads calculated based on an internal pressure coefficient of -0.55 are used, because by observation they are the controlling pattern. After all applicable forces, including gravity loads, are applied to the systems, the lateral displacements are plotted as shown in Figure 5.6. In this figure, the basement of the building is labeled as floor “0”, and the roof is floor “21.”

As expected, the rigid frame deflects the least, while the hybrid system with most semi-rigid connections experiences the largest deformations. In all hybrid frames, significant lateral sways are observed at the stories where rigid connections are replaced by partially restrained connections. Again, cases $BL\_20-0:5-A-236-0.01-1{,}000$ and $BL\_20-9:13-A-236-0.01-1{,}000$ have average performance, but in this analysis frame $BL\_20-0:5-A-236-0.01-1{,}000$ allows for the larger top displacement of the two hybrid systems.

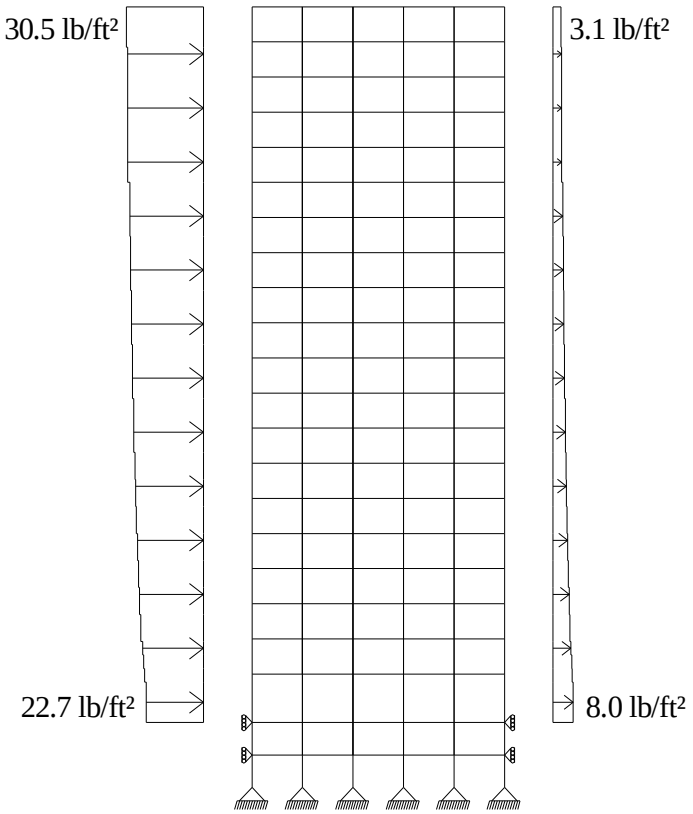

Figure 5.5 Wind Load Pressures

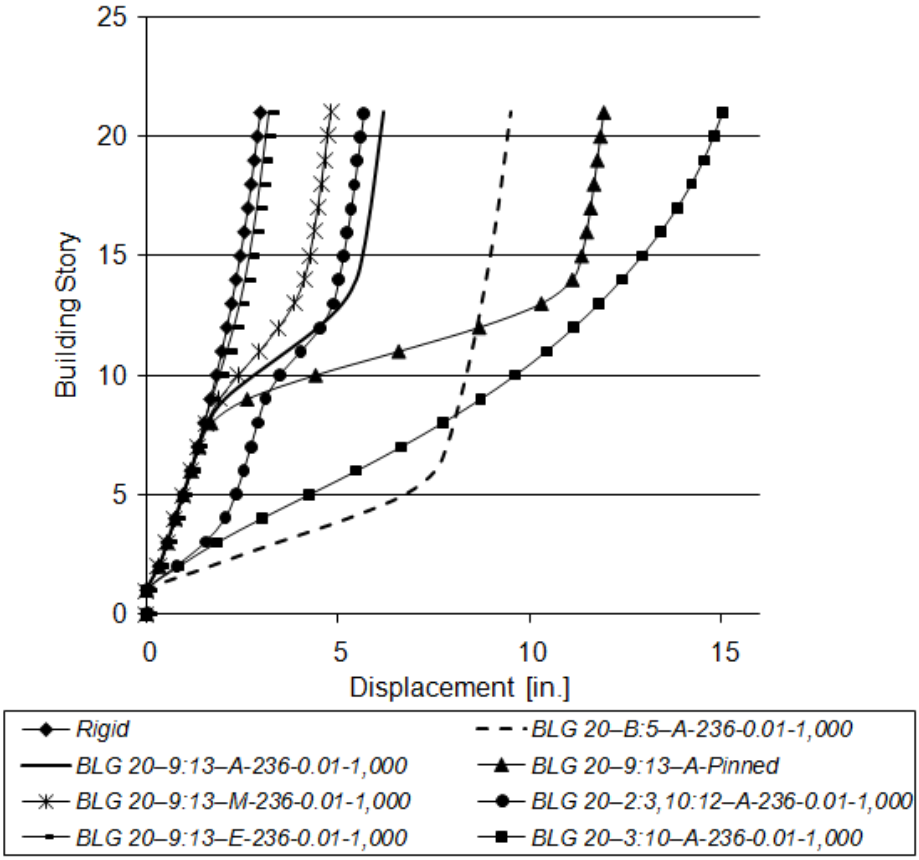

Figure 5.6 Lateral Displacement for Wind Load Analysis

Although other hybrid systems experience smaller lateral deformations when subjected to either wind loads or static load controlled analysis, their energy dissipation is insufficient compared to frames $BL\_20-0:5-A-236-0.01-1{,}000$ and $BL\_20-9:13-A-236-0.01-1{,}000$. These two cases have relatively large yet satisfactory static sways, and they are further subjected to multiple records from past earthquakes. The results are used to evaluate the buildings' potential in earthquake engineering design and to forecast their performance during future seismic activities.

5.3. Earthquake Analysis

The two hybrid models chosen from the static analyses are presented again in Figure 5.7 and Figure 5.8 for clarity. They are next subjected to horizontal acceleration time histories recorded during past earthquakes. These records are obtained from the SAC ground motion database and from the Pacific Earthquake Engineering Research (PEER) center database. The data obtained from the first source is generated for Los Angeles having probabilities of exceedence of 10% in 50 years. While the acceleration time histories from the SAC database reflect the natural ground motion during a given earthquake, their mean response spectrum has been modified to comply with the 1997 NEHRP design spectrum. Therefore, data provided by the SAC Joint Venture is useful during the design process. On the other hand, the PEER ground motion data provides the actual acceleration values recorded during an earthquake. Thus, it allows the evaluation of buildings' relevant performance.

A variety of earthquake frequencies is used to present a comprehensive evaluation of the proposed hybrid combinations. El Centro and Northridge earthquakes represent the high-frequency range, while two site records of an earthquake in Turkey in 1999 provide information for structural behavior during low-frequency earthquakes. Another record from the Parkfield, California earthquake exemplifies medium-frequency earthquakes. The presentation of all results is organized based on the data source.

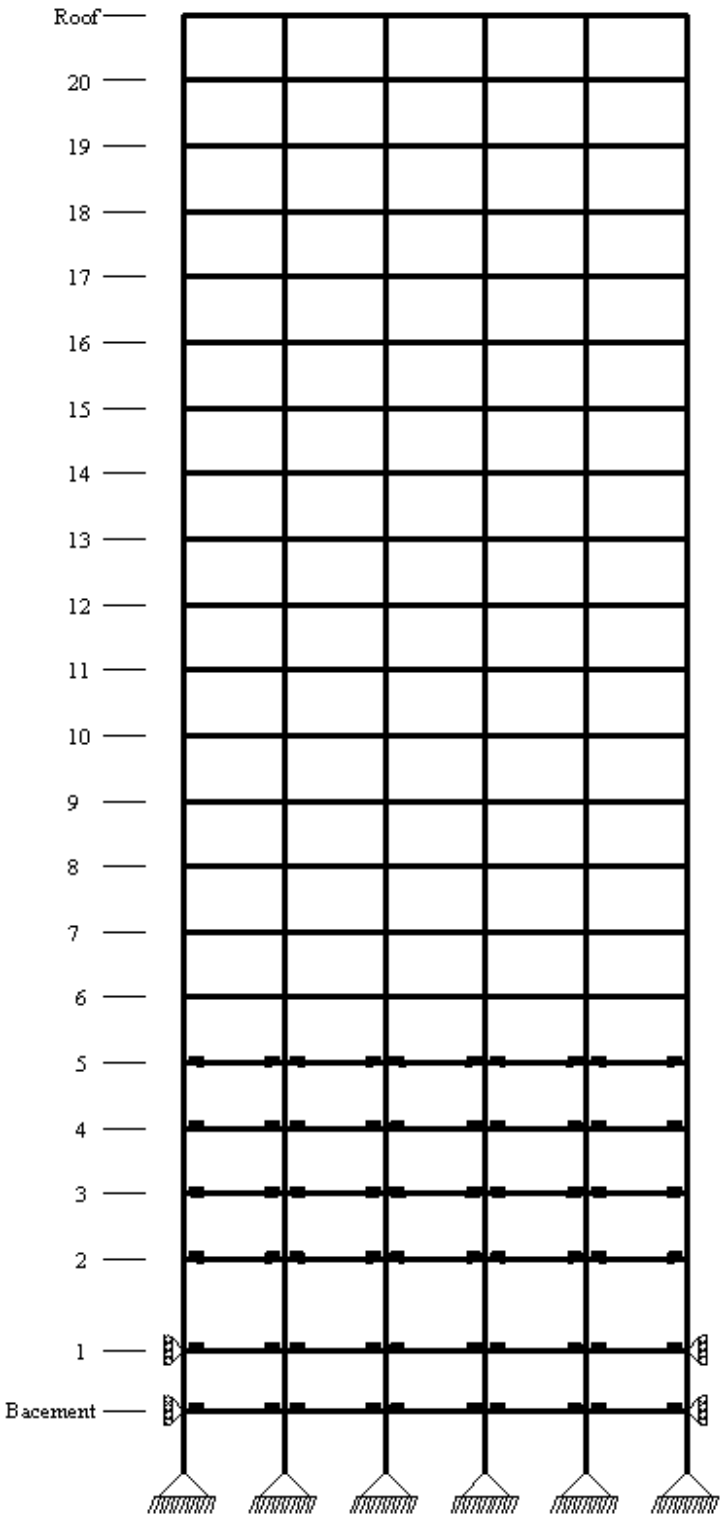

Figure 5.7 Hybrid Model $BL\_20-0:5-A$

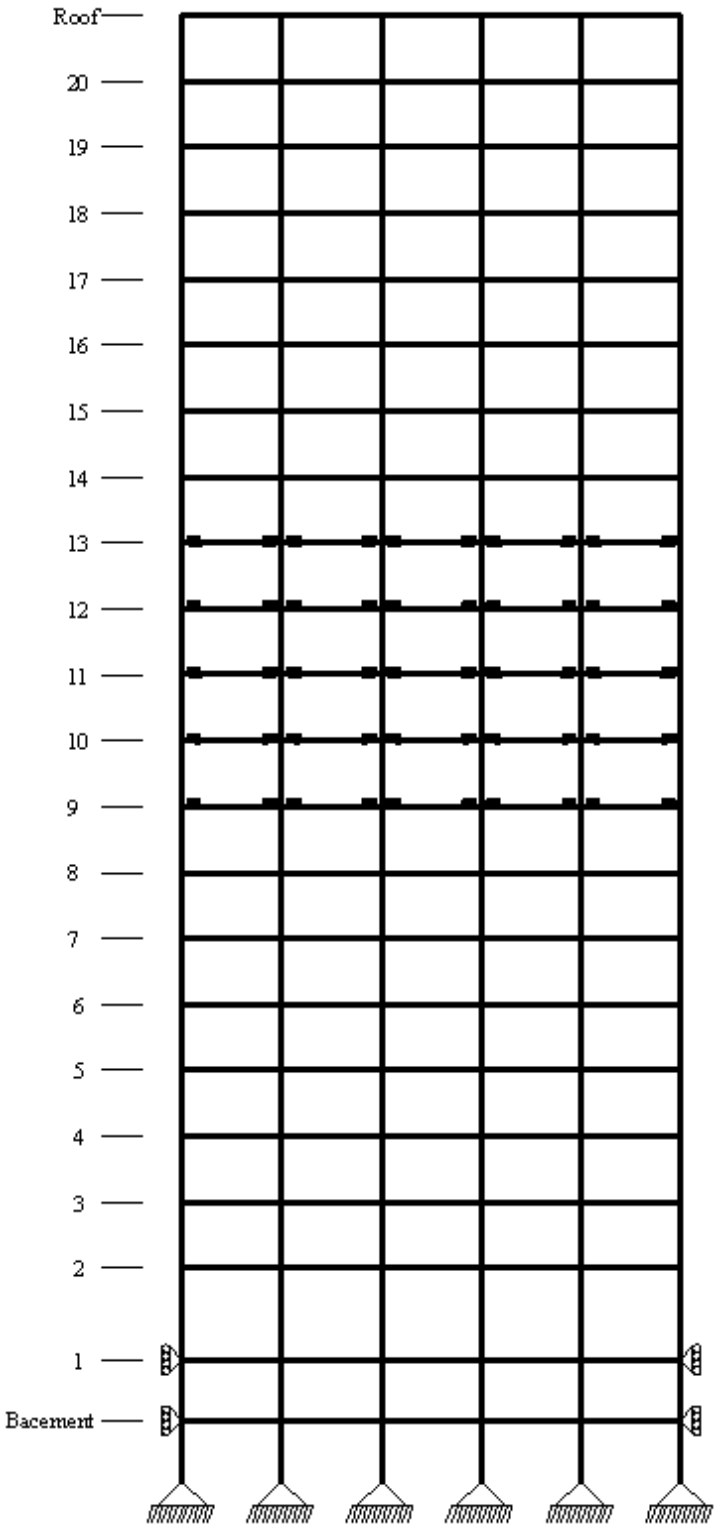

Figure 5.8 Hybrid Model $BL\_20-9:13-A$

5.3.1. SAC Records

5.3.1.1. El Centro Earthquake

This research uses two SAC earthquake records, one of which has an epicenter in El Centro, California. It occurred on May 19, 1940, and it is chosen because of its popularity among scientists. The exact site where data was collected is Imperial Valley, which is located 6 miles away from the epicenter. The earthquake magnitude is 6.9 on the Richter scale, and the total duration of the record is 53.5 seconds. Data collected during the ground shaking is scaled by a factor of 2.0 to allow for adequate building design. The earthquake frequency varies between 1.0 Hz and 2.25 Hz; therefore, this event is a sample of high frequency ground shaking. Figure 5.9 presents the acceleration time history of El Centro earthquake in terms of the gravitational acceleration, g. Since the majority of the earthquake energy is concentrated in the first 30 seconds of the record, only this portion of the data is inflicted on the tested buildings.

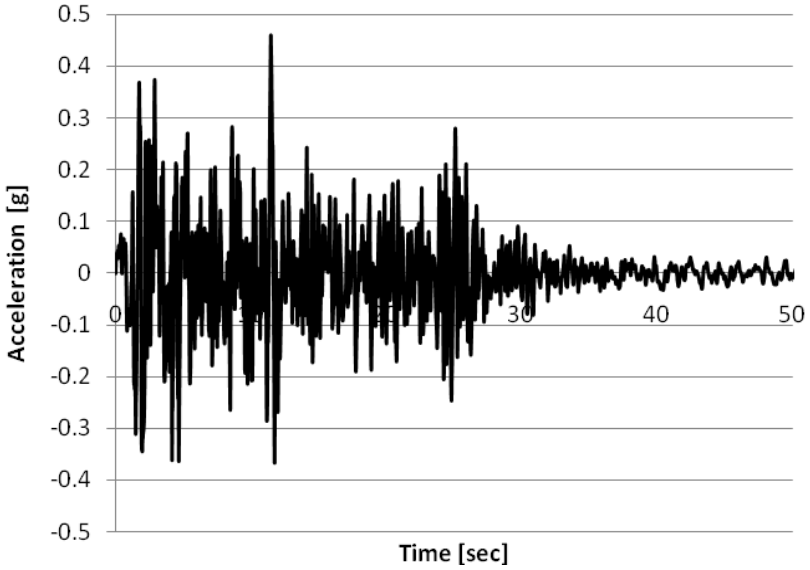

Figure 5.9 El Centro Earthquake Acceleration Time History

Several connection properties are introduced for the earthquake analysis. The connections' specifics such as initial and post-yield slopes and yield moments are taken as the average values of the full-scale test results presented in "Energy Dissipation Characteristics of Semi-Rigid Connections" (Abolmaali et.al 2008). Five most commonly used partially restrained connections are adopted from this study. They are incorporated into the hybrid geometries selected from the static analyses. The modeled connections are bolted/bolted double web angle, welded/bolted double web angle, top and seat angle, flush end-plate, and extended end-plate. A total of six hybrid frames are analyzed for each earthquake; one system uses the analytical connection properties from the static analyses, and the rest model the discussed commonly used connections. The new systems follow the frame notation introduced in Chapter 3 and reflect the changes in the semi-rigid connection properties.

Table 5.1 summarizes the connections' characteristics used throughout this analysis. As noted in Chapter 4, a bi-linear model with no ultimate capacity is used to simulate the behavior of semi-rigid connections; thus, the three connection parameters are adequate. Welded/bolted double web angle and top and seat angle connections have the same connection parameters, because the average values of their test results are similar.

Table 5.1 Connection Properties

	Initial Stiffness (*10^3) [kips/in] (kN/m)	Initial to Post-Yield Stiffness Ratio	Yield Moment [kips] (kN)
Analytical	236 (41,328)	0.01	1,000 (4,448)
Bolted/Bolted Double Web Angle	100 (17,512)	0.1	120 (534)
Welded/Bolted Double Web Angle	500 (87,559)	0.05	500 (2,224)
Top and Seat Angle	500 (87,559)	0.05	500 (2,224)
Flush End-Plate	800 (140,095)	0.1	2,300 (10,231)
Extended End-Plate	2,500 (437,795)	0.05	2,000 (8,896)

Once the earthquake record is applied, lateral displacements in each frame are compared to the rigid building. The sways at the roof and ninth floor are monitored as they provide information for displacement at the top and middle of the tested buildings. The results are presented graphically in Figures B.1 through B.6. These figures compare information for structures, which have the same hybrid geometries but different partially restrained connection

properties. Figures B.5 and B.6 allow comparison between buildings with partially restrained connections from the basement through the fifth floor, notated $BL\_20-0:5-A-236-0.01-1{,}000$, and buildings with partially restrained connections from the ninth through thirteenth floors, notated $BL\_20-9:13-A-236-0.01-1{,}000$. For clarity, only the results from the analytical connection properties introduced in the static analysis are graphed in these figures.

Member forces developed in each hybrid frame are compared in Appendices C through E. Appendix C provides information on member moments, Appendix D presents member shear forces, and Appendix E introduces member axial forces. The ratios of members' maximum end moments in the hybrid frames to their corresponding values in the rigid frame for the El Centro earthquake are plotted in Figures C.1 through C.10. Every story has six columns and five beams, which is reflected by the number of data points at each unit mark. Only the maximum end moments developed in the members due to the earthquake and gravity loads are extracted. It should be noted that these values do not necessarily occur at the same time step, but they reflect the maximum moment each member experiences when subjected to the El Centro earthquake.

Four graphs for each connection type are presented in Appendix C. The first couple provides information for columns and beams in the hybrid combination, where all rigid connections in the first five stories are replaced by

partially restrained connections. For example, Figures C.1, C.3, C.5, C.7 and C.9 provide this information for the frames subjected to the El Centro earthquake. The second pair presents results for columns and beams in the frames, where all rigid connections in the ninth through thirteenth stories are substituted by semi-rigid connections. Figures C.2, C.4, C.6, C.8 and C.10 exemplify this information for the frames subjected to the El Centro earthquake. In these figures, “M1” is a hybrid-to-rigid frames ratio of moments in the left and bottom nodes of beams and columns respectively, while “M2” provides the same information for the right and top nodes, respectively. Therefore, for ratios greater than one the moment demand at the node has increased when semi-rigid connections are used. The shear and axial force information for the El Centro earthquake is presented in a similar format in Figures D.1 through D.10 and E.1 through E.10, respectively.

5.3.1.2. Northridge Earthquake

The other earthquake obtained from the SAC database has an epicenter in Northridge, California. It occurred on January 17, 1994, and it is chosen because of its unanticipated damage on steel structures. Many earthquake design procedures were significantly revised as a result of research revolving around this event. The exact site where data was collected is Sylmar, Olive View, which is located 4 miles away from the epicenter. The earthquake magnitude is 6.7 on the Richter scale, and the total duration of the record is 59.9 seconds. Data collected during the ground shaking is scaled by a factor of

0.99 to allow for adequate building design per National Earthquake Hazard Reduction Program (NEHRP) provisions. The earthquake frequency varies between 0.4 Hz and 3.3 Hz; therefore, this event is a sample of high frequency ground shaking. Figure 5.10 presents the acceleration time history of Northridge earthquake in terms of the gravitational acceleration, g. Since the majority of the earthquake energy is concentrated at the beginning of the earthquake, only the first 50 seconds of the record are inflicted on the tested buildings.

Once the earthquake record is applied, lateral sways in each frame are again compared to the rigid building. These results are used to evaluate different partially restrained connection properties assigned to the hybrid geometries. The same nodal displacements assessed in the previous section are presented for the Northridge earthquake analysis. As seen from the results presented in Figures B.7 through B.12, connection characteristics are less influential for the structural performance than is the presence of beneficial semi-rigid connection patterns. The frames derived from the two hybrid combinations develop less lateral sway than the rigid frame for nearly all connection properties and record locations. Similar behavior was observed for the El Centro analysis; therefore, the hybrid combinations introduced in this study become strong candidates for alternatives to current earthquake design practices.

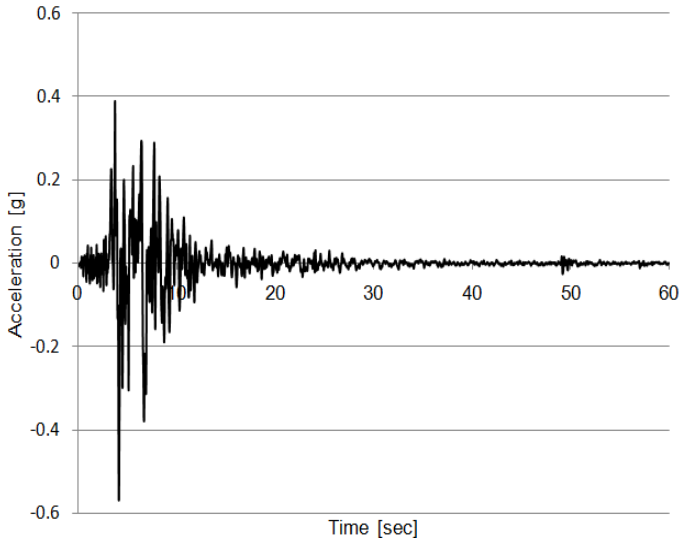

Figure 5.10 Northridge Earthquake Acceleration Time History

The ratios of members' maximum end moments in the hybrid frames to their corresponding values in the rigid frame for the Northridge earthquake are plotted in Figures C.11 through C.20. Similarly, Figures D.11 through D.20 present the hybrid-to-rigid shear force ratios obtained for this earthquake. Finally, the hybrid-to-rigid ratios for the axial forces developed in each member during the Northridge earthquake are shown in Figures E.11 through E.20.

Much like the El Centro earthquake results, most end moments in the hybrid systems subjected to Northridge earthquake decrease in value compared to the rigid frame. The exceptions to this observation are usually perceived in the graphs presenting results for the columns. These promising results are additionally discussed after more earthquake records are presented.

5.3.2. PEER Records

5.3.2.1. Parkfield Earthquake

The remaining three earthquake records are obtained from the PEER database. The epicenter of the first ground shaking covered in this section is in Parkfield, California. It occurred on June 28, 1966, and it is chosen because it represents the medium-frequency earthquake spectrum. Its dominant frequencies vary between 0.5 Hz and 1.75 Hz as obtained from the SeismoSignal software. The exact site where data was collected is station Cholame. The earthquake magnitude is 6.1 on the Richter scale, and the total duration of the record is 43.7 seconds. Data collected during the ground shaking is not scaled as this analysis aims to provide the actual response of the building. Figure 5.11 presents the acceleration time history of Parkfield earthquake in terms of the gravitational acceleration, g. The first 40 seconds of the record are inflicted on the tested buildings.

Once the earthquake record is applied, lateral sways in each frame are again compared to the results from the rigid building. These results are used to evaluate different partially restrained connection properties assigned to the hybrid geometries. The nodal displacements for the Parkfield earthquake analysis are presented in Figures B.13 through B.18.

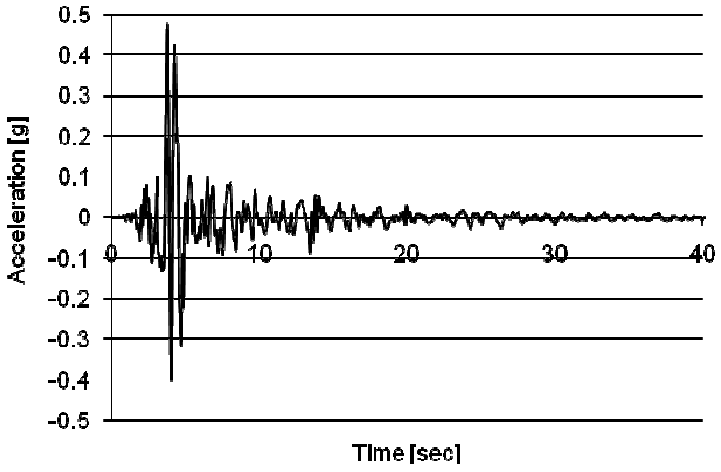

Figure 5.11 Parkfield Earthquake Acceleration Time History

Member forces developed in each hybrid frame as a result of the Parkfield earthquake are compared next. The ratios of members' maximum end moments in the hybrid frames to their corresponding values in the rigid frame are plotted in Figures C.21 through C.30. Similarly, Figures D.21 through D.30 present the hybrid-to-rigid shear force ratios, and Figures E.21 through E.30 show the hybrid-to-rigid ratios for the axial forces.

The results from this medium frequency earthquake are satisfactory, because most end moments in the hybrid systems decrease in value compared to the rigid frame. However, larger number of column ends and some beam ends experience moment demands greater than those observed for the rigid frame when compared to the El Centro and Northridge earthquakes. Larger variety of earthquake frequencies is needed to allow for thorough evaluation of the proposed combinations.

5.3.2.2. Kocaeli Earthquake

The last earthquake record used in the dynamic analyses of this study is also obtained from the PEER database. Its epicenter is located in Kocaeli, Turkey. It occurred on August 17, 1999, and it is chosen because it represents the low-frequency earthquake spectrum. Its dominant frequencies vary between 0.84 Hz and 1.0 Hz based on results obtained from the SeismoSignal software. Two site locations are used for this earthquake; one is Afyon Bay, Turkey and the other is Aydin, Turkey. The earthquake magnitude is 7.4 on the Richter scale, and the total duration of the record for each side is 180.6 and 220.2 seconds respectively. Data collected during the ground shaking is not scaled as this analysis aims to provide the actual response of the building. Figure 5.12 and Figure 5.13 present the acceleration time history for Afyon Bay and Aydin earthquake records in terms of the gravitational acceleration, g. The first 180 and 200 seconds of the respective record are inflicted on the tested buildings.

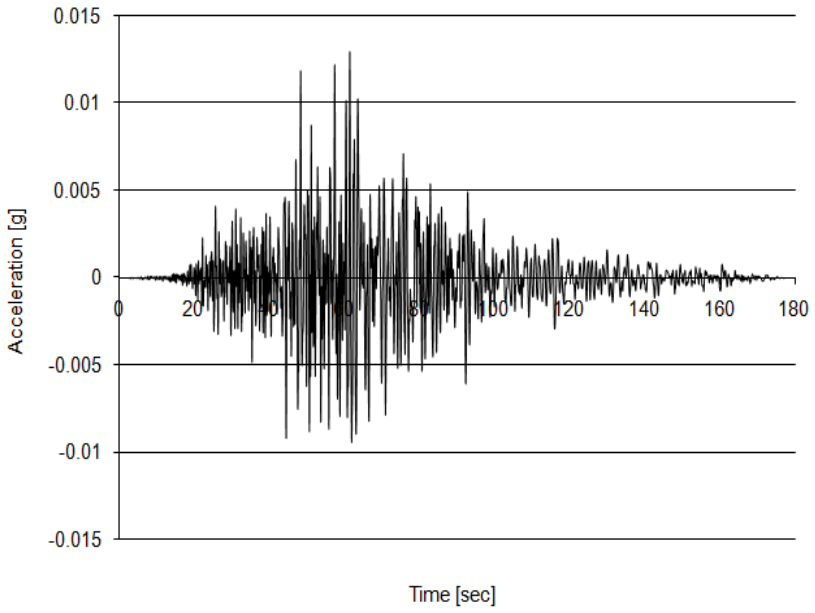

Figure 5.12 Afyon Bay Earthquake Acceleration Time History

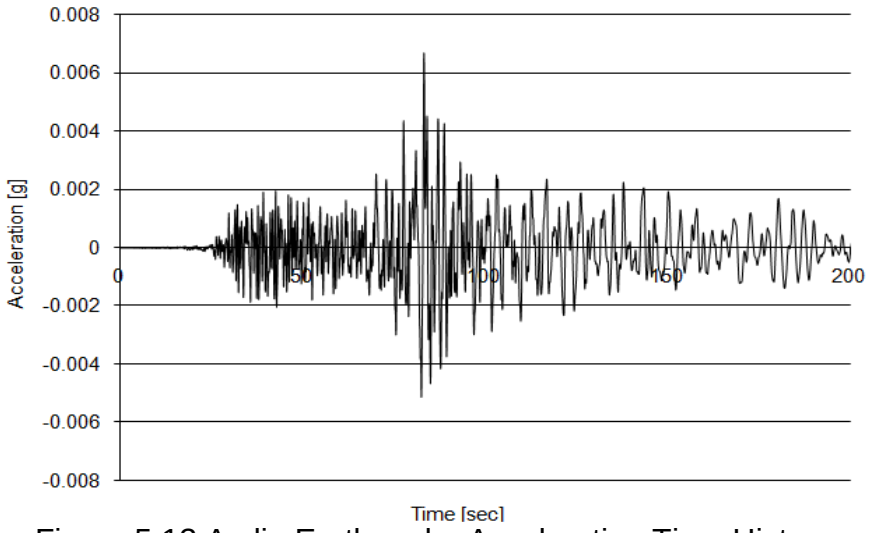

Figure 5.13 Aydin Earthquake Acceleration Time History

Once each earthquake record is applied, lateral sways in the frames are again compared to the rigid building. The nodal displacements for both acceleration histories are presented in Figures B.19 through B.30. Next, the ratios of members' maximum end moments in the hybrid frames to their

corresponding values in the rigid frame for the Koaceli earthquake are plotted in Figures C.31 through C.50. Similarly, Figures D.31 through D.50 present the hybrid-to-rigid shear force ratios obtained for this earthquake. Finally, the hybrid-to-rigid ratios for the axial forces developed in each member during the Kocaeli earthquake are shown in Figures E.31 through E.50.

5.4. Discussion of the Results

The static analyses of the 20-story frame suggest the hybrid frames with semi-rigid connections from the basement to the fifth floor for one combination and from the ninth to the thirteenth stories for another combination are good candidates for alternatives to current design practices in earthquake engineering. These cases were subjected to five earthquake acceleration records to determine their performance under dynamic loading. The displacements at the top and middle of the frames for the El Centro and Northridge earthquakes indicate the hybrid frames result in significant decrease of lateral sway when compared to results obtained from a rigid frame with identical geometry and loads. Similar observations were drawn for the displacements developed during the Parkfield earthquake; however, the hybrid frames' superior performance was not as evident as it was for the previously mentioned earthquakes. The last two earthquake acceleration histories recorded at Afyon Bay and Aydin, Turkey in 1999 result in increased lateral sways at the top and middle of the tested frames. Therefore, the addition of semi-rigid connections has adverse effects for these dynamic records.

This response is justified by comparing building frequencies to earthquake frequencies. Table 5.2 presents building frequencies for the first ten modes of the tested hybrid combinations, while earthquake characteristics are discussed in the relevant section introductions. The frame frequencies presented in Table 5.2 are obtained using OpenSees software framework, while the frequency of each dynamic acceleration history is acquired through SeismoSignal, a strong-motion data processing program developed by Seismosoft Earthquake Engineering Software Solutions. SeismoSignal is capable of computing predominant and mean periods, effective design acceleration, acceleration and velocity spectrum intensity, elastic and constant-ductility inelastic response spectra, Fourier and Power spectra, and its validity is confirmed by S.M.Ashfaqul Hoq (2010).

Table 5.2 Building Frequencies

Mode	Rigid [Hz]	$BL\_20-0:5-A-236-0.01-1{,}000$ Configuration [Hz]	$BL\_20-9:13-A-236-0.01-1{,}000$ Configuration [Hz]
1	0.446	0.230	0.254
2	1.279	1.028	1.081
3	2.136	1.933	1.622
4	3.004	2.640	2.428
5	3.994	3.422	3.453
6	5.113	4.582	4.194
7	6.292	5.832	5.619
8	7.620	7.079	6.784
9	8.984	8.354	8.099
10	10.386	9.731	9.617

The frequencies presented in Table 5.2 indicate that incorporating partially restrained connections into a building's geometry decreases the

frequencies of its dominant modes. As a result, hybrid frames experience higher resonant effects when subjected to low frequency dynamic loads such as the Turkey earthquake in 1999. The effect of semi-rigid connections on the frequencies of the frames also explains the decrease in lateral sway when they are subjected to earthquakes in the medium and high frequency ranges, where the El Centro and Northridge earthquakes exemplify high frequency dynamic loads and the Parkfield earthquake represents medium frequency vibrations. This observation also explains results for demands on frame members.

Generally, most end moments in the hybrid systems subjected to the El Centro and Northridge earthquakes decrease in value compared to the rigid frame, since large number of the ratios in Figures C.1 through C.20 are less than 1. The largest reduction in column moment demands for the El Centro earthquake is produced by case $BL\_20-0:5-A-100-0.1-120$, where a column experiences almost 16 time less moment than it would if a rigid frame is used instead of the hybrid frame. Case $BL\_20-0:5-A-500-0.05-500$ produces the largest moment decrease in a column for the Northridge earthquake, where the demand on a node is reduced by more than 30 times. These promising results are reinforced by maximum reduction in beam moments of over 83 times for the El Centro earthquake and over 133 times for the Northridge earthquake.

The moment demands on rigid connections in the hybrid frames decrease consistently regardless of the partially restrained connection patterns

or properties. In Figures C.1 through C.20, floors where semi-rigid connections are applied are easily identified, since moment redistribution causes scattering of data points. Some of these points have values greater than 1, which means the nodes that these points represent experience larger moment demands compared to the rigid frame. For example, the largest increase in .column moment demands during the El Centro was observed for case $BL\_20-0:5-A-800-0.1-2{,}300$, where the moment at a node was doubled. The same hybrid case also produces the largest moment increase in columns of 62 percent during the Northridge earthquake. However, this increase in column moment demands for some nodes does not automatically stipulate larger member sizes. According to the current design practice only the higher value of the two end moments in a member is used to determine its size. Therefore, an observed increase in moments on one side of an element does not always result in a larger section for the column, since the other end of the member may experience the controlling design moment. Finally, it is noted that no moment increase in beams is observed for either the El Centro or Northridge earthquakes.

The Parkfield earthquake provides similar results. Again, the moment demands on rigid connections in the hybrid frames decrease consistently regardless of the partially restrained connection patterns or properties. The largest decrease in column moment demands for this earthquake is developed for case $BL\_20-9:13-A-100-0.1-120$, where a node experienced 560

time less moment than it would if a rigid frame is used instead of the hybrid frame. This case also produces the largest beam moment reduction of 774 times less moment than the rigid building. As observed for the two high frequency earthquakes, this medium frequency earthquake produces some moment increase in floors where semi-rigid connections are applied. The maximum increase in column moments of 130 percent is acquired from case $BL\_20-9:13-A-236-0.01-1{,}000$, while the maximum increase in beam moments of 37 percent is obtained from case $BL\_20-9:13-A-800-0.1-2{,}300$. However, this increase in moment is relatively insignificant compared to decreased moment demands in the majority of the frame elements.

Both records from the Koaceli earthquake produce less satisfactory results than the rest of the earthquakes, which is contributed to resonant effects. A larger number of data points in Figures C.31 though C.50 read values larger than 1, which indicates that more nodes experience increased moment demands. The largest moment increase is obtained from case $BL\_20-0:5-A-236-0.01-1{,}000$ for the Aydin acceleration history, where a column node experiences 8 times as much moment as it would if a rigid frame is used instead of the hybrid frame, and the demand on a beam node is increased almost 3 times. Conversely, case $BL\_20-0:5-A-100-0.1-120$ for the Afyon Bay acceleration history produces maximum moment reduction of 27 times for a column node and 15 times for a beam node. Overall, the

moment demands induced by this low-frequency earthquake in the hybrid frames are less satisfactory than the rest of the earthquake records. However, low-frequency earthquakes tend to have low acceleration magnitudes; thus, despite the reduced performance of hybrid structures, their operation is unlikely to be at sake under this type of dynamic load.

Shear forces are also compared to provide adequate evaluation of the studied hybrid frames. Nearly all shear force ratios for the El Centro and Northridge earthquakes remain less than 1 as shown in Figures E.1 through E.20. Therefore, almost all nodes in the hybrid frames experience reduction in shear force demands compared to the magnitudes they would experience if a rigid frame is implemented. Similarly to the observations for member moments, the shear demands on rigid connections in the hybrid frames subjected to the El Centro and Northridge earthquakes decrease consistently regardless of the partially restrained connection patterns or properties. The maximum decrease in shear for these dynamic acceleration histories is obtained for nodes in case $BL\_20-0:5-A-100-0.1-120$, where the El Centro earthquake produces 9 times less shear than the corresponding value in the rigid frame and the Northridge earthquake presents 15 times less shear demand. Some of the shear force ratios at the stories where semi-rigid connections are applied surpass the value of one, which indicates the shear demand is amplified. The greatest increase in shear occurs for case $BL\_20-0:5-A-800-0.1-2{,}300$,

where this force is enlarged by a factor of 3 for the El Centro earthquake and by 63 percent for the Northridge earthquake.

The results for the Parkfield earthquake are similar to those obtained for the El Centro and Northridge earthquakes. No rigid connection in the hybrid frames experience shear force increase, while some nodes in the floors where semi-rigid connections are applied encounter larger shear demands. The largest reduction in shear demands is produced by case $BL\_20-0:5-A-100-0.1-120$, where a column experiences almost 11 time less shear force than it would if a rigid frame is used, and a beam's shear force is decreased by a factor of 9. The same case also produces the maximum increase in column shear forces of almost 140 percent, while the maximum increase in beam shear forces of 55 times the value of shear recorded from the rigid frame is obtained from case $BL\_20-9:13-A-100-0.1-120$.

Figures E.31 though E.50 show that shear force demands during the Kocaeli earthquake records are increased for more members compared to previously discussed earthquakes. This observation is consistent with results for lateral sways and moments. Case $BL\_20-0:5-A-236-0.01-1{,}000$ for the Aydin acceleration history produces maximum reduction in shear demands in columns of over 11 times that in the rigid frame and a maximum of 50 percent higher demands in beams. Conversely, case $BL\_20-0:5-A-100-0.1-120$ for the Afyon Bay acceleration history results in the largest decrease in member

shear forces in the amount of 740 percent for columns and 54 percent for beams.

Reflecting on the response of the hybrid frames to all dynamic loads, connection characteristics tend to be less influential for the structural performance than is the presence of beneficial semi-rigid connection pattern placement. This placement of partially restrained connections acts as a natural building damper and tends to decouple the movement of the building from the shaking of the ground beneath it. As a result, greater amount of energy is dissipated, while demands on the structure are decreased. This highly desirable effect reveals the potential of hybrid systems and the opportunity they present for more economical earthquake design.

Overall, the analyses of the 20-story frame showed that the studied hybrid systems can significantly improve structural performance of high-rise buildings. This conclusion is justified by applying data obtained from on-site tests of commonly used partially restrained connections and by loading the frames with past earthquake acceleration history records. Hybrid structural systems and particularly the two configurations proposed in this study prove to have more potential in earthquake design of tall buildings than the amount credited to them in the past.

CHAPTER 6

SUMMARY, CONCLUSIONS AND RECOMMENDATIONS

6.1. Summary

This study investigates the performance of hybrid frames subjected to dynamic loading. Two building geometries are presented to provide a range of building proportions. A 2-story, 3-bay frame is used to represent low-rise structures; while a 20-story, 5-bay frame developed by the SAC Joint Venture is used to draw conclusions for tall buildings. First, arbitrary locations, at which rigid connections are replaced by partially restrained connections, are selected for the 2-story frame. No dynamic loads are applied. Static pushover analyses are performed instead to determine the most suitable hybrid combinations. The selected cases are then used to apply conceptually similar semi-rigid connections' pattern for the 20-story frame. Connection properties obtained from test results are applied to model specific connection types. Earthquake records covering a wide range of frequencies are applied to the tall building to evaluate the effect of semi-rigid connections on member forces and displacements. The impact of implementing different connection properties is also studied. The proposed hybrid combinations are compared, and these cases that present the best results for member forces and lateral displacements are recommended.

This study implements geometric and material non-linearities by accounting for the P-Δ effect and the steel yielding of a member cross section. Plastic hinges are assumed to develop at the element ends, and they are modeled by zero-length springs. Their stiffness, which is used to simulate inelastic response in the material, is given a bi-linear relationship, and no ultimate capacity is specified. The remaining section of the member is assumed to stay elastic. The non-linear computational procedure is solved using the conventional Newton-Raphson method.

6.2. Conclusions

The analyses of the 2-story frame showed that the arrangement where semi-rigid connections are positioned at both ends of the middle bay beams for both stories produces best overall results for energy dissipation. Some of the partially restrained connections in this combination experience reversed loading after being loaded beyond their yield limits. At this instant, the spring stiffness of the semi-rigid connections increases from the post-yield value to the initial elastic value, and they provide higher resistance to the applied load. As a result, this load is redistributed to other less resilient members in the structure. Since the mentioned hybrid combination provides satisfactory results for the three criteria being considered, namely lateral displacement, member forces and connection hysteresis moment-rotation relationship in the semi-rigid connections, it was used to develop parallel hybrid systems for the 20-story frame.

Two hybrid combinations for the SAC 20-story frame proved to have great potential in earthquake engineering, namely $BL\_20-0:5-A-236-0.01-1{,}000$ and $BL\_20-9:13-A-236-0.01-1{,}000$. The results from pushover and wind analyses were acceptable; however, a cyclic displacement controlled analysis suggested that the two cases produced significant improvement in building energy dissipation compared to the rigid frame or other proposed hybrid frames. As a result, the aforementioned hybrid structures were subjected to multiple earthquake acceleration histories. Their models demonstrated promising results for high-frequency earthquakes such as those with epicenters in El Centro, California and Northridge, California. Once additional earthquake records were applied, it became obvious that the dynamic response of the structures is altered relative to the rigid case, because the addition of semi-rigid connections reduces the structure's period. Resonant effects during high frequency earthquakes are reduced, but they increase if lower frequency earthquake records are applied. This behavior is observed in the drift diagrams presented in Figure 6.1 and Figure 6.2. In these figures the maximum lateral sway at each floor for all earthquakes is graphed for $BL\_20-0:5-A-236-0.01-1{,}000$, $BL\_20-9:13-A-236-0.01-1{,}000$ and the rigid frame, respectively. It should be noted that the deflection at each floor plotted on these graphs does not necessarily occur at the same time step of the earthquake record. Rather, it reflects the largest anticipated lateral sway for each story during a given earthquake.

Comparison of the three figures shows that lateral displacement is decreased for high and medium frequency earthquakes. The two acceleration histories exemplifying low-frequency earthquakes produce small deformations as a result of their low earthquake magnitudes. Therefore, these earthquakes produce relatively insufficient structural demands despite their reduced performance as a result of the introduction of semi-rigid connections as shown in Figures B.19 through B.30.

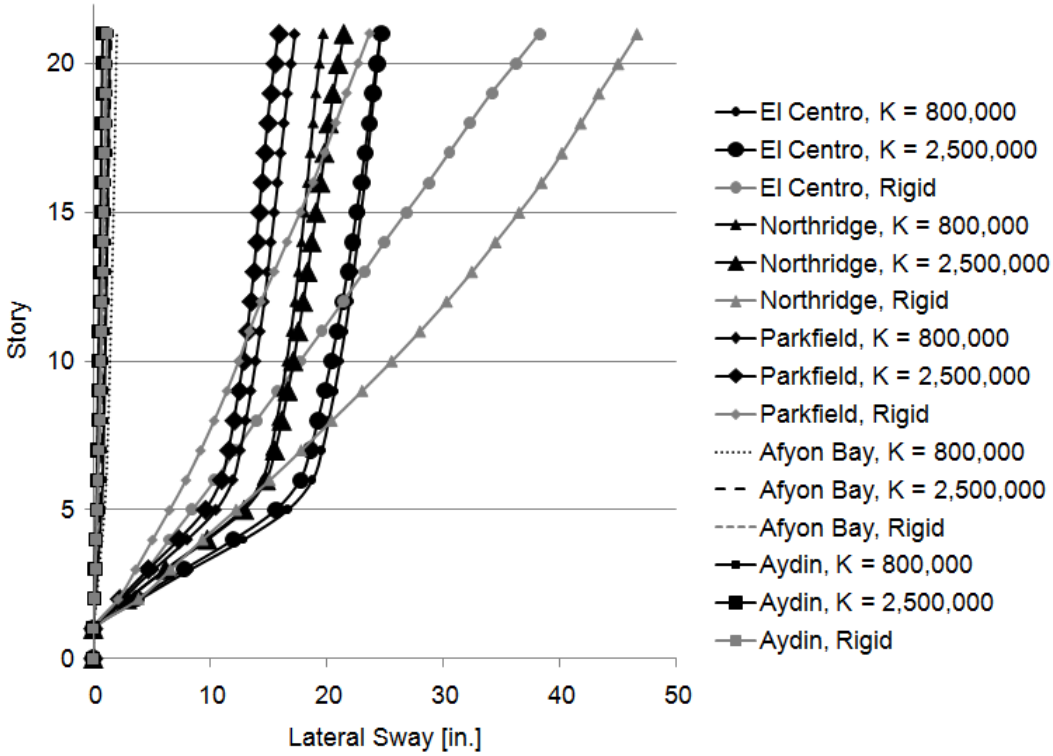

Figure 6.1 Maximum Lateral Sway for $BL\_20-0:5-A-236$ Obtained from Dynamic Analysis

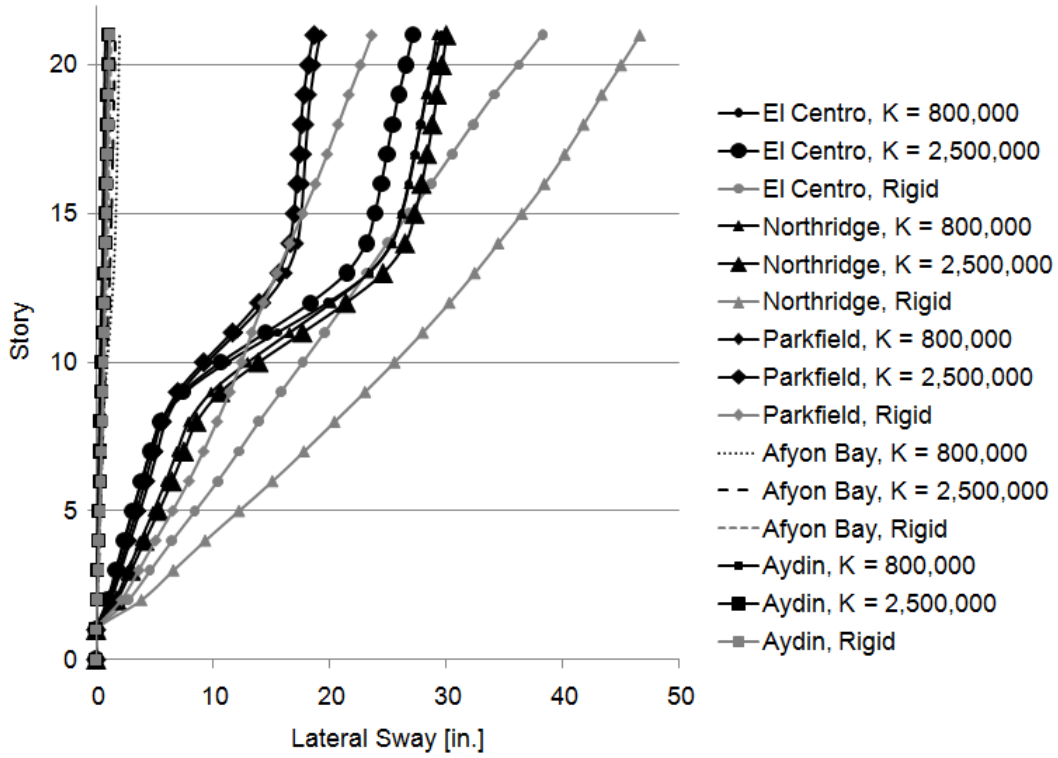

Figure 6.2 Maximum Lateral Sway for $BL\_20-9:13-A-236$ Obtained from Dynamic Analysis

Figure 6.1 and Figure 6.2 also compare hybrid frames, which are assigned different connection properties. The flush end-plate and extended end-plate partially restrained connections, which have initial stiffness of 800,000 kips/in (140,095,000 kN/m) and 2,500,000 kips/in (437,795,000 kN/m), respectively, are chosen to establish variation in structural response due to connections' characteristics. Both figures show that lateral sway is altered as different connections are incorporated. Therefore, the type of semi-rigid connection used in the analyses of the hybrid frames is influential to the overall structural outcome.

The major conclusions drawn from this research are summarized in the following list:

- Replacing rigid connections with partially restrained connections for multiple floors decouples ground vibration from the building movement similarly to the effect a spring has when installed in a rigid cantilever beam.
- Hybrid patterns $BL\_20-0:5-A$ and $BL\_20-9:13$ are considered most effective among the combinations proposed in this research for the 20-story frame based on their results for moment, shear and axial force demands, lateral sways and energy dissipation. They produce constant reduction in member demands for earthquakes representing the high and medium frequency ranges.
- Semi-rigid connections decrease the frequencies of hybrid frames' dominant modes.
- Hybrid frames experience less resonant effects during high frequency earthquakes, which results in reduction of demands on members.
- Placement of partially restrained connections is important, since some proposed patterns produce more beneficiary results than other hybrid combinations.

- The type of semi-rigid connections used in the analysis of the hybrid frames is influential.
- Energy dissipation is improved, which results in less lateral deformations and member demands.
- The average maximum end moments for the three high frequency earthquakes decreased by 71% for hybrid frame $BL\_20-0:5-A$ and by 51% for hybrid frame $BL\_20-9:13$ by using semi-rigid connections.
- The average maximum shear for the three high frequency earthquakes decreased by 72% for hybrid frame $BL\_20-0:5-A$ and by 61% for hybrid frame $BL\_20-9:13$ by using semi-rigid connections.

These observations and the proposed hybrid frames can be used to develop a new generation of earthquake resisting buildings. The research presented in this paper verifies hybrid buildings contain unexplored potential in engineering for dynamic loads.

6.3. Recommendations

Since this study covers a relatively new and unfamiliar subject, the following recommendations that may become beneficial in design for earthquake response are made:

1. The concept in this paper needs to be applied to additional building geometries. The enlarged spectrum would allow drawing more

generalized conclusions that could later be implemented by the appropriate overseeing institution.

2. A guideline for positioning of semi-rigid connections, which is applicable to a range of structural geometries needs to be established. The conclusions drawn in this study are specific to the tested building geometries and selected hybrid combinations. A procedure is needed to enable the selected hybrid systems to be relevant to any building geometry.
3. Change member sizes to study their influence on the response of the hybrid frames.
4. Compare results from 2-dimensional models, which are utilized in this research, to equivalent 3-dimensional models.

APPENDIX A

WIND LOAD CALCULATIONS FOR SAC FRAME

Wind load calculations for the 20-story SAC building follow ASCE 7-05 provisions. All figures and equations presented in this section are referenced from this design manual. Calculations are based on the simplified procedure outlined in Sec. 6.4.

Step 1. Determine the basic wind speed, V, and wind directionality factor, Kd.

The basic wind speed, V, for a typical site on the west coast is 85 mph (137 km/h) as shown in ASCE 7-05 Figure 6-1. The wind directionality factor, Kd, is 0.85 in accordance with Table 6-4.

Step 2. Determine Importance factor, I.

According to Table 1-1 of the ASCE 7-05 provisions the studied building is considered to be of category II. Therefore, the importance factor used for the wind calculations of the frame is 1.0 per Table 6-1.

Step 3. Determine exposure category and velocity pressure exposure coefficient, Kz or Kh.

The SAC frame is assumed to have a surface roughness C as defined in Section 6.5.6.2 of the ASCE 7-05 provisions and an exposure category C as discussed in Section 6.5.6.3. These assumptions and Table 6-3 are used to determine the velocity pressure exposure coefficient Kz (Kh) is 1.5768.

Step 4. Determine the topographic factor, Kzt.

The topographic factor Kzt is conservatively taken equal to 1.0 as proposed in Section 6.5.7.2 of the ASCE 7-05 provisions.

Step 5. Determine the gust effect factor, G or Gf.

The gust effect factor, G, is taken as 0.85 in accordance with Section 6.5.8.1.

Step 6. Determine the exposure classification.

The studied building is assumed to be partially enclosed.

Step 7. Determine the internal pressure coefficient, GCpi.

The values of the internal pressure coefficient, GCpi, for partially enclosed structures acting toward and away from the internal surfaces are 0.55 or -.55 respectively.

Step 8. Determine the external pressure coefficient, Cp.

The values of the internal pressure coefficient, Cp, for the main wind load resisting system of partially enclosed buildings is 0.8 for the windward wall and -0.5 for the leeward wall as specified by ASCE 7-05.

Step 9. Determine the velocity pressure, qz.

Equation 6-13 of the ASCE 7-05 provisions allows the computation of the velocity pressure, qz. This equation is repeated here for convenience.

$$q_z = 0.00256 K_z K_{zt} K_d V^2 I$$

Using the values of the variables obtained in previous steps, the velocity pressure for the SAC building is found to be 24.79 lb/ft² (1,187 N/m²).

Step 10. Determine the design wind pressures, p.

The design wind pressures for each wall, p, are calculated based on Equation 6-15 of the ASCE 7-05 provisions. This equation is repeated in the space below for convenience.

$$p = qGC_p - q_i(GC_{pi})$$

It is used to calculate the final load applied to the SAC building during the wind analysis of the 20-story frame.

APPENDIX B

LATERAL DISPLACEMENTS FOR SAC FRAME IN EARTHQUAKE ANALYSIS

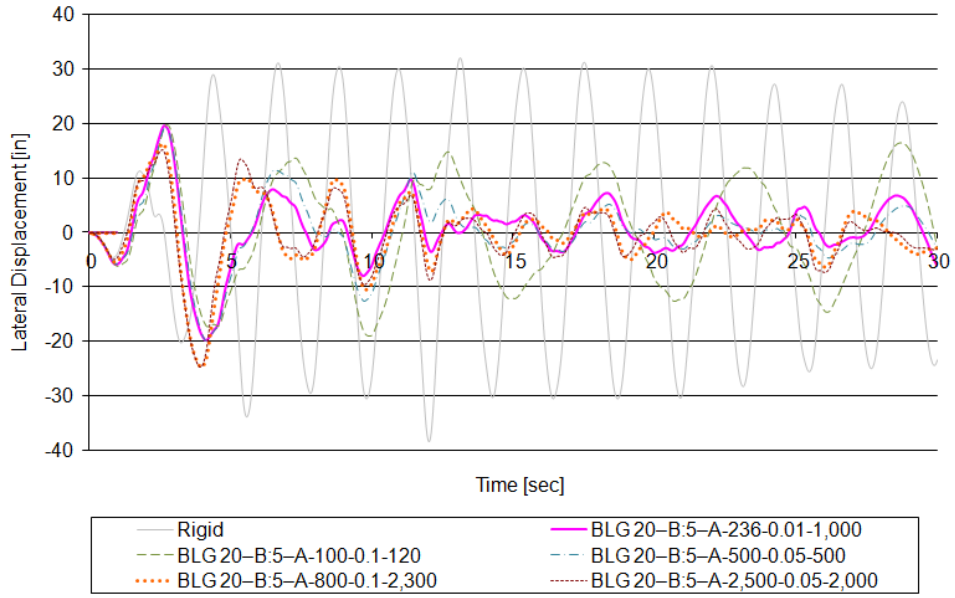

Figure B.1 Top Lateral Displacement for $BL\_20-0:5-A$ Configuration Subjected to El Centro

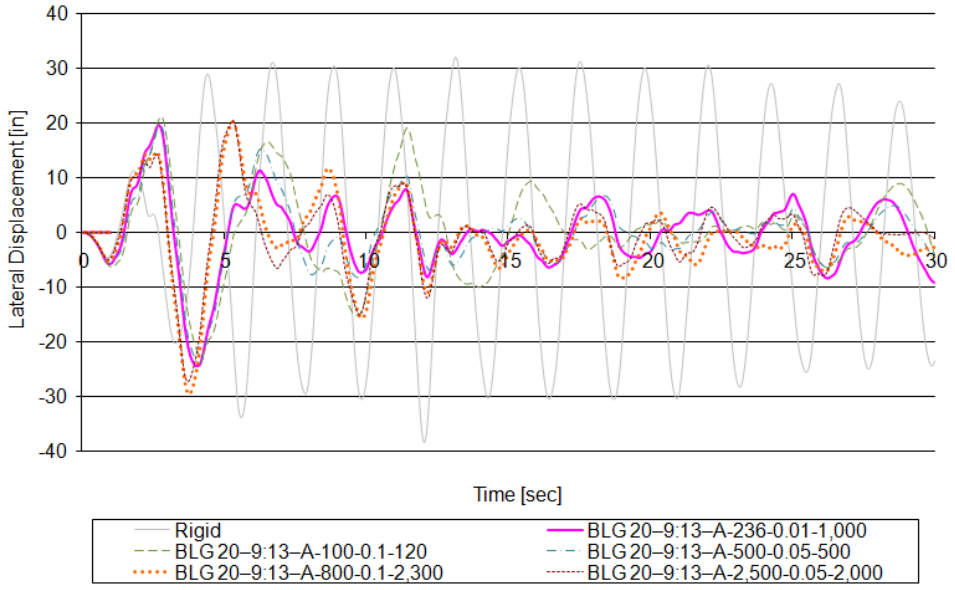

Figure B.2 Top Lateral Displacement for $BL\_20-9:13-A$ Configuration Subjected to El Centro

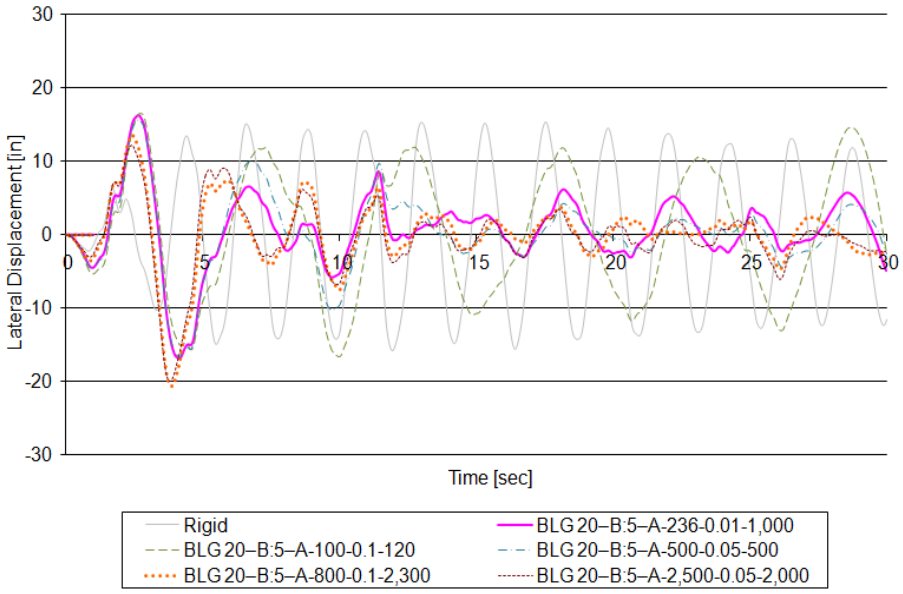

Figure B.3 The 9th Floor Lateral Displacement for $BL\_20-0:5-A$ Configuration Subjected to El Centro

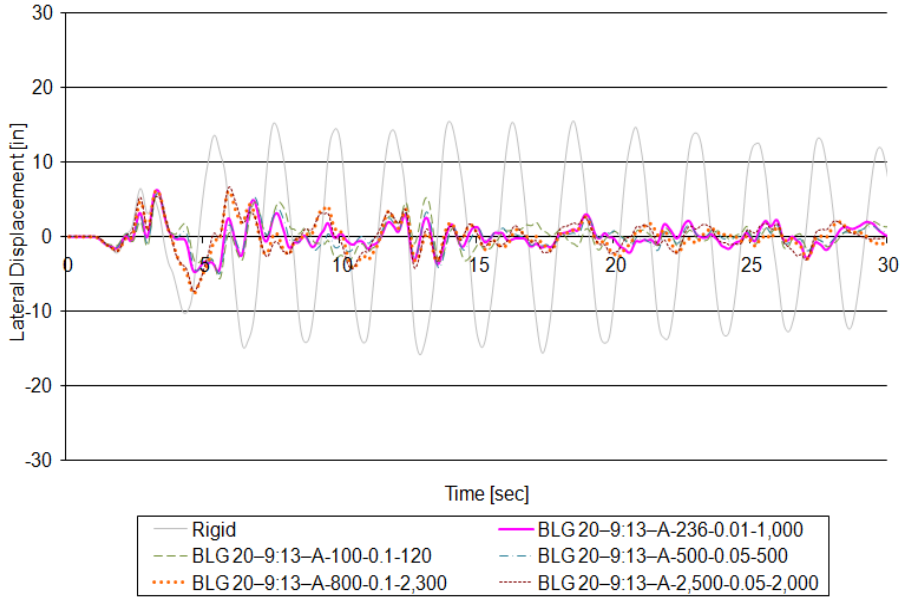

Figure B.4 The 9th Floor Lateral Displacement for $BL\_20-9:13-A$ Configuration Subjected to El Centro

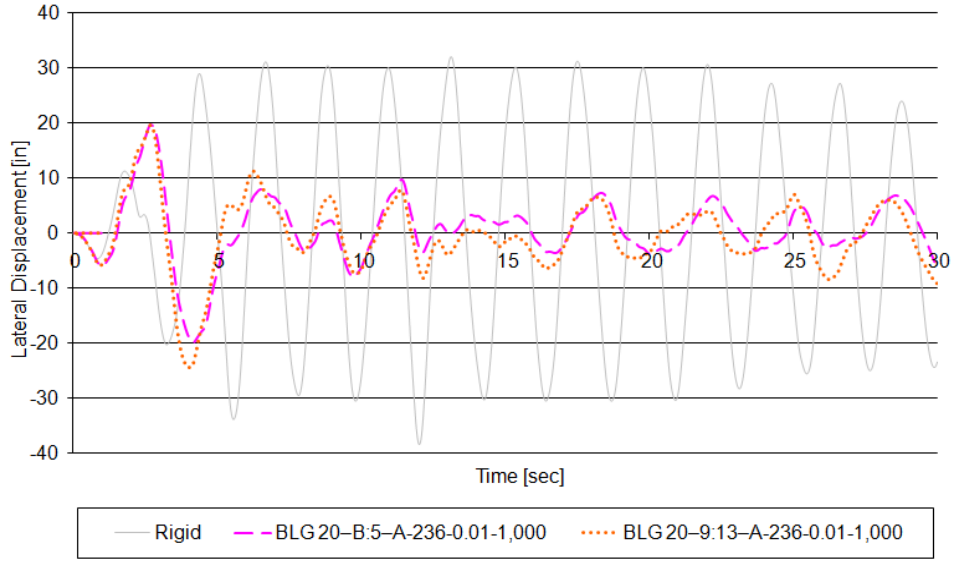

Figure B.5 Top Lateral Displacement Comparison Subjected to El Centro

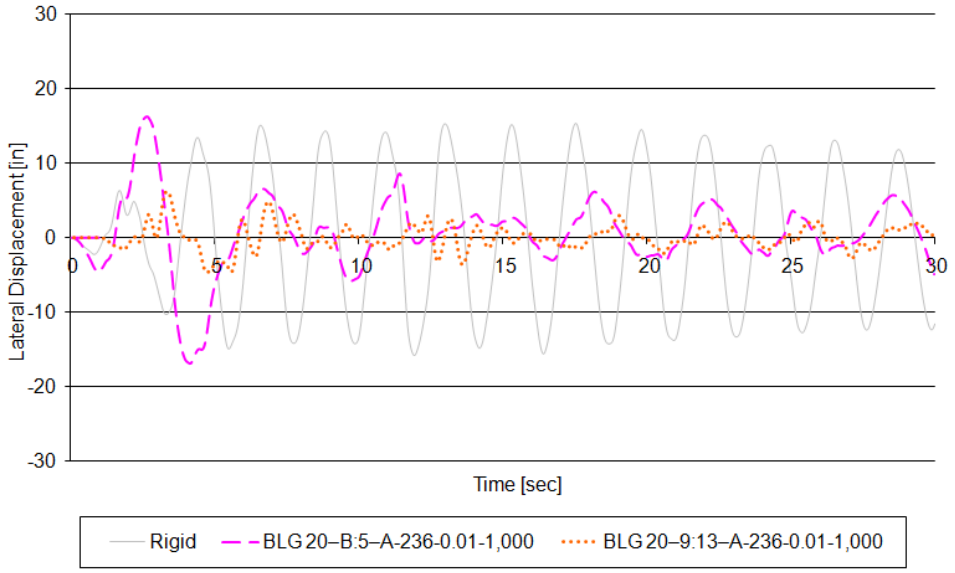

Figure B.6 The 9th Floor Lateral Displacement Comparison Subjected to El Centro

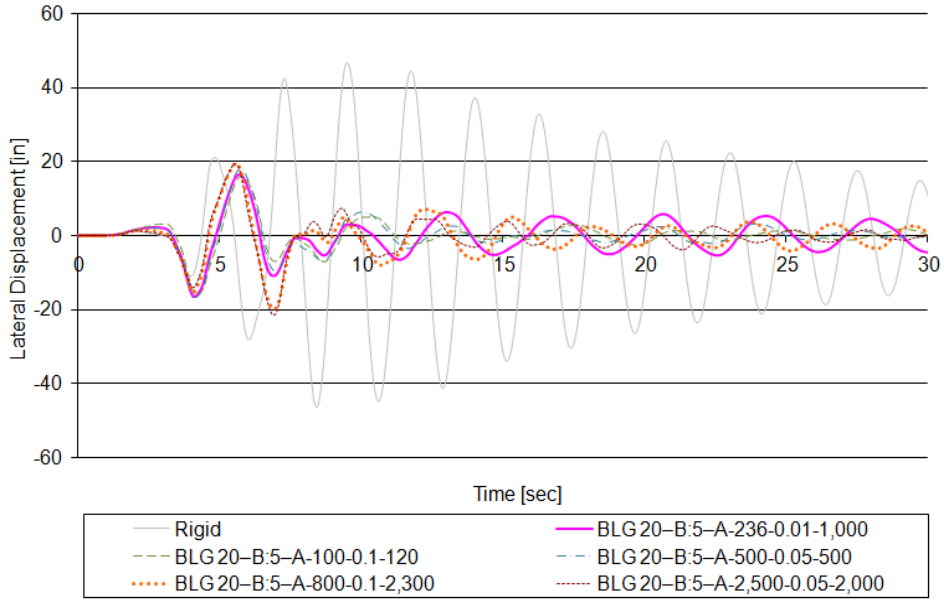

Figure B.7 Top Lateral Displacement for $BL\_20-0:5-A$ Configuration Subjected to Northridge

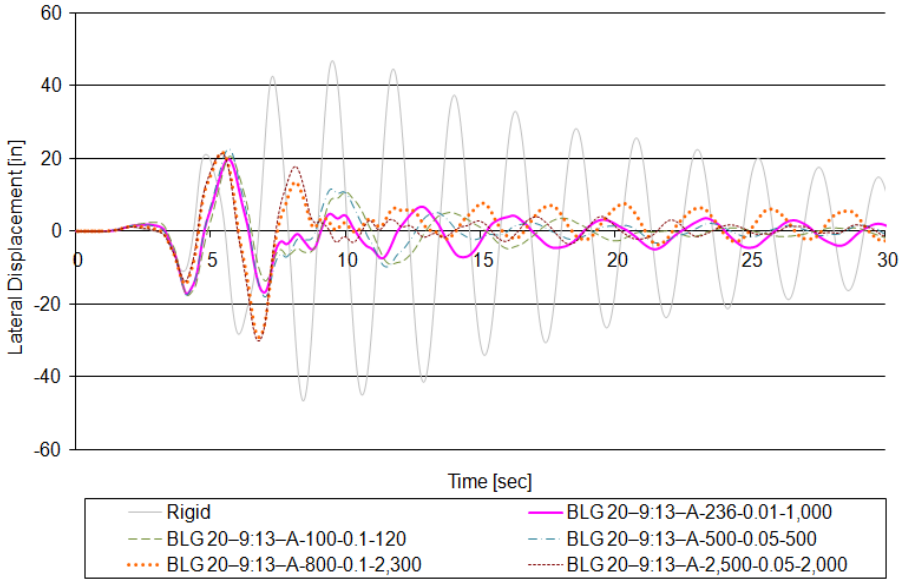

Figure B.8 Top Lateral Displacement for $BL\_20-9:13-A$ Configuration Subjected to Northridge

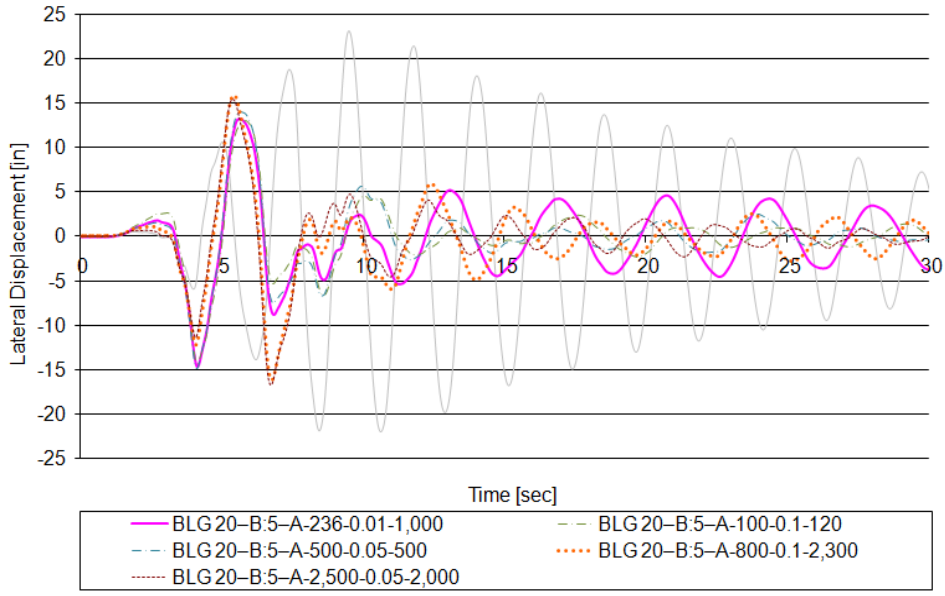

Figure B.9 The 9th Floor Lateral Displacement for $BL\_20-0:5-A$ Configuration Subjected to Northridge

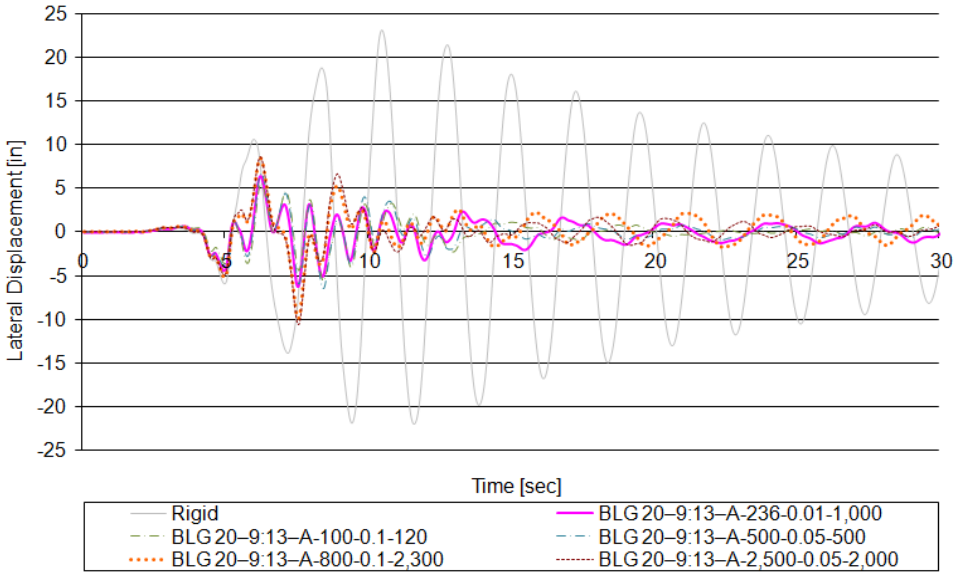

Figure B.10 The 9th Floor Lateral Displacement for $BL\_20-9:13-A$ Configuration Subjected to Northridge

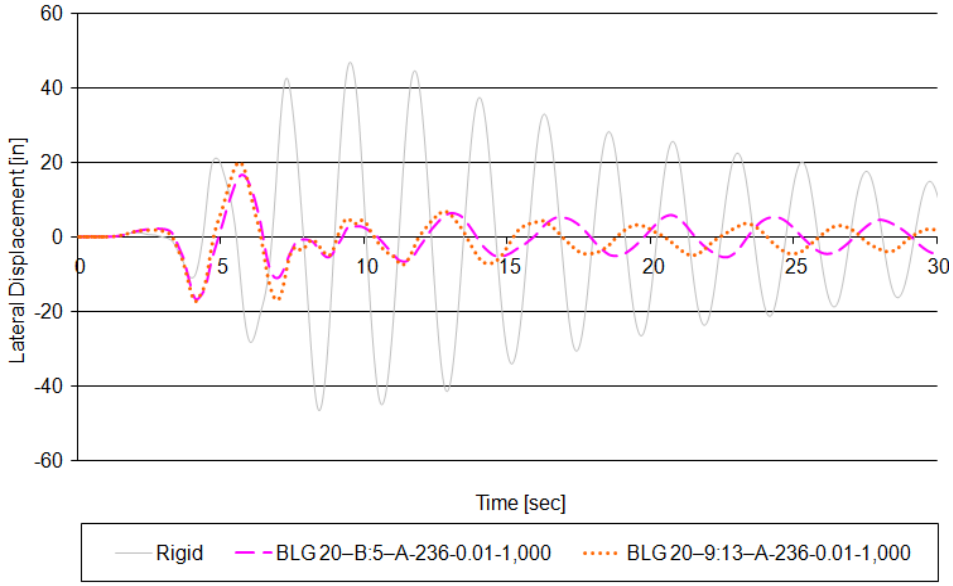

Figure B.11 Top Lateral Displacement Comparison Subjected to Northridge

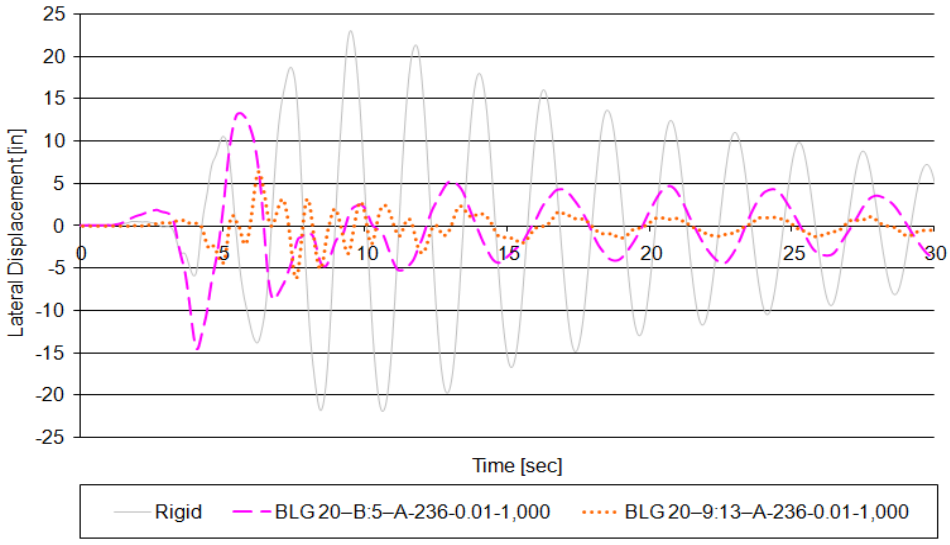

Figure B.12 The 9th Floor Lateral Displacement Comparison Subjected to Northridge

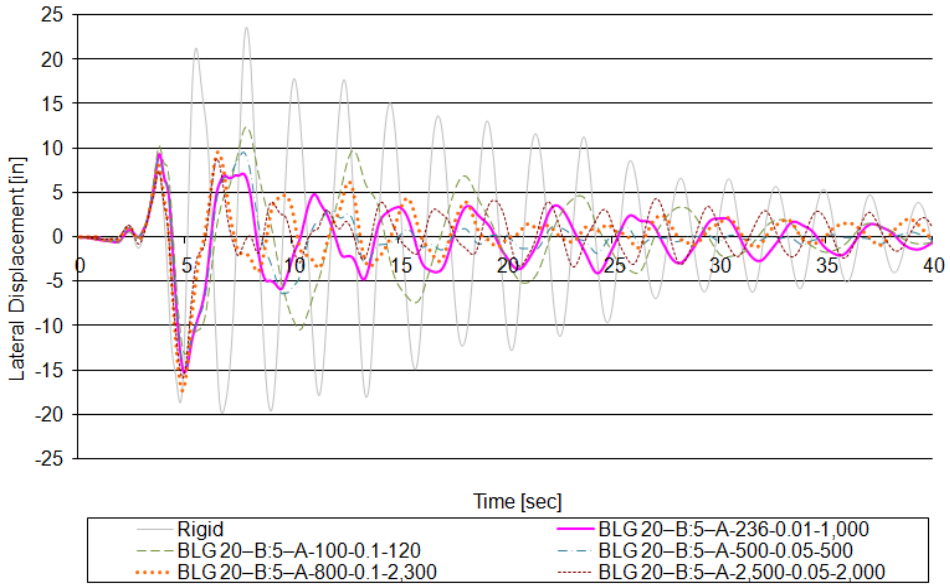

Figure B.13 Top Lateral Displacement for $BL\_20-0:5-A$ Configuration Subjected to Parkfield

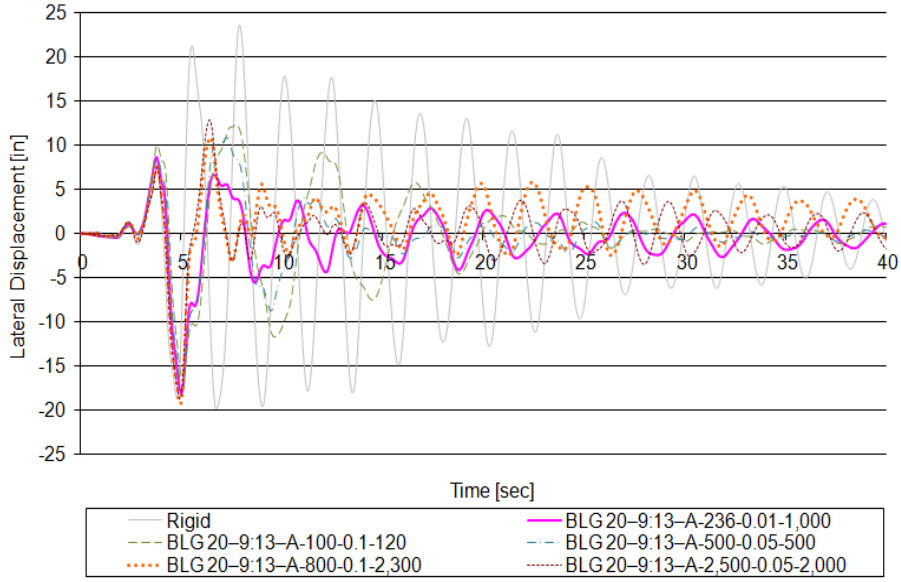

Figure B.14 Top Lateral Displacement for $BL\_20-9:13-A$ Configuration Subjected to Parkfield

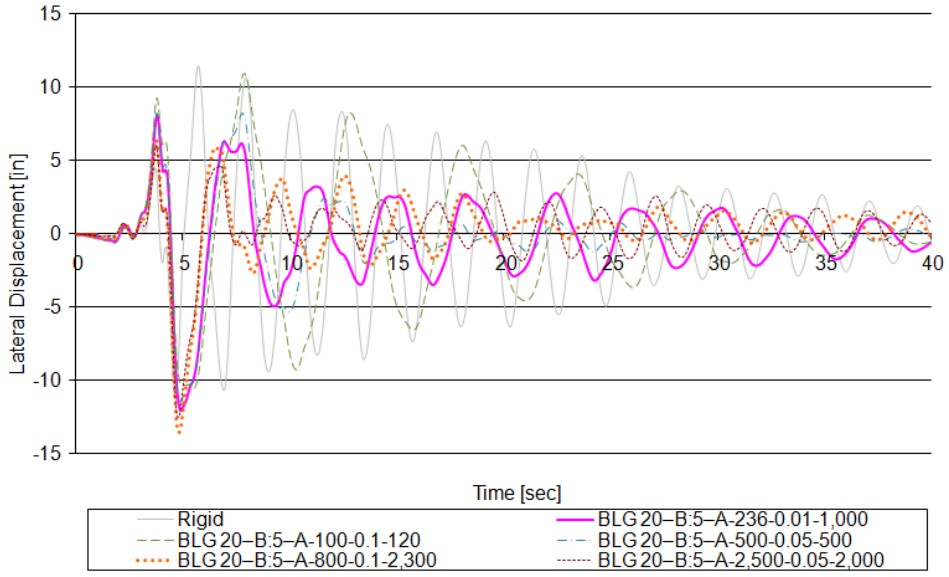

Figure B.15 The 9th Floor Lateral Displacement for $BL\_20-0:5-A$ Configuration Subjected to Parkfield

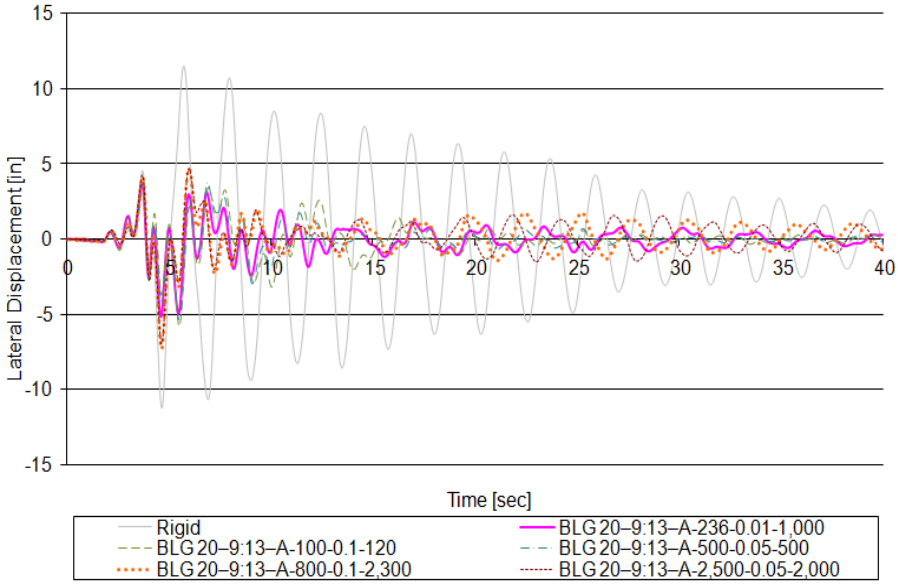

Figure B.16 The 9th Floor Lateral Displacement for $BL\_20-9:13-A$ Configuration Subjected to Parkfield

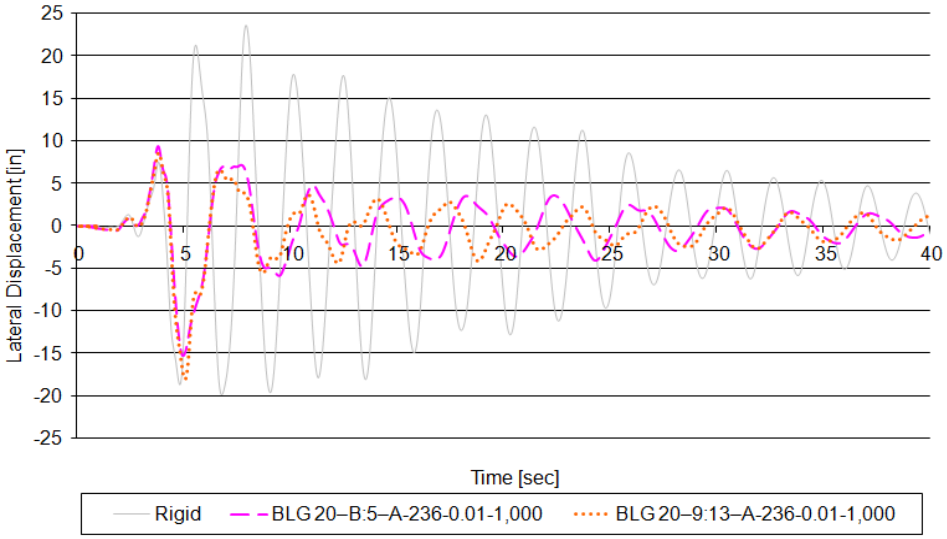

Figure B.17 Top Lateral Displacement Comparison Subjected to Parkfield

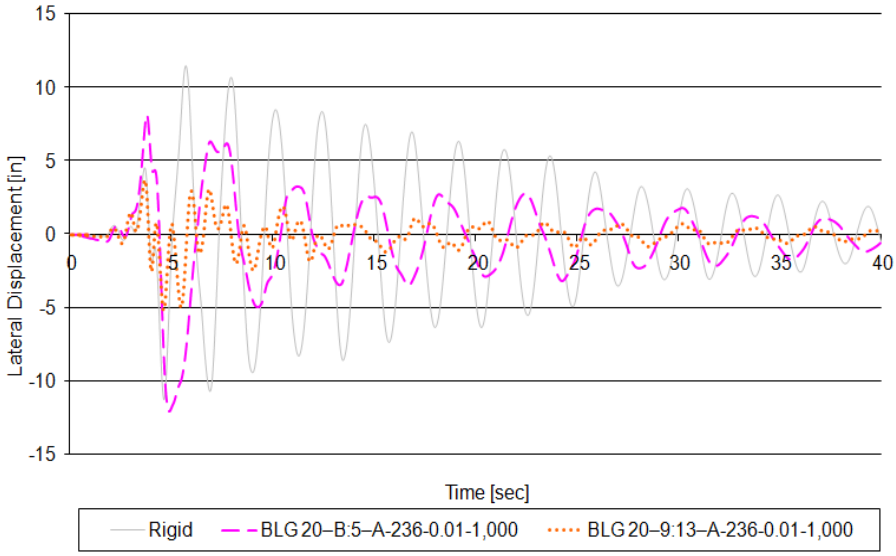

Figure B.18 The 9th Floor Lateral Displacement Comparison Subjected to Parkfield

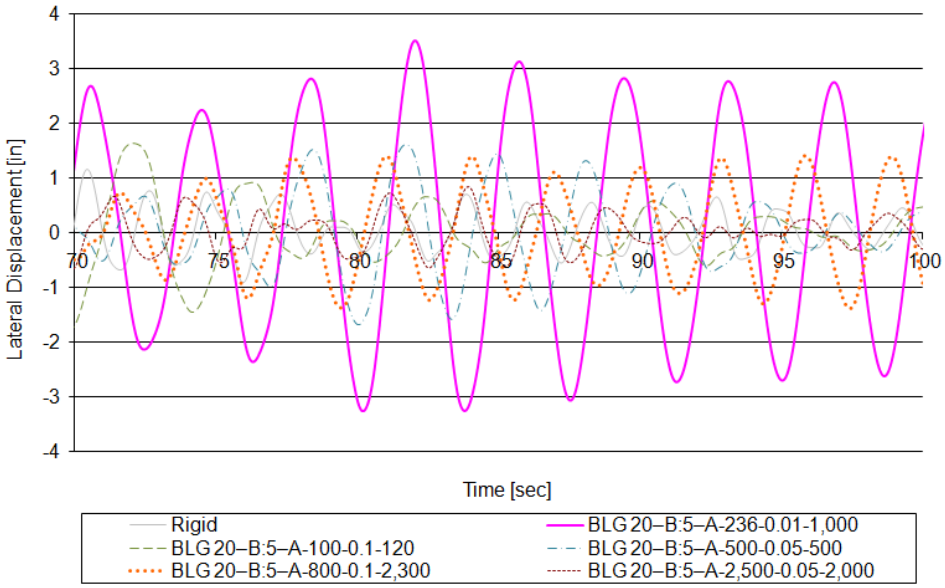

Figure B.19 Top Lateral Displacement for $BL\_20-0:5-A$ Configuration Subjected to Afyon Bay

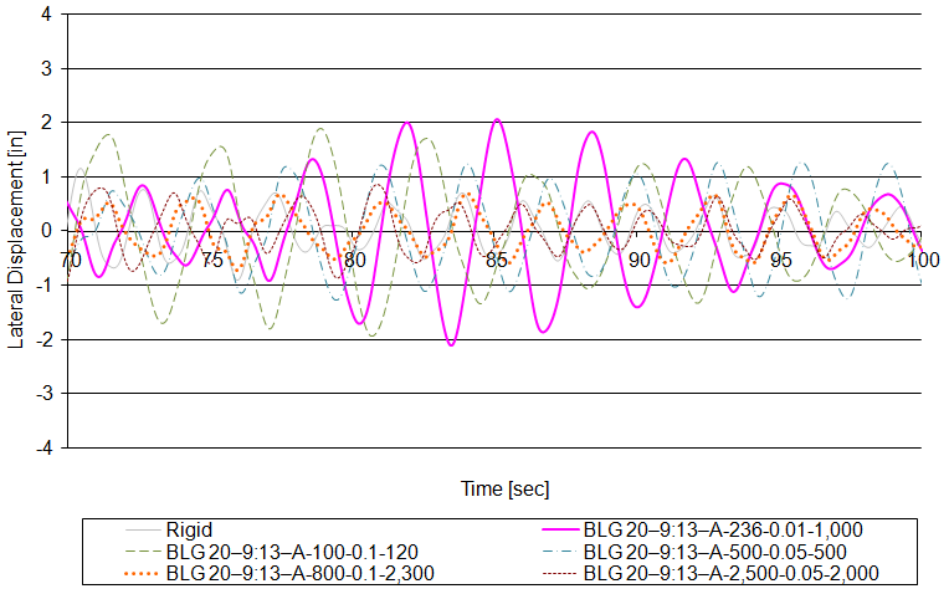

Figure B.20 Top Lateral Displacement for $BL\_20-9:13-A$ Configuration Subjected to Afyon Bay

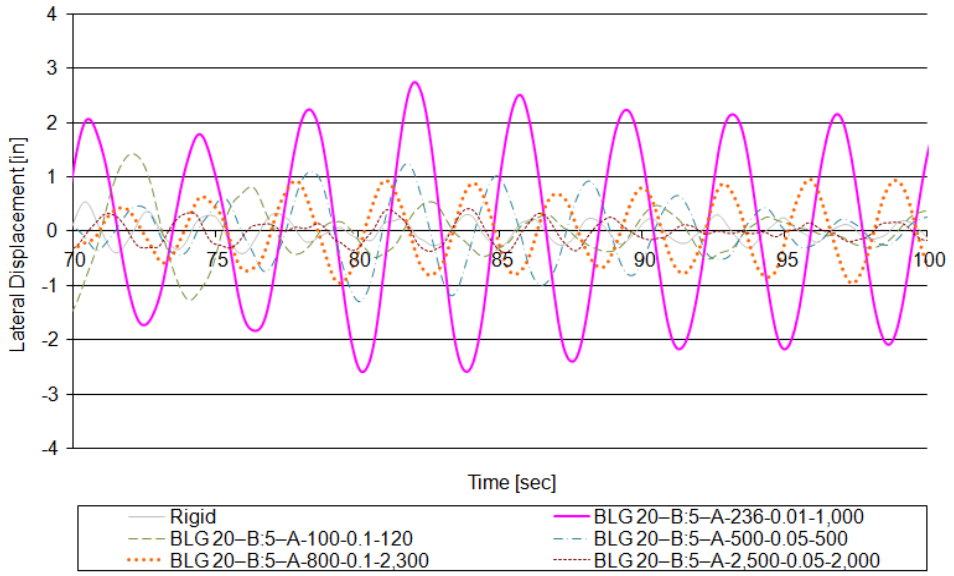

Figure B.21 The 9th Floor Lateral Displacement for $BL\_20-0:5-A$ Configuration Subjected to Afyon Bay

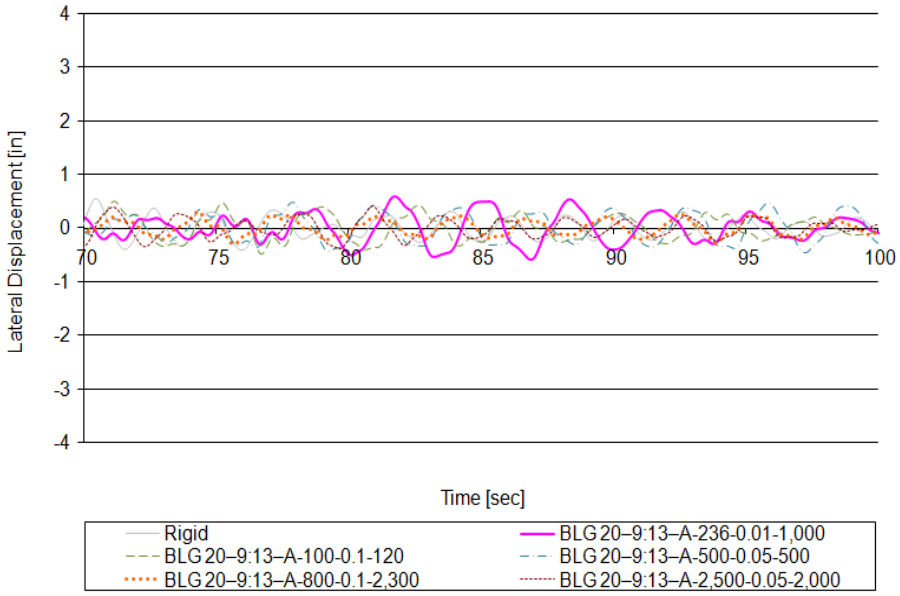

Figure B.22 The 9th Floor Lateral Displacement for $BL\_20-9:13-A$ Configuration Subjected to Afyon Bay

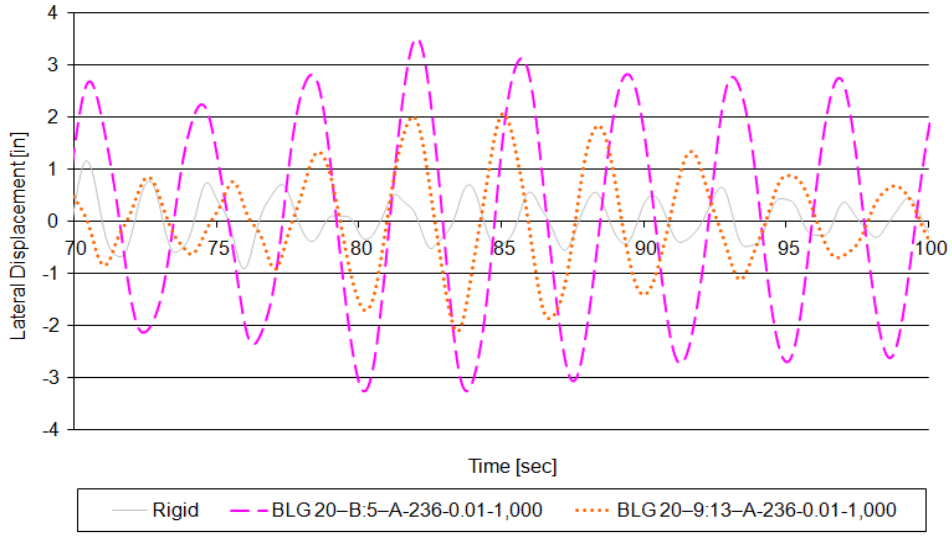

Figure B.23 Top Lateral Displacement Comparison Subjected to Afyon Bay

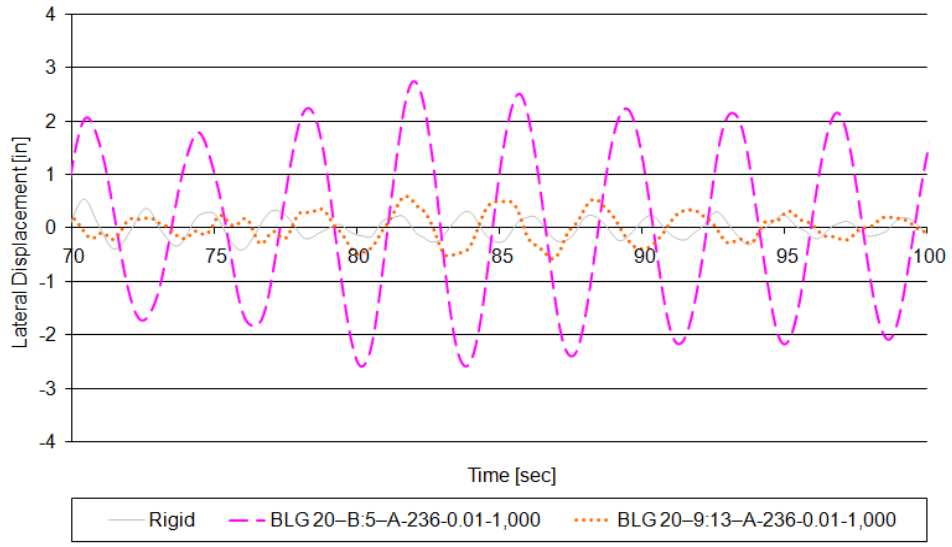

Figure B.24 The 9th Floor Lateral Displacement Comparison Subjected to Afyon Bay

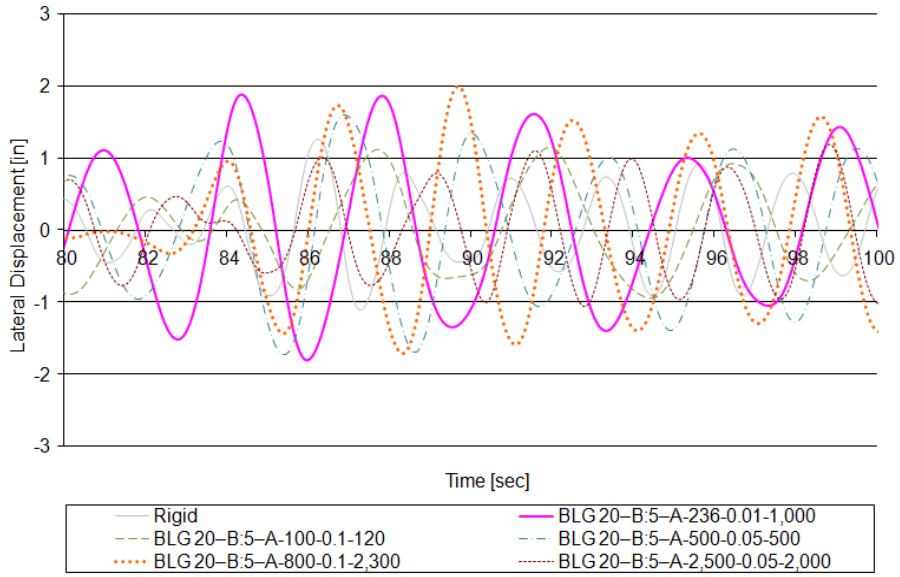

Figure B.25 Top Lateral Displacement for $BL\_20-0:5-A$ Configuration Subjected to Aydin

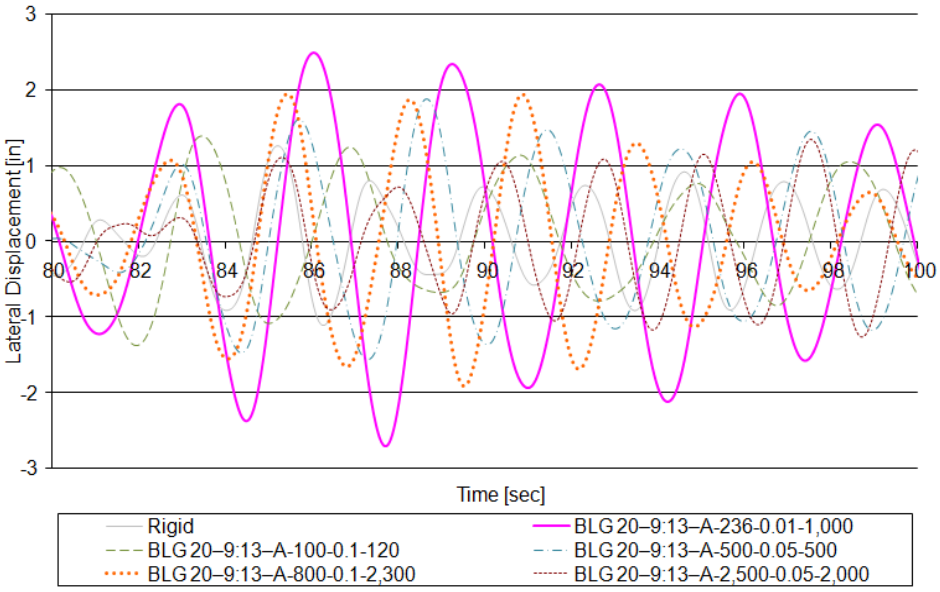

Figure B.26 Top Lateral Displacement for $BL\_20-9:13-A$ Configuration Subjected to Aydin

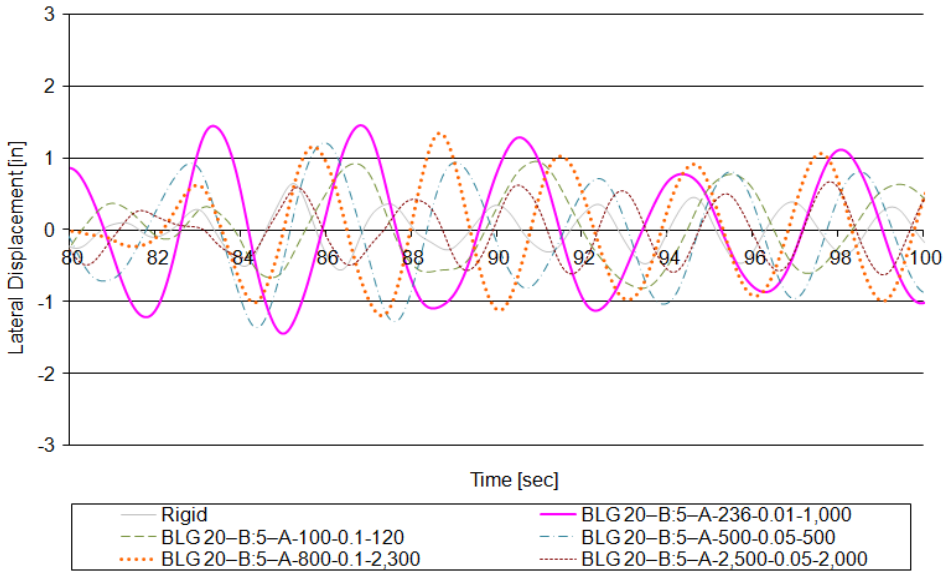

Figure B.27 The 9th Floor Lateral Displacement for $BL\_20-0:5-A$ Configuration Subjected to Aydin

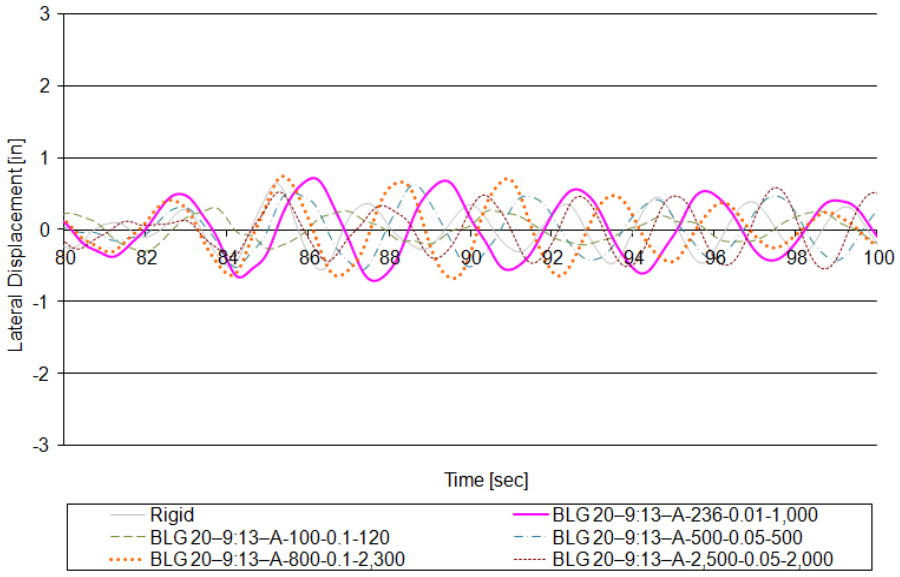

Figure B.28 The 9th Floor Lateral Displacement for $BL\_20-9:13-A$ Configuration Subjected to Aydin

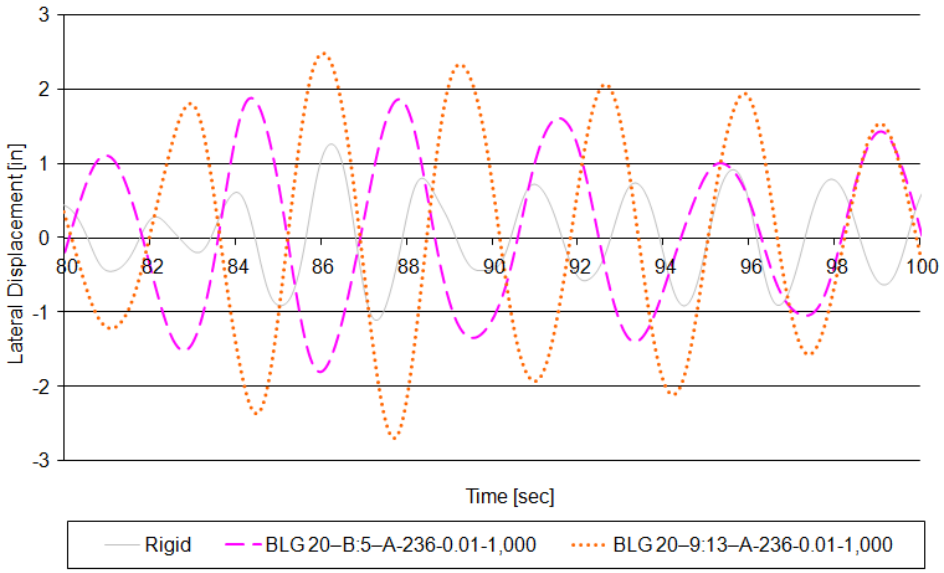

Figure B.29 Top Lateral Displacement Comparison Subjected to Aydin

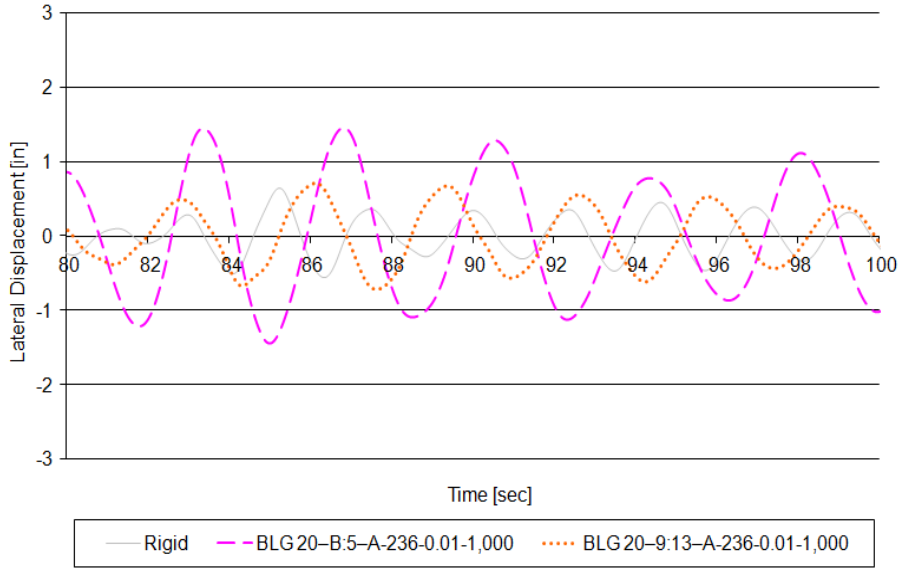

Figure B.30 The 9th Floor Lateral Displacement Comparison Subjected to Aydin

APPENDIX C

MOMENTS FOR SAC FRAME IN EARTHQUAKE ANALYSIS

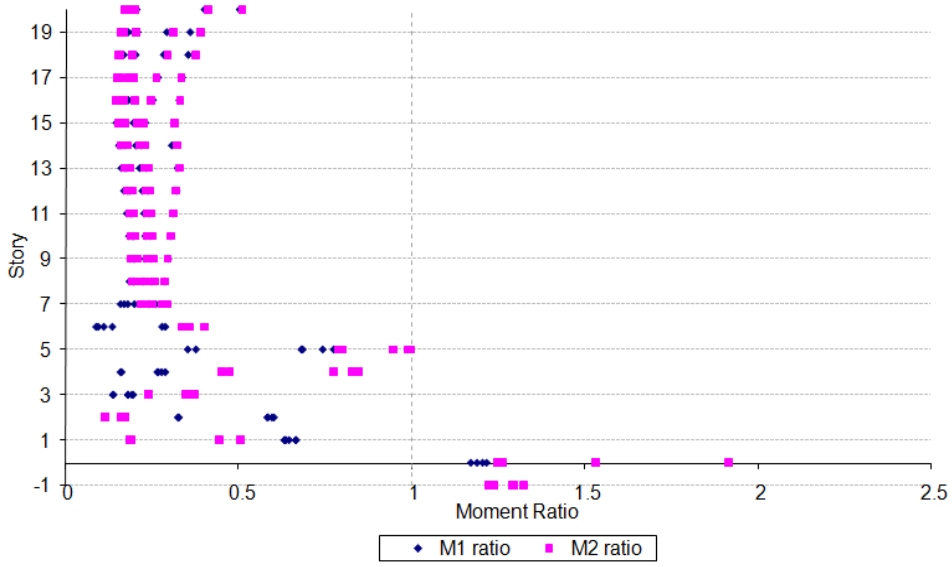

a)

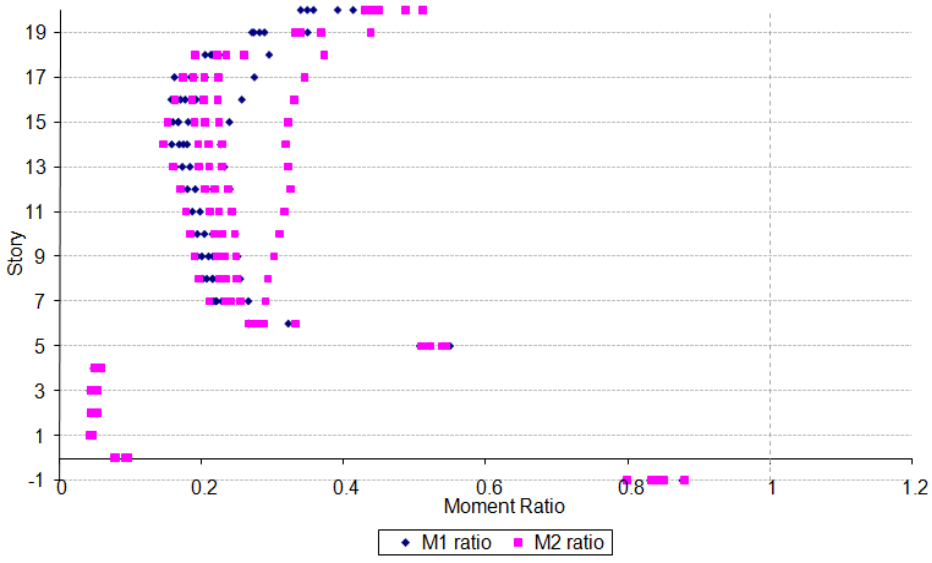

b)

Figure C.1 Moment Ratios for $BL\_20-0:5-A-236-0.01-1{,}000$ Subjected to El Centro: a) Columns, b) Beams

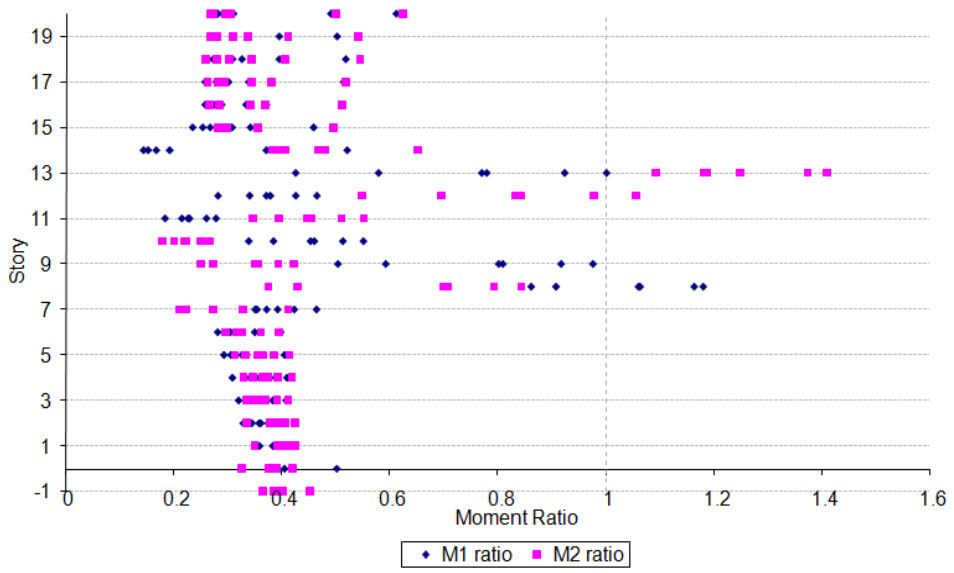

a)

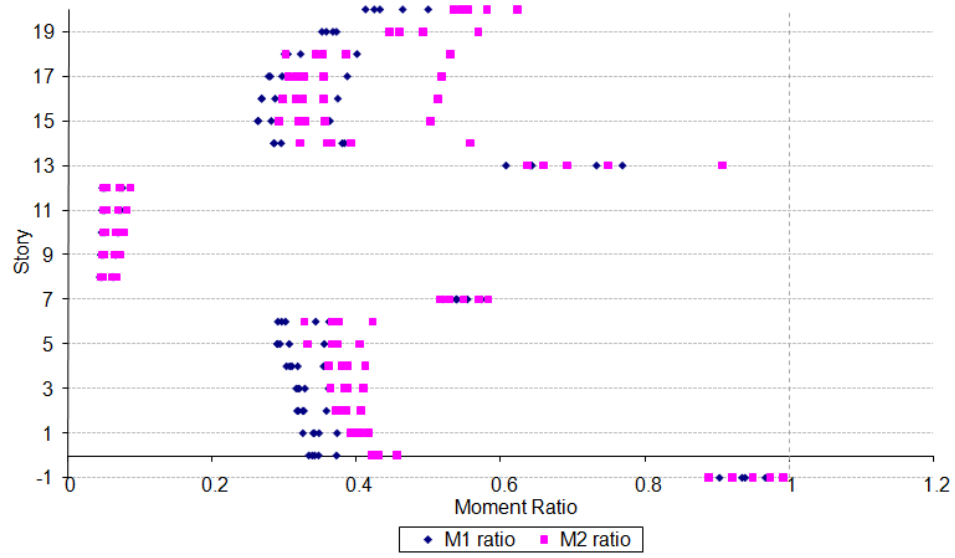

b)

Figure C.2 Moment Ratios for $BL\_20-9:13-A-236-0.01-1{,}000$ Subjected to El Centro: a) Columns, b) Beams

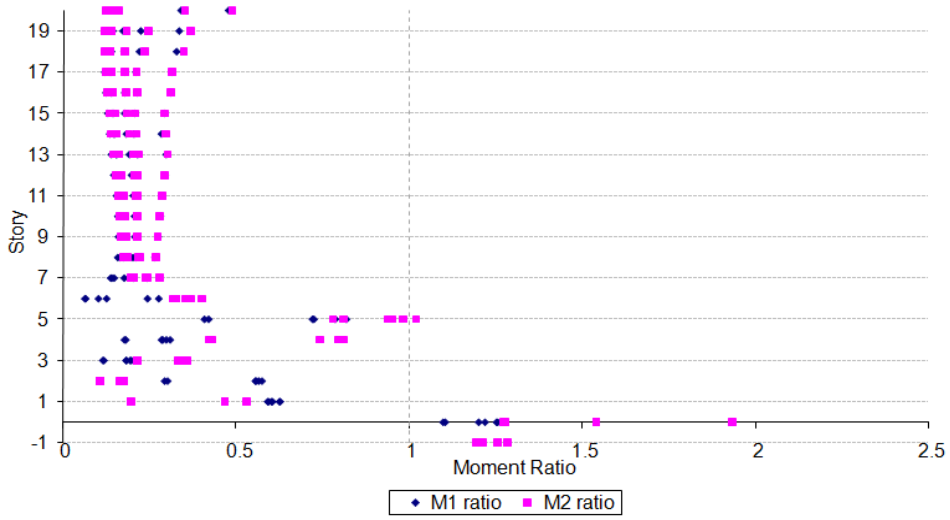

a)

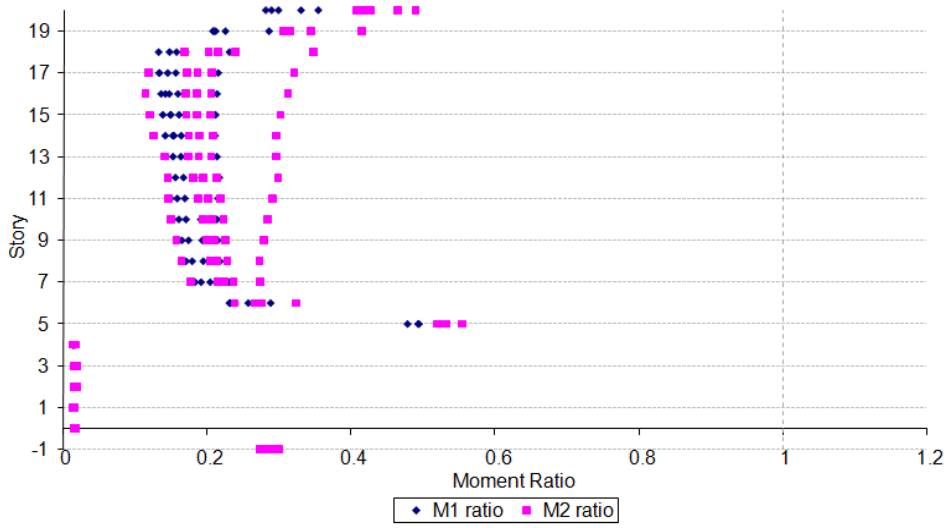

b)

Figure C.3 Moment Ratios for $BL\_20-0:5-A-100-0.1-120$ Subjected to El Centro: a) Columns, b) Beams

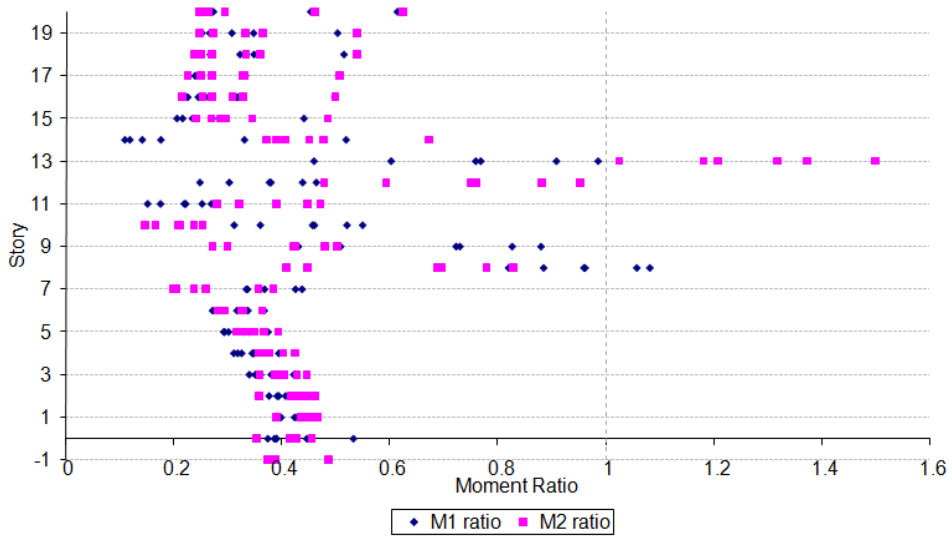

a)

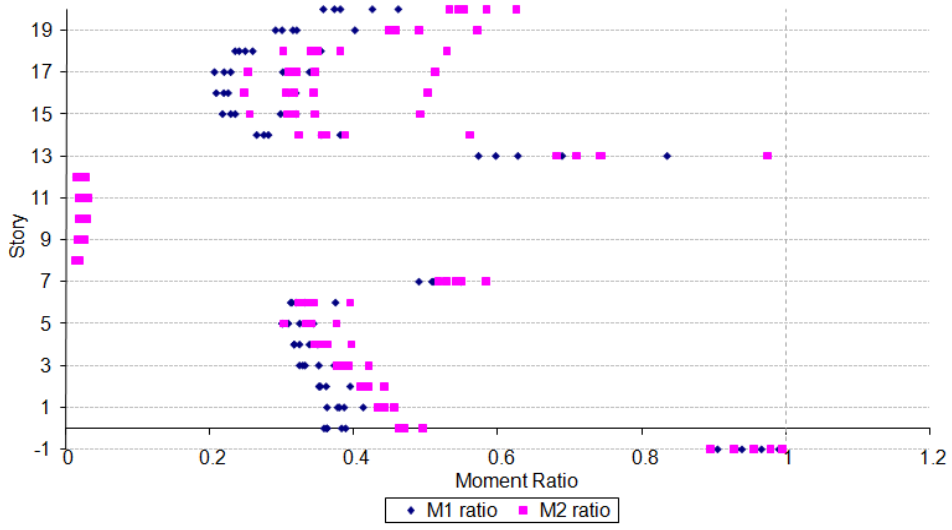

b)

Figure C.4 Moment Ratios for $BL\_20-9:13-A-100-0.1-120$ Subjected to El Centro: a) Columns, b) Beams

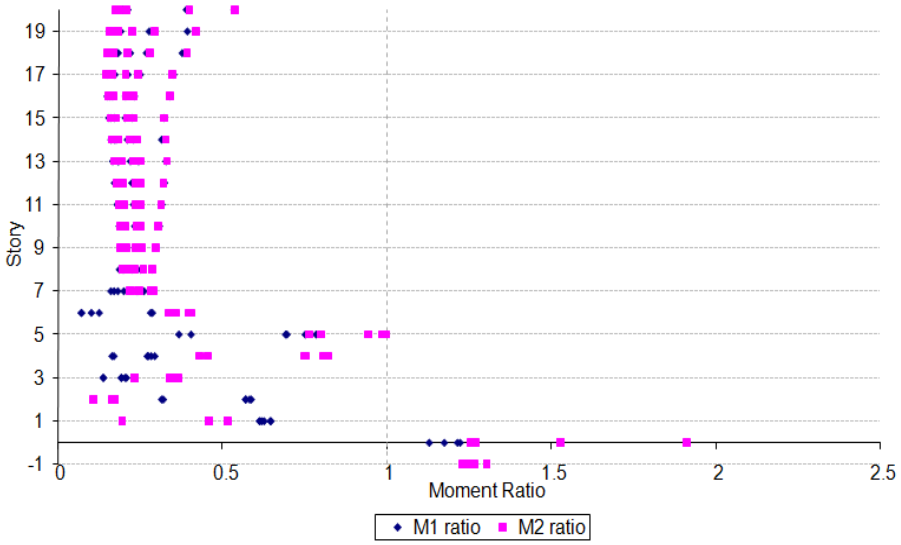

a)

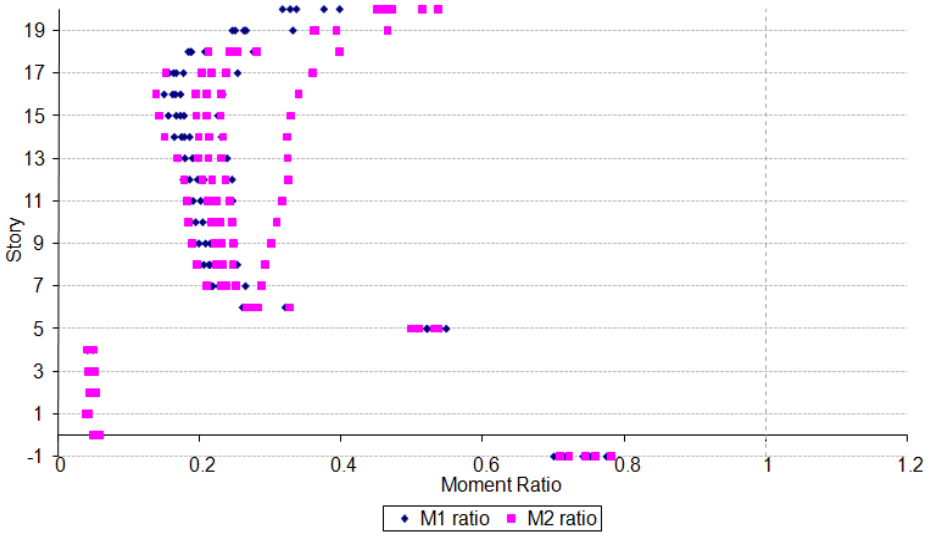

b)

Figure C.5 Moment Ratios for $BL\_20-0:5-A-500-0.05-500$ Subjected to El Centro: a) Columns, b) Beams

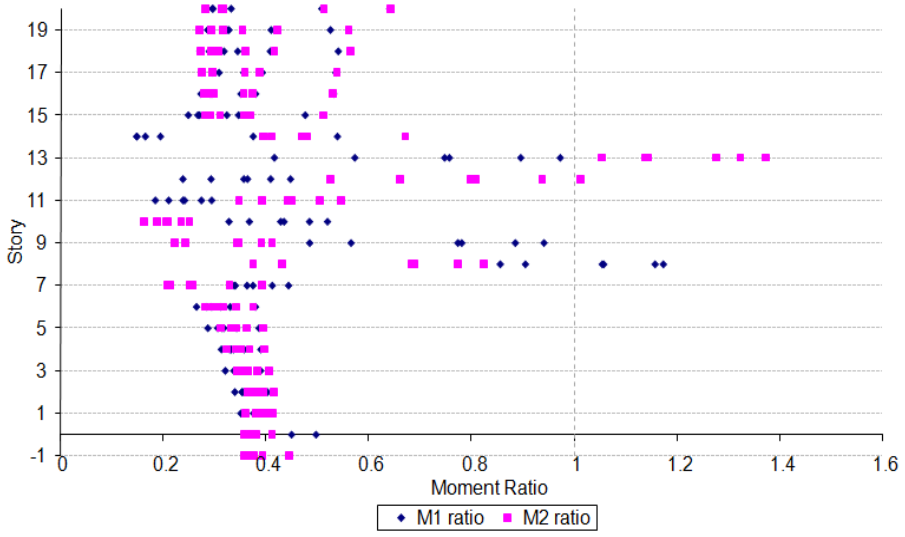

a)

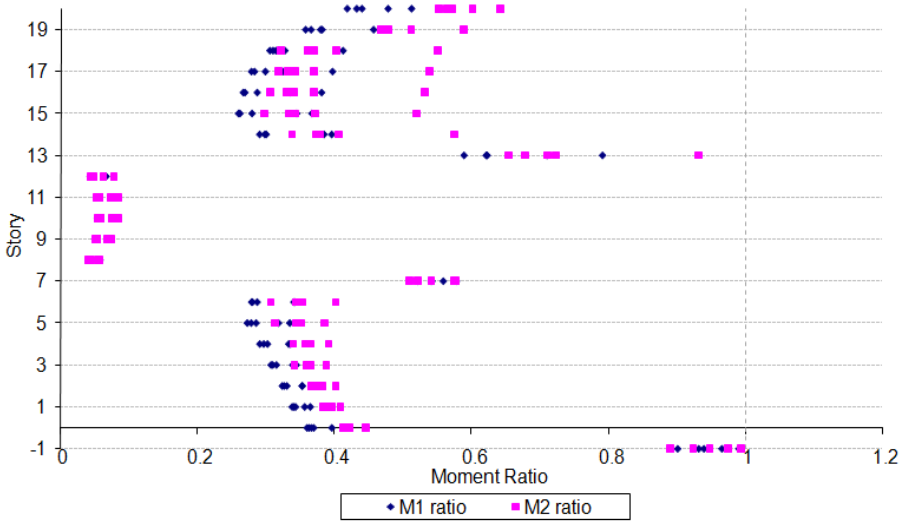

b)

Figure C.6 Moment Ratios for $BL\_20-9:13-A-500-0.05-500$ Subjected to El Centro: a) Columns, b) Beams

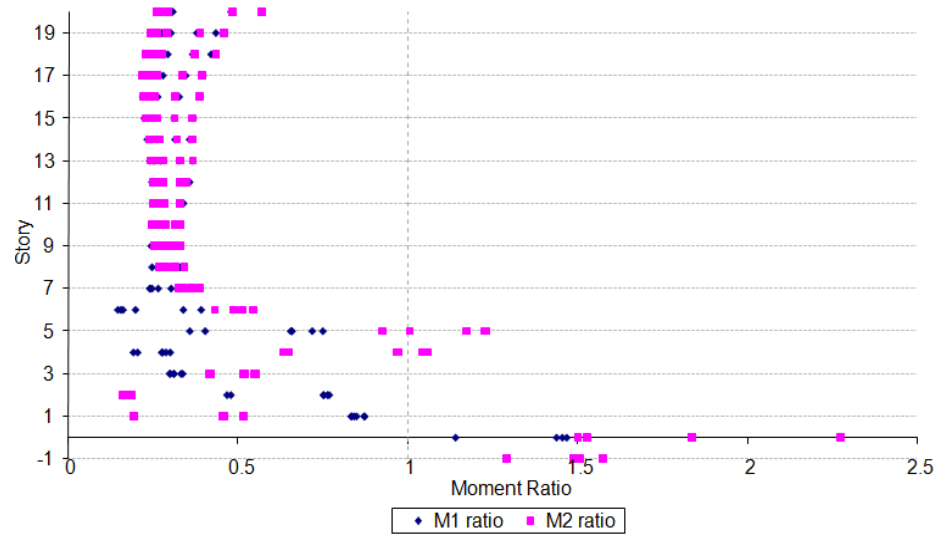

a)

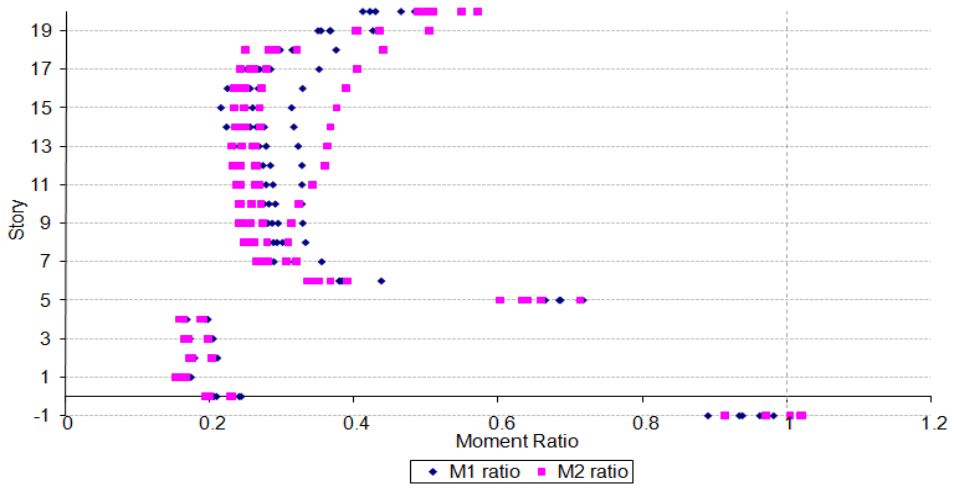

b)

Figure C.7 Moment Ratios for $BL\_20-0:5-A-800-0.1-2{,}300$ Subjected to El Centro: a) Columns, b) Beams

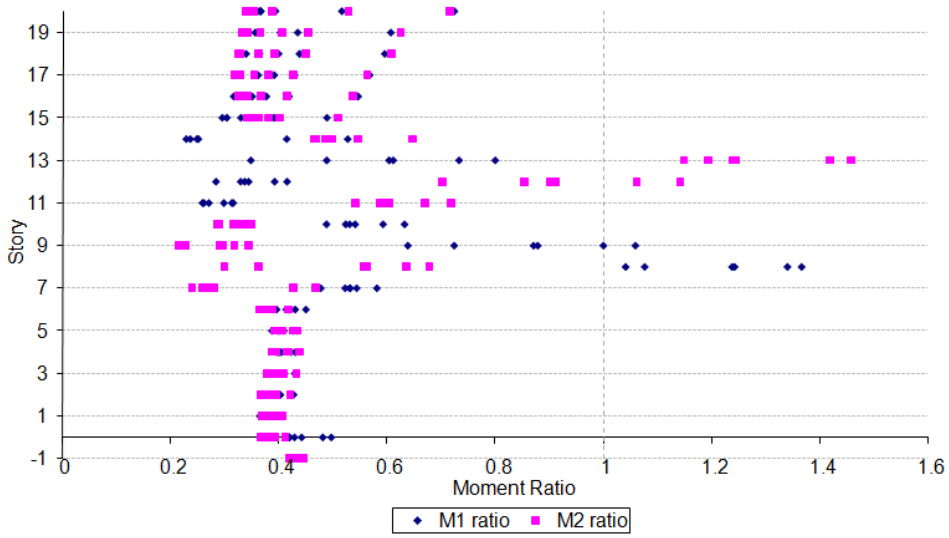

a)

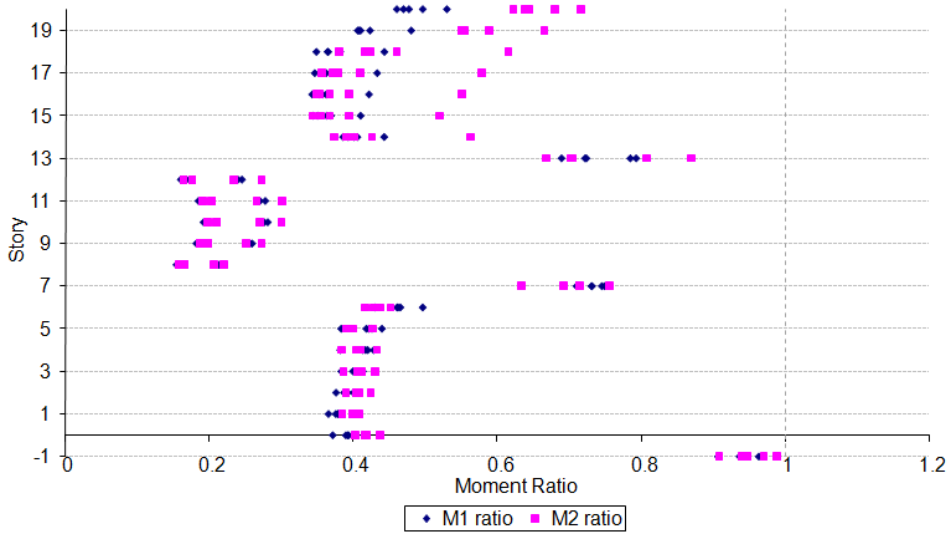

b)

Figure C.8 Moment Ratios for $BL\_20-9:13-A-800-0.1-2{,}300$ Subjected to El Centro: a) Columns, b) Beams

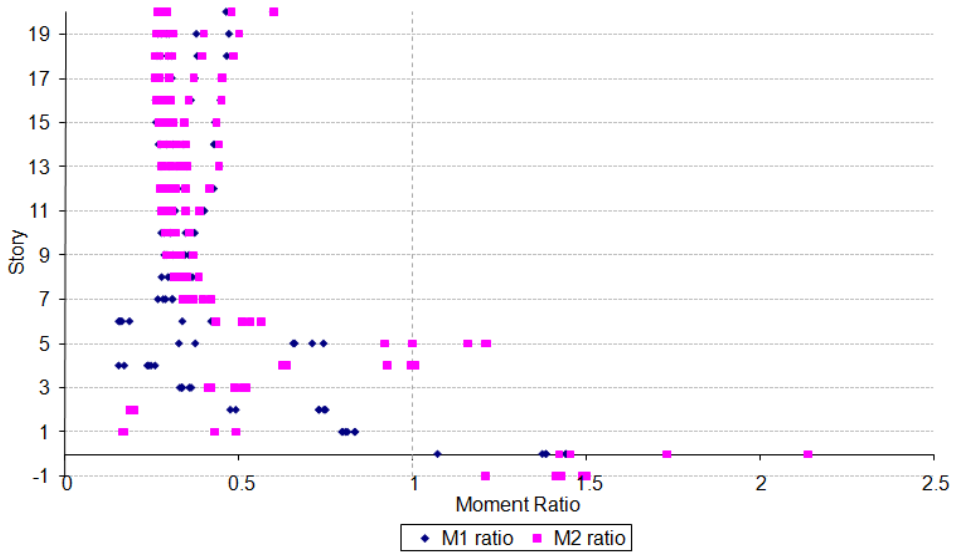

a)

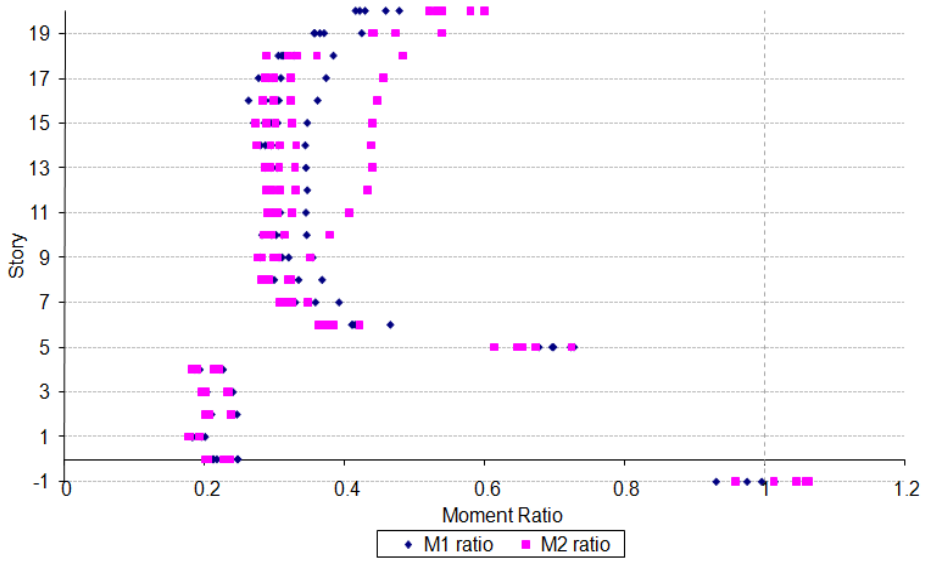

b)

Figure C.9 Moment Ratios for $BL\_20-0:5-A-2{,}500-0.05-2{,}000$ Subjected to El Centro: a) Columns, b) Beams

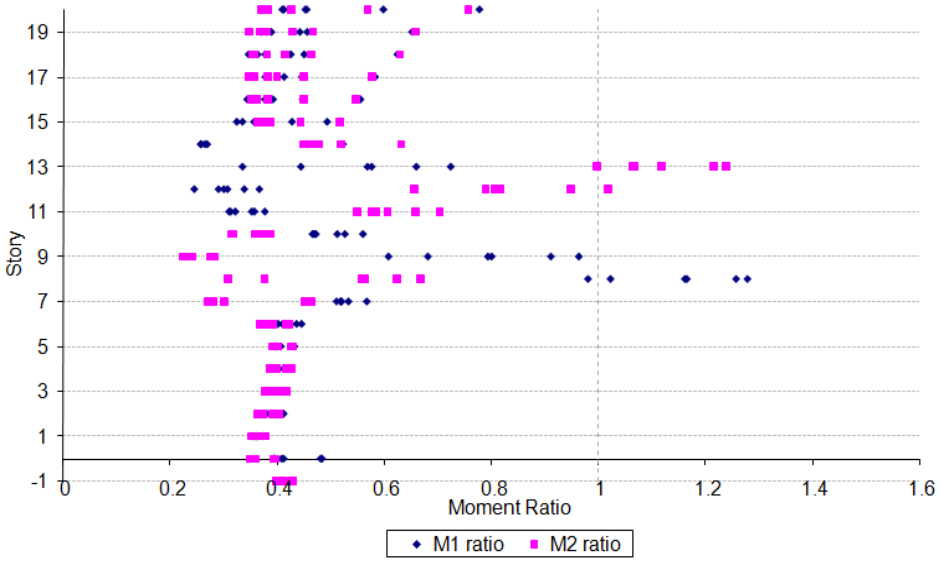

a)

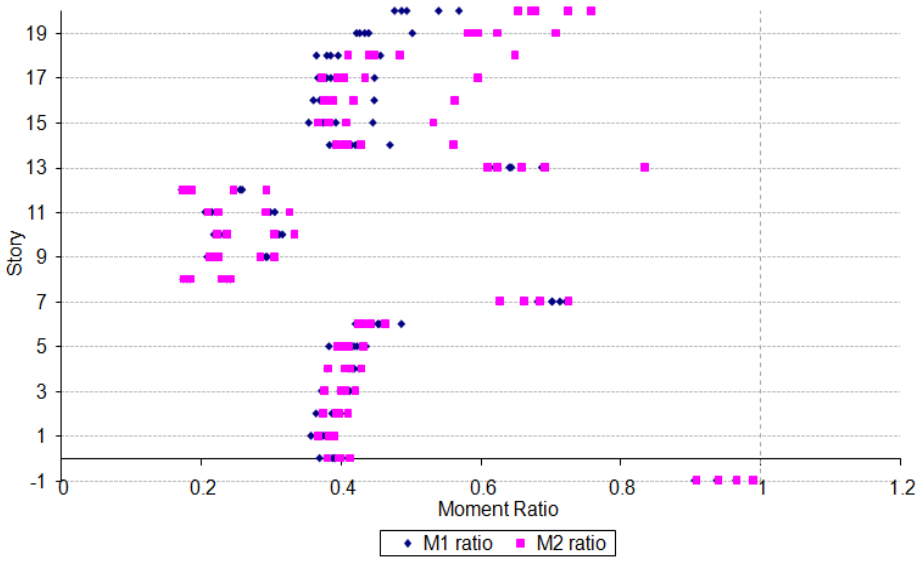

b)

Figure C.10 Moment Ratios for $BL\_20-9:13-A-2{,}500-0.05-2{,}000$ Subjected to El Centro: a) Columns, b) Beams

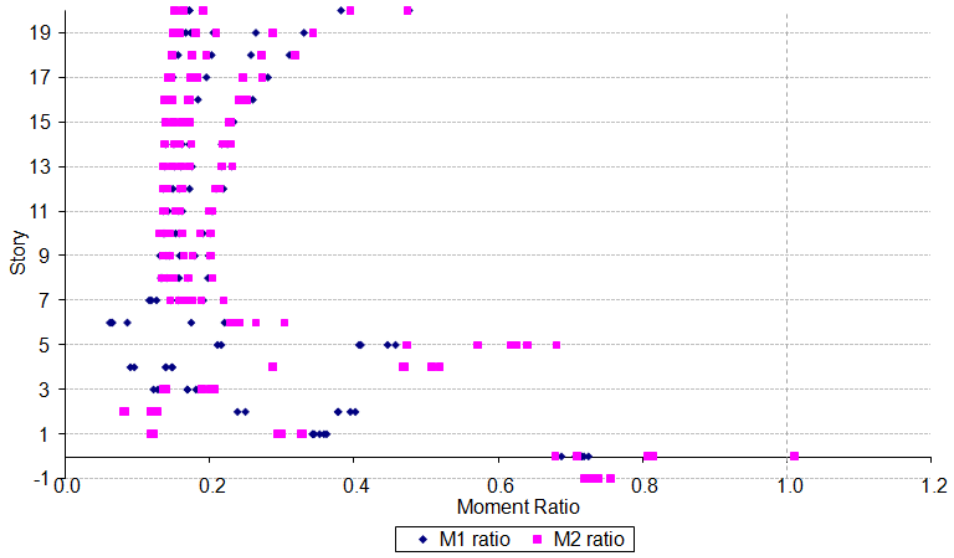

a)

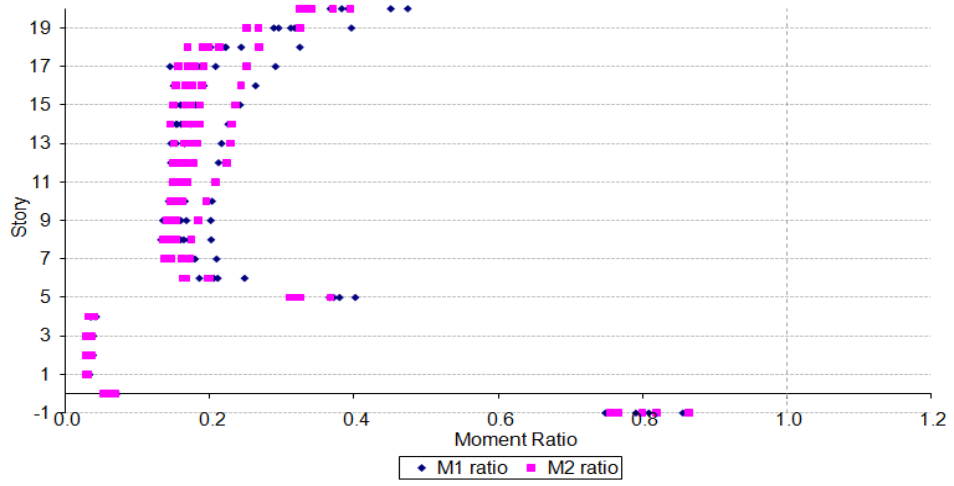

b)

Figure C.11 Moment Ratios for $BL\_20-0:5-A-236-0.01-1{,}000$ Subjected to Northridge: a) Columns, b) Beams

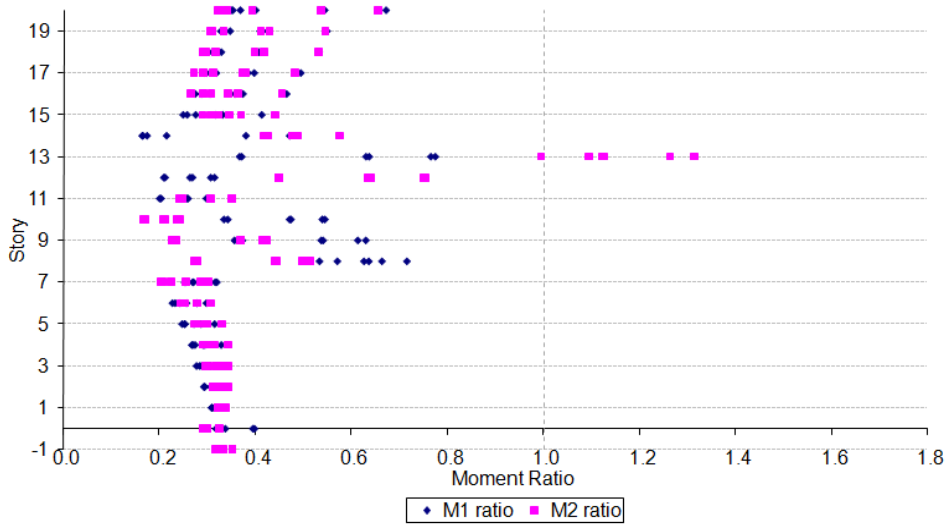

a)

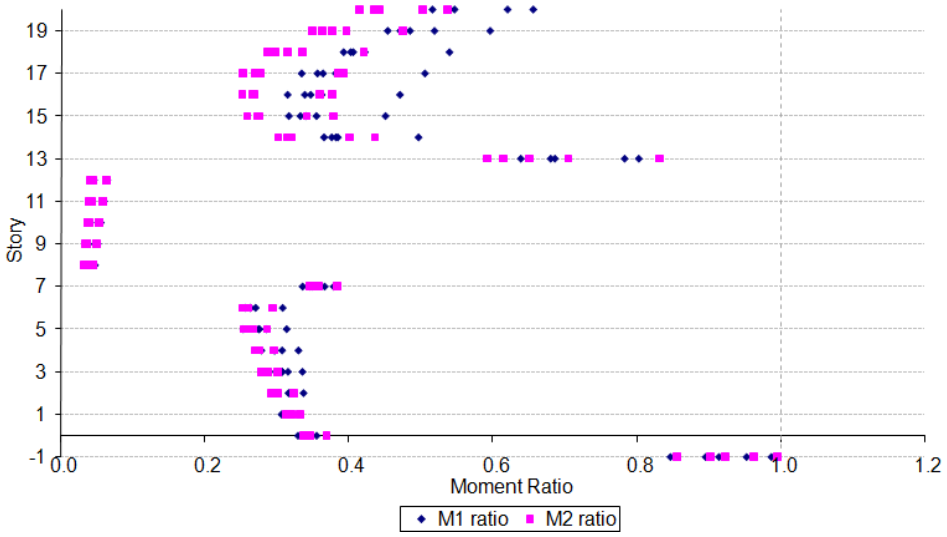

b)

Figure C.12 Moment Ratios for $BL\_20-9:13-A-236-0.01-1{,}000$ Subjected to Northridge: a) Columns, b) Beams

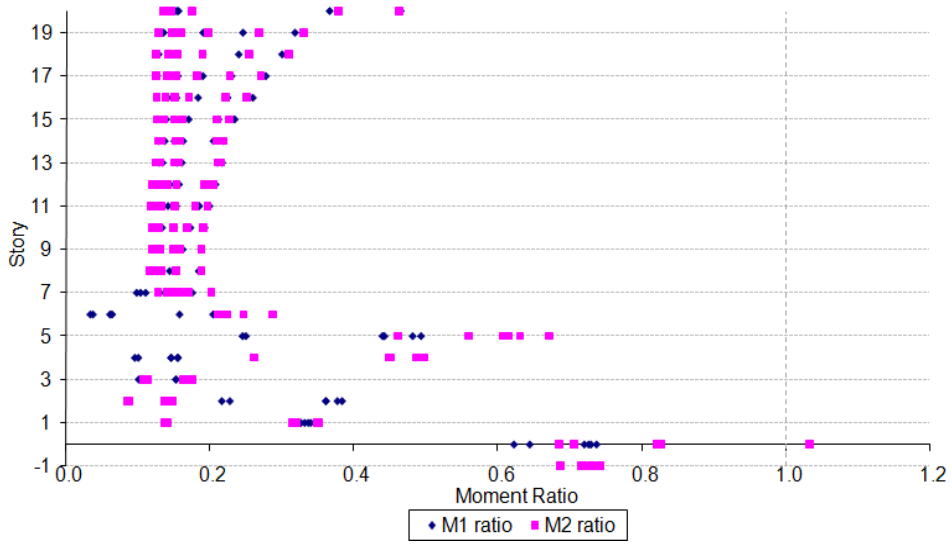

a)

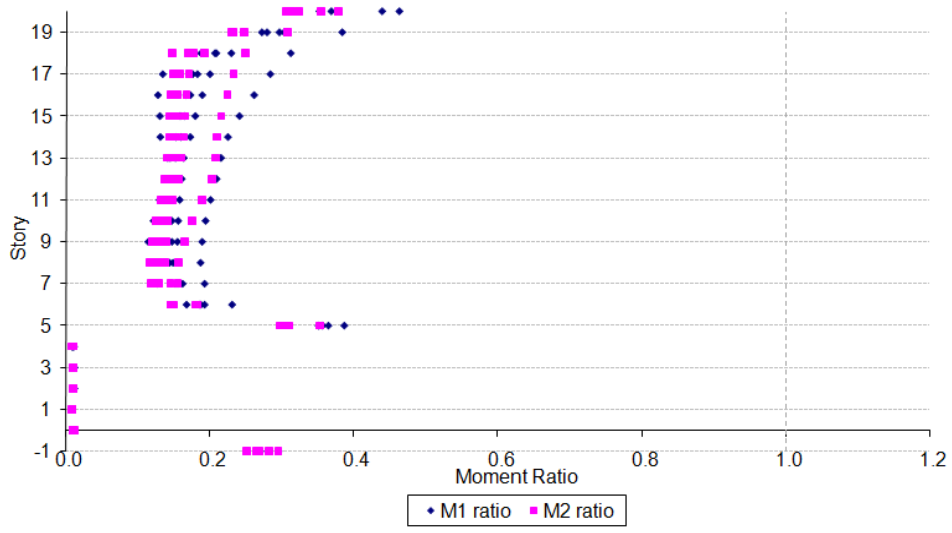

b)

Figure C.13 Moment Ratios for $BL\_20-0:5-A-100-0.1-120$ Subjected to Northridge: a) Columns, b) Beams

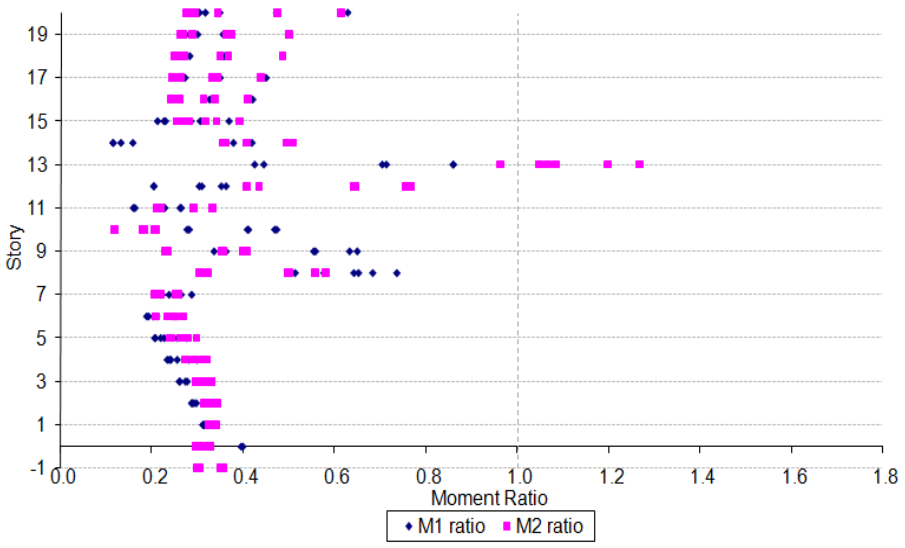

a)

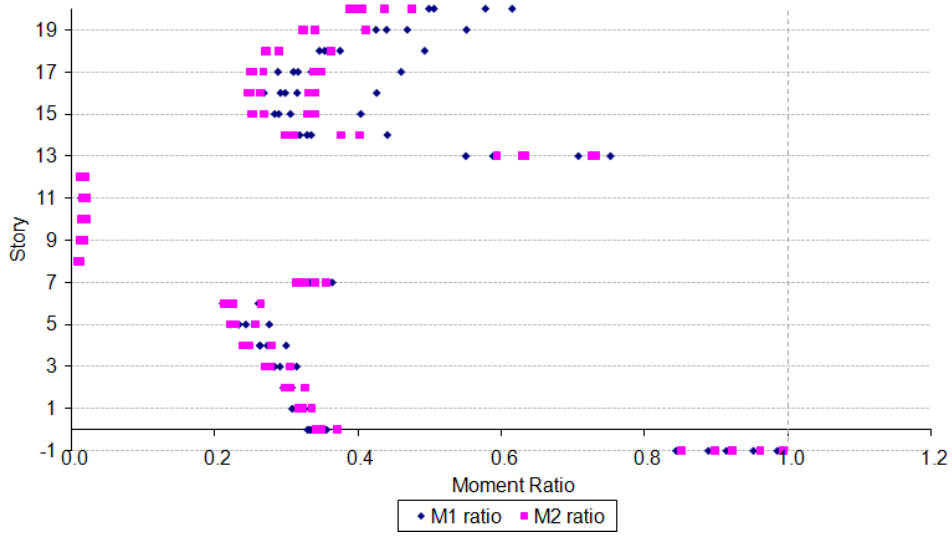

b)

Figure C.14 Moment Ratios for $BL\_20-9:13-A-100-0.1-120$ Subjected to Northridge: a) Columns, b) Beams

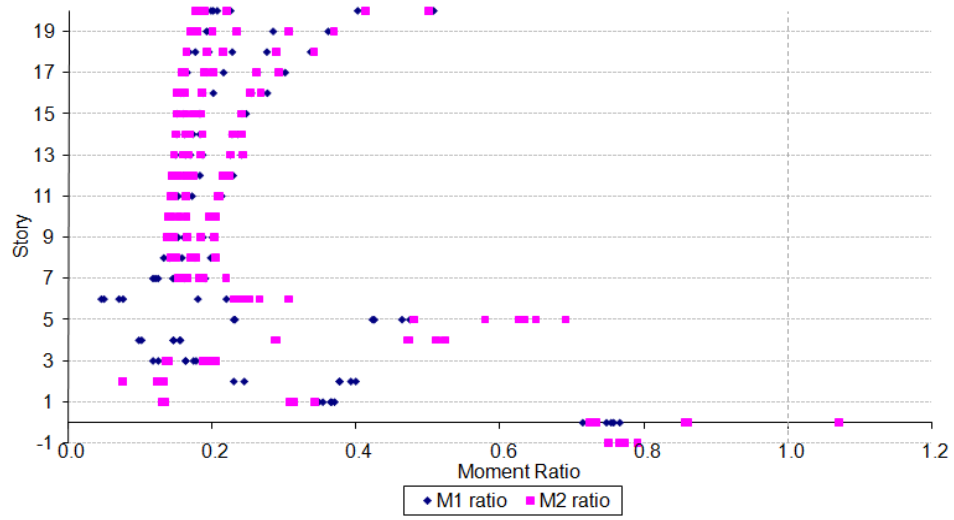

a)

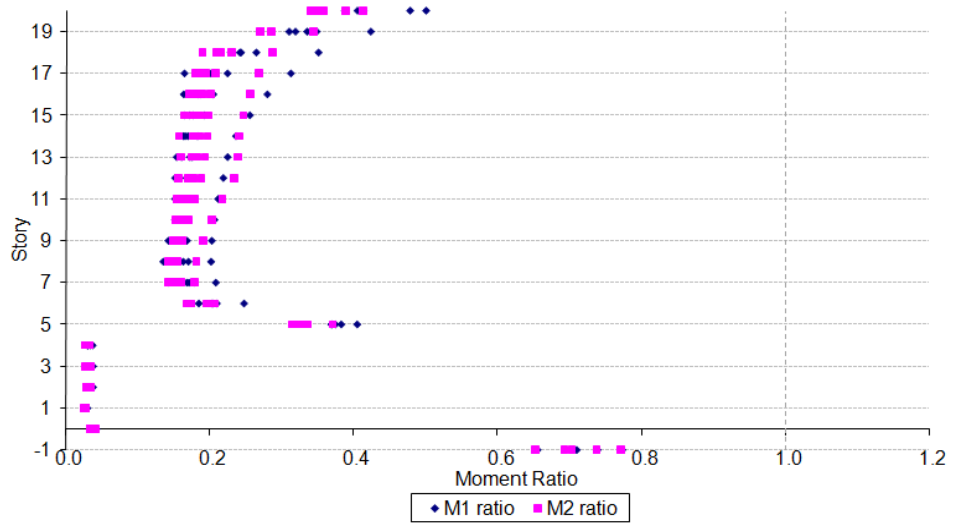

b)

Figure C.15 Moment Ratios for $BL\_20-0:5-A-500-0.05-500$ Subjected to Northridge: a) Columns, b) Beams

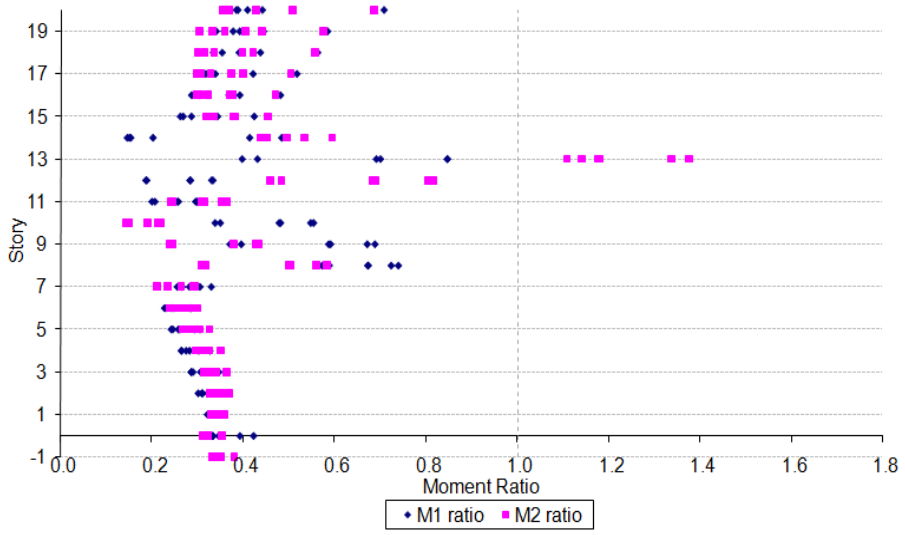

a)

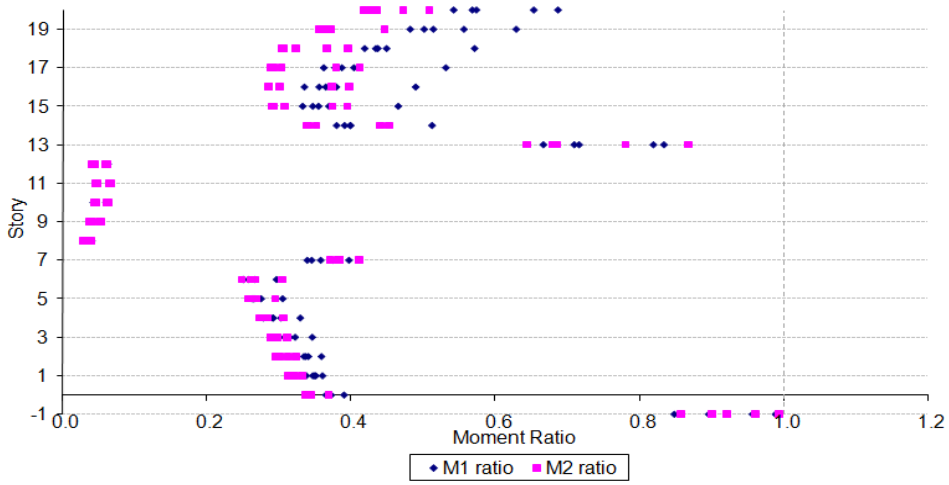

b)

Figure C.16 Moment Ratios for $BL\_20-9:13-A-500-0.05-500$ Subjected to Northridge: a) Columns, b) Beams

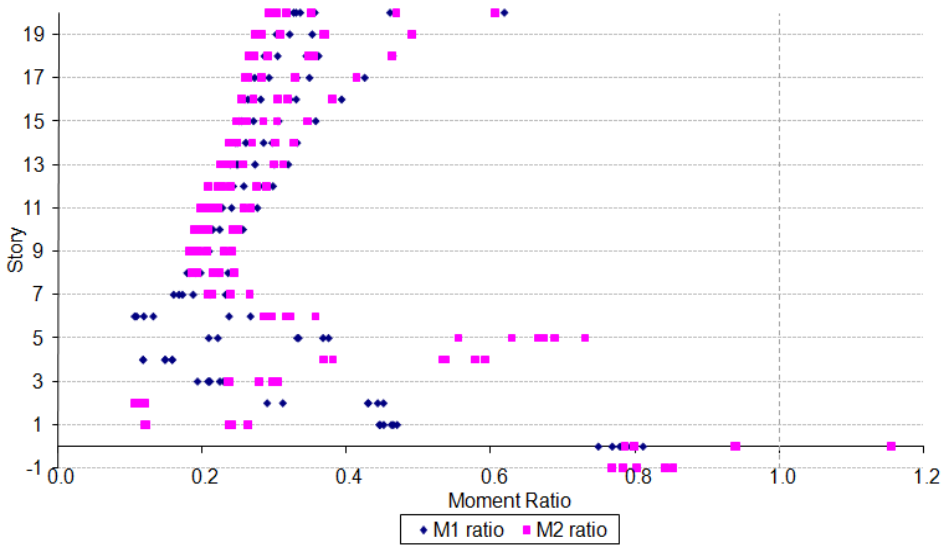

a)

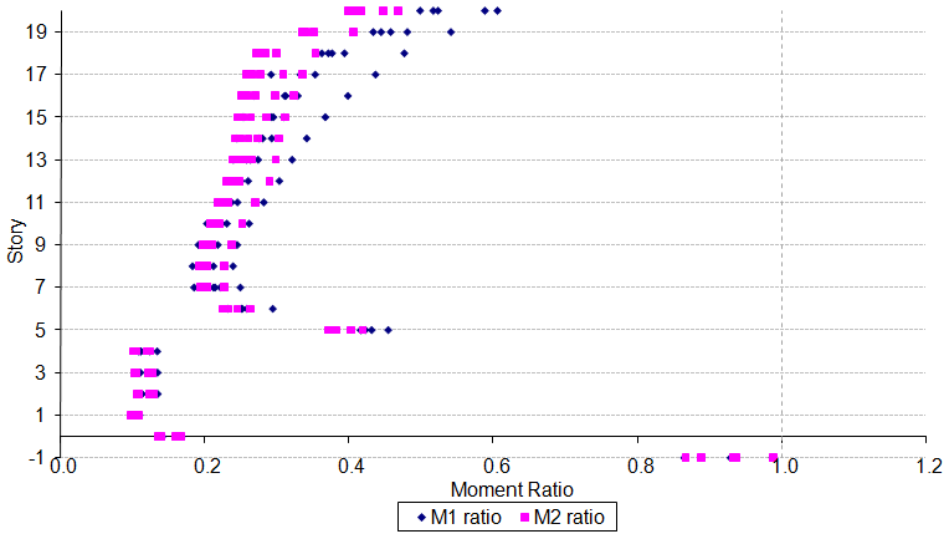

b)

Figure C.17 Moment Ratios for $BL\_20-0:5-A-800-0.1-2{,}300$ Subjected to Northridge: a) Columns, b) Beams

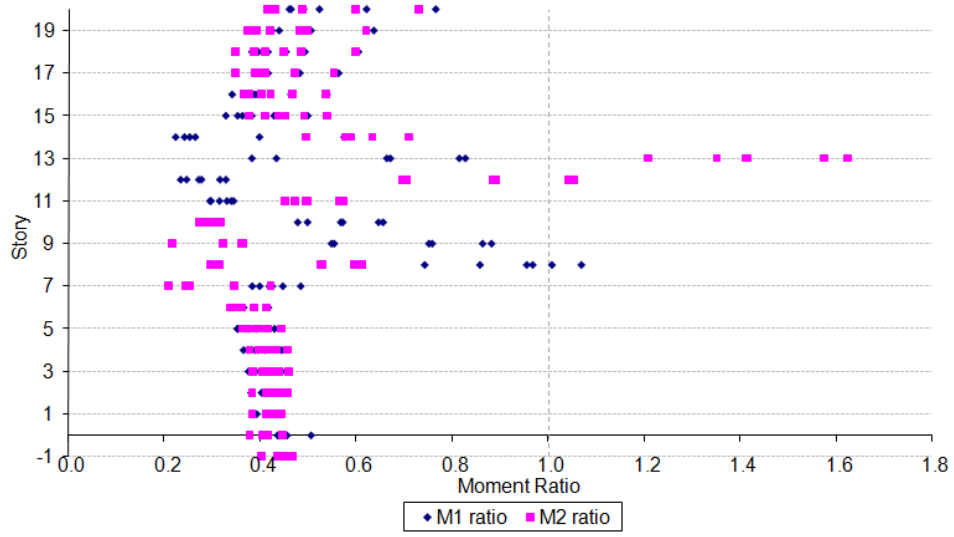

a)

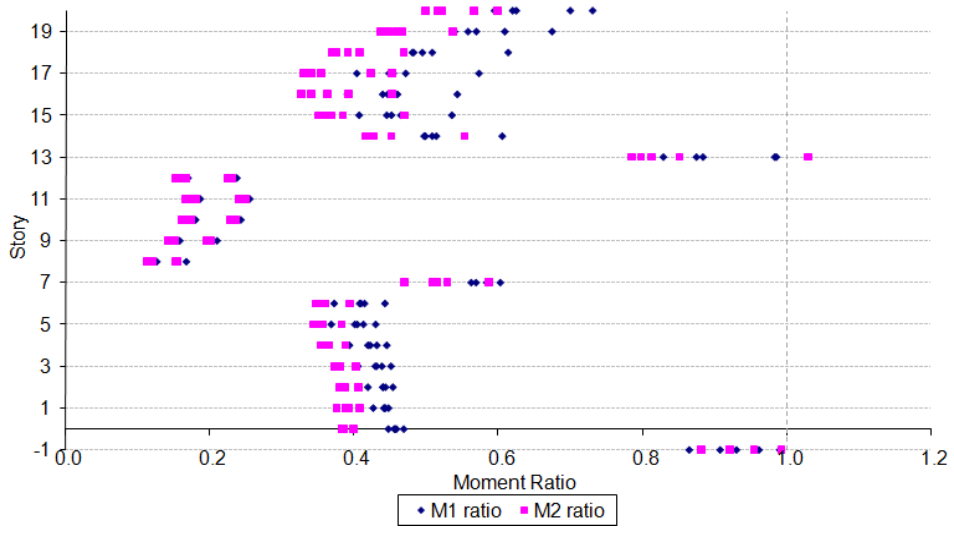

b)

Figure C.18 Moment Ratios for $BL\_20-9:13-A-800-0.1-2{,}300$ Subjected to Northridge: a) Columns, b) Beams

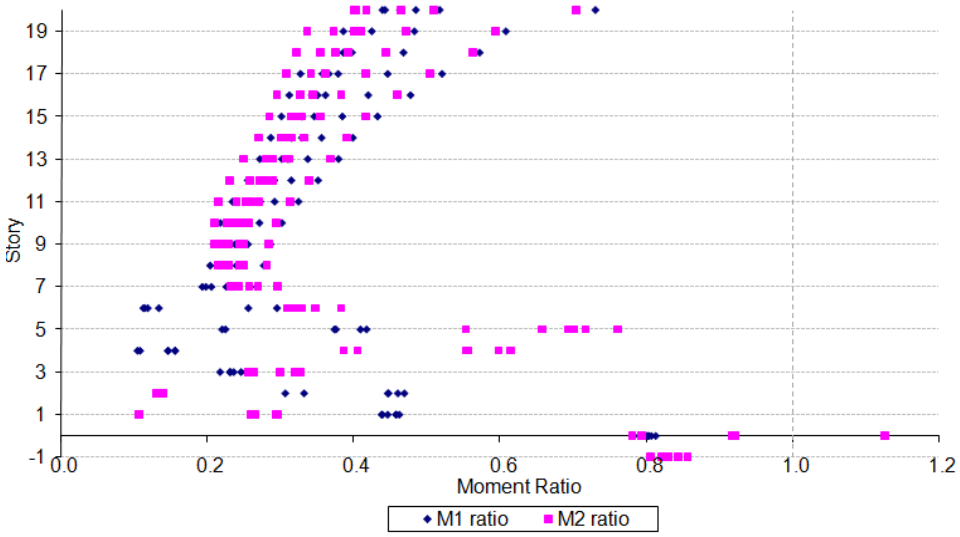

a)

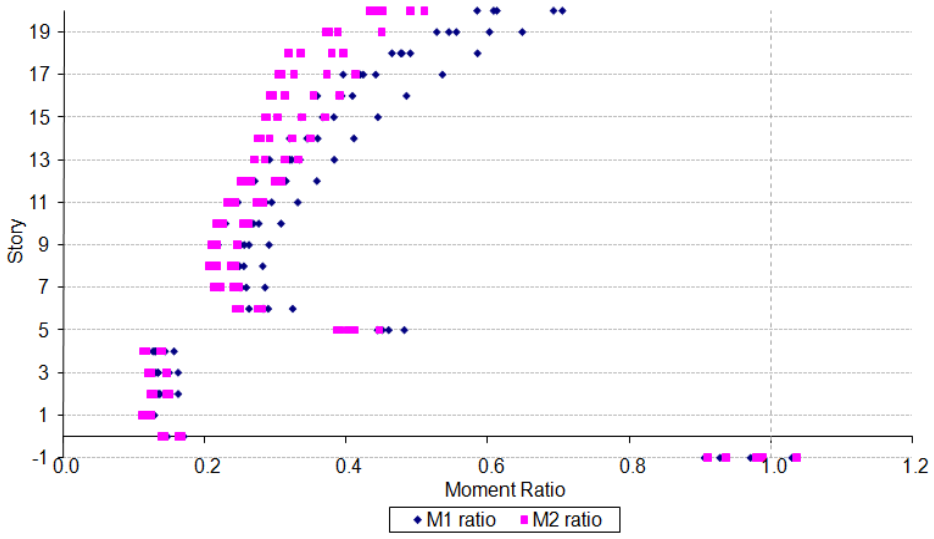

b)

Figure C.19 Moment Ratios for $BL\_20-0:5-A-2{,}500-0.05-2{,}000$ Subjected to Northridge: a) Columns, b) Beams

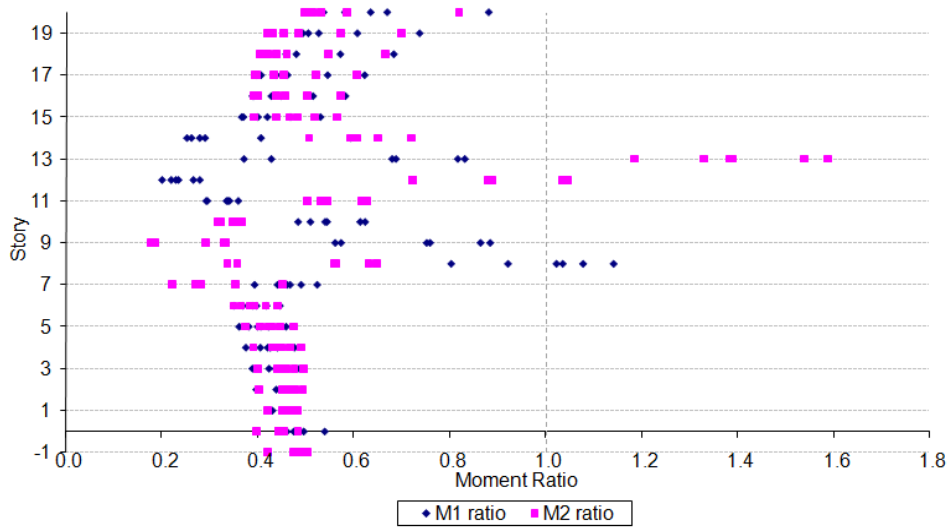

a)

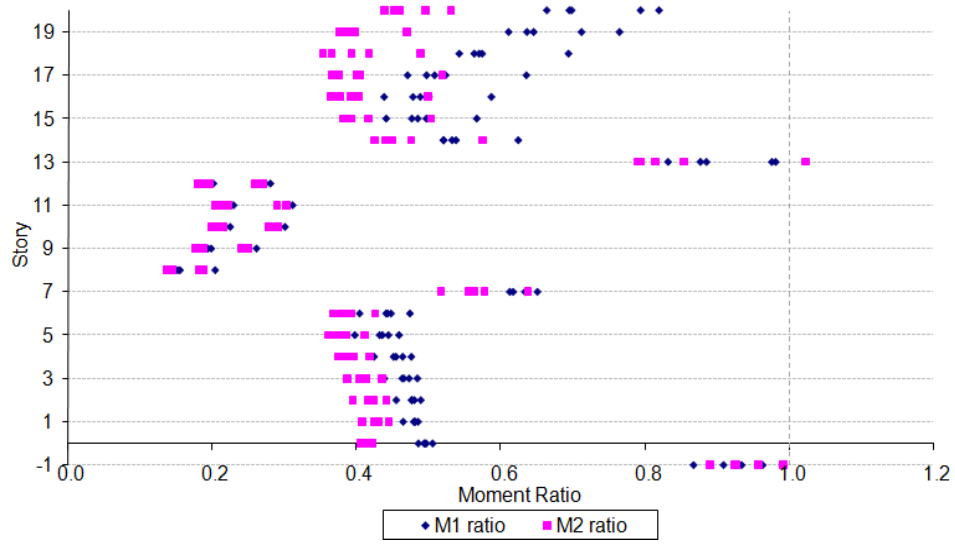

b)

Figure C.20 Moment Ratios for $BL\_20-9:13-A-2{,}500-0.05-2{,}000$ Subjected to Northridge: a) Columns, b) Beams

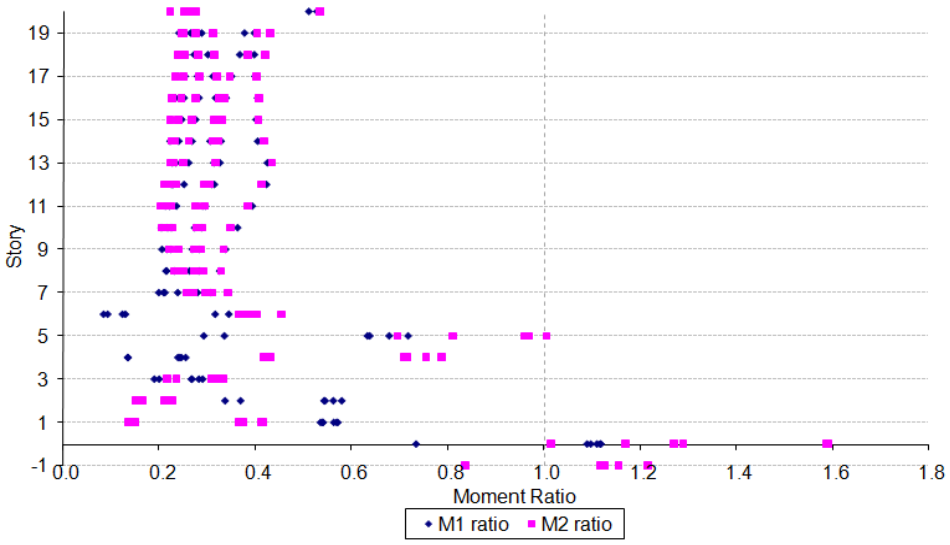

a)

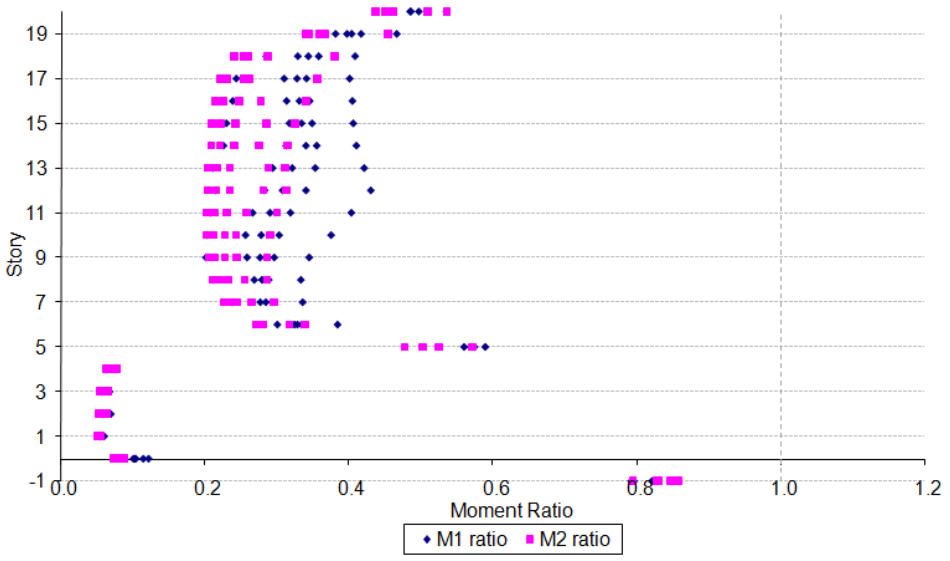

b)

Figure C.21 Moment Ratios for $BL\_20-0:5-A-236-0.01-1{,}000$ Subjected to Parkfield: a) Columns, b) Beams

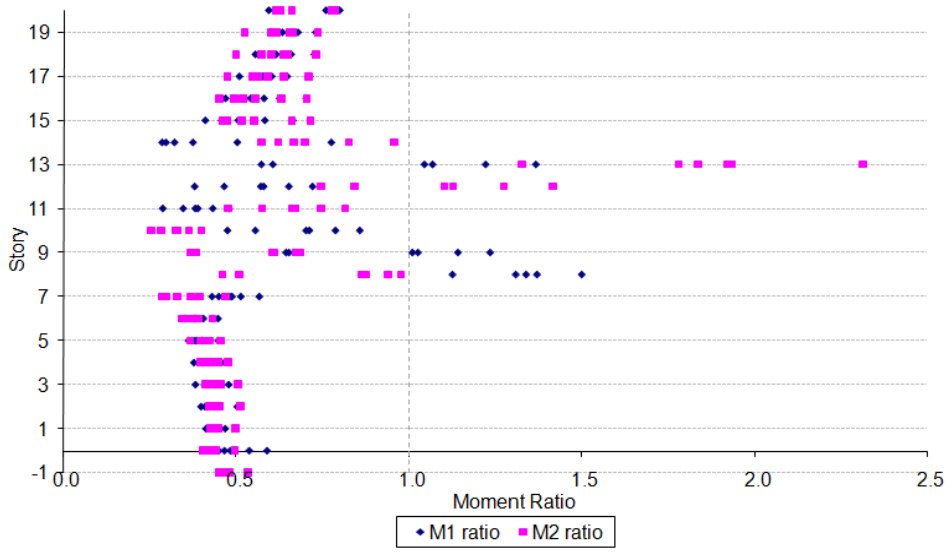

a)

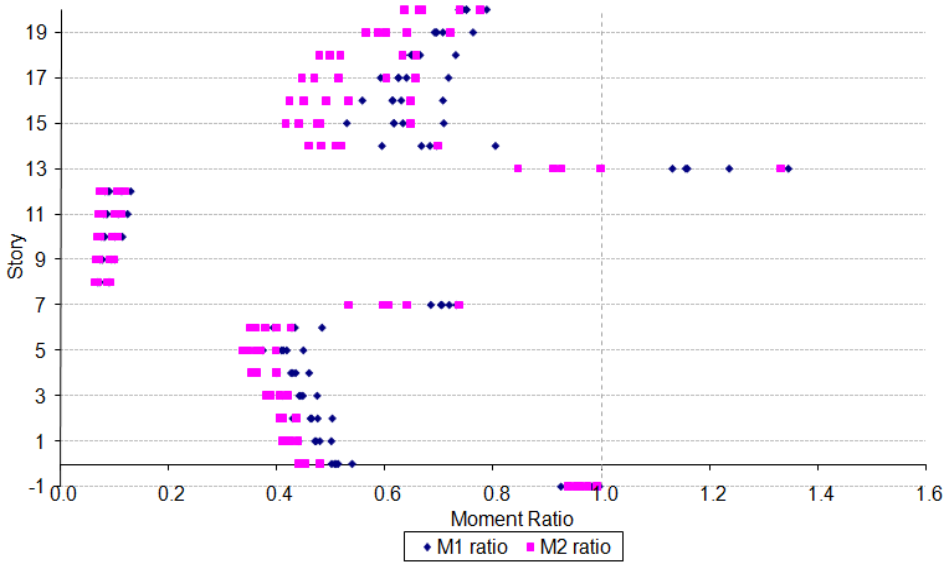

b)

Figure C.22 Moment Ratios for $BL\_20-9:13-A-236-0.01-1{,}000$ Subjected to Parkfield: a) Columns, b) Beams

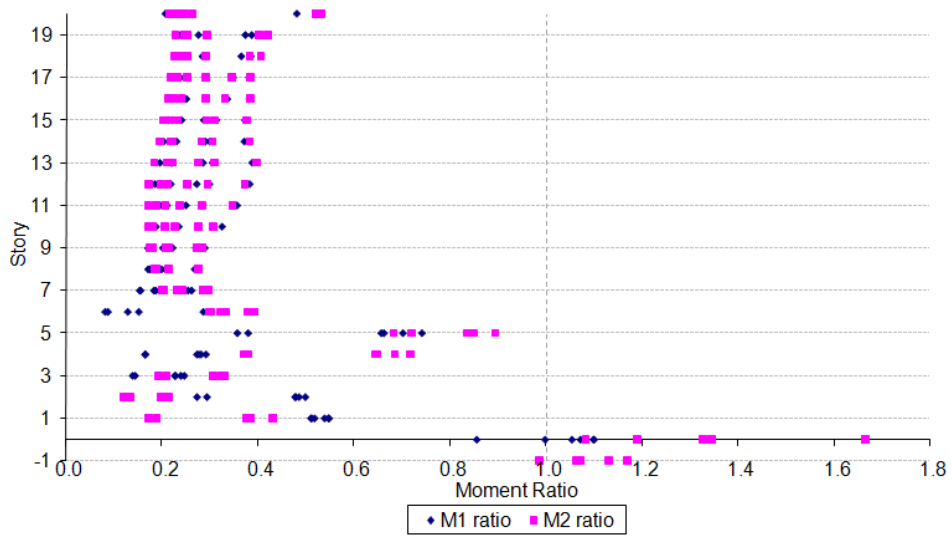

a)

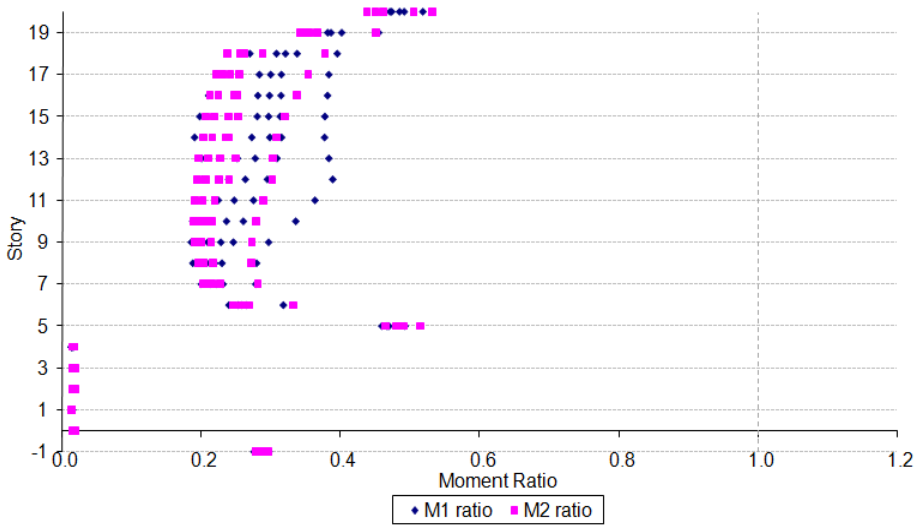

b)

Figure C.23 Moment Ratios for $BL\_20-0:5-A-100-0.1-120$ Subjected to Parkfield: a) Columns, b) Beams

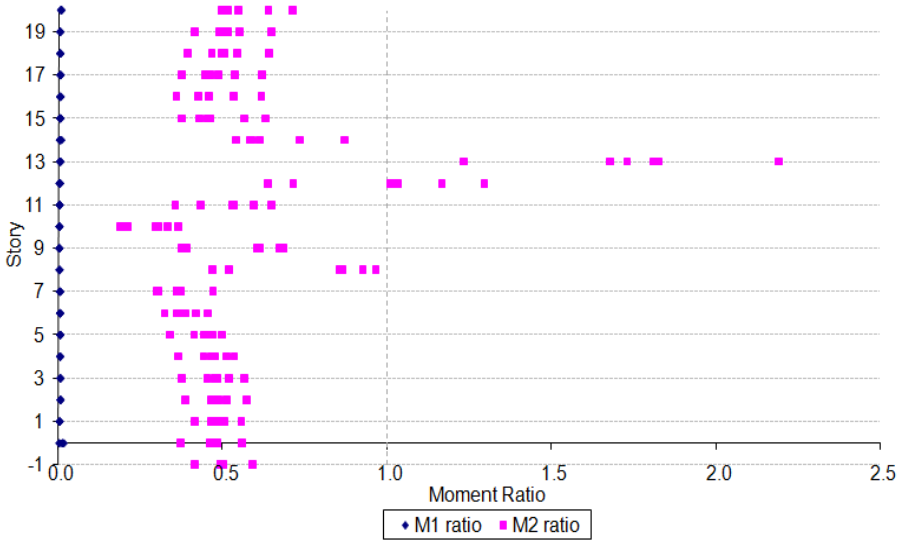

a)

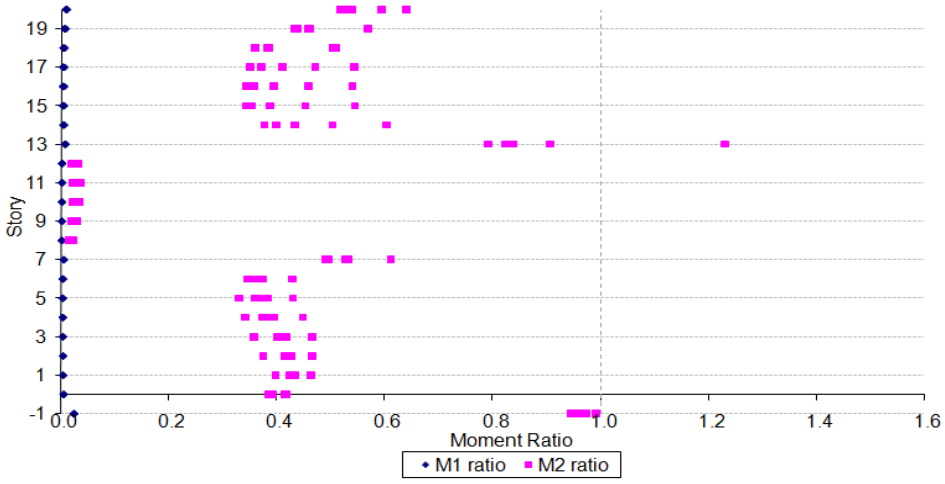

b)

Figure C.24 Moment Ratios for $BL\_20-9:13-A-100-0.1-120$ Subjected to Parkfield: a) Columns, b) Beams

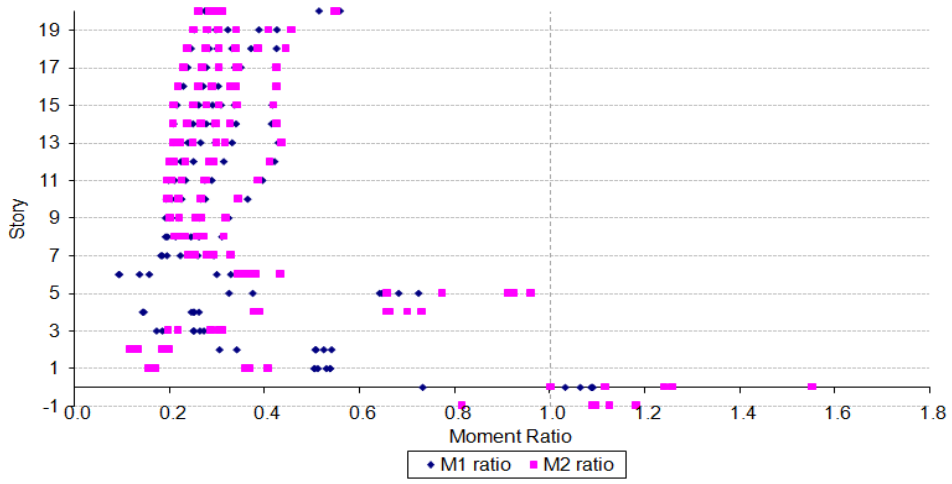

a)

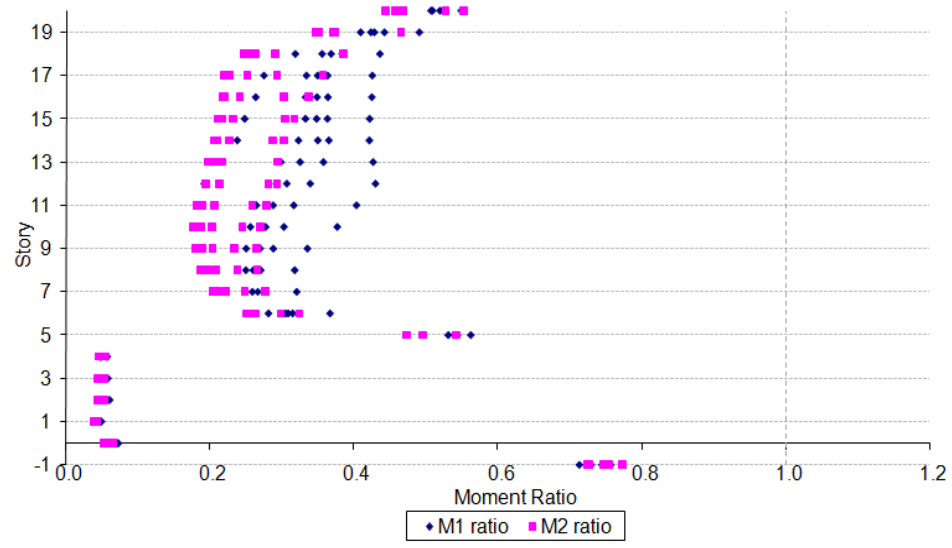

b)

Figure C.25 Moment Ratios for $BL\_20-0:5-A-500-0.05-500$ Subjected to Parkfield: a) Columns, b) Beams

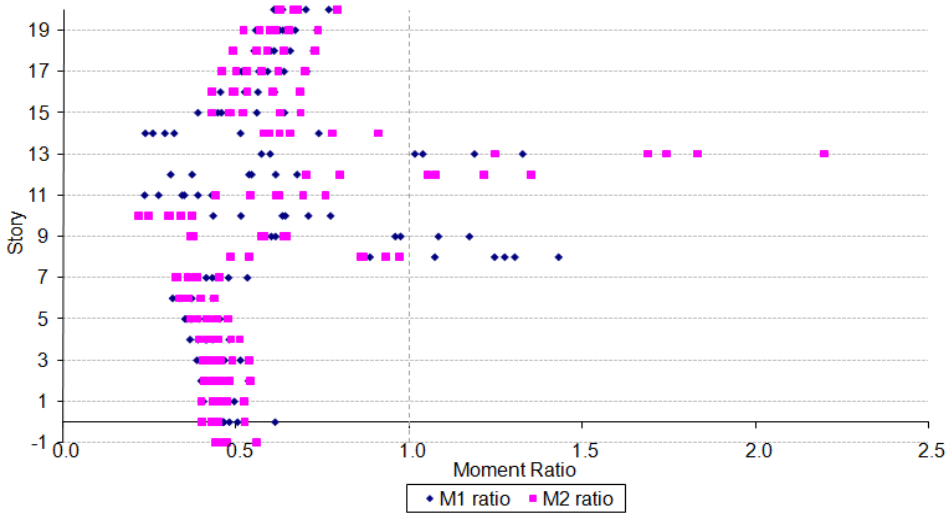

a)

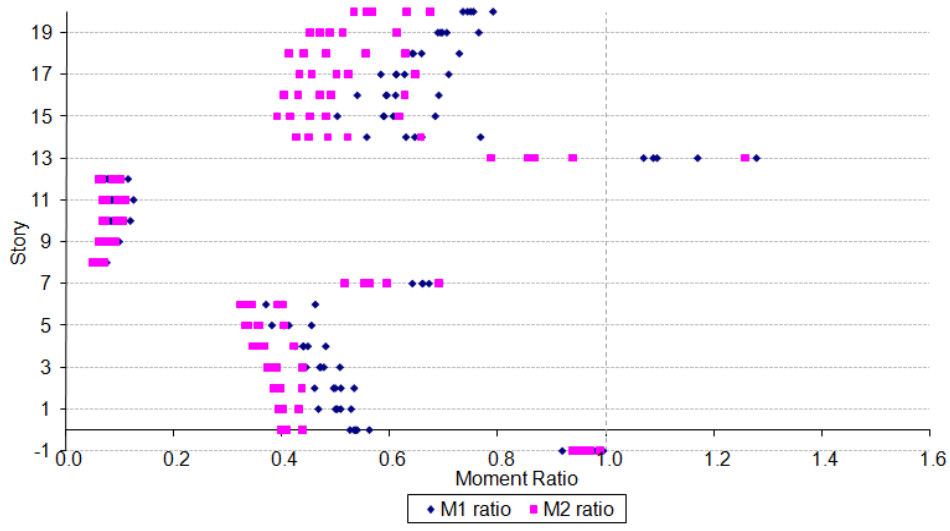

b)

Figure C.26 Moment Ratios for $BL\_20-9:13-A-500-0.05-500$ Subjected to Parkfield: a) Columns, b) Beams

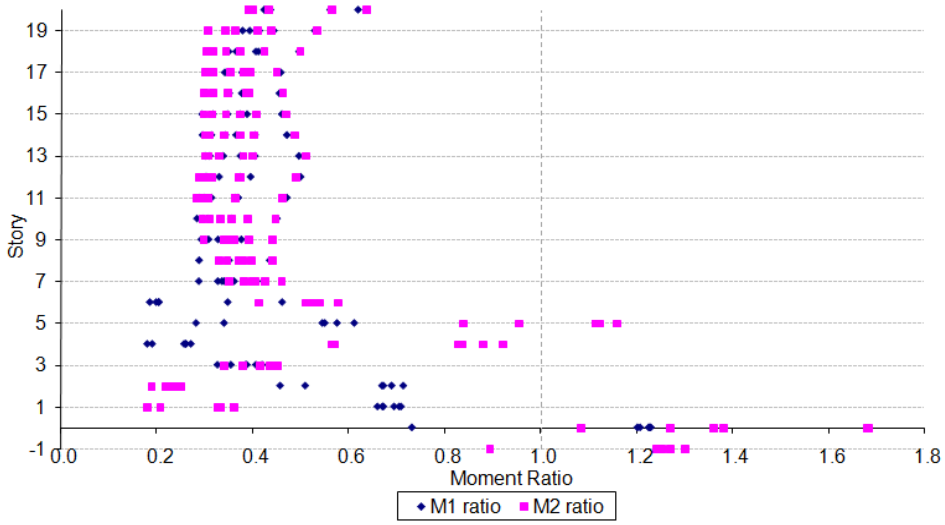

a)

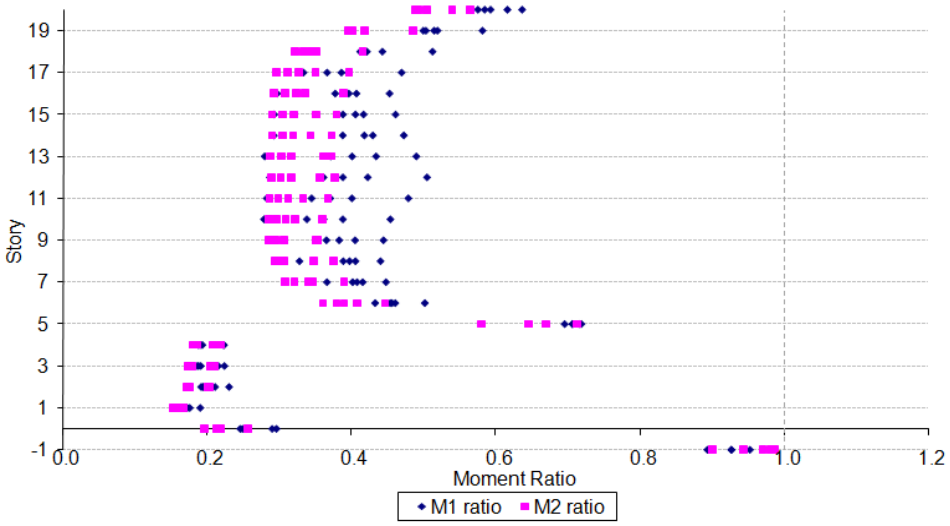

b)

Figure C.27 Moment Ratios for $BL\_20-0:5-A-800-0.1-2{,}300$ Subjected to Parkfield: a) Columns, b) Beams

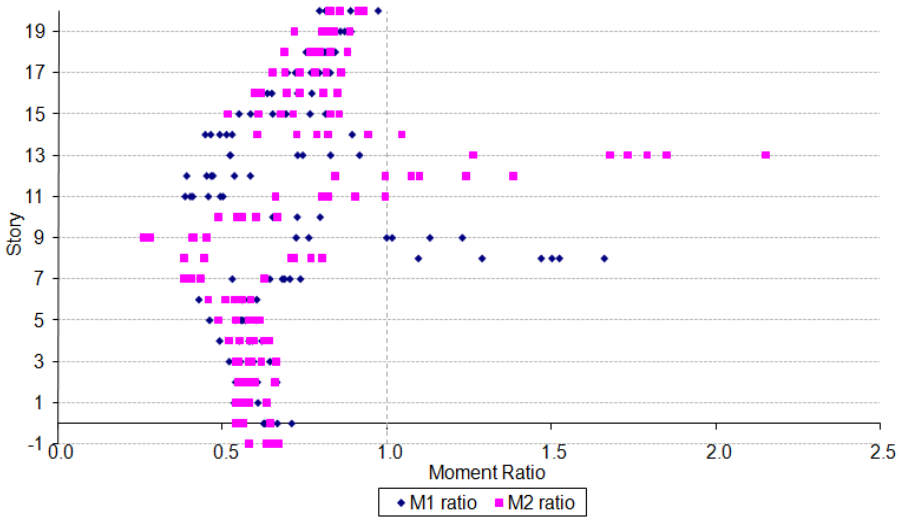

a)

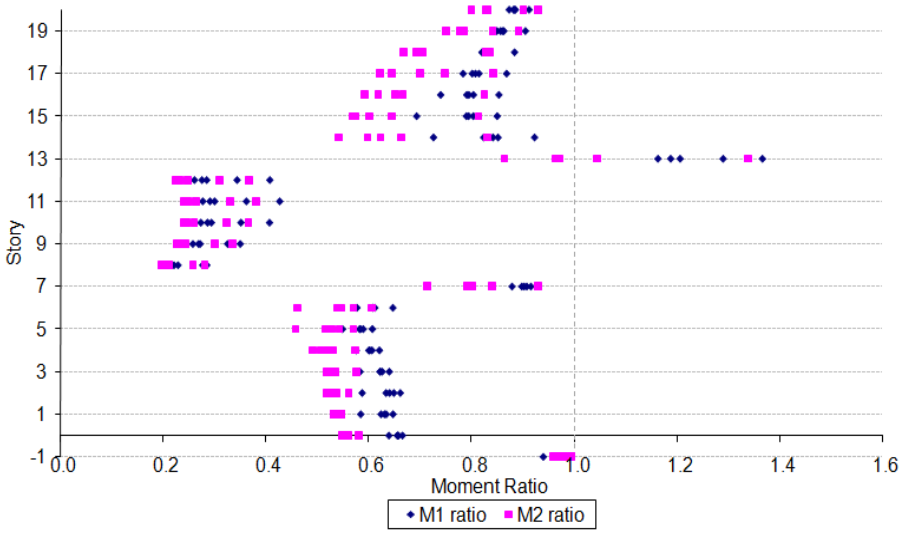

b)

Figure C.28 Moment Ratios for $BL\_20-9:13-A-800-0.1-2{,}300$ Subjected to Parkfield: a) Columns, b) Beams

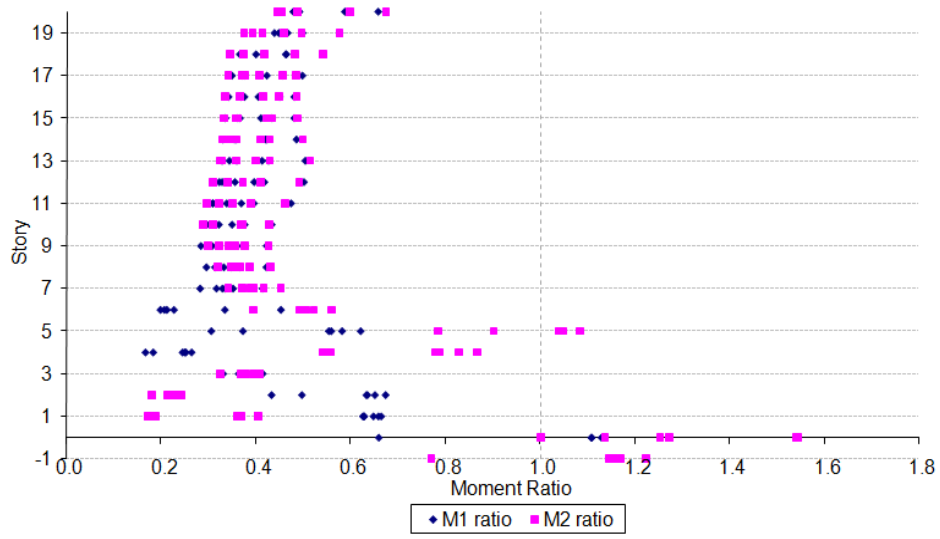

a)

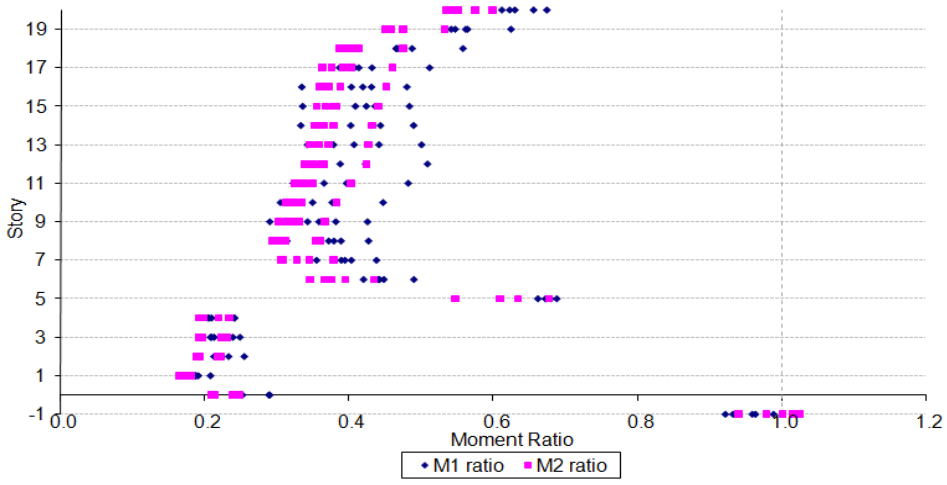

b)

Figure C.29 Moment Ratios for $BL\_20-0:5-A-2{,}500-0.05-2{,}000$ Subjected to Parkfield: a) Columns, b) Beams

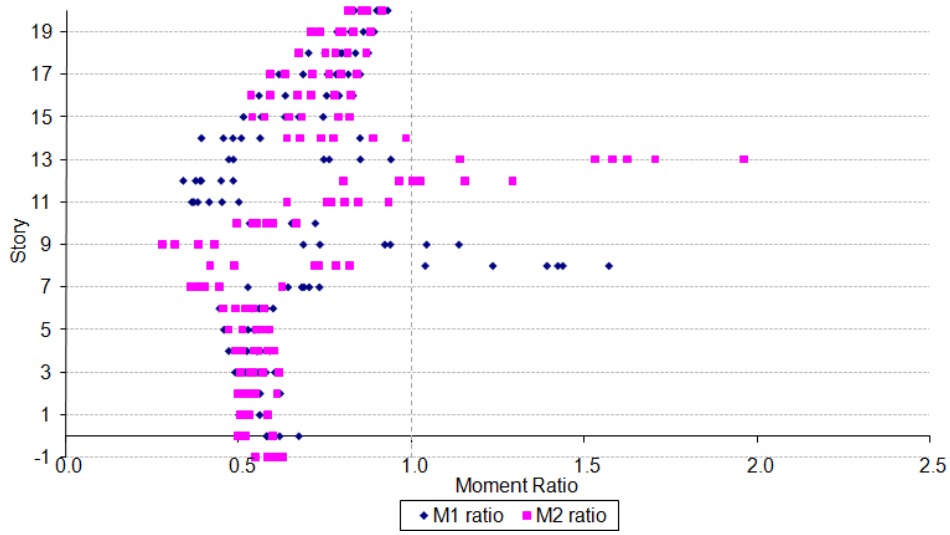

a)

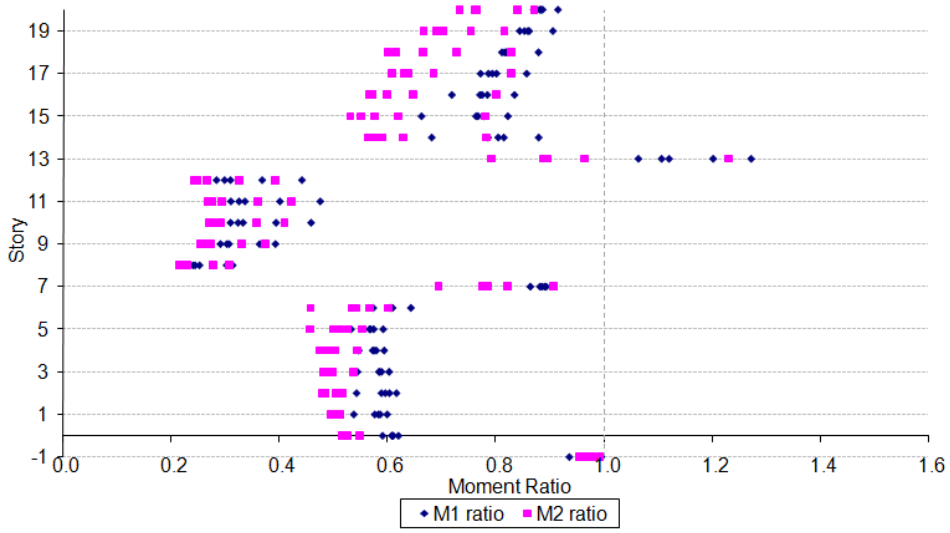

b)

Figure C.30 Moment Ratios for $BL\_20-9:13-A-2{,}500-0.05-2{,}000$ Subjected to Parkfield: a) Columns, b) Beams

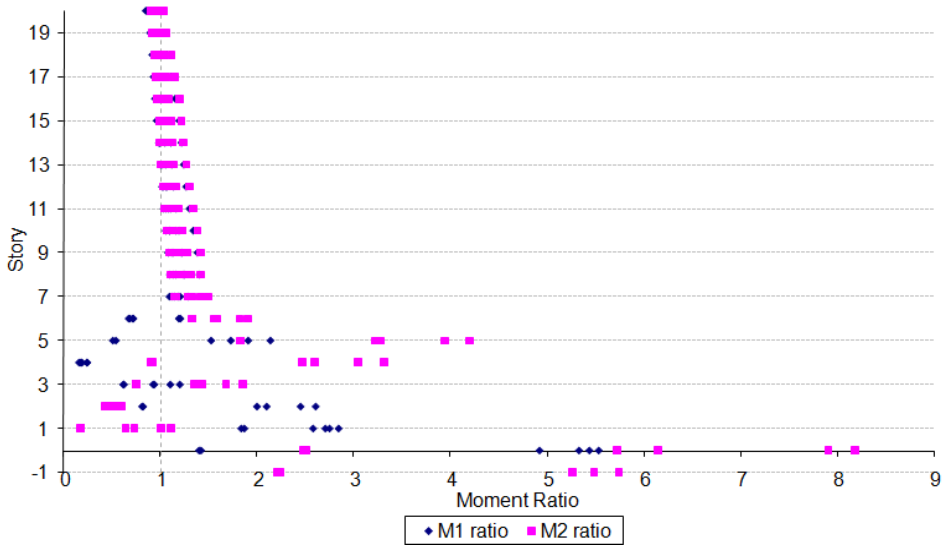

a)

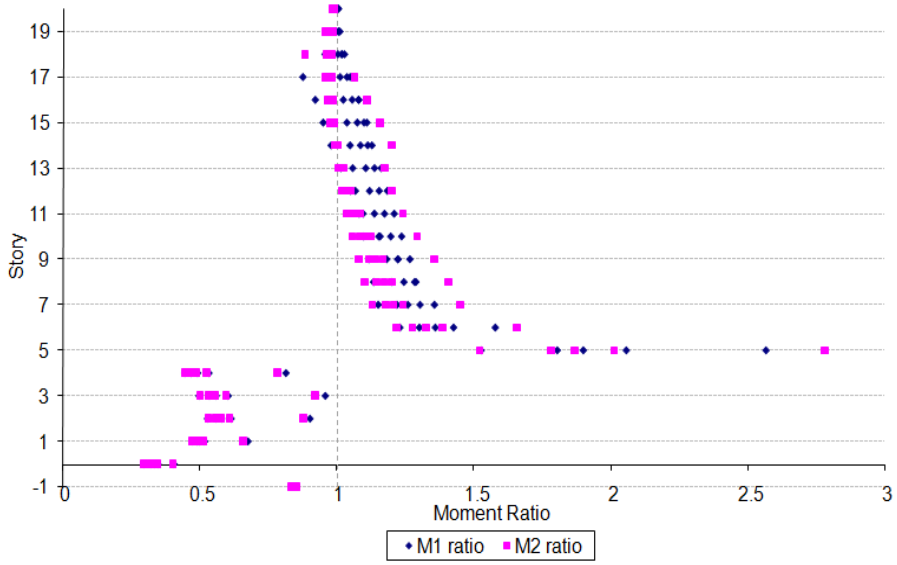

b)

Figure C.31 Moment Ratios for $BL\_20-0:5-A-236-0.01-1{,}000$ Subjected to Afyon Bay: a) Columns, b) Beams

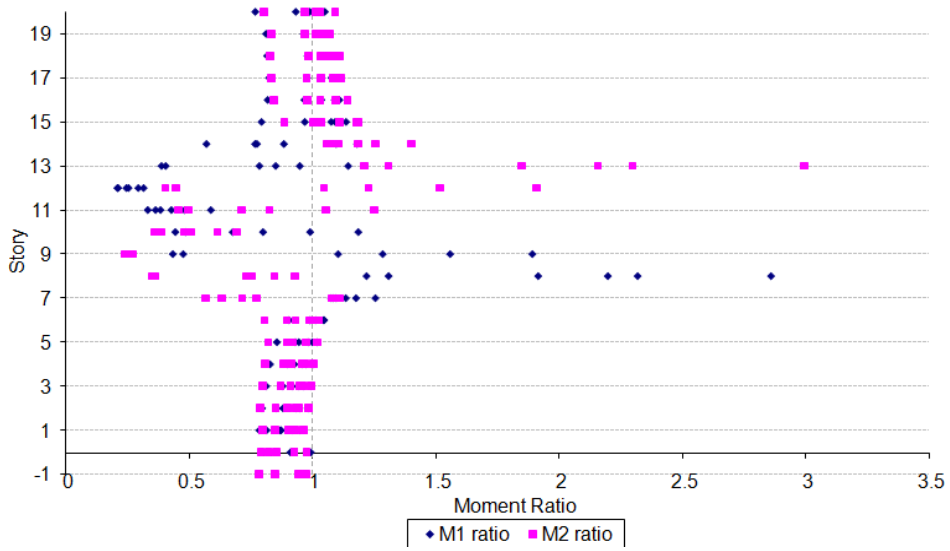

a)

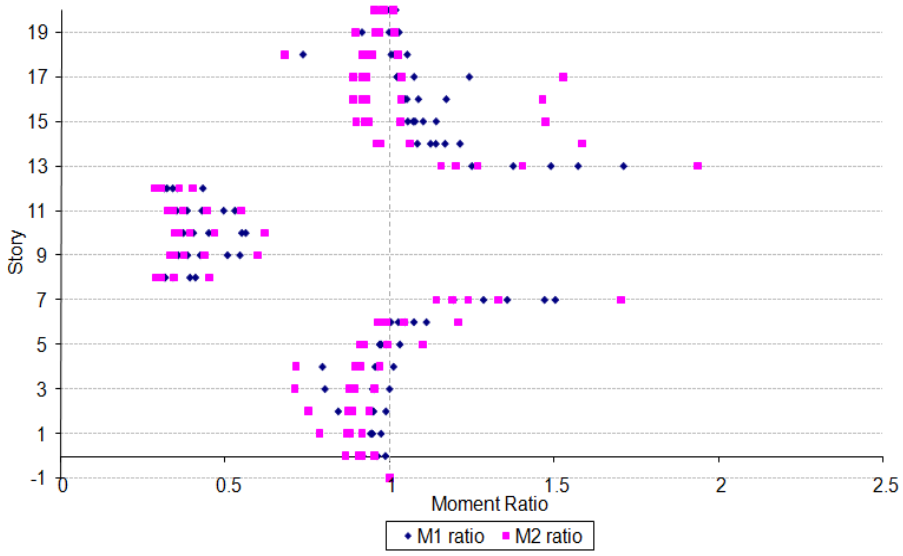

b)

Figure C.32 Moment Ratios for $BL\_20-9:13-A-236-0.01-1{,}000$ Subjected to Afyon Bay: a) Columns, b) Beams

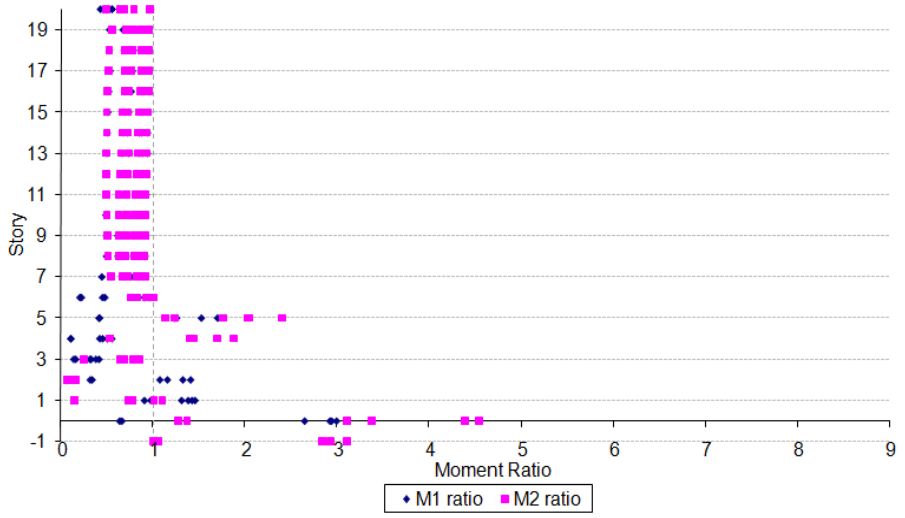

a)

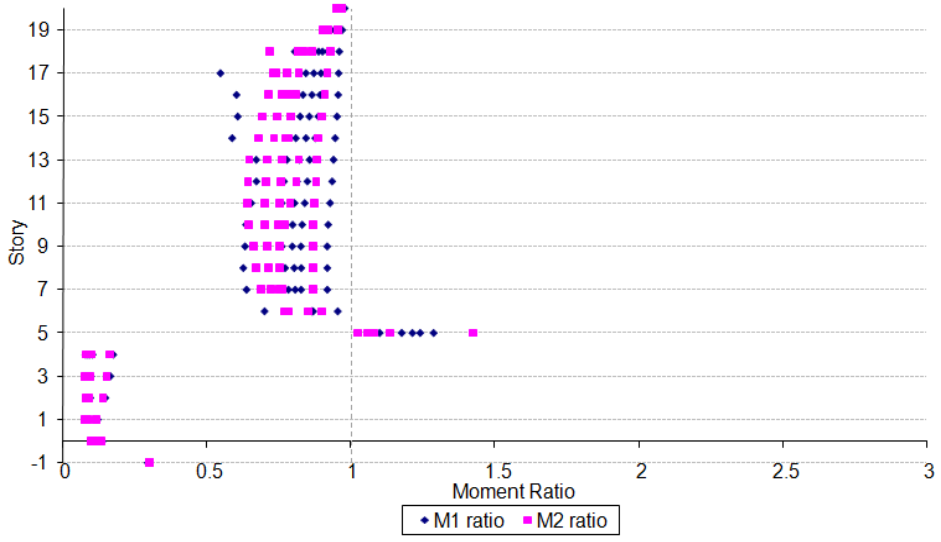

b)

Figure C.33 Moment Ratios for $BL\_20-0:5-A-100-0.1-120$ Subjected to Afyon Bay: a) Columns, b) Beams

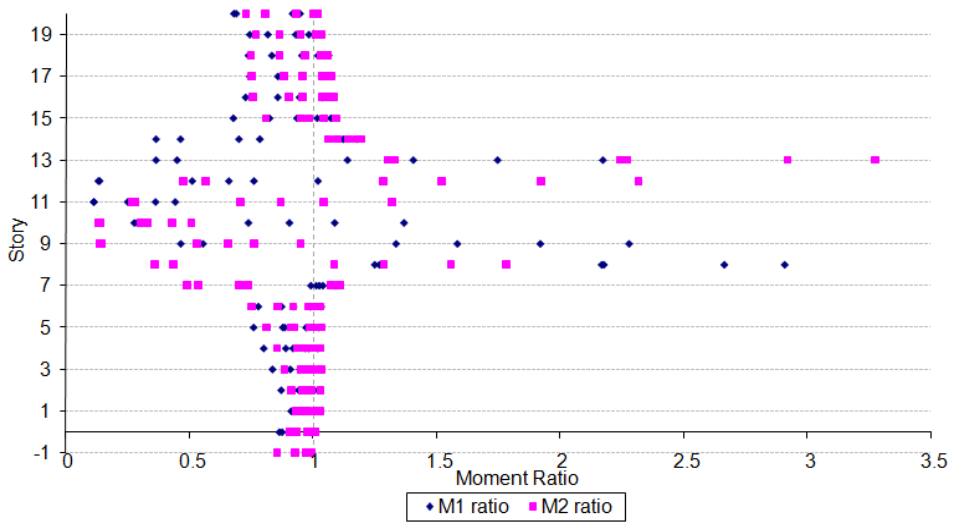

a)

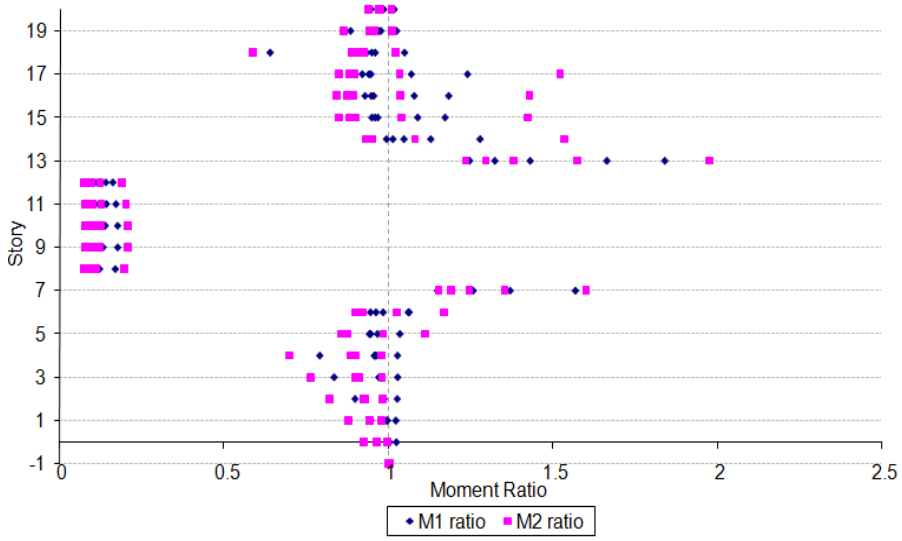

b)

Figure C.34 Moment Ratios for $BL\_20-9:13-A-100-0.1-120$ Subjected to Afyon Bay: a) Columns, b) Beams

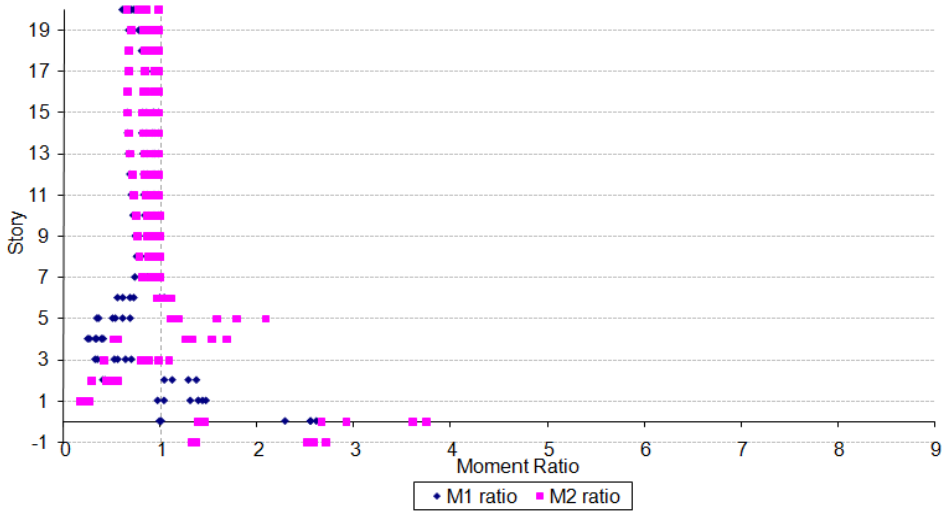

a)

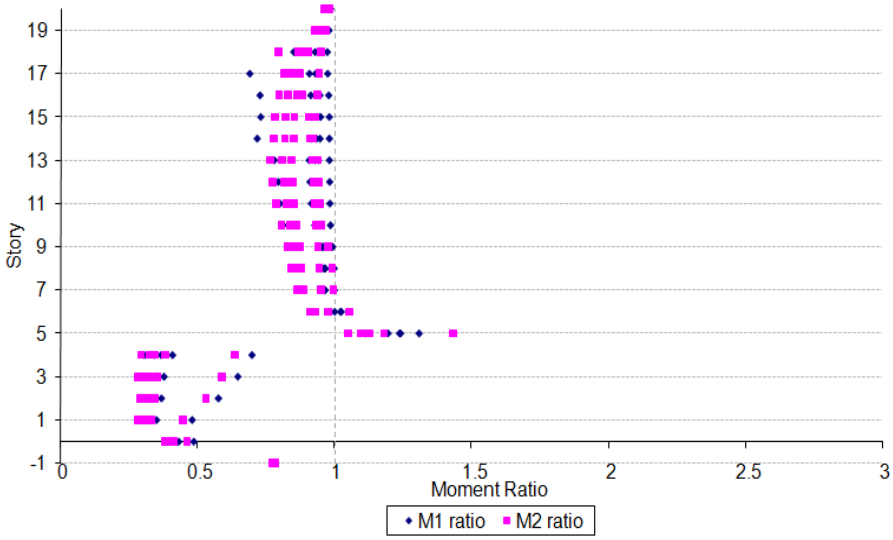

b)

Figure C.35 Moment Ratios for $BL\_20-0:5-A-500-0.05-500$ Subjected to Afyon Bay: a) Columns, b) Beams

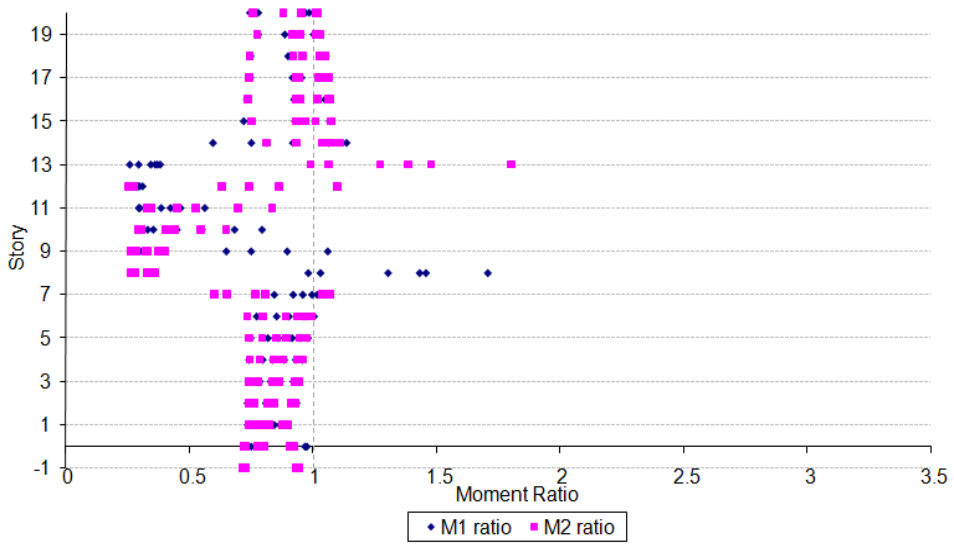

a)

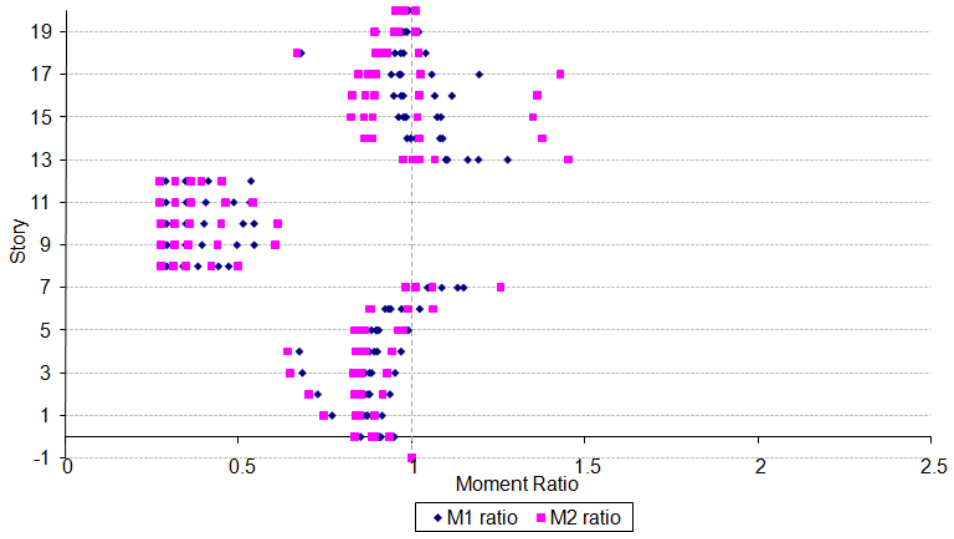

b)

Figure C.36 Moment Ratios for $BL\_20-9:13-A-500-0.05-500$ Subjected to Afyon Bay: a) Columns, b) Beams

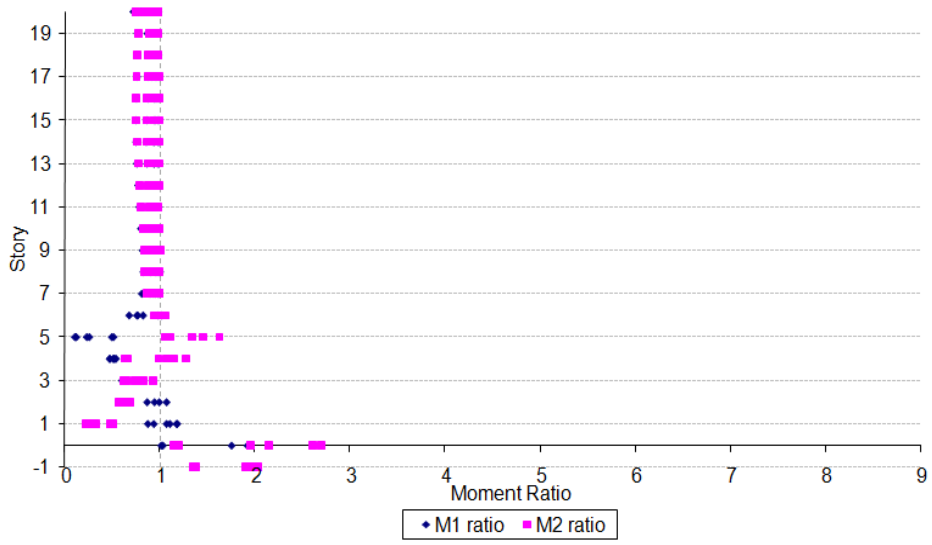

a)

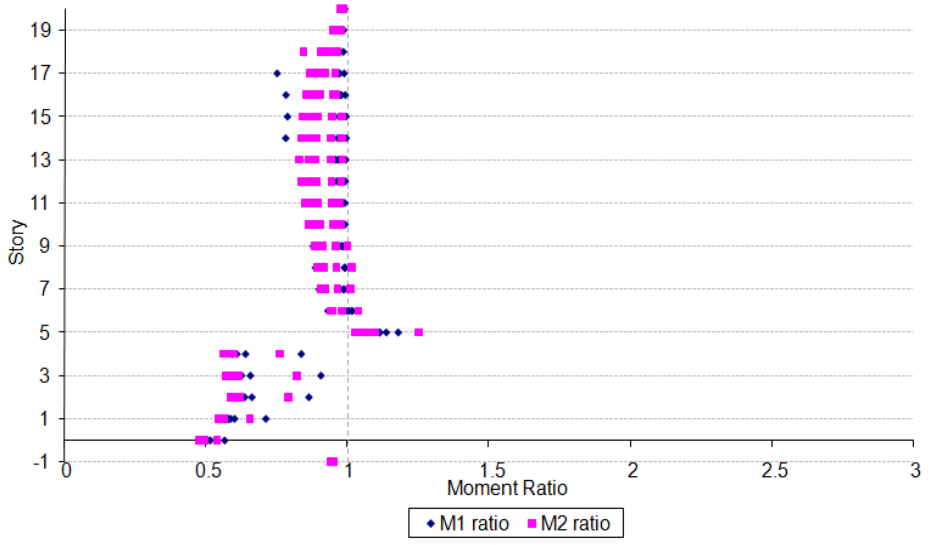

b)

Figure C.37 Moment Ratios for $BL\_20-0:5-A-800-0.1-2{,}300$ Subjected to Afyon Bay: a) Columns, b) Beams

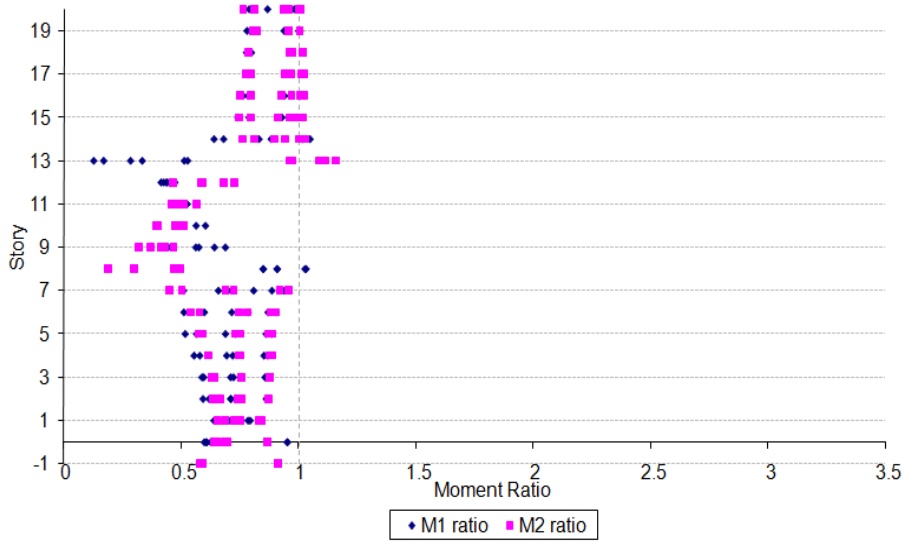

a)

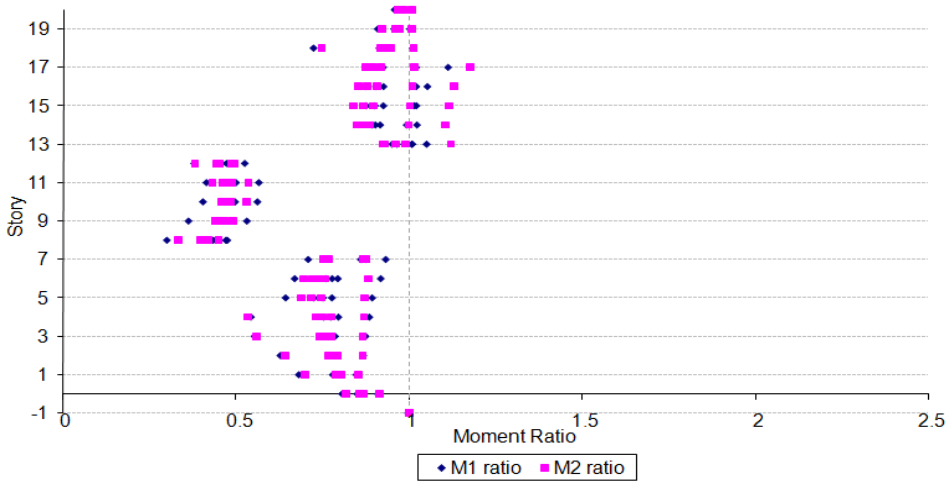

b)

Figure C.38 Moment Ratios for $BL\_20-9:13-A-800-0.1-2{,}300$ Subjected to Afyon Bay: a) Columns, b) Beams

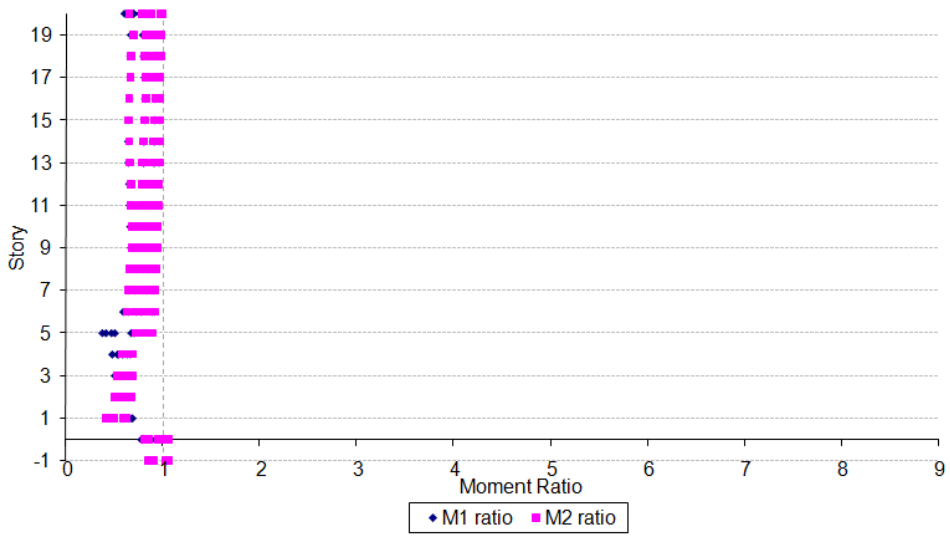

a)

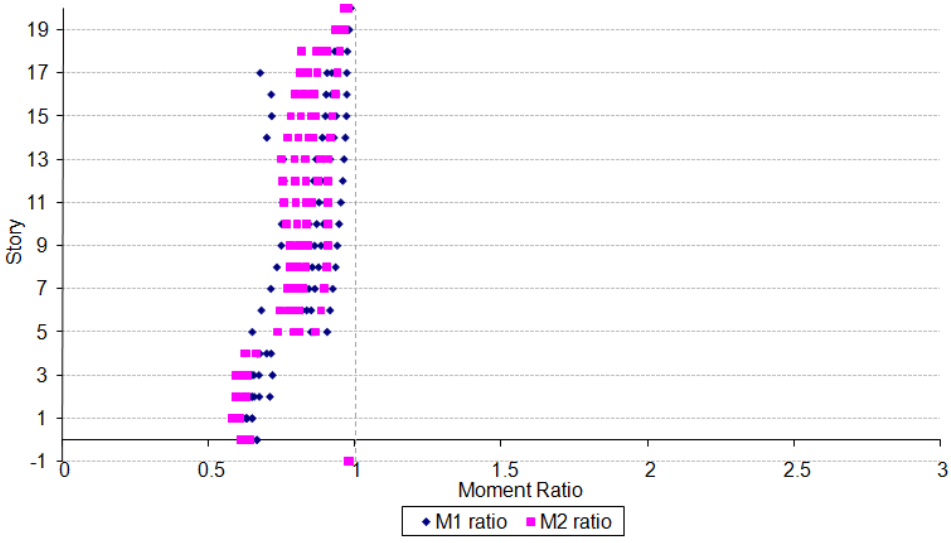

b)

Figure C.39 Moment Ratios for $BL\_20-0:5-A-2{,}500-0.05-2{,}000$ Subjected to Afyon Bay: a) Columns, b) Beams

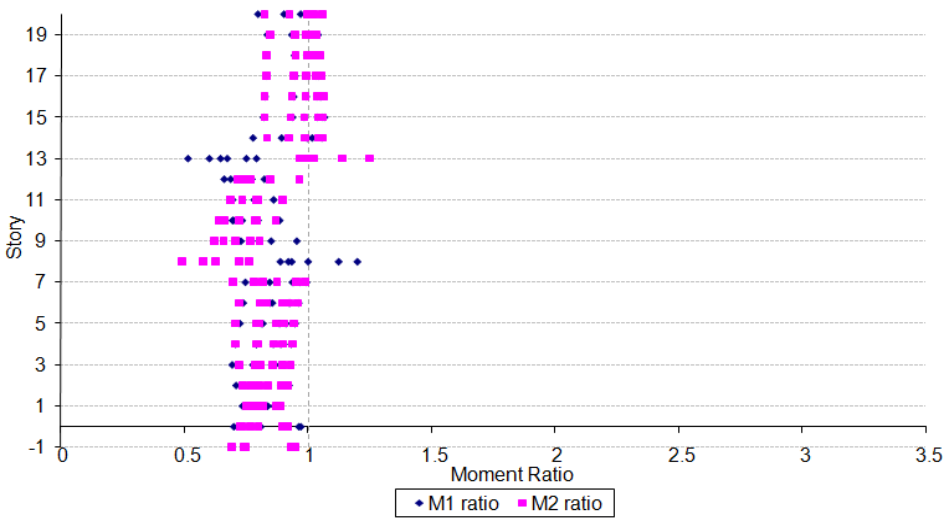

a)

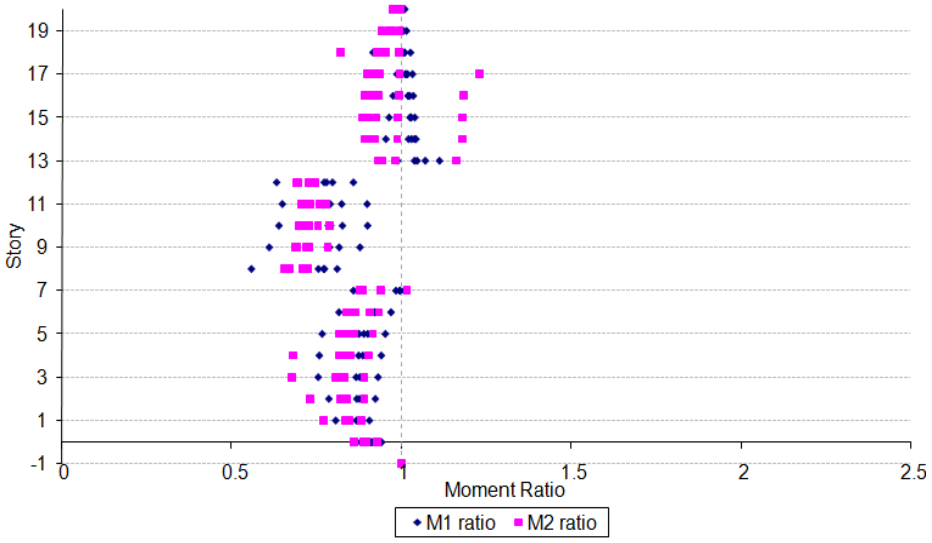

b)

Figure C.40 Moment Ratios for $BL\_20-9:5-A-2{,}500-0.05-2{,}000$ Subjected to Afyon Bay: a) Columns, b) Beams

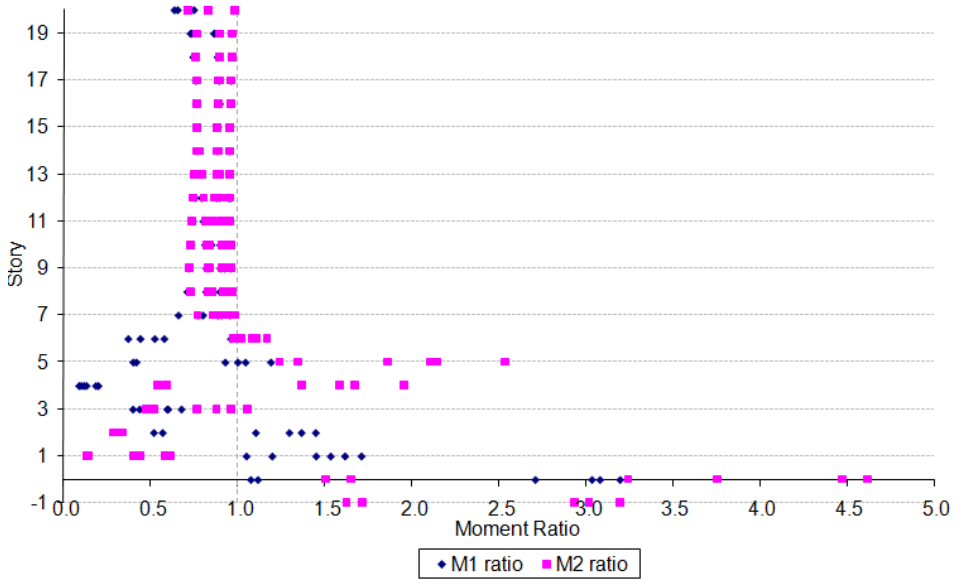

a)

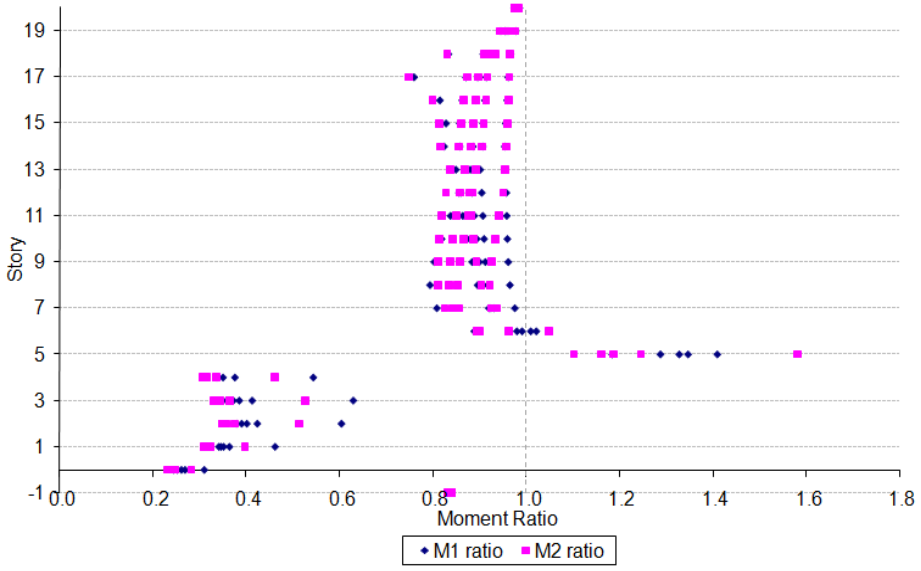

b)

Figure C.41 Moment Ratios for $BL\_20-0:5-A-236-0.01-1{,}000$ Subjected to Aydin: a) Columns, b) Beams

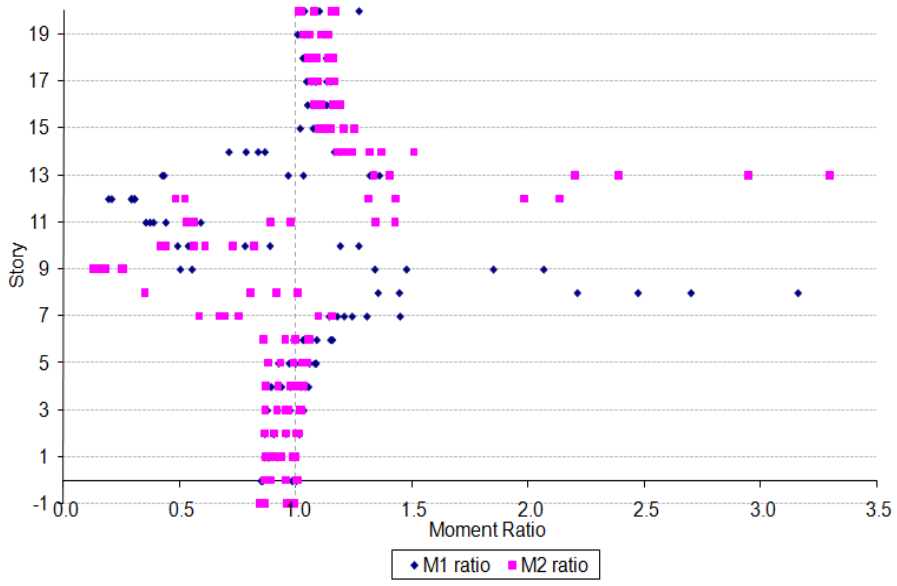

a)

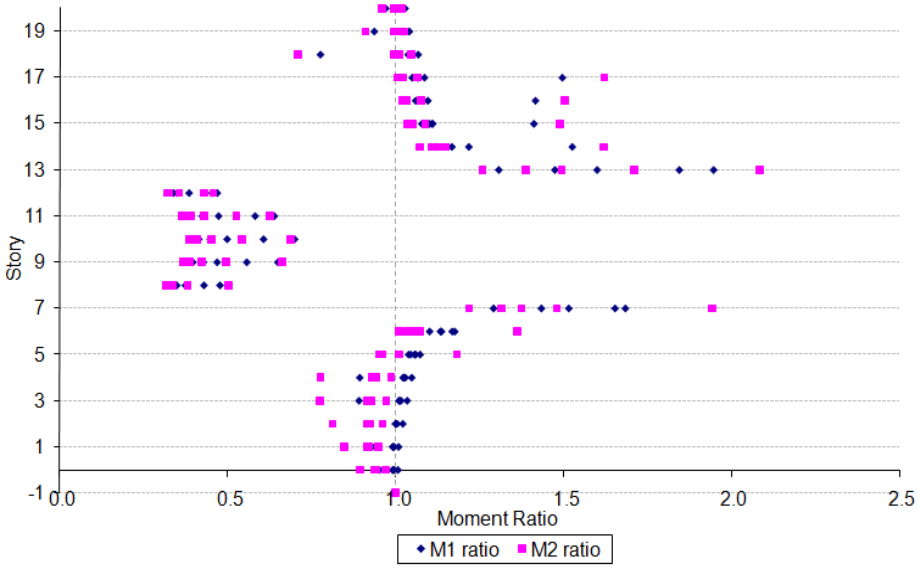

b)

Figure C.42 Moment Ratios for $BL\_20-9:13-A-236-0.01-1{,}000$ Subjected to Aydin: a) Columns, b) Beams

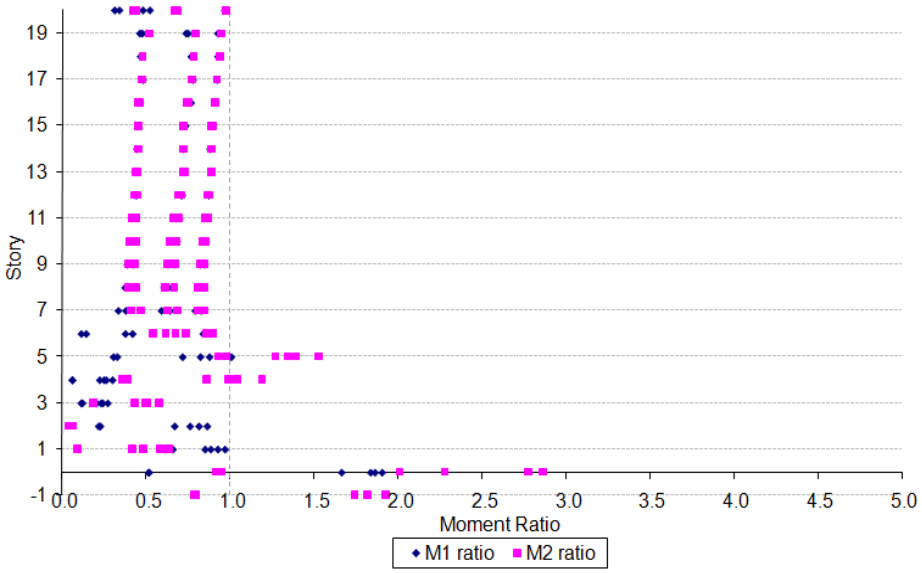

a)

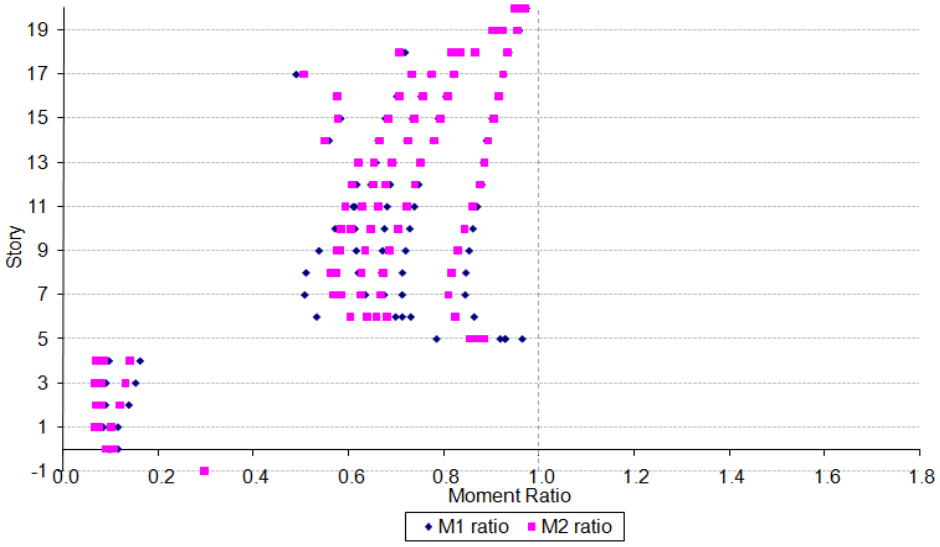

b)

Figure C.43 Moment Ratios for $BL\_20-0:5-A-100-0.1-120$ Subjected to Aydin: a) Columns, b) Beams

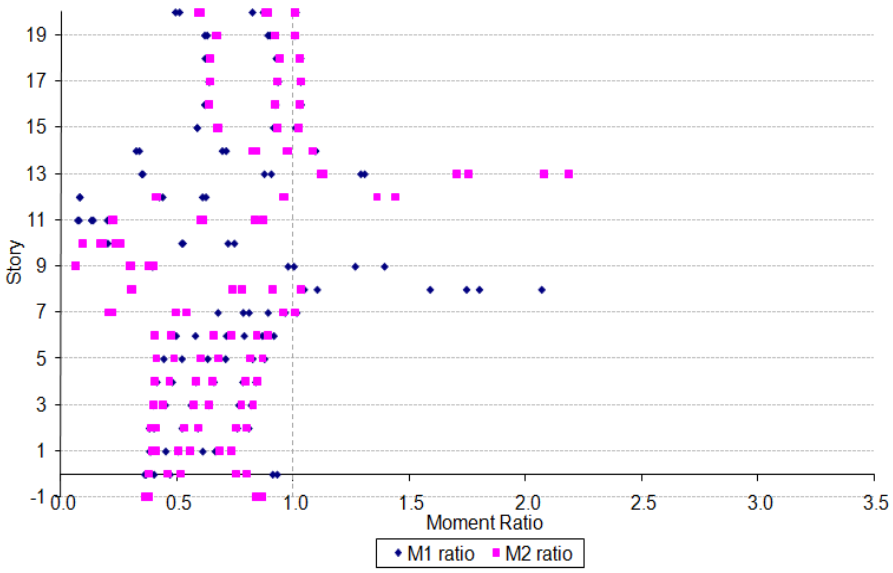

a)

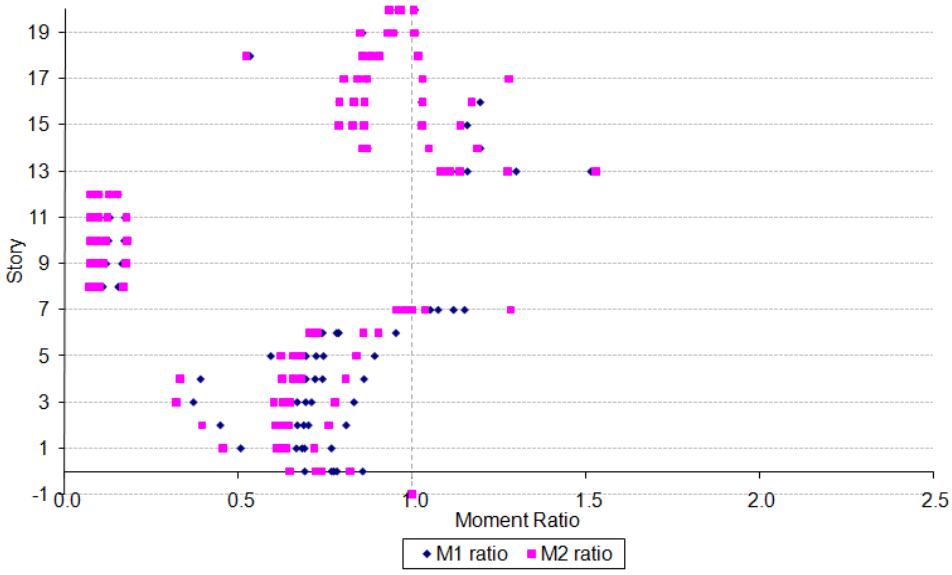

b)

Figure C.44 Moment Ratios for $BL\_20-9:13-A-100-0.1-120$ Subjected to Aydin: a) Columns, b) Beams

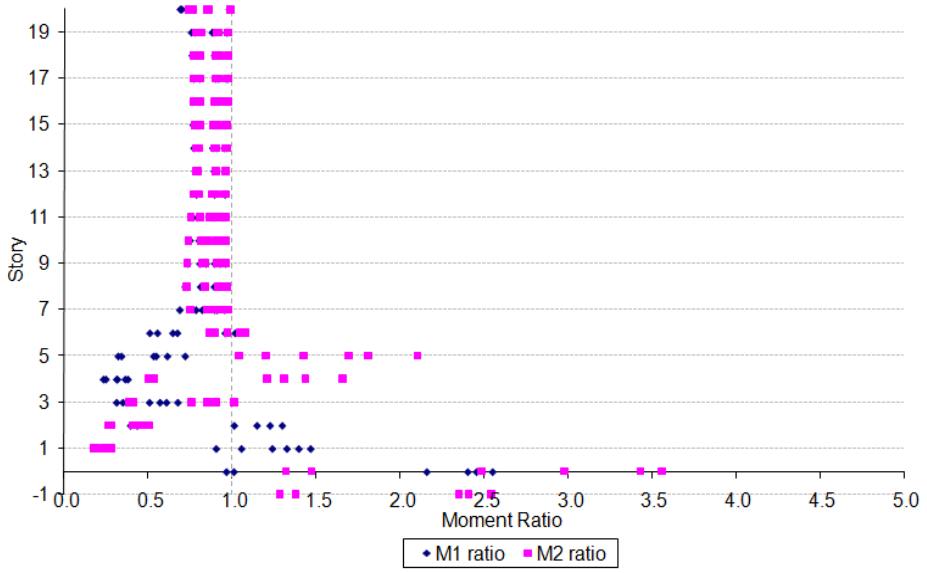

a)

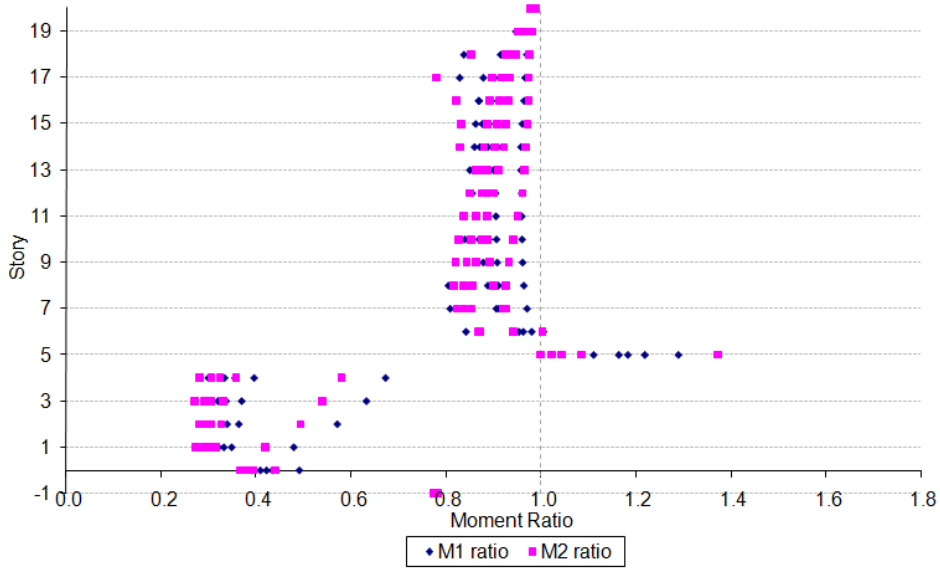

b)

Figure C.45 Moment Ratios for $BL\_20-0:5-A-500-0.05-500$ Subjected to Aydin: a) Columns, b) Beams

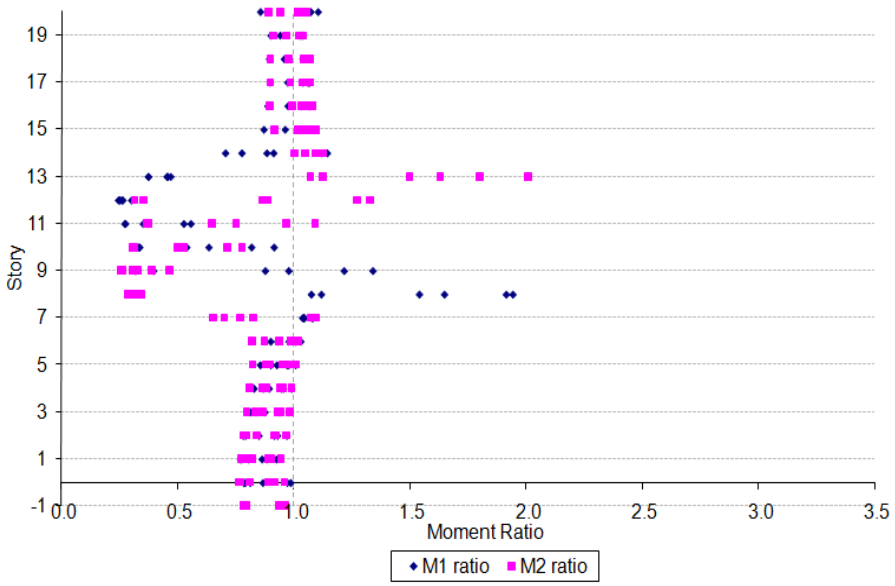

a)

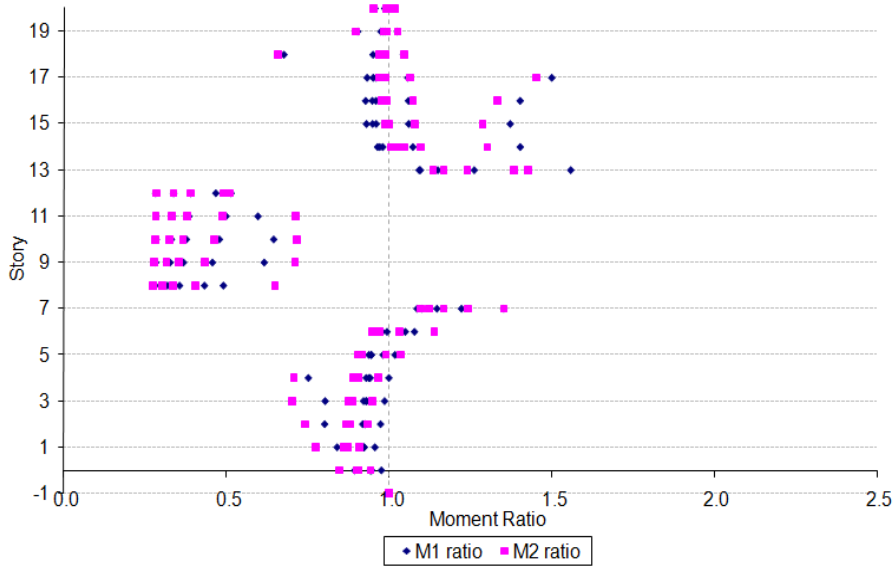

b)

Figure C.46 Moment Ratios for $BL\_20-9:13-A-500-0.05-500$ Subjected to Aydin: a) Columns, b) Beams

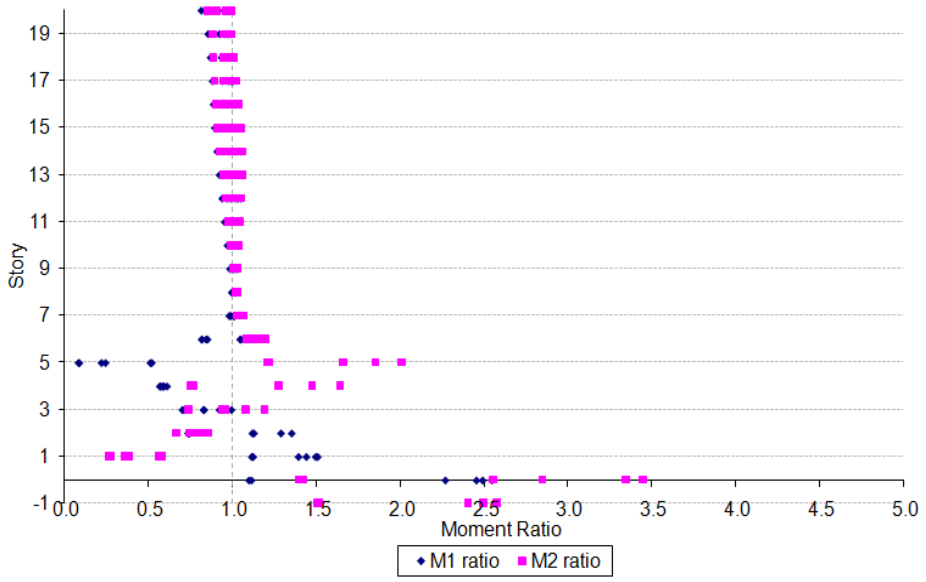

a)

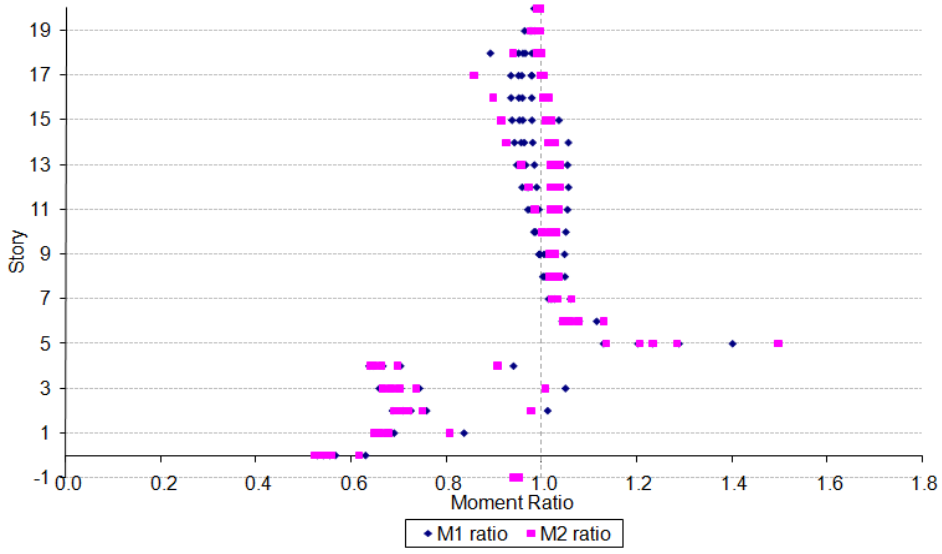

b)

Figure C.47 Moment Ratios for $BL\_20-0:5-A-800-0.1-2{,}300$ Subjected to Aydin: a) Columns, b) Beams

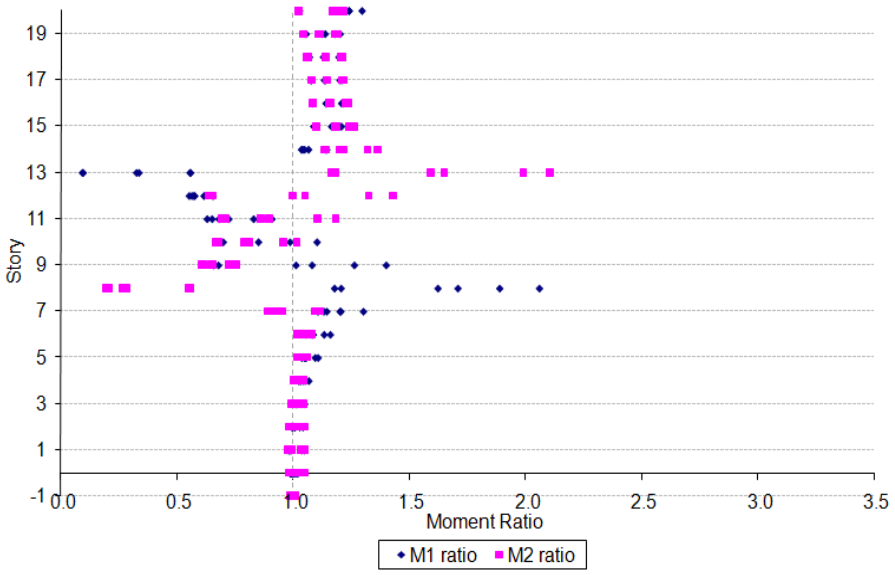

a)

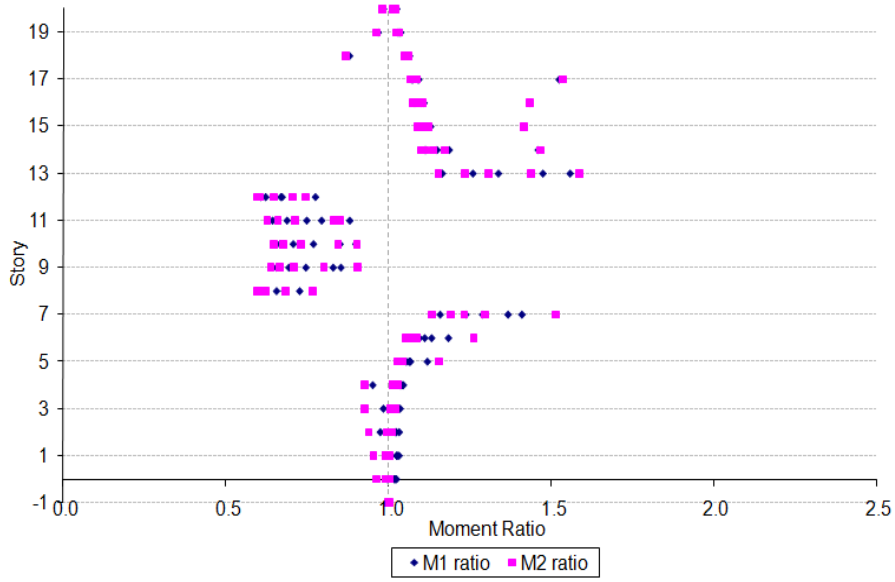

b)

Figure C.48 Moment Ratios for $BL\_20-9:13-A-800-0.1-2{,}300$ Subjected to Aydin: a) Columns, b) Beams

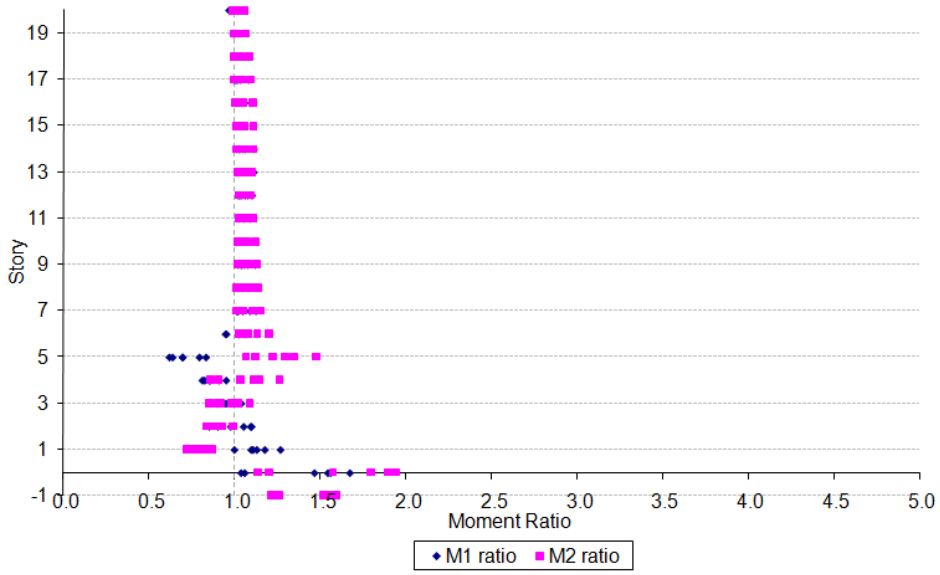

a)

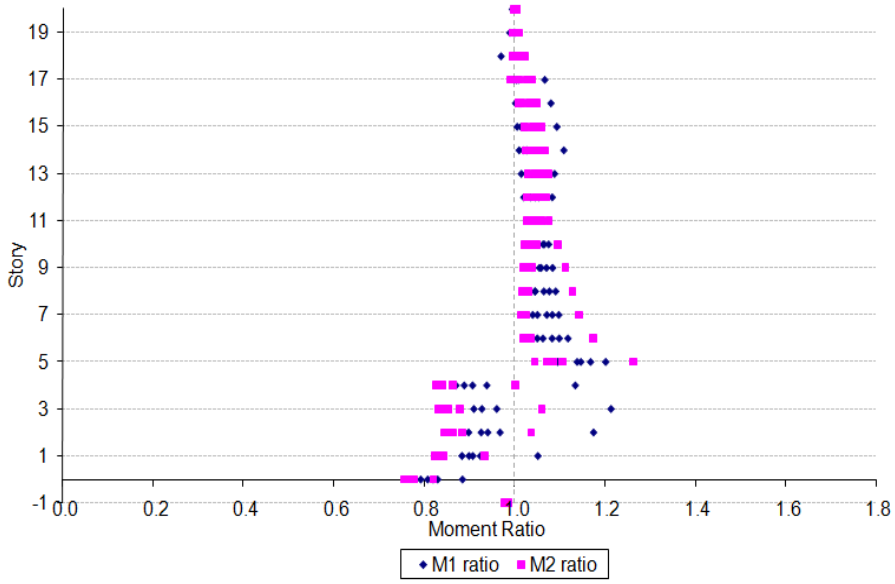

b)

Figure C.49 Moment Ratios for $BL\_20-0:5-A-2{,}500-0.05-2{,}000$ Subjected to Aydin: a) Columns, b) Beams

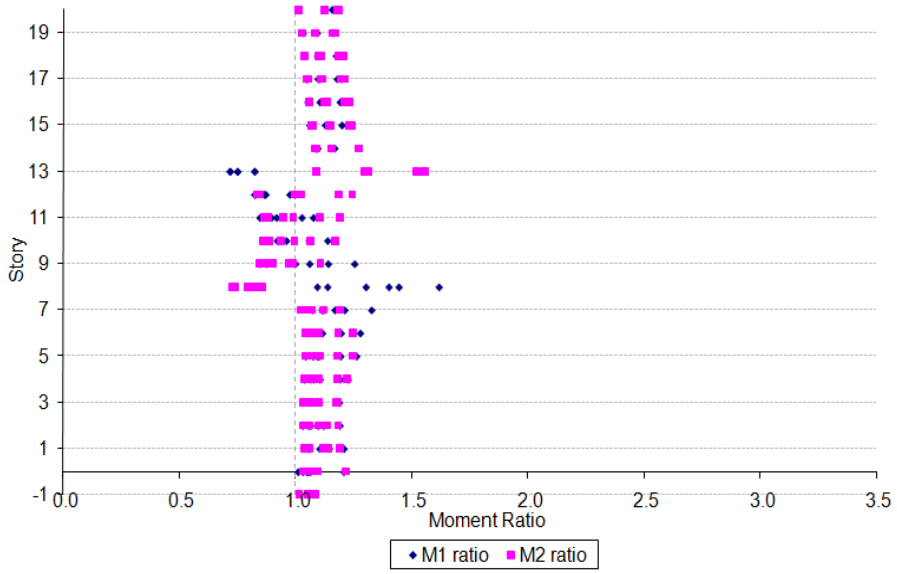

a)

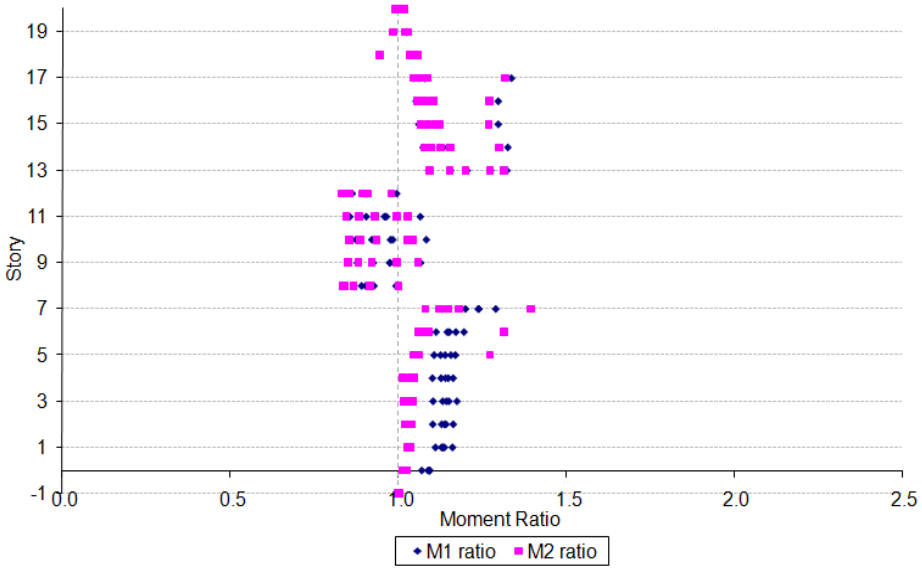

b)

Figure C.50 Moment Ratios for $BL\_20-9:13-A-2{,}500-0.05-2{,}000$ Subjected to Aydin: a) Columns, b) Beams

APPENDIX D

SHEAR FORCES FOR SAC FRAME IN EARTHQUAKE ANALYSIS

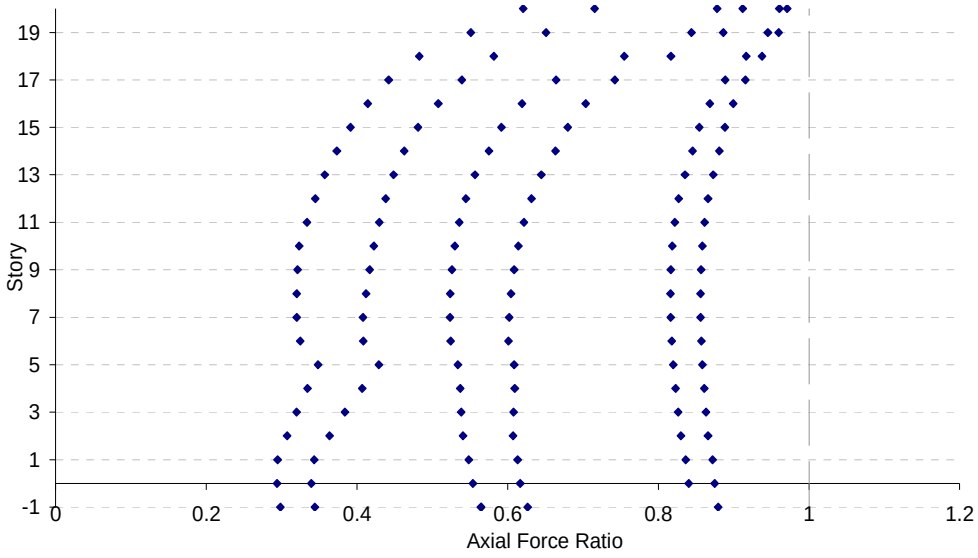

a)

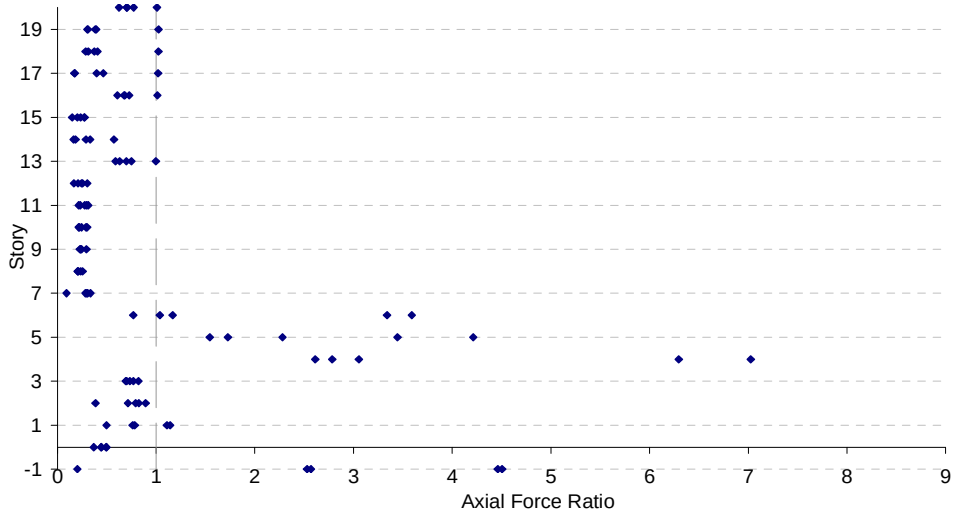

b)

Figure D.1 Axial Force Ratios for $BL\_20-0:5-A-236-0.01-1{,}000$ Subjected to El Centro: a) Columns, b) Beams

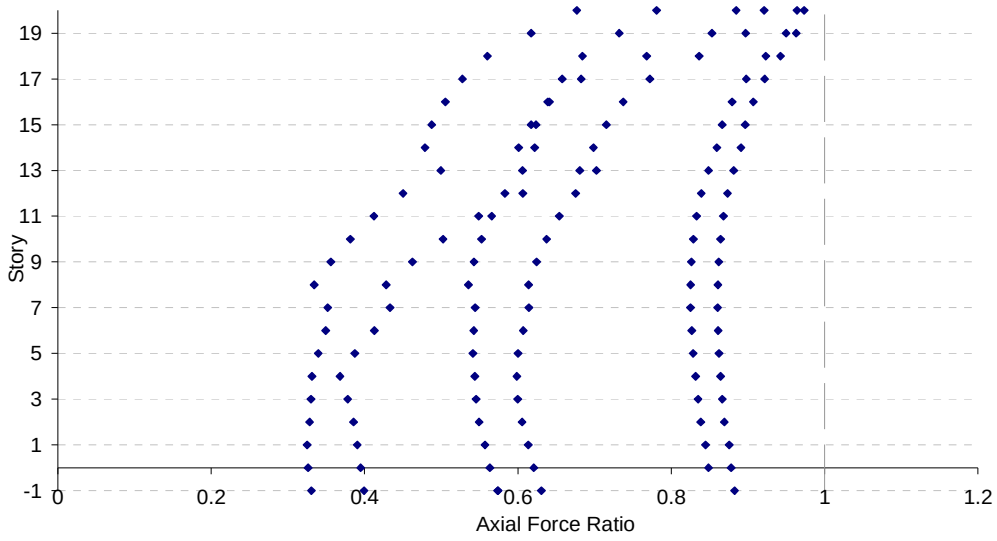

a)

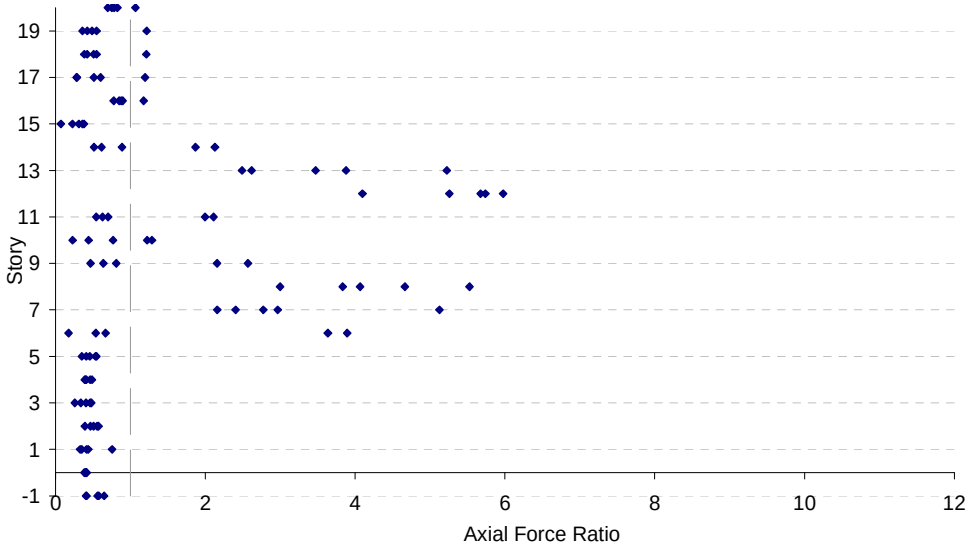

b)

Figure D.2 Axial Force Ratios for $BL\_20-9:13-A-236-0.01-1{,}000$ Subjected to El Centro: a) Columns, b) Beams

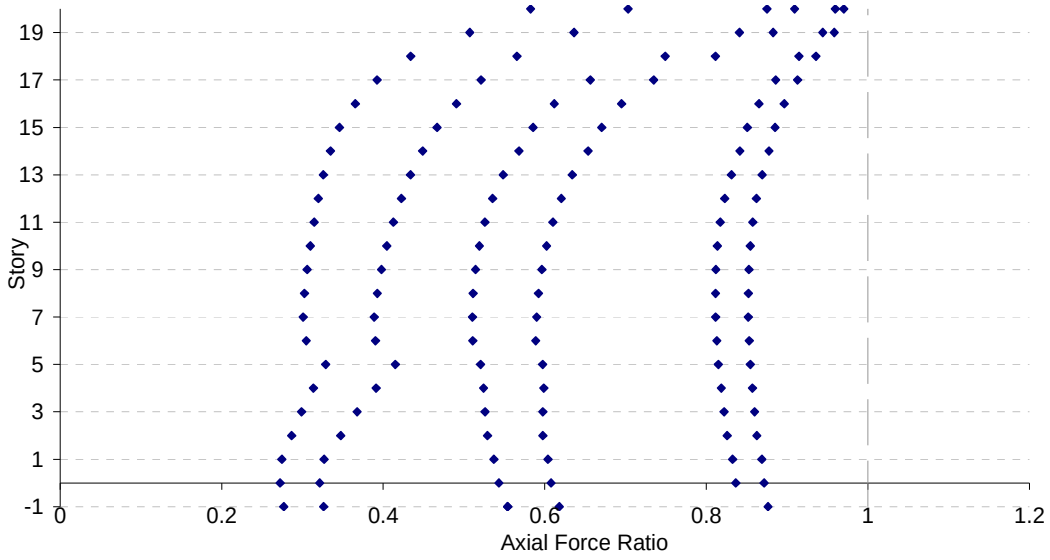

a)

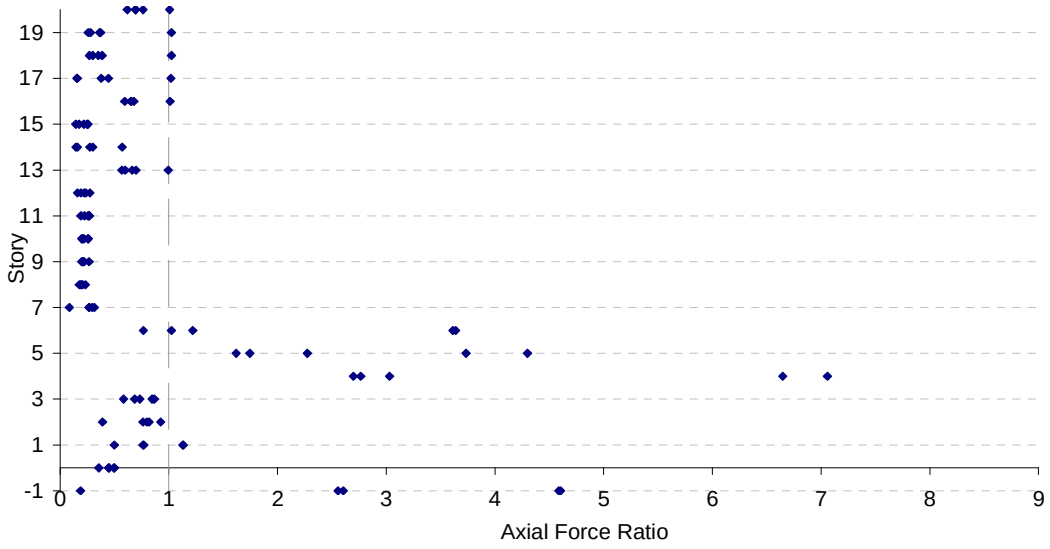

b)

Figure D.3 Axial Force Ratios for $BL\_20-0:5-A-100-0.1-120$
Subjected to El Centro: a) Columns, b) Beams

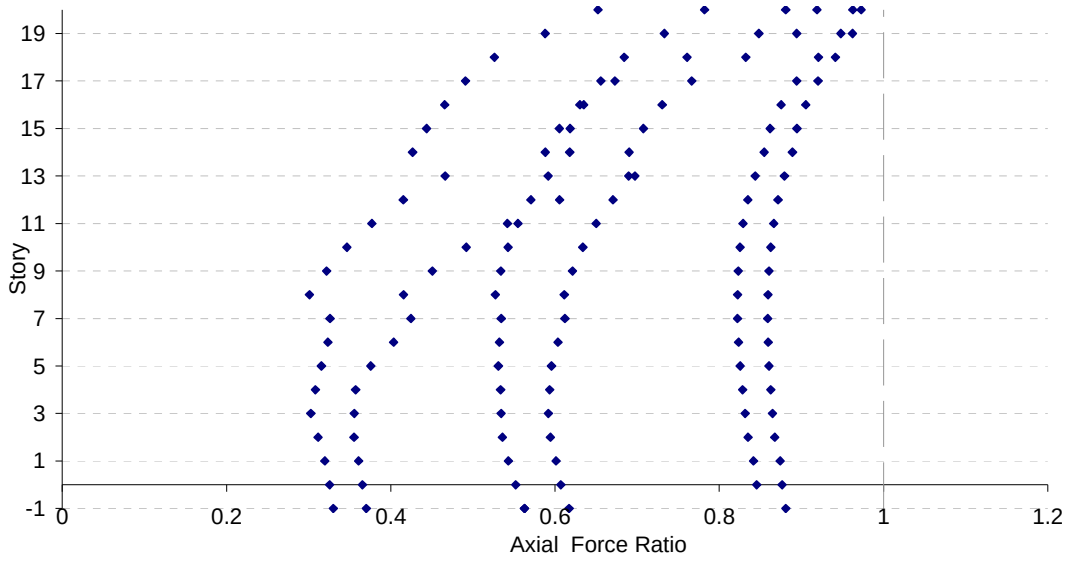

a)

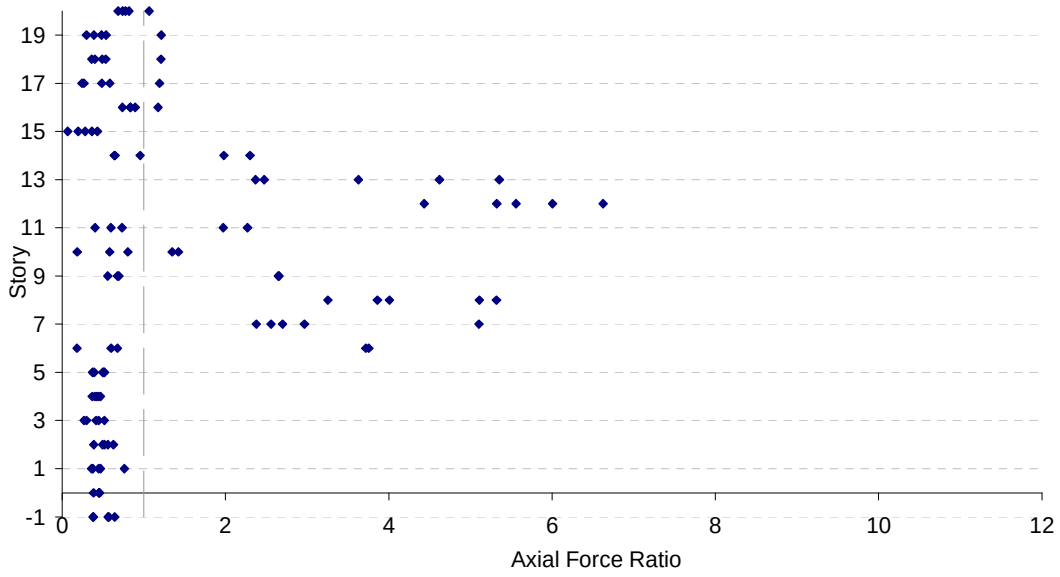

b)

Figure D.4 Axial Force Ratios for $BL\_20-9:13-A-100-0.1-120$ Subjected to El Centro: a) Columns, b) Beams

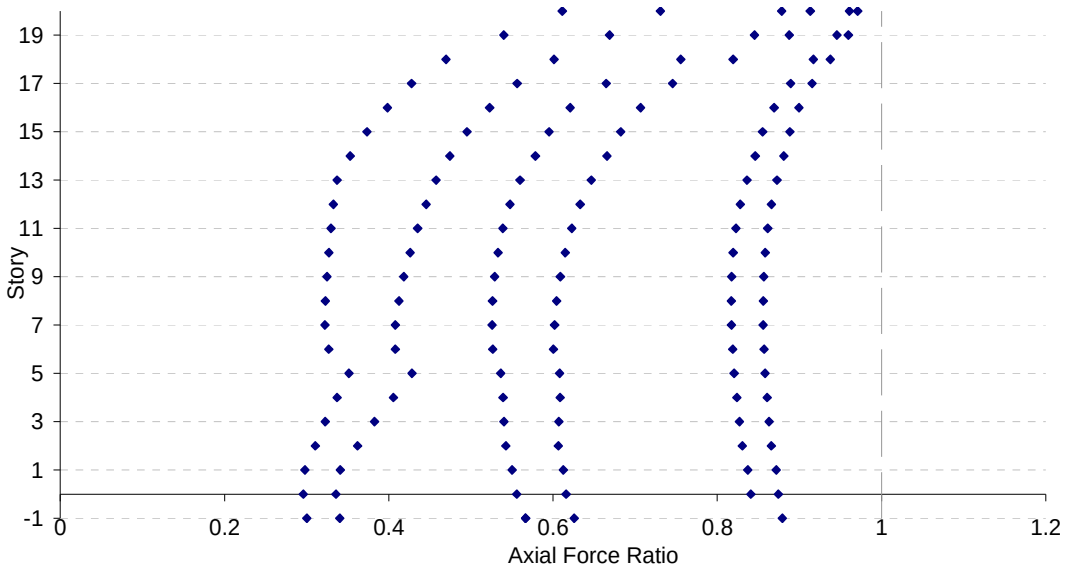

a)

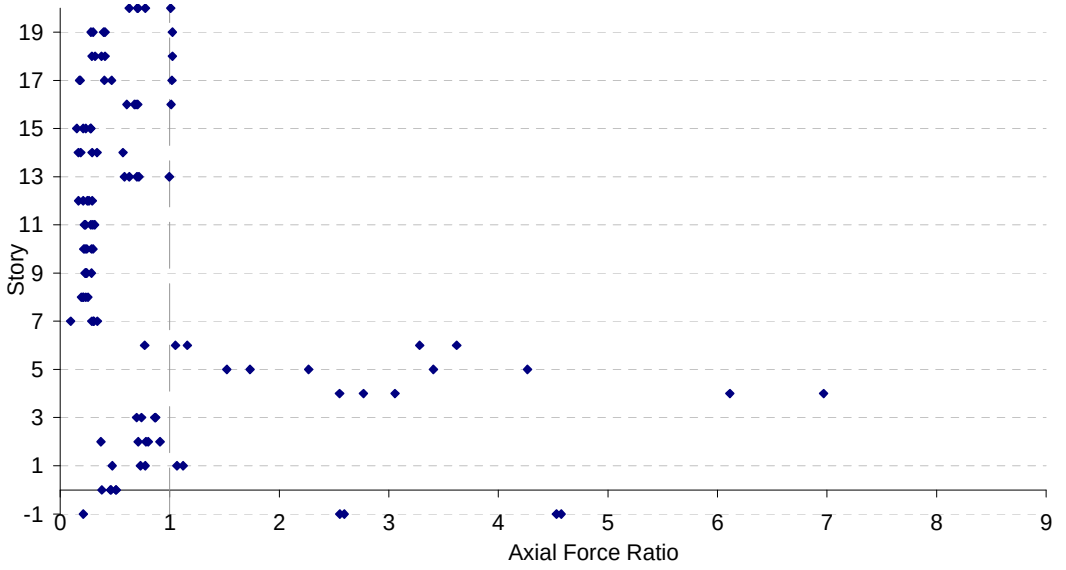

b)

Figure D.5 Axial Force Ratios for $BL\_20-0:5-A-500-0.05-500$ Subjected to El Centro: a) Columns, b) Beams

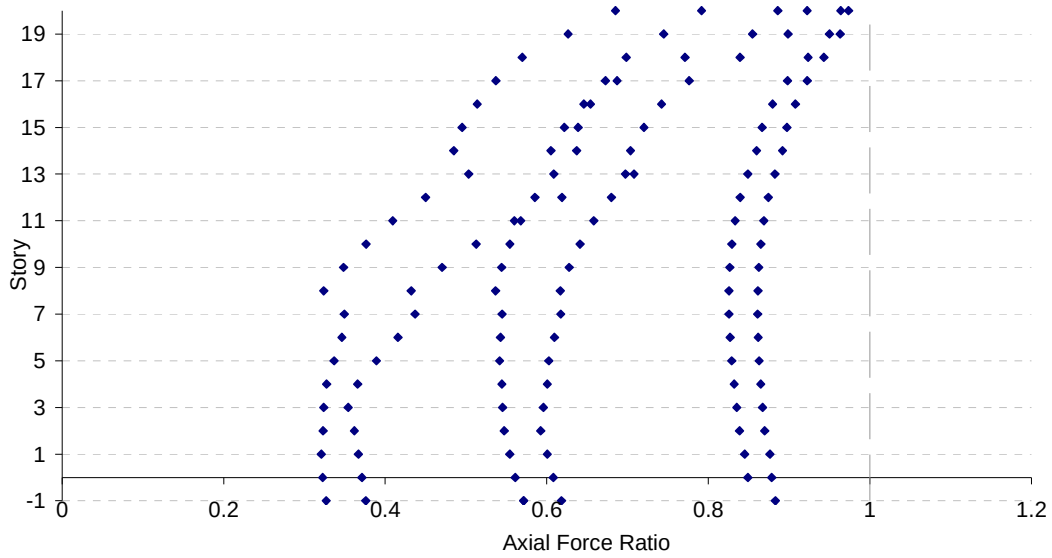

a)

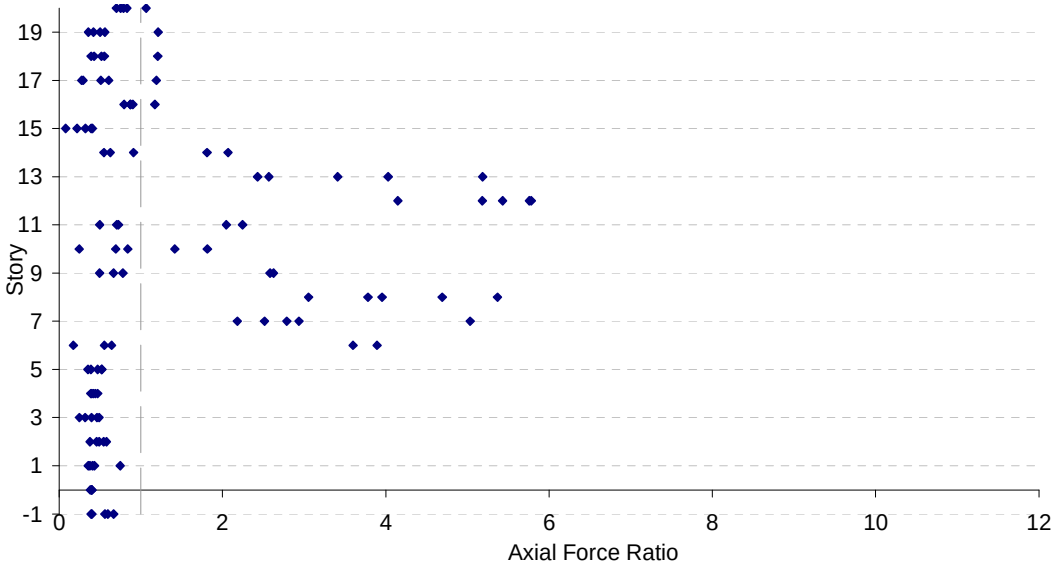

b)

Figure D.6 Axial Force Ratios for $BL\_20-9:13-A-500-0.05-500$ Subjected to El Centro: a) Columns, b) Beams

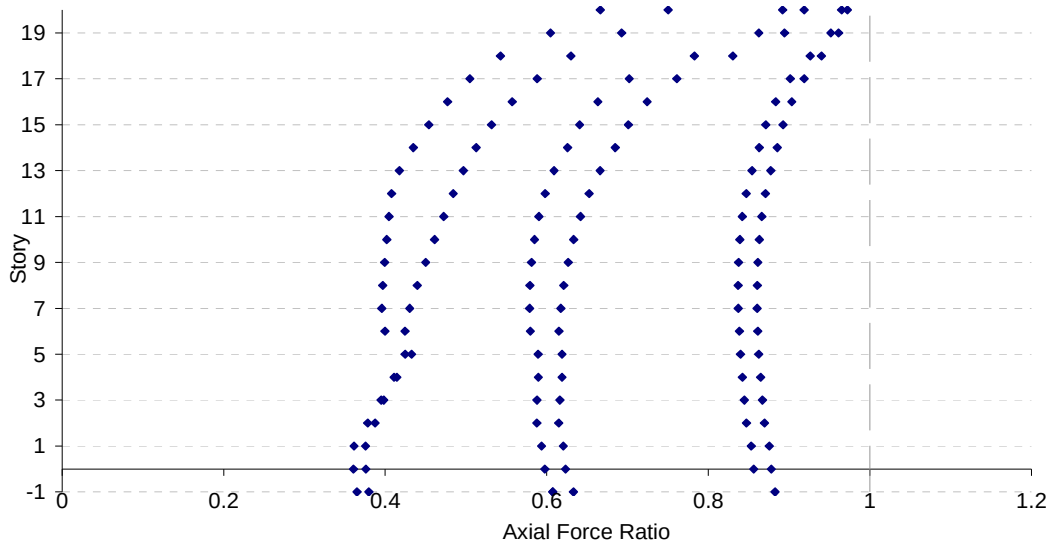

a)

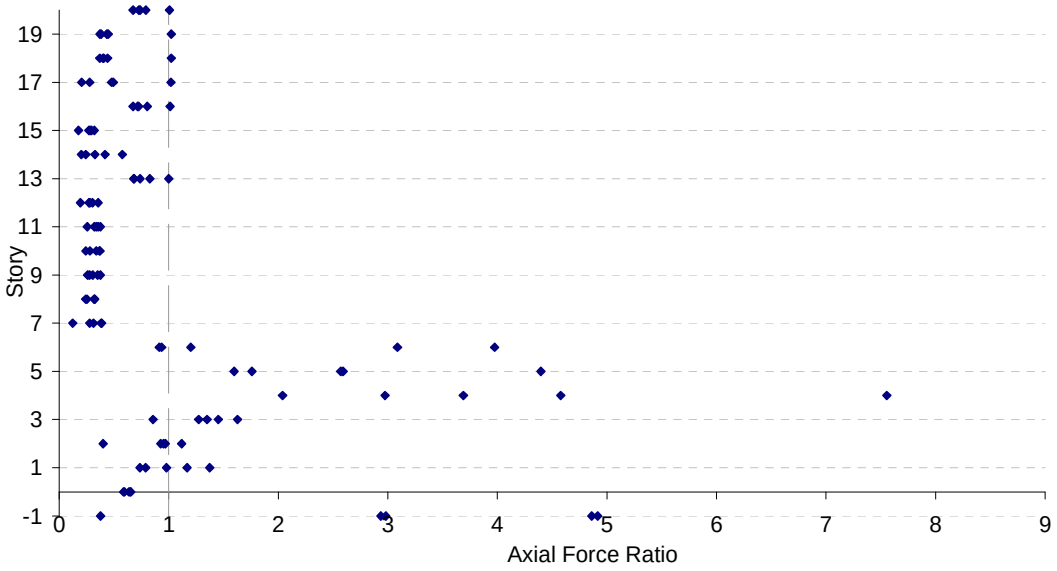

b)

Figure D.7 Axial Force Ratios for $BL\_20-0:5-A-800-0.1-2{,}300$ Subjected to El Centro: a) Columns, b) Beams

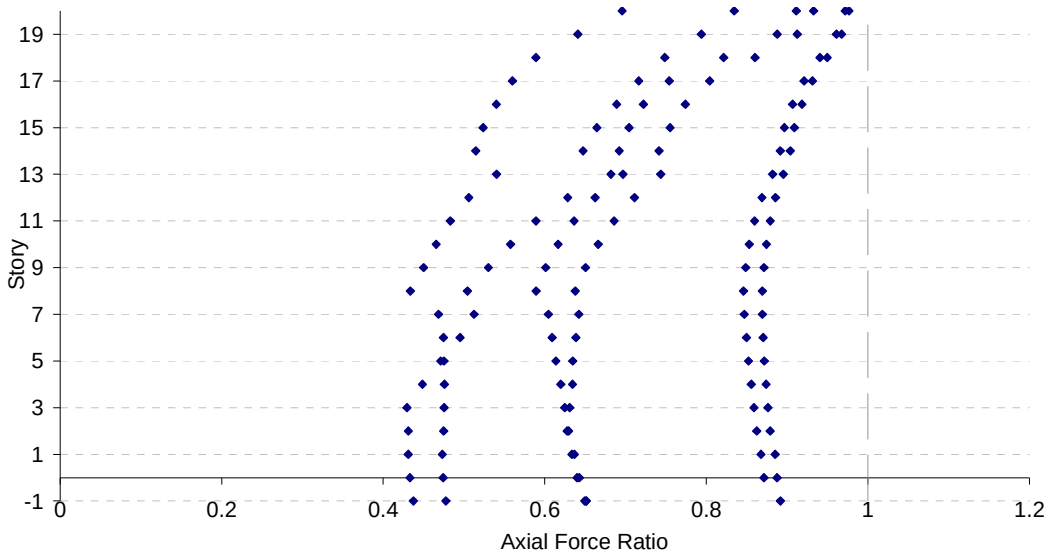

a)

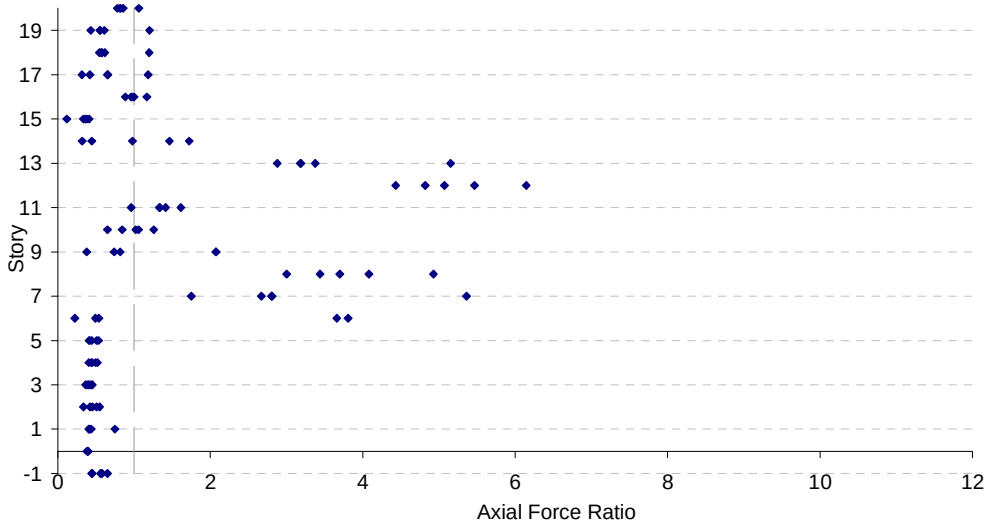

b)

Figure D.8 Axial Force Ratios for $BL\_20-9:13-A-800-0.1-2{,}300$ Subjected to El Centro: a) Columns, b) Beams

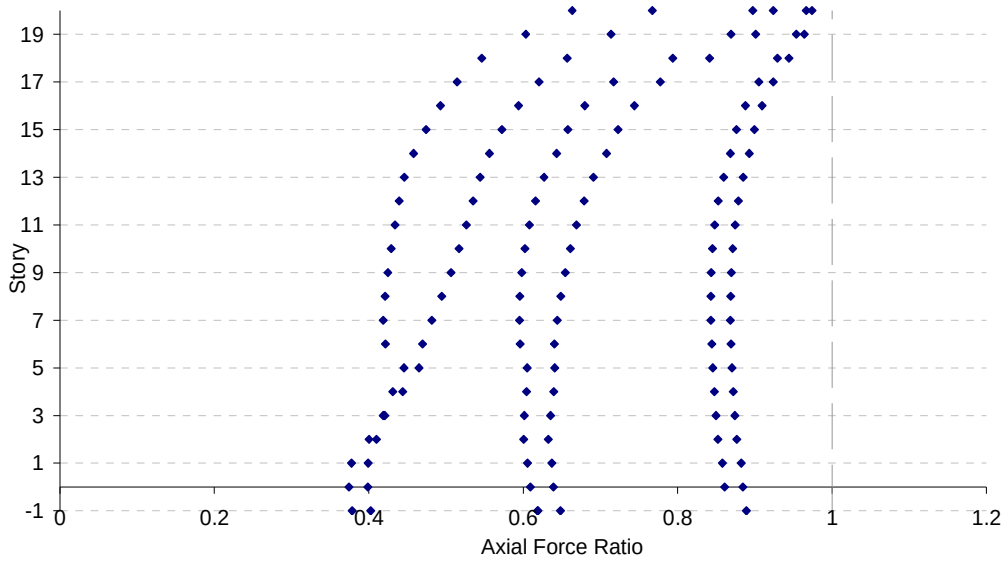

a)

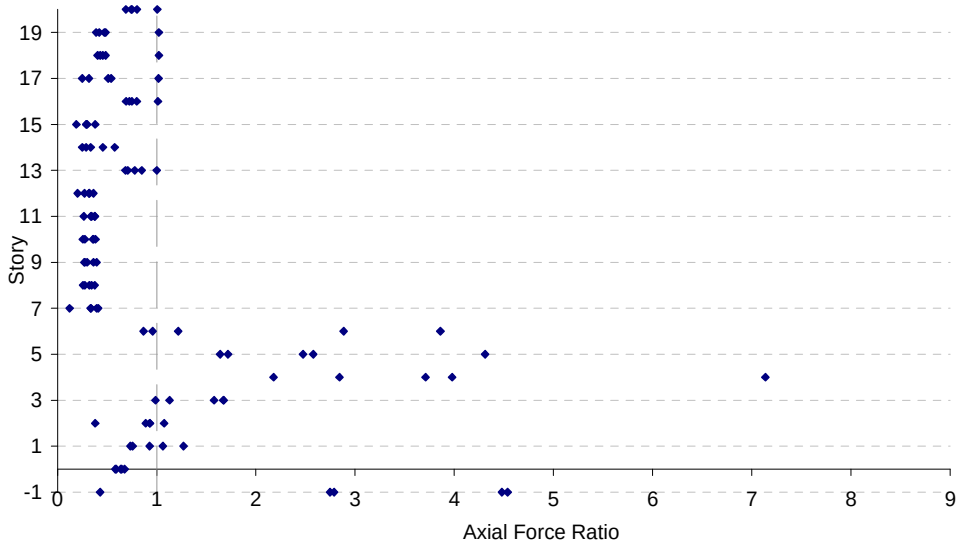

b)

Figure D.9 Axial Force Ratios for $BL\_20-0:5-A-2{,}500-0.05-2{,}000$ Subjected to El Centro: a) Columns, b) Beams

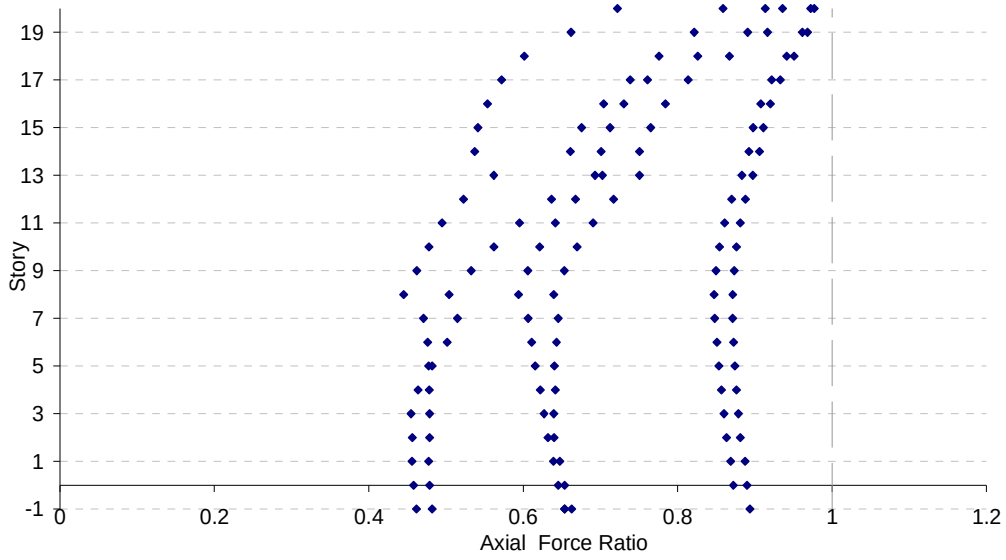

a)

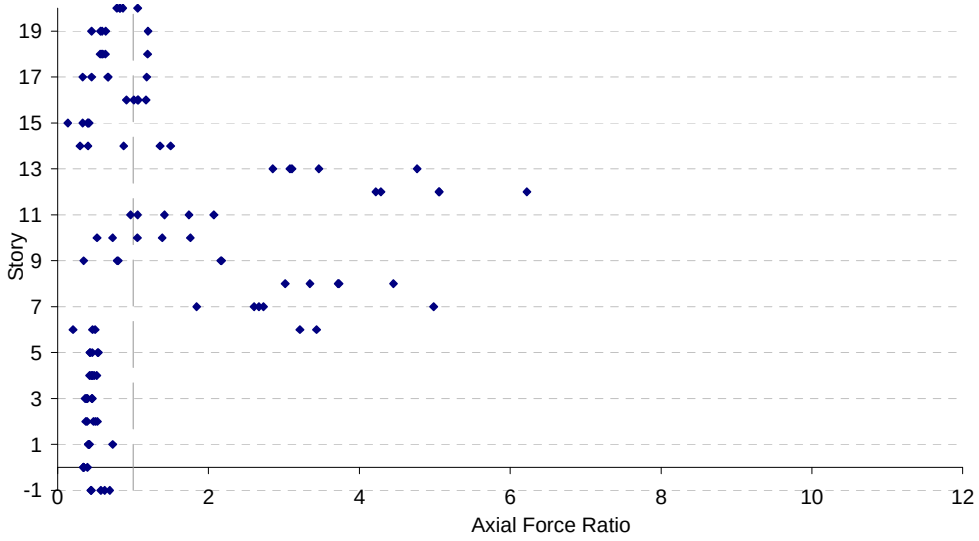

b)

Figure D.10 Axial Force Ratios for $BL\_20-9:13-A-2{,}500-0.05-2{,}000$ Subjected to El Centro: a) Columns, b) Beams

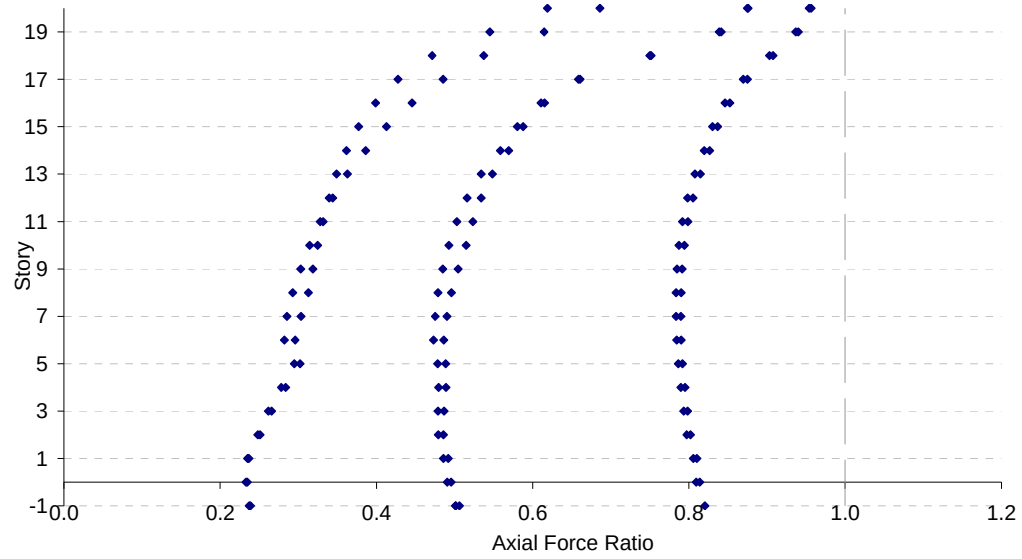

a)

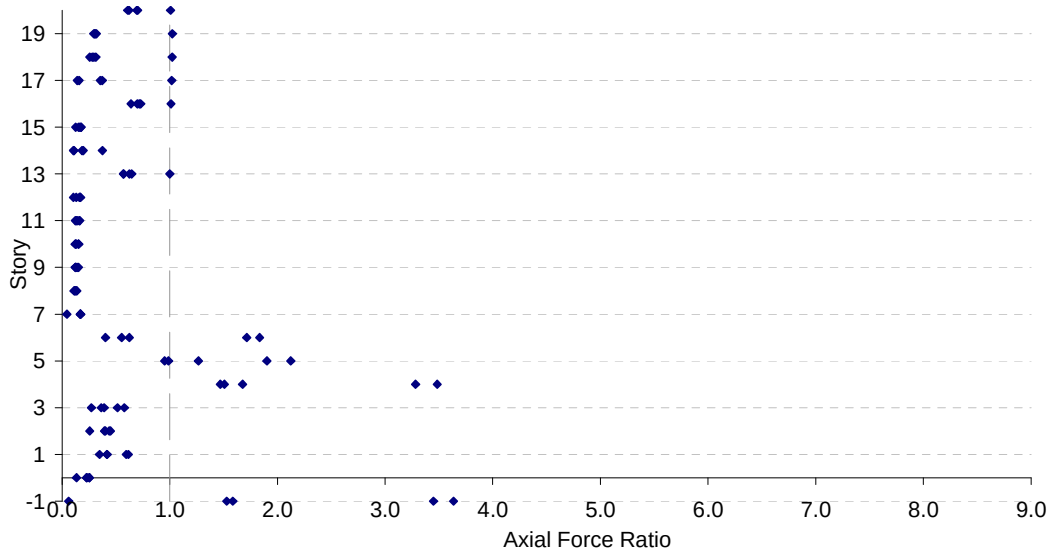

b)

Figure D.11 Axial Force Ratios for $BL\_20-0:5-A-236-0.01-1{,}000$ Subjected to Northridge: a) Columns, b) Beams

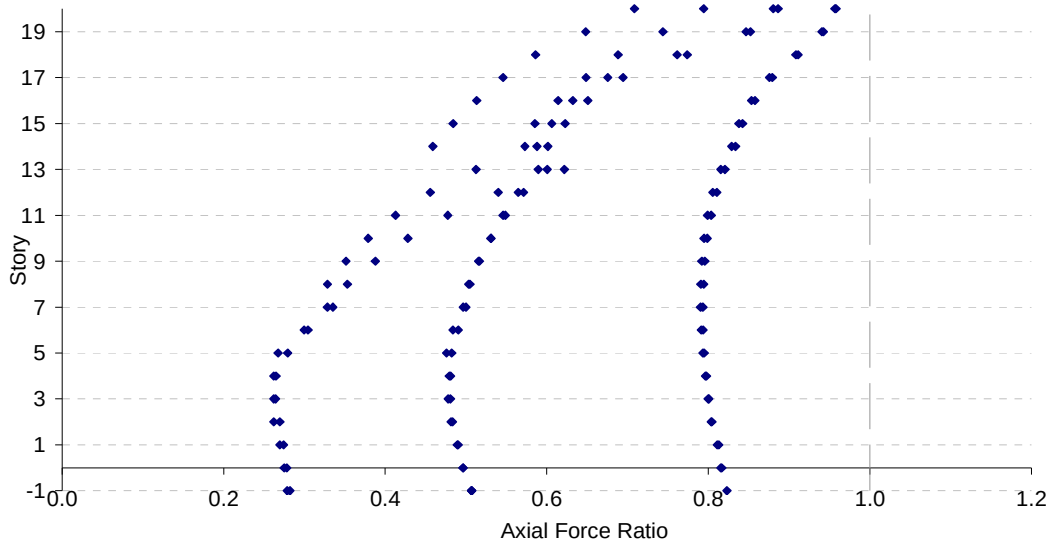

a)

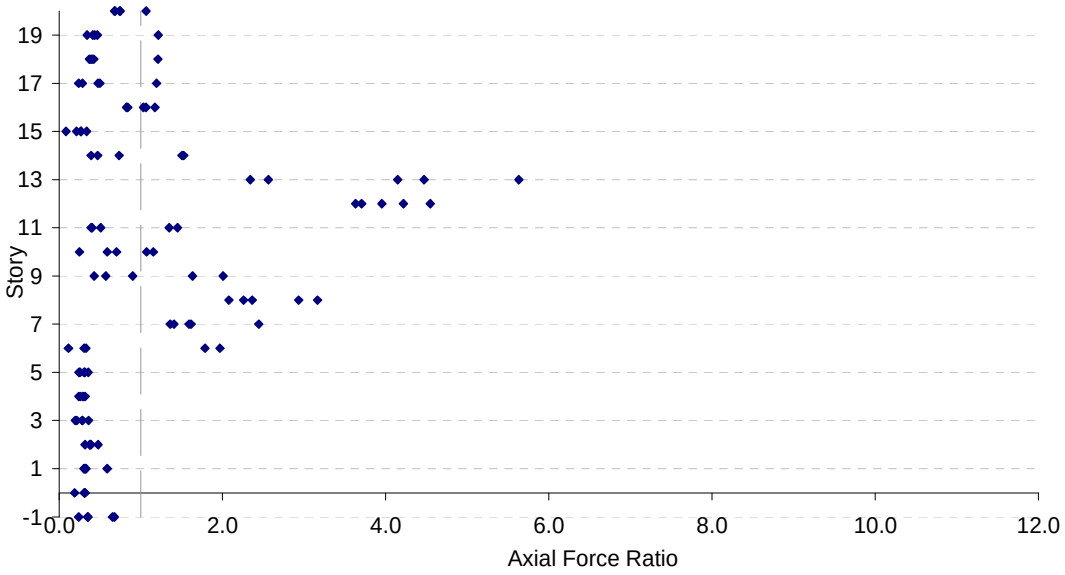

b)

Figure D.12 Axial Force Ratios for $BL\_20-9:13-A-236-0.01-1{,}000$ Subjected to Northridge: a) Columns, b) Beams

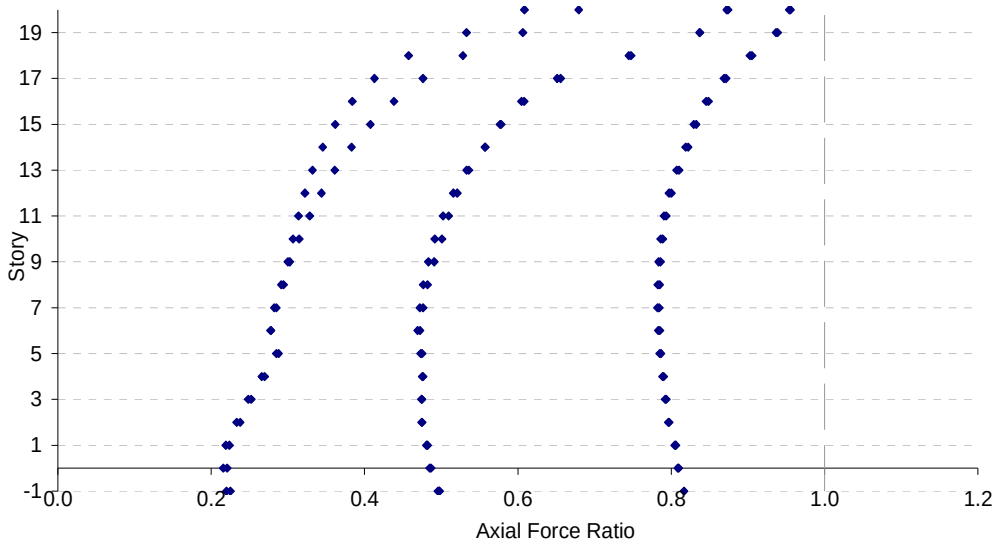

a)

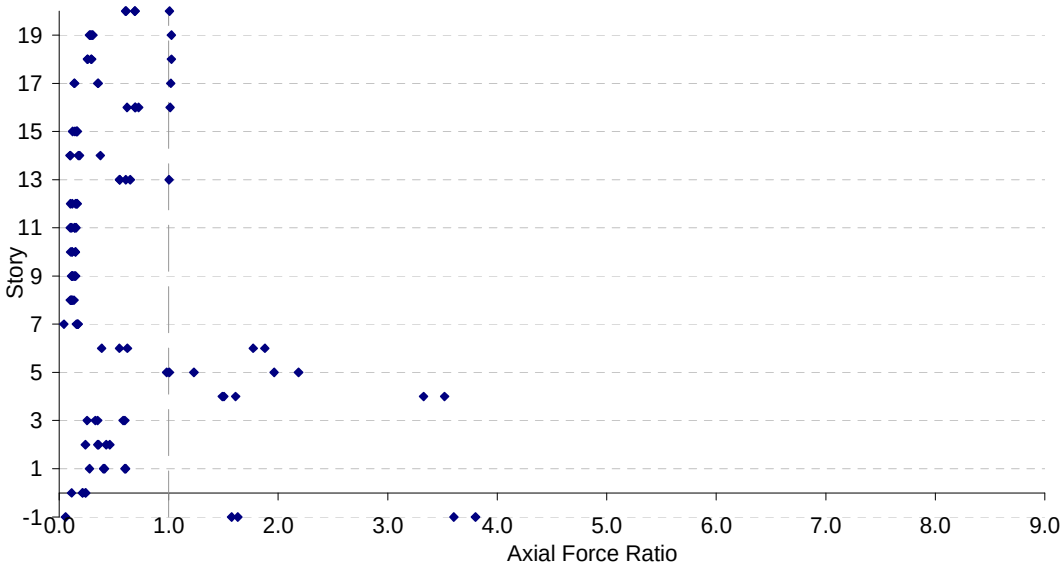

b)

Figure D.13 Axial Force Ratios for $BL\_20-0:5-A-100-0.1-120$ Subjected to Northridge: a) Columns, b) Beams

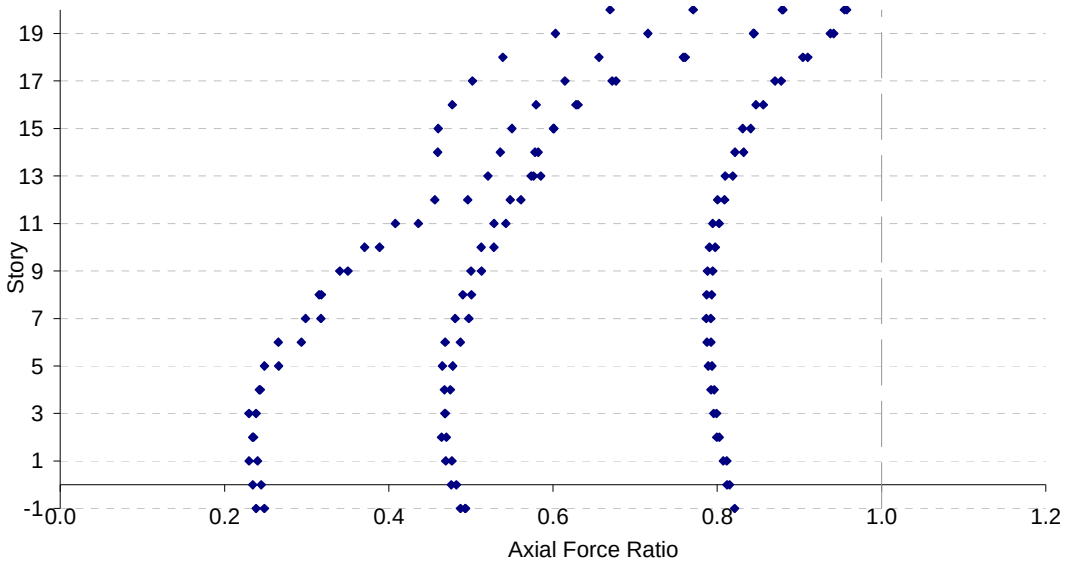

a)

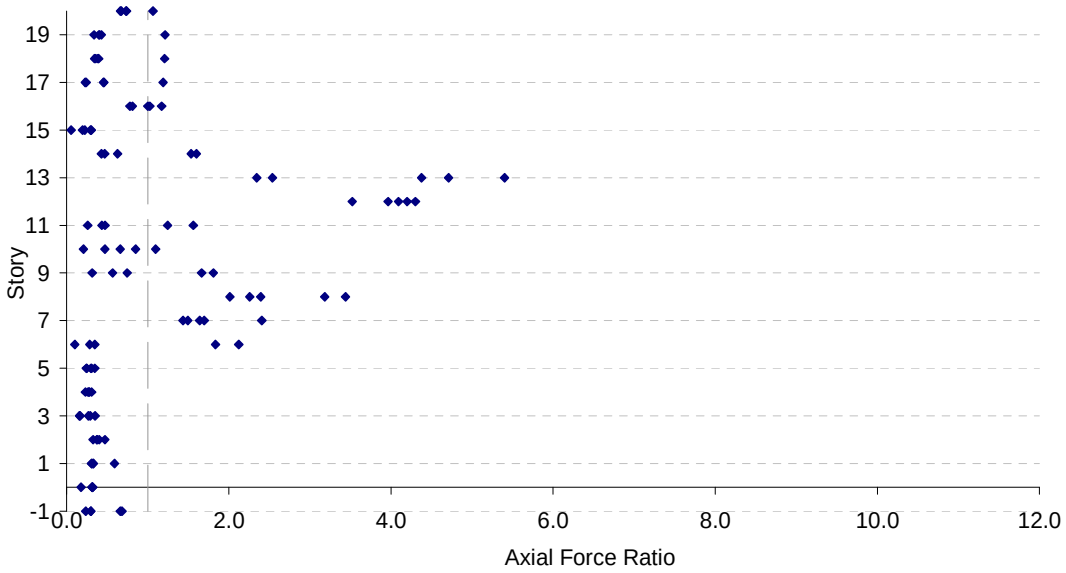

b)

Figure D.14 Axial Force Ratios for $BL\_20-9:13-A-100-0.1-120$ Subjected to Northridge: a) Columns, b) Beams

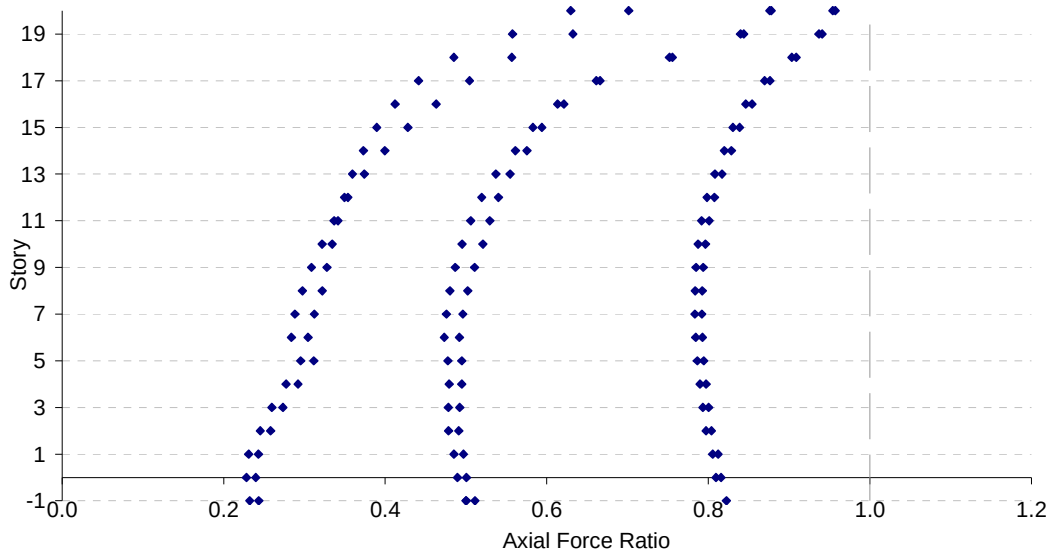

a)

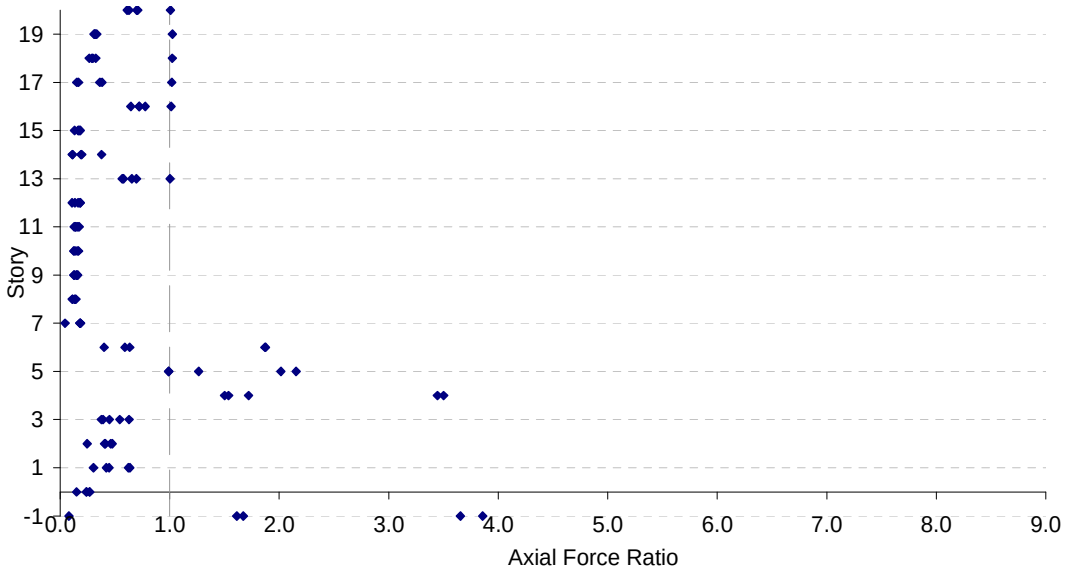

b)

Figure D.15 Axial Force Ratios for $BL\_20-0:5-A-500-0.05-500$ Subjected to Northridge: a) Columns, b) Beams

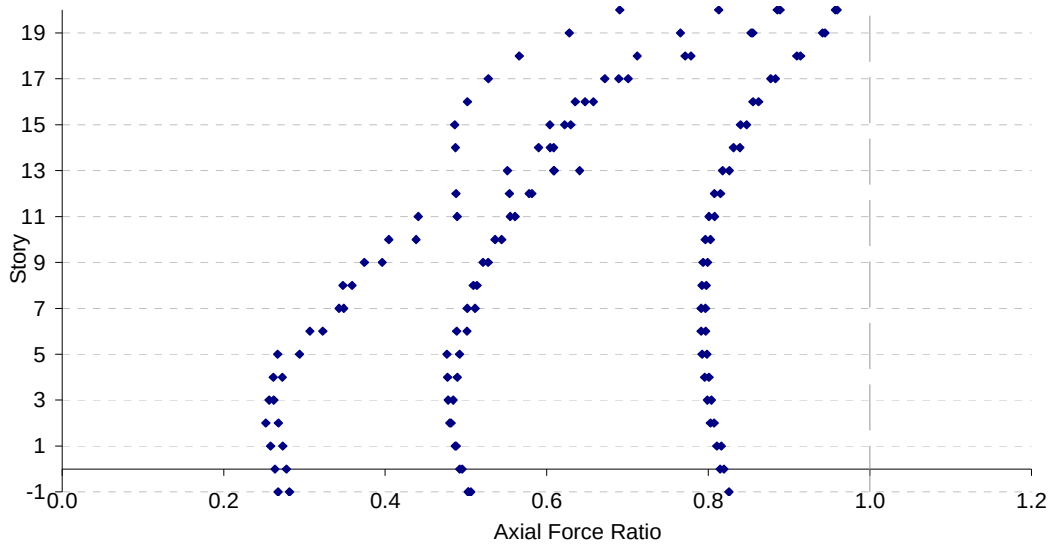

a)

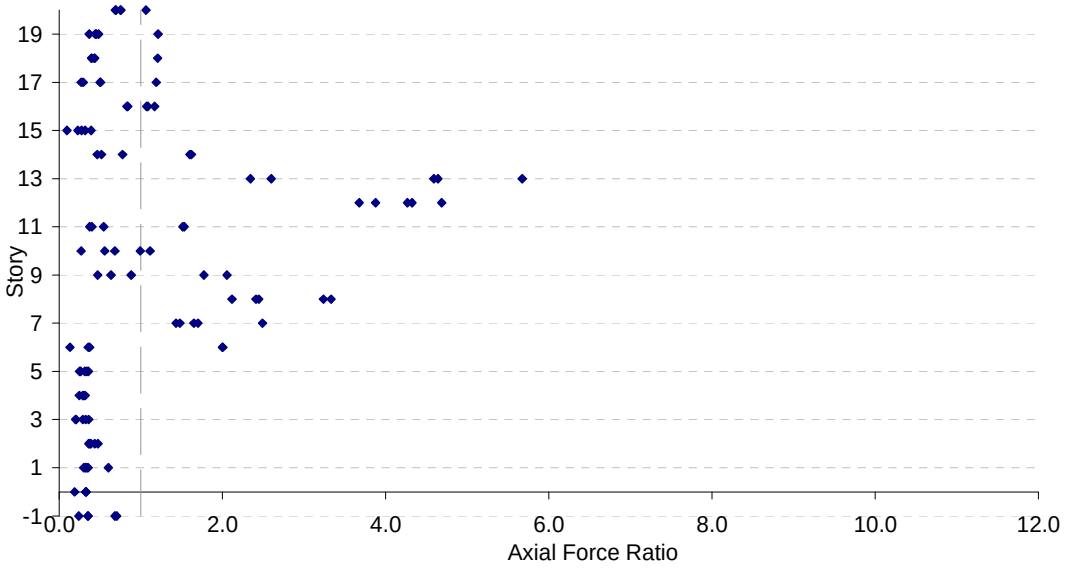

b)

Figure D.16 Axial Force Ratios for BLG $BL\_20-9:13-A-500-0.05-500$ Subjected to Northridge: a) Columns, b) Beams

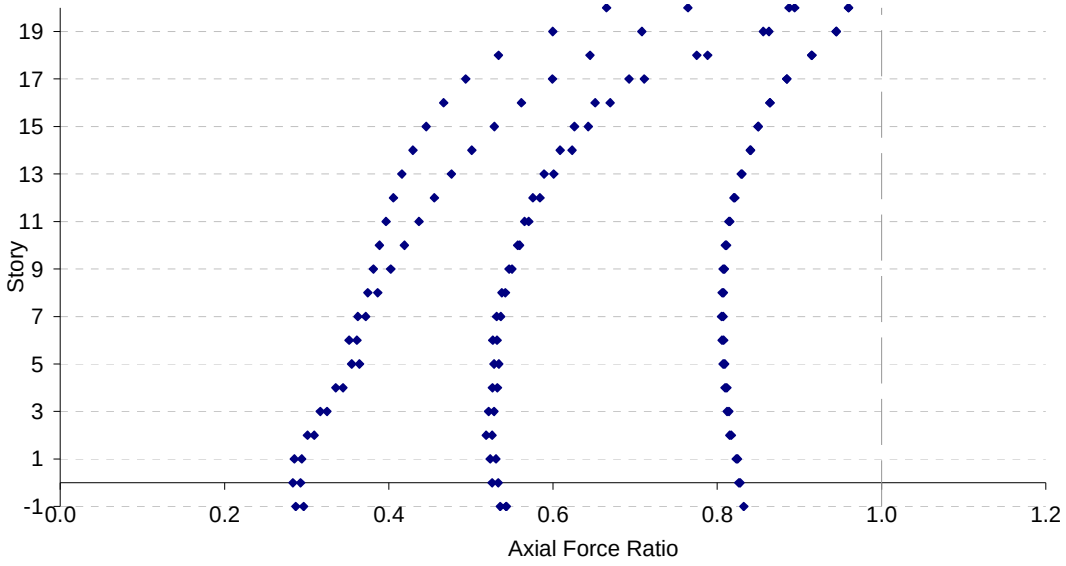

a)

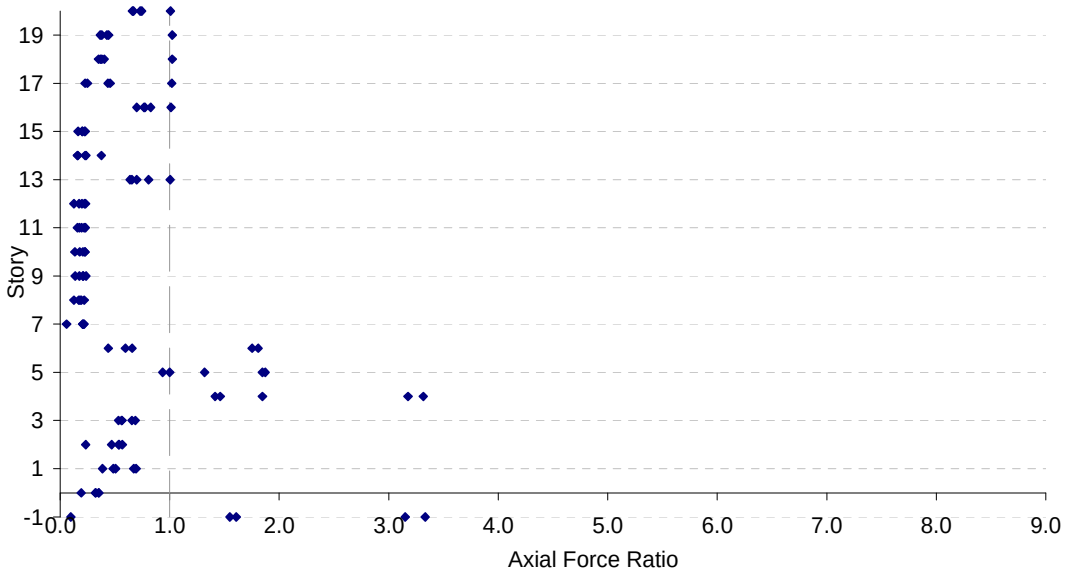

b)

Figure D.17 Axial Force Ratios for $BL\_20-0:5-A-800-0.1-2{,}300$ Subjected to Northridge: a) Columns, b) Beams

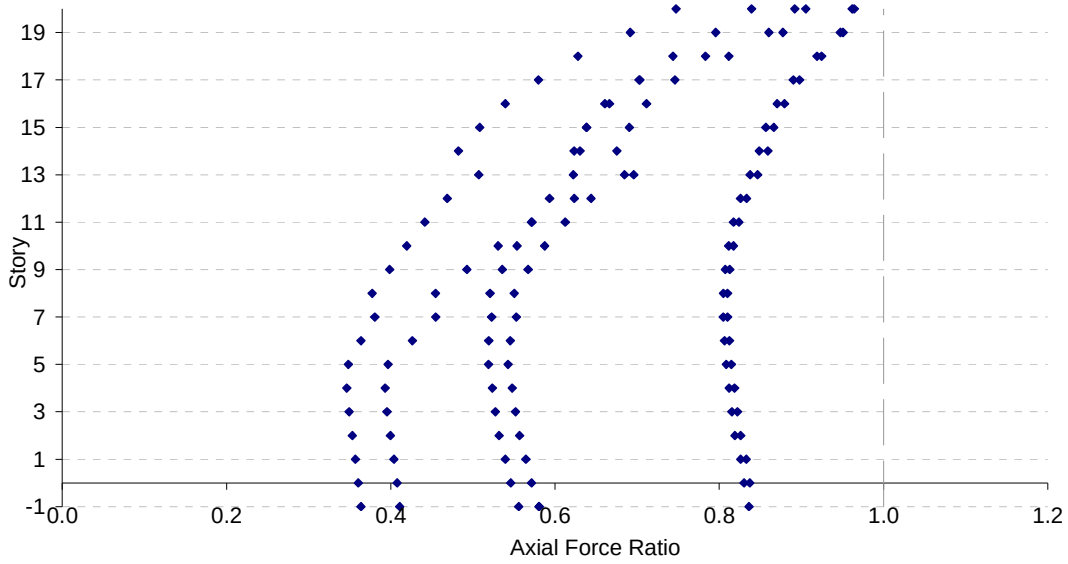

a)

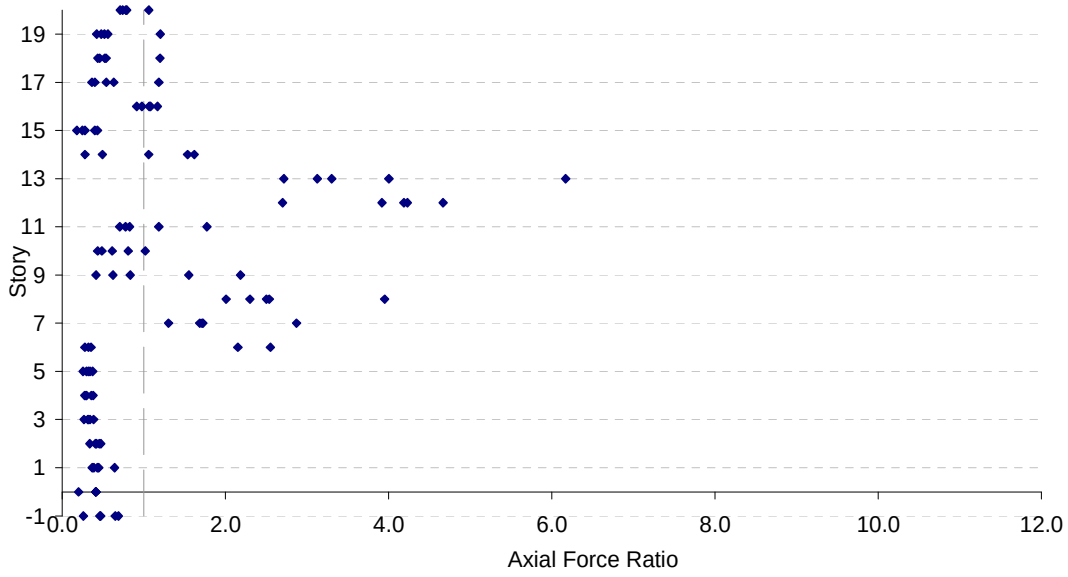

b)

Figure D.18 Axial Force Ratios for $BL\_20-9:13-A-800-0.1-2{,}300$ Subjected to Northridge: a) Columns, b) Beams

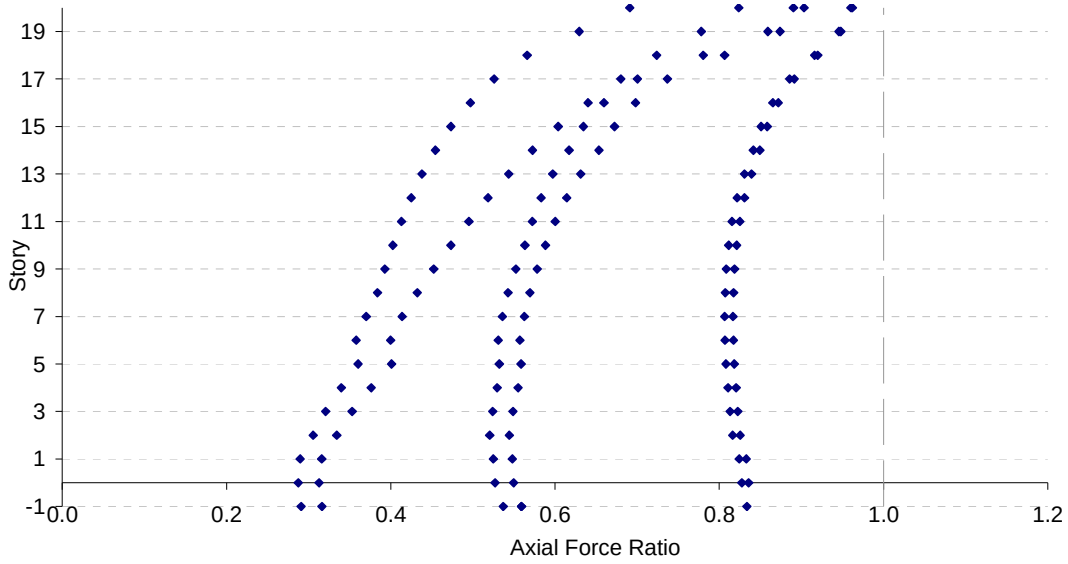

a)

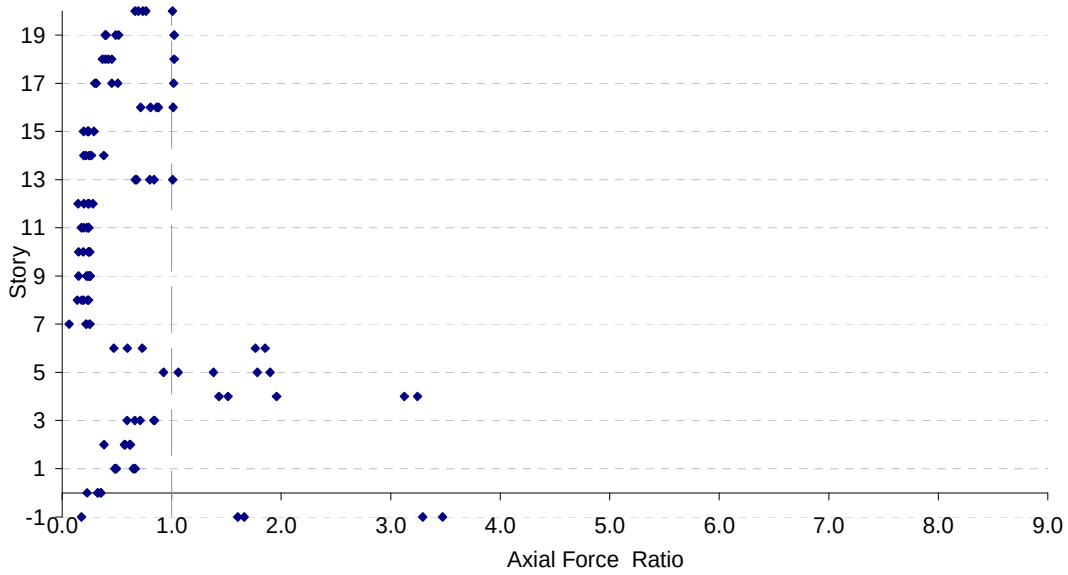

b)

Figure D.19 Axial Force Ratios for $BL\_20-0:5-A-2{,}500-0.05-2{,}000$ Subjected to Northridge: a) Columns, b) Beams

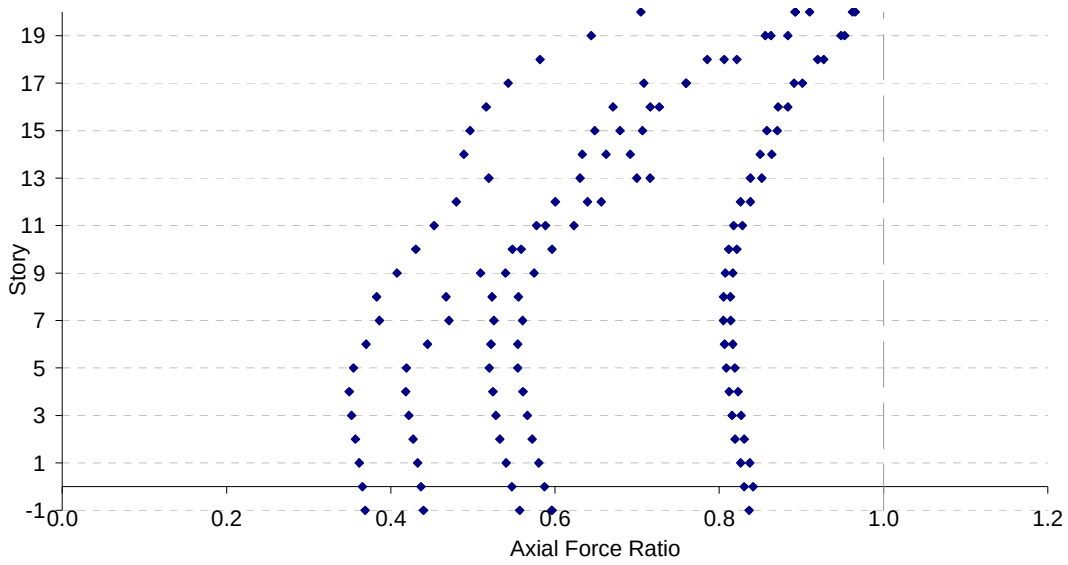

a)

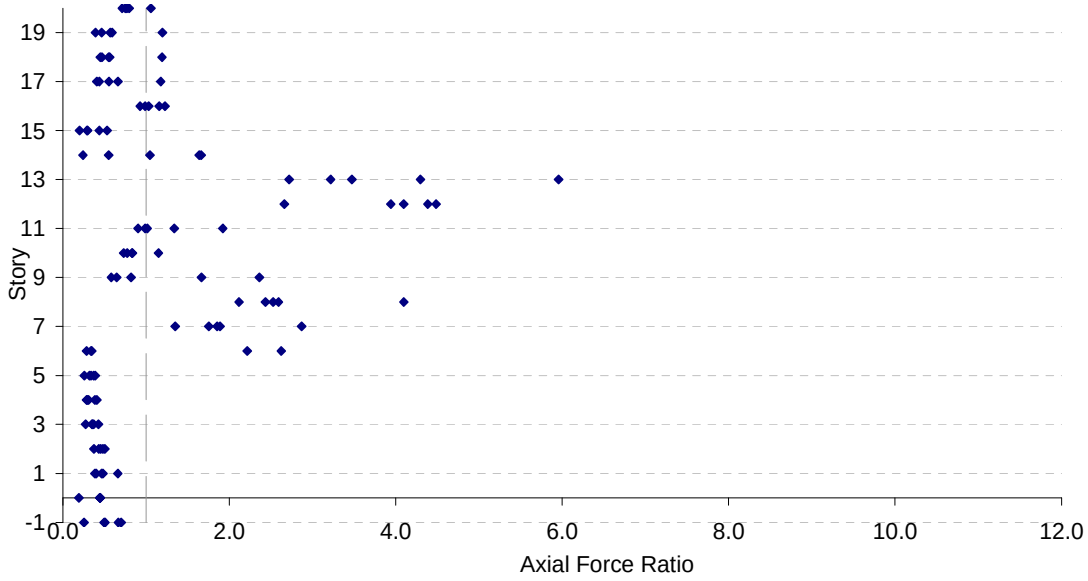

b)

Figure D.20 Axial Force Ratios for $BL\_20-9:13-A-2{,}500-0.05-2{,}000$ Subjected to Northridge: a) Columns, b) Beams

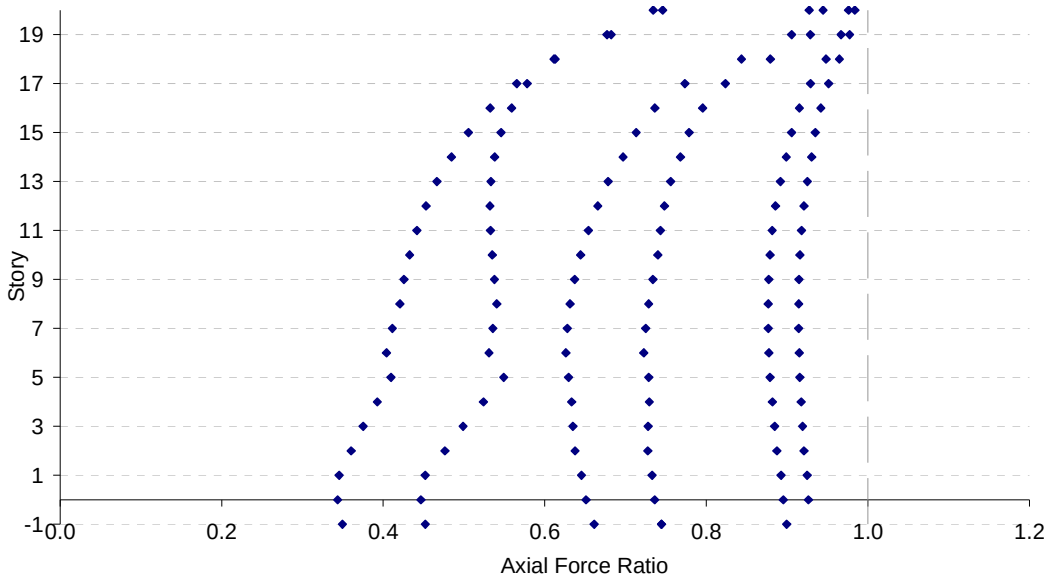

a)

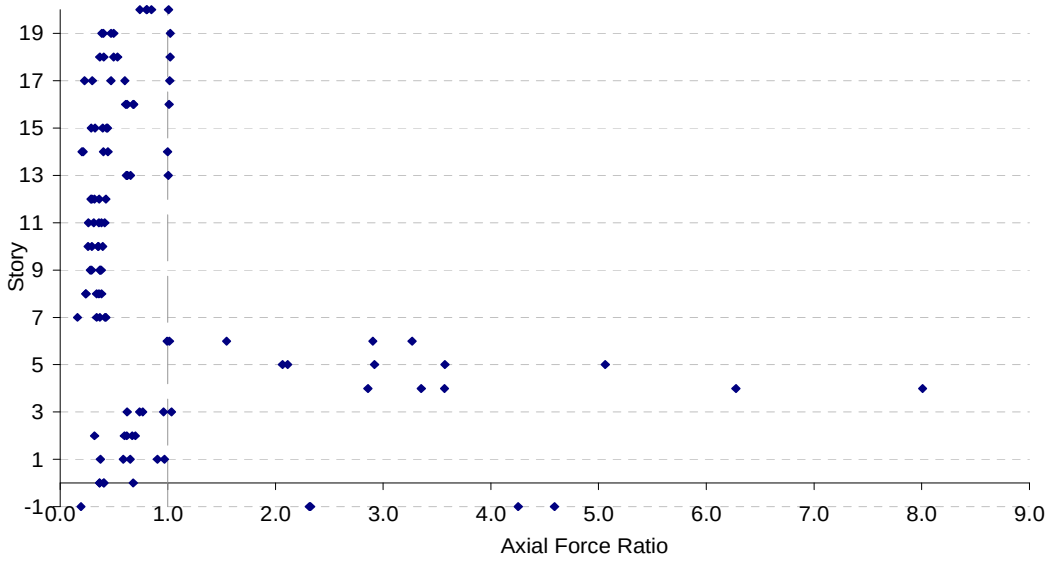

b)

Figure D.21 Axial Force Ratios for $BL\_20-0:5-A-236-0.01-1{,}000$ Subjected to Parkfield: a) Columns, b) Beams

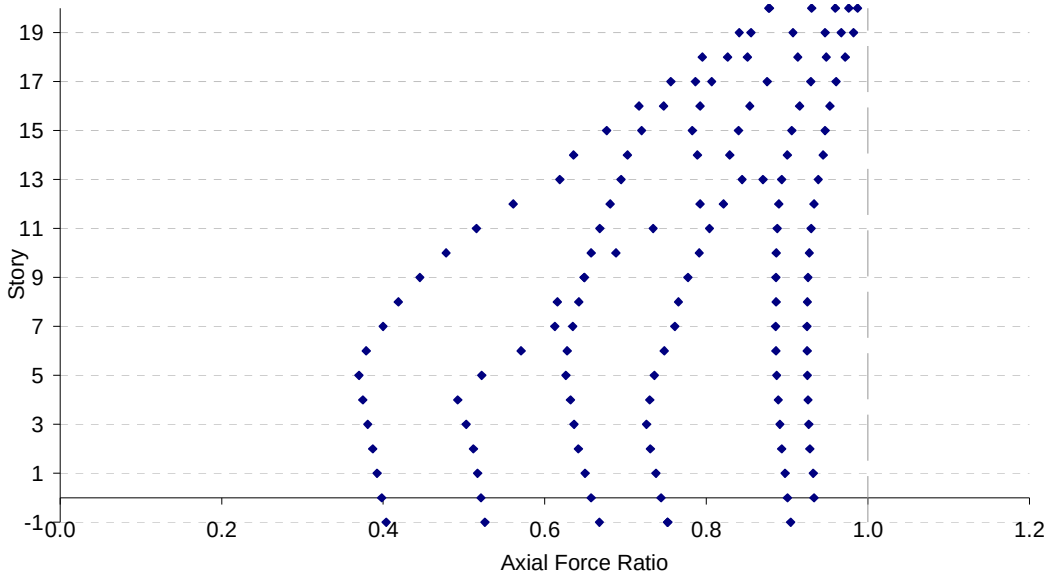

a)

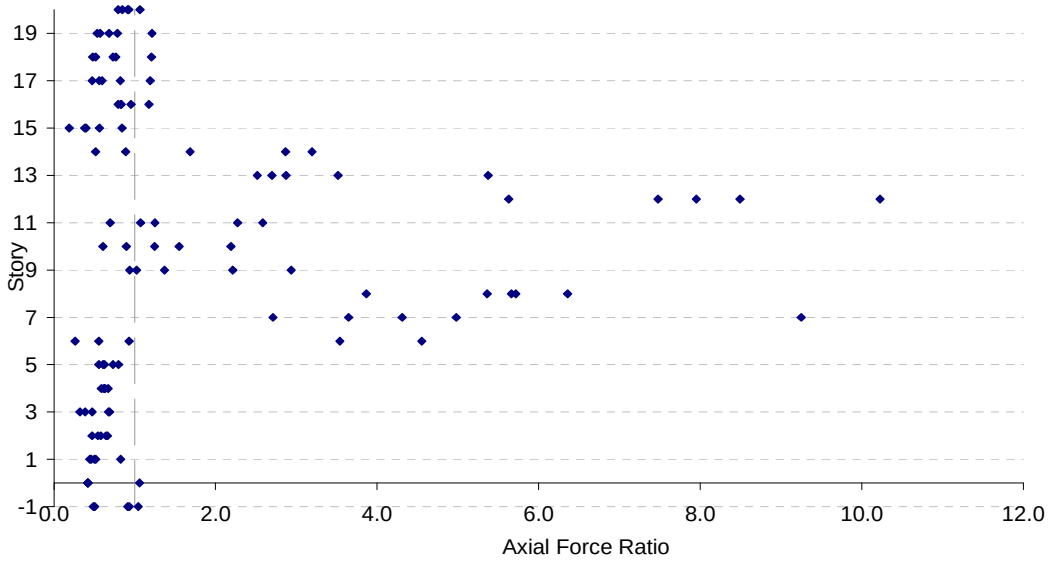

b)

Figure D.22 Axial Force Ratios for $BL\_20-9:13-A-236-0.01-1{,}000$ Subjected to Parkfield: a) Columns, b) Beams

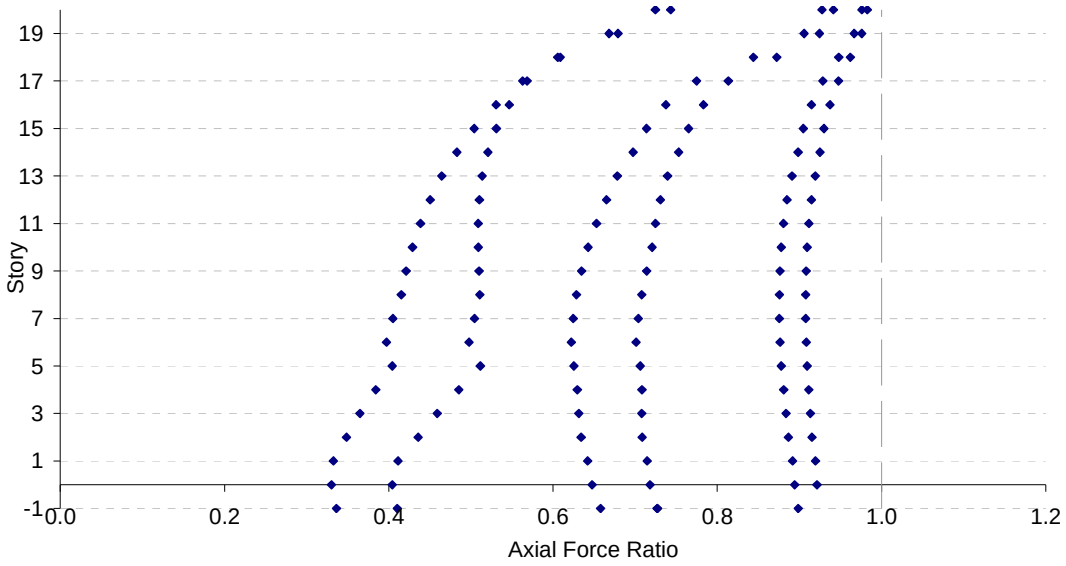

a)

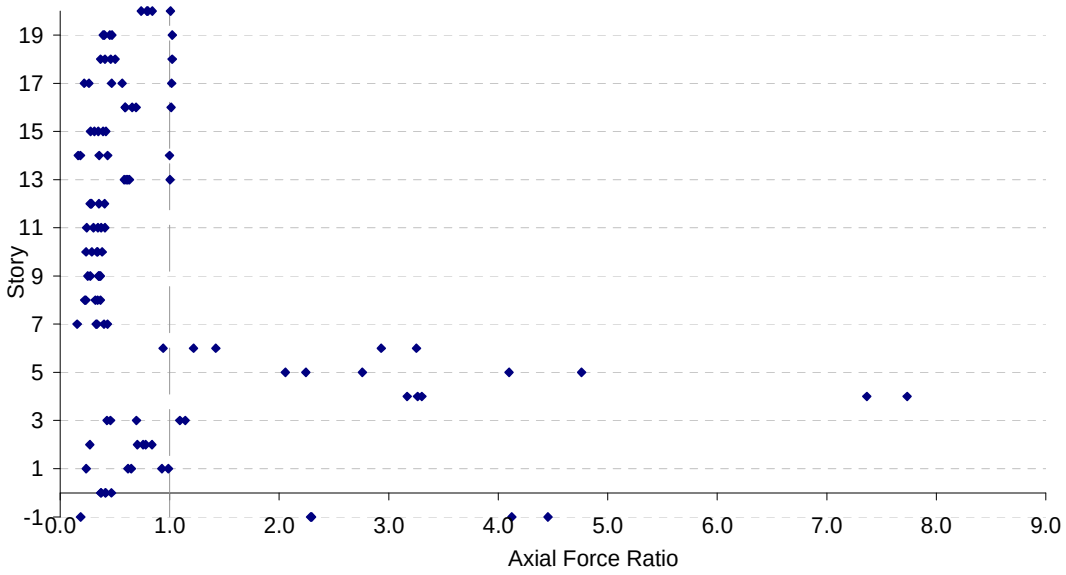

b)

Figure D.23 Axial Force Ratios for $BL\_20-0:5-A-100-0.1-120$ Subjected to Parkfield: a) Columns, b) Beams

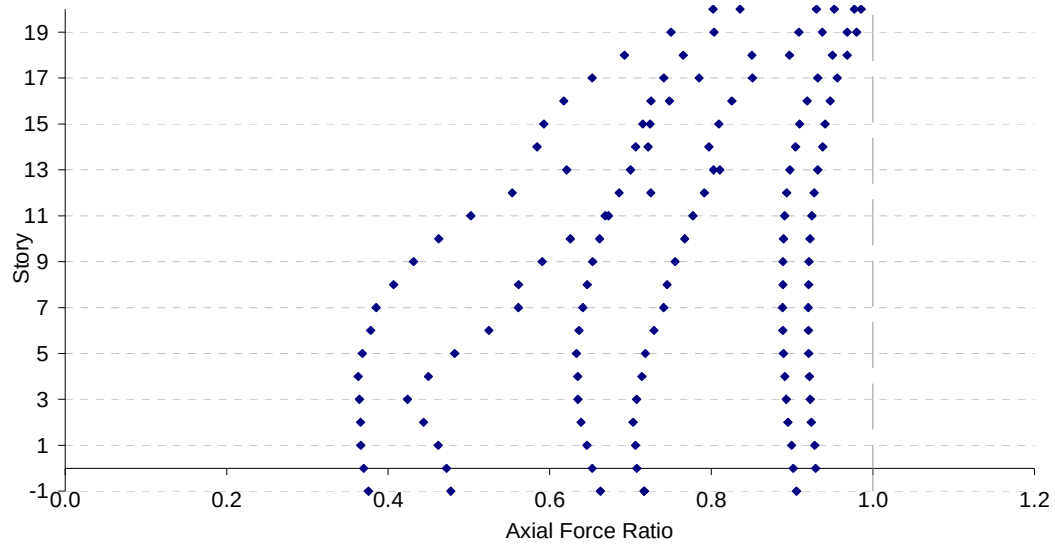

a)

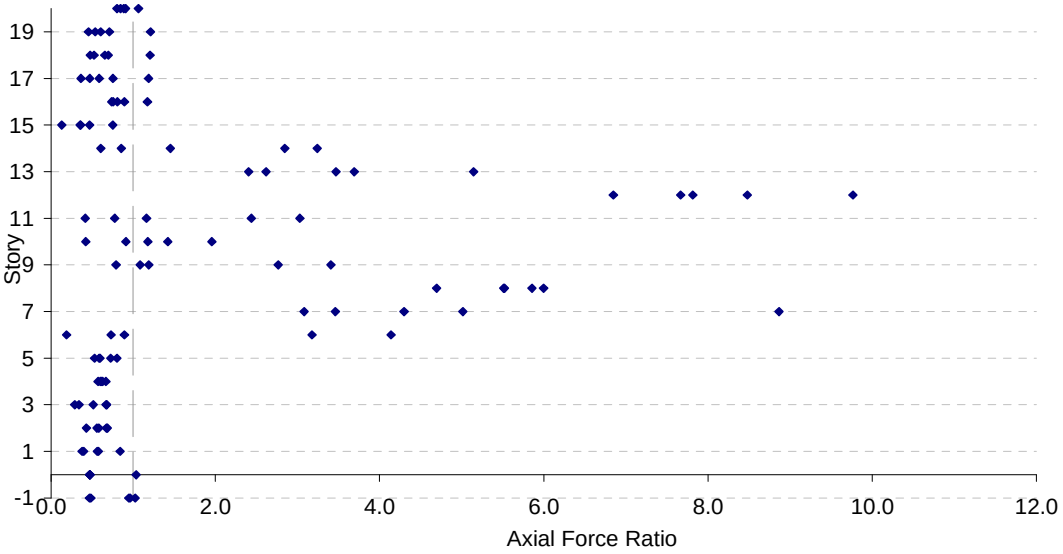

b)

Figure D.24 Axial Force Ratios for $BL\_20-9:13-A-100-0.1-120$ Subjected to Parkfield: a) Columns, b) Beams

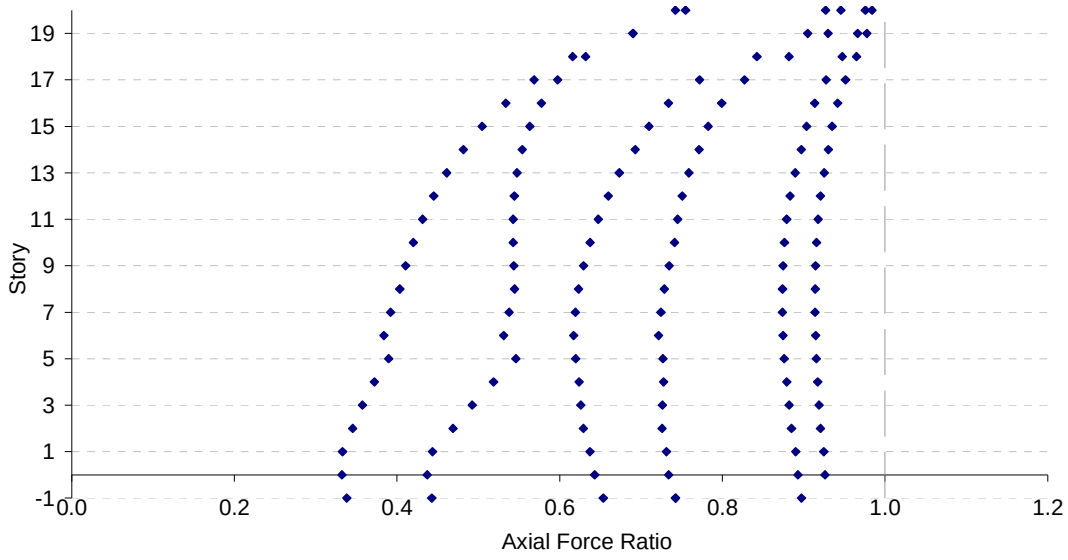

a)

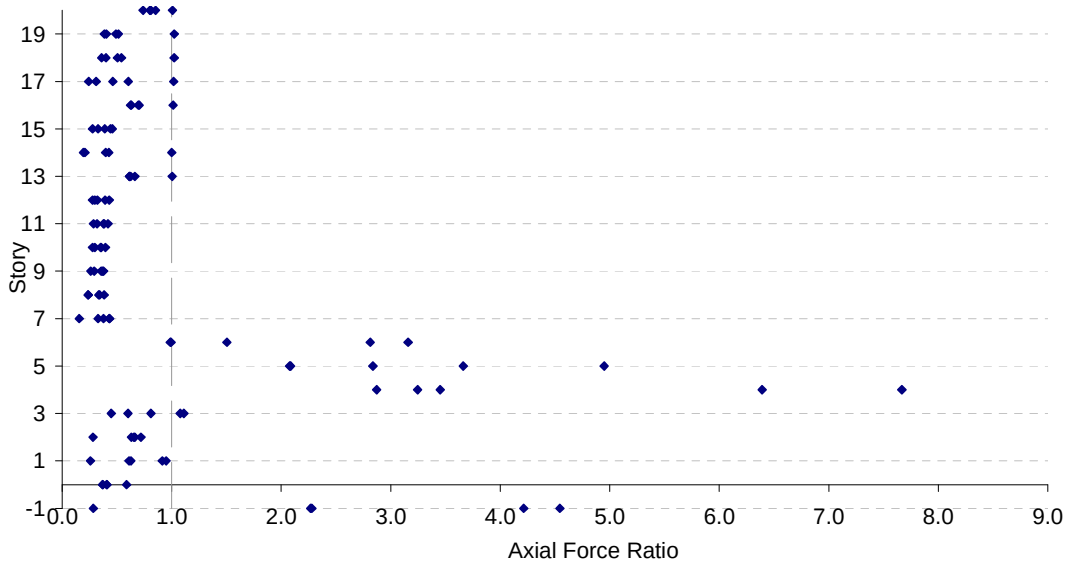

b)

Figure D.25 Axial Force Ratios for $BL\_20-0:5-A-500-0.05-500$ Subjected to Parkfield: a) Columns, b) Beams

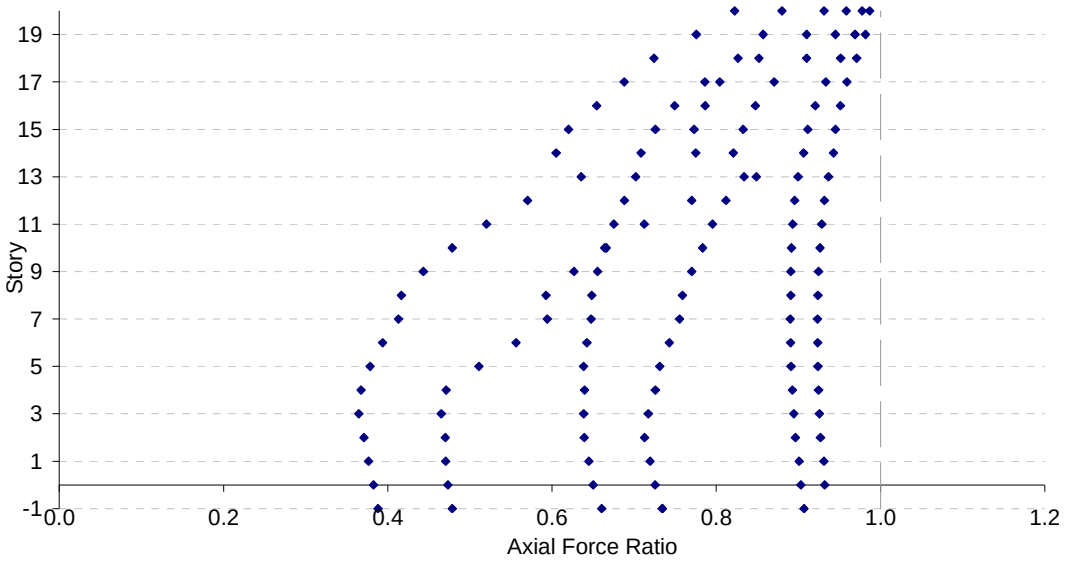

a)

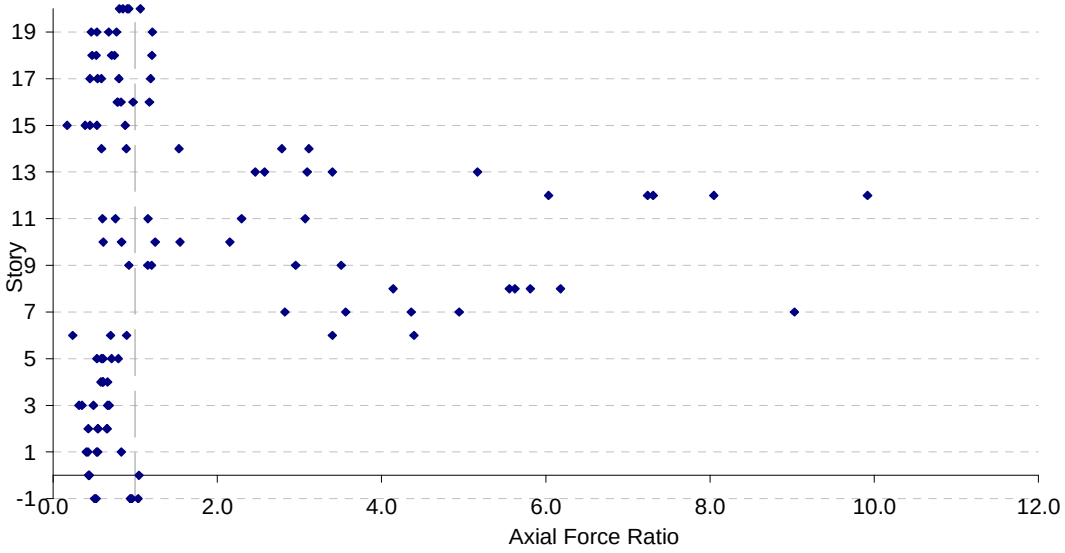

b)

Figure D.26 Axial Force Ratios for $BL\_20-9:13-A-500-0.05-500$ Subjected to Parkfield: a) Columns, b) Beams

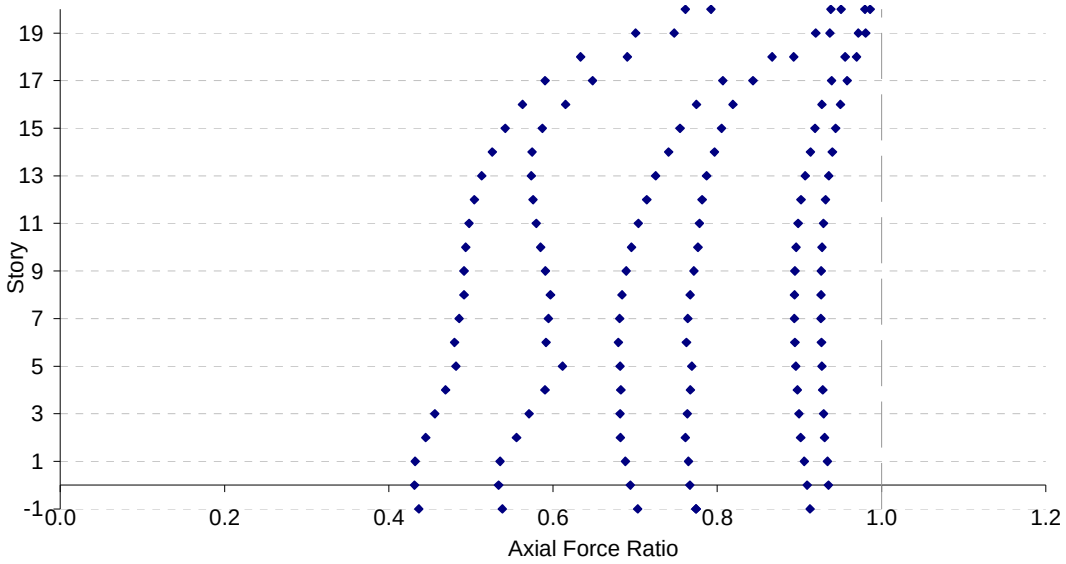

a)

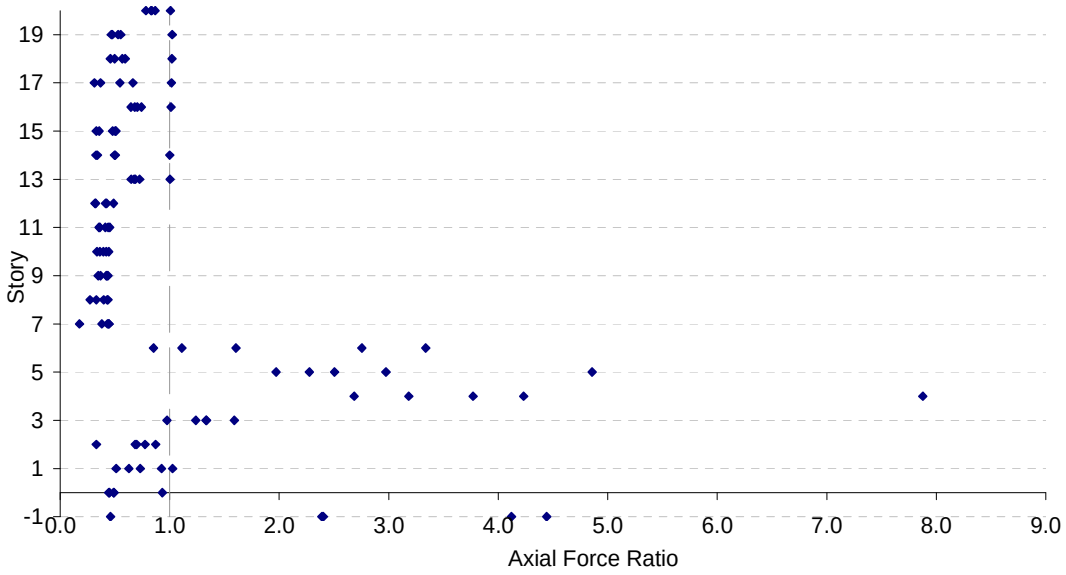

b)

Figure D.27 Axial Force Ratios for $BL\_20-0:5-A-800-0.1-2{,}300$ Subjected to Parkfield: a) Columns, b) Beams

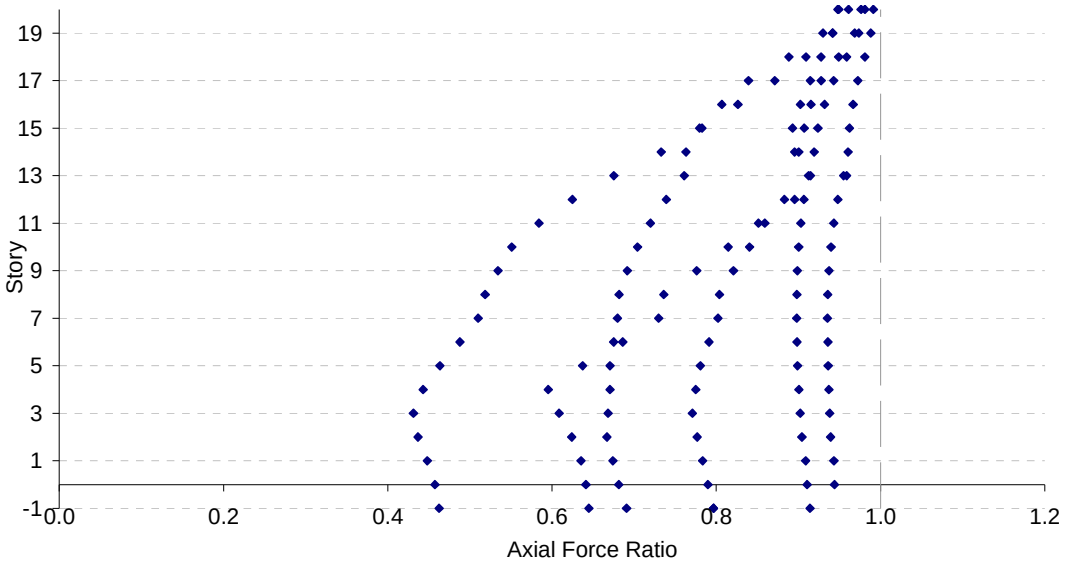

a)

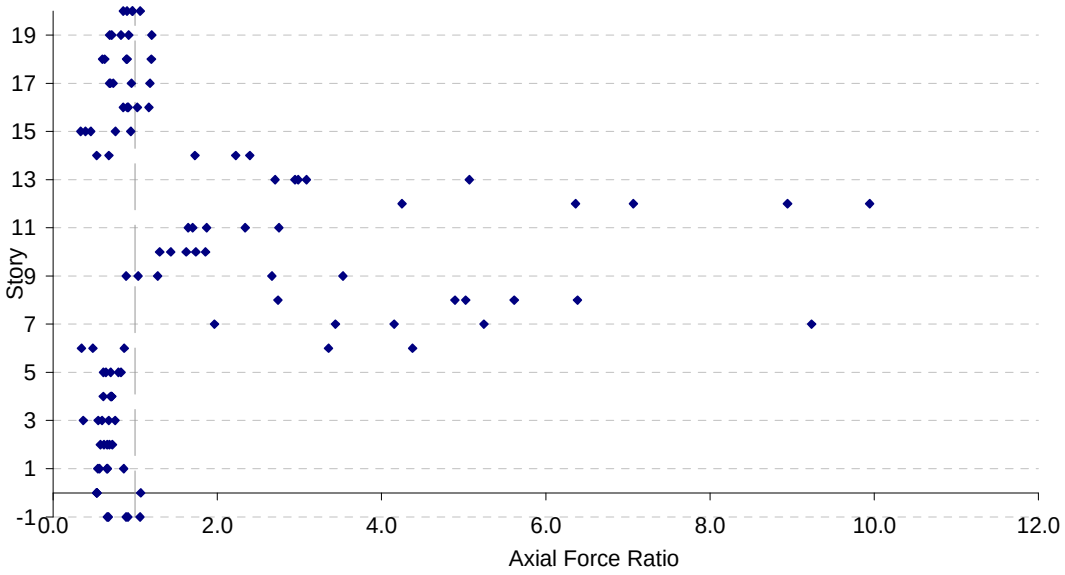

b)

Figure D.28 Axial Force Ratios for $BL\_20-9:13-A-800-0.1-2{,}300$ Subjected to Parkfield: a) Columns, b) Beams

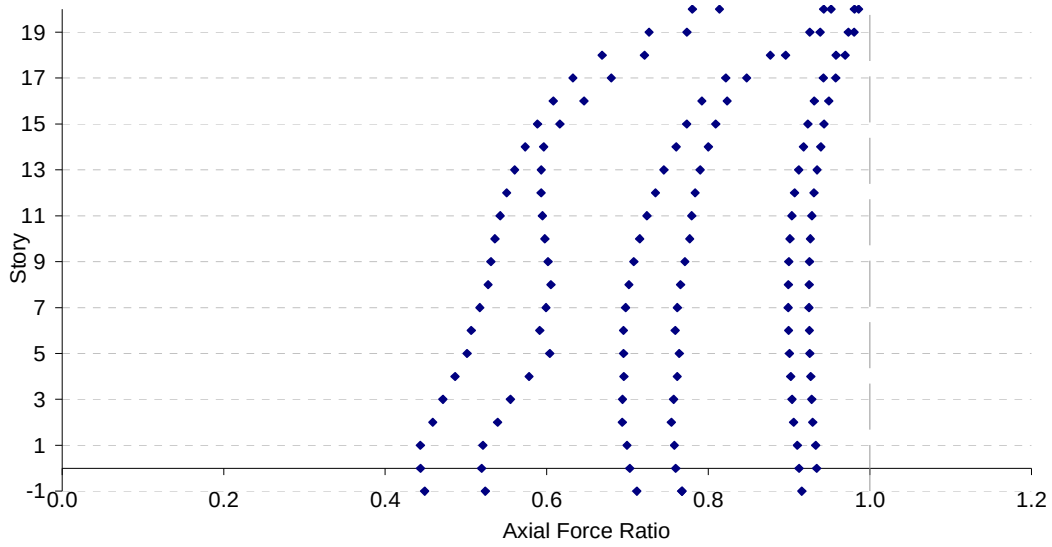

a)

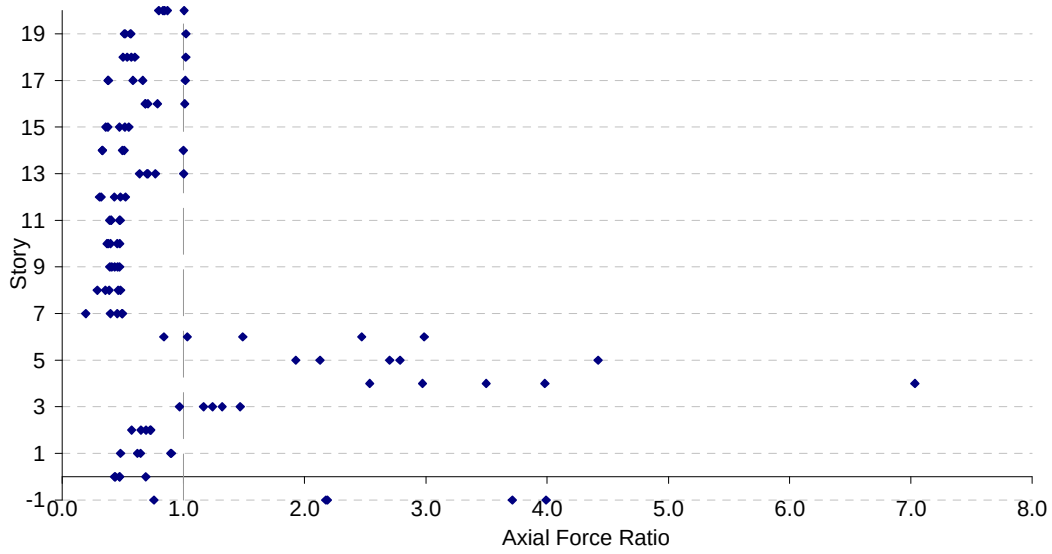

b)

Figure D.29 Axial Force Ratios for $BL\_20-0:5-A-2{,}500-0.05-2{,}000$ Subjected to Parkfield: a) Columns, b) Beams

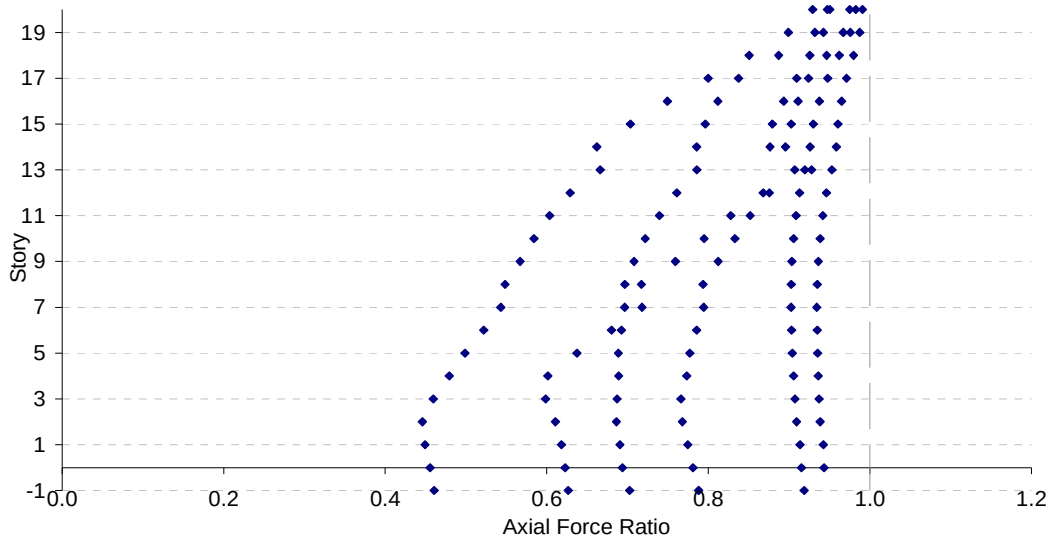

a)

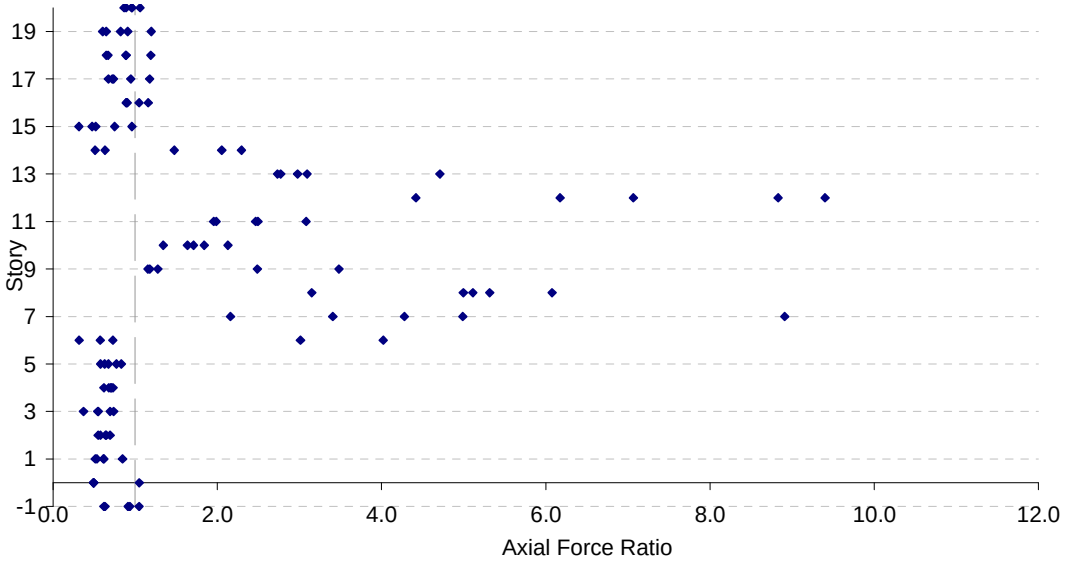

b)

Figure D.30 Axial Force Ratios for $BL\_20-9:13-A-2{,}500-0.05-2{,}000$ Subjected to Parkfield: a) Columns, b) Beams

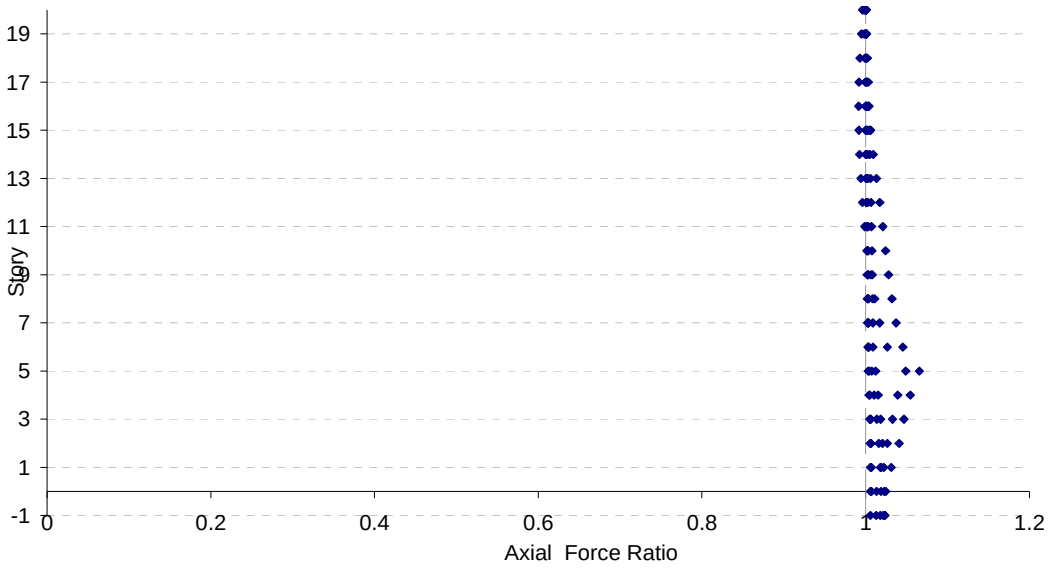

a)

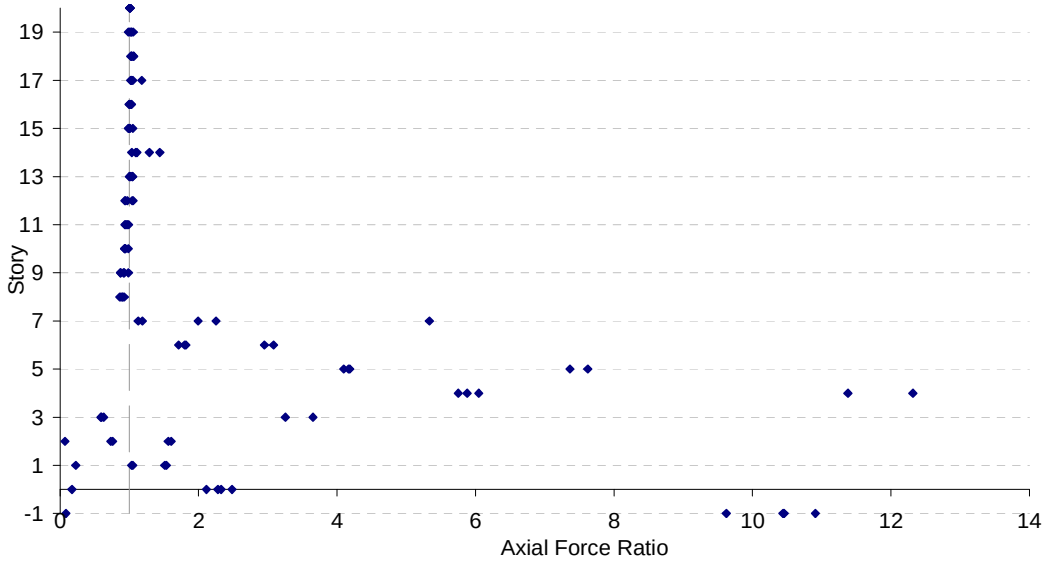

b)

Figure D.31 Axial Force Ratios for $BL\_20-0:5-A-236-0.01-1{,}000$ Subjected to Afyon Bay: a) Columns, b) Beams

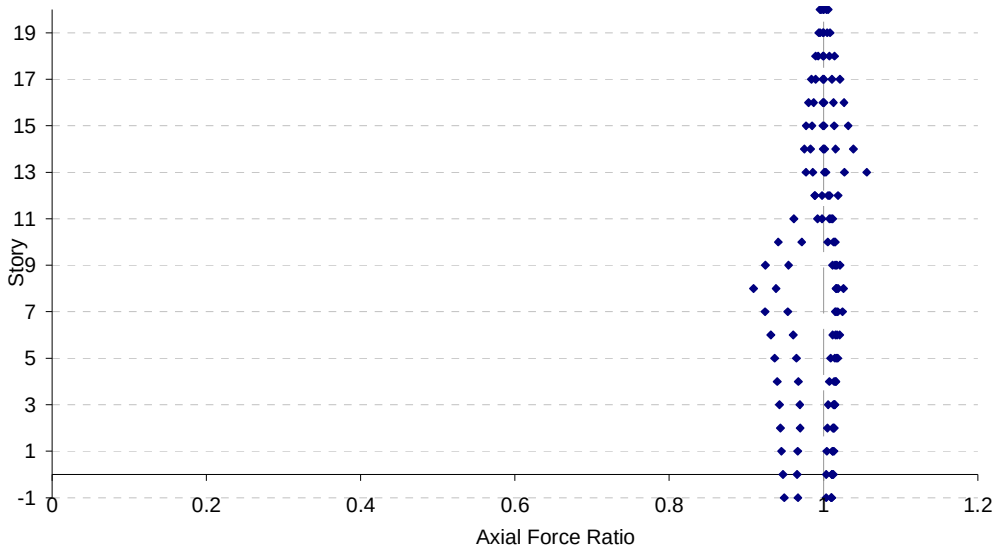

a)

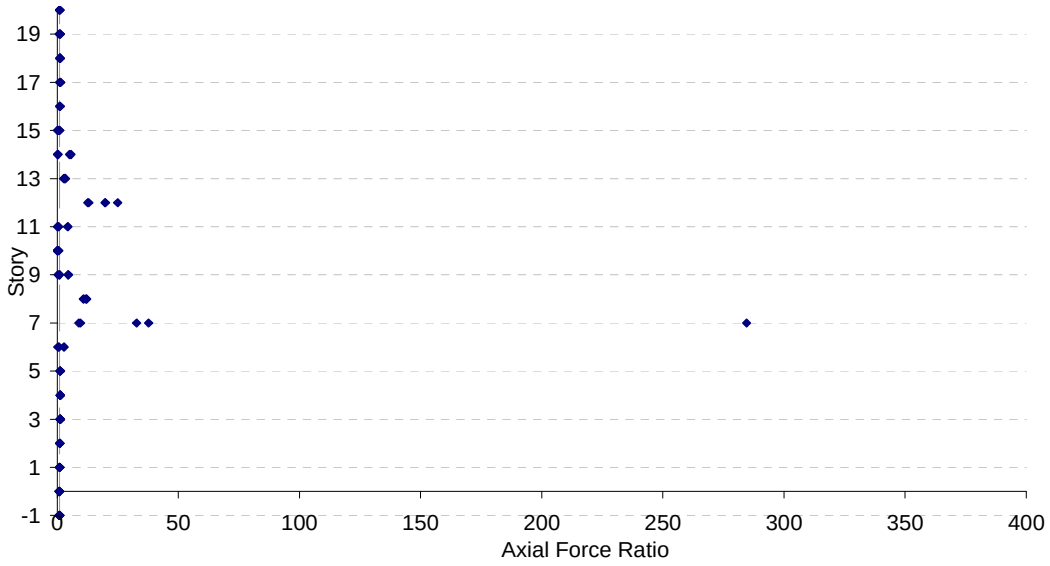

b)

Figure D.32 Axial Force Ratios for $BL\_20-9:13-A-236-0.01-1{,}000$ Subjected to Afyon Bay: a) Columns, b) Beams

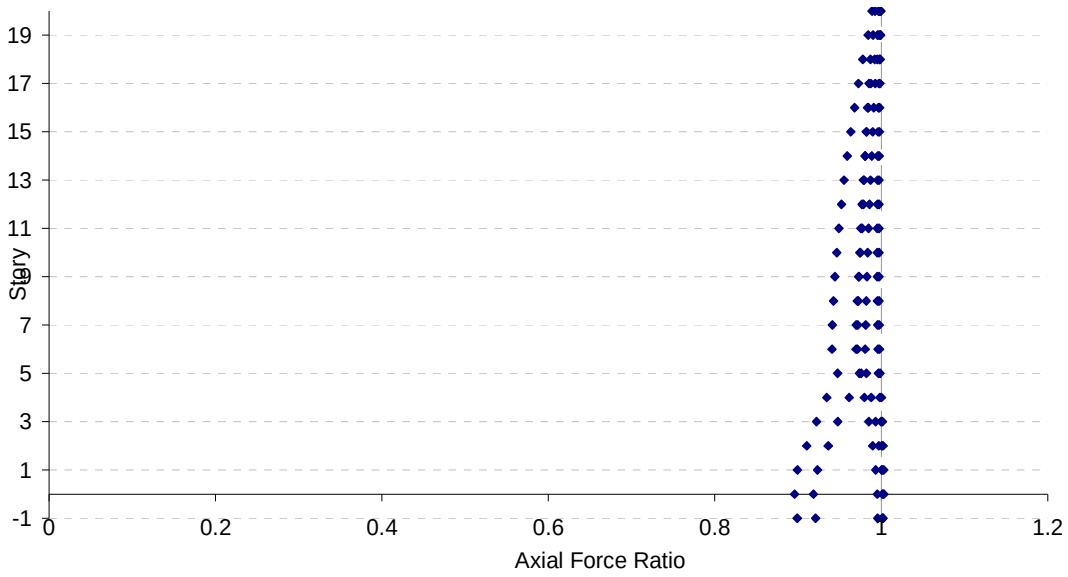

a)

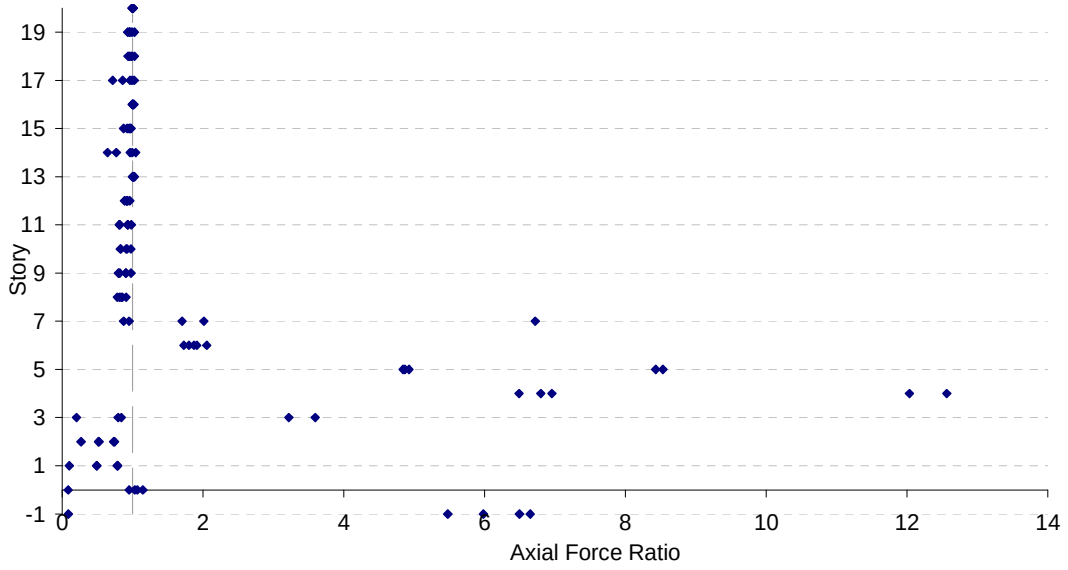

b)

Figure D.33 Axial Force Ratios for $BL\_20-0:5-A-100-0.1-120$ Subjected to Afyon Bay: a) Columns, b) Beams

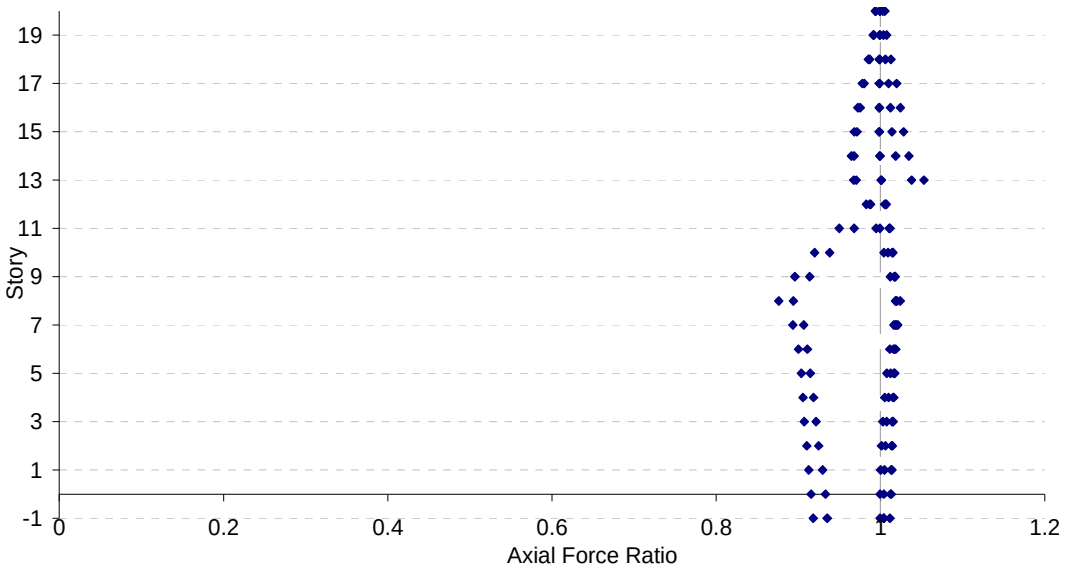

a)

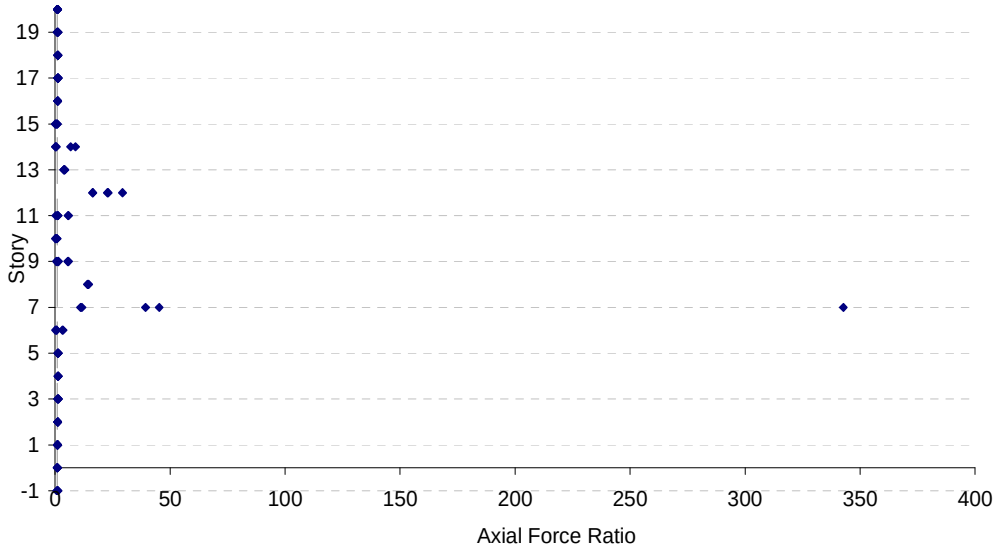

b)

Figure D.34 Axial Force Ratios for $BL\_20-9:13-A-100-0.1-120$ Subjected to Afyon Bay: a) Columns, b) Beams

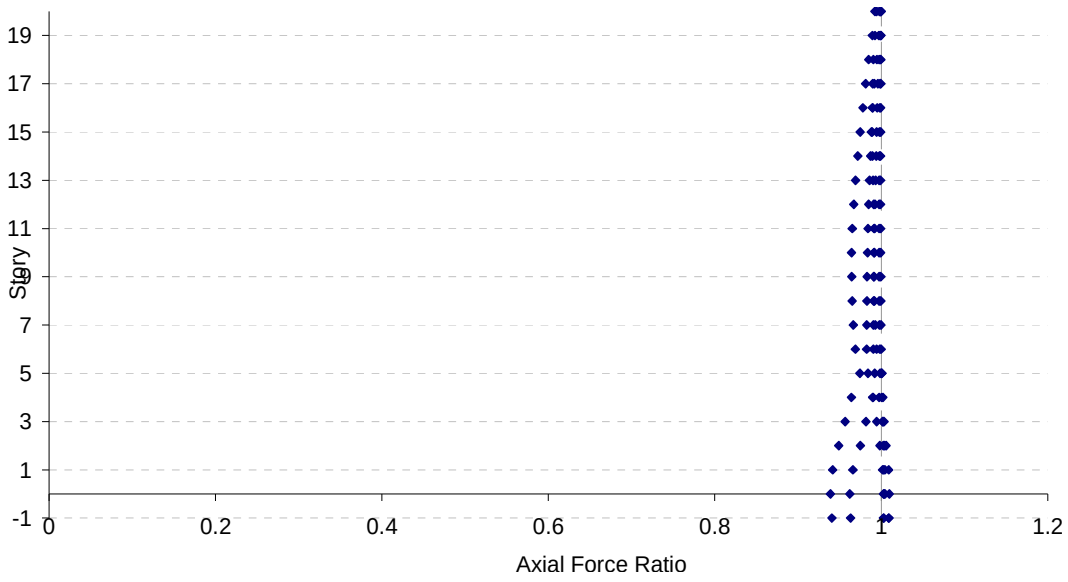

a)

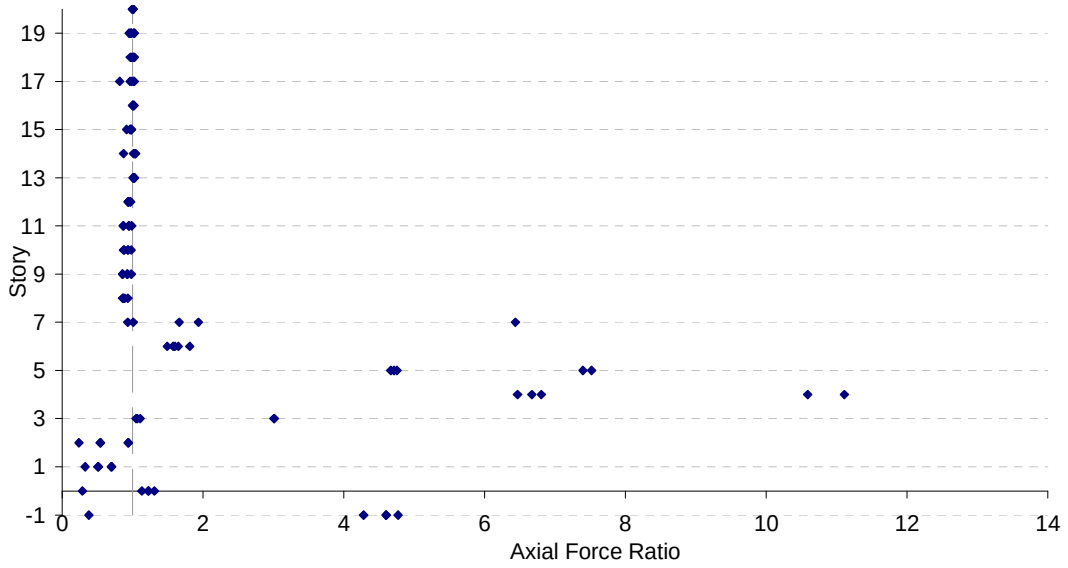

b)

Figure D.35 Axial Force Ratios for $BL\_20-0:5-A-500-0.05-500$ Subjected to Afyon Bay: a) Columns, b) Beams

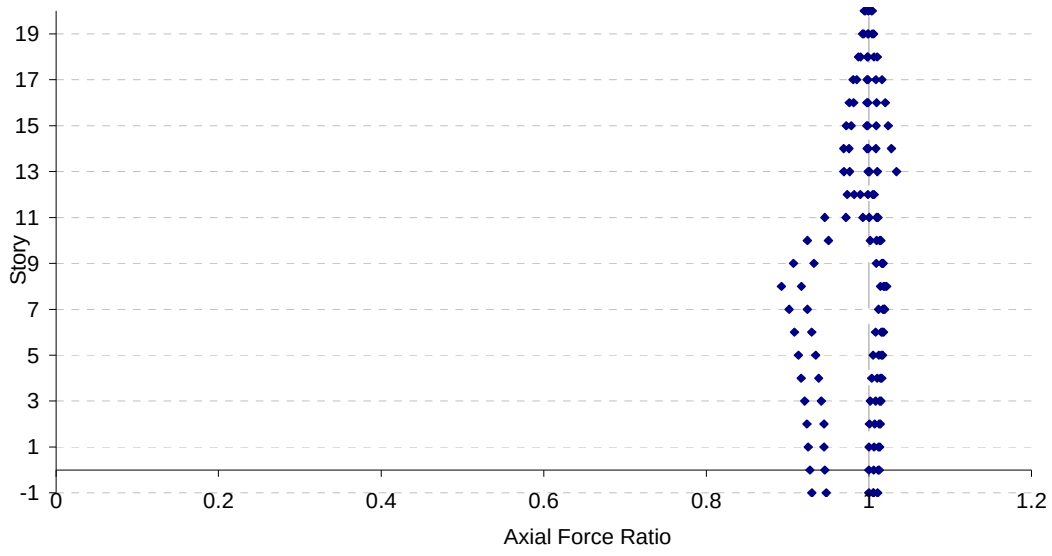

a)

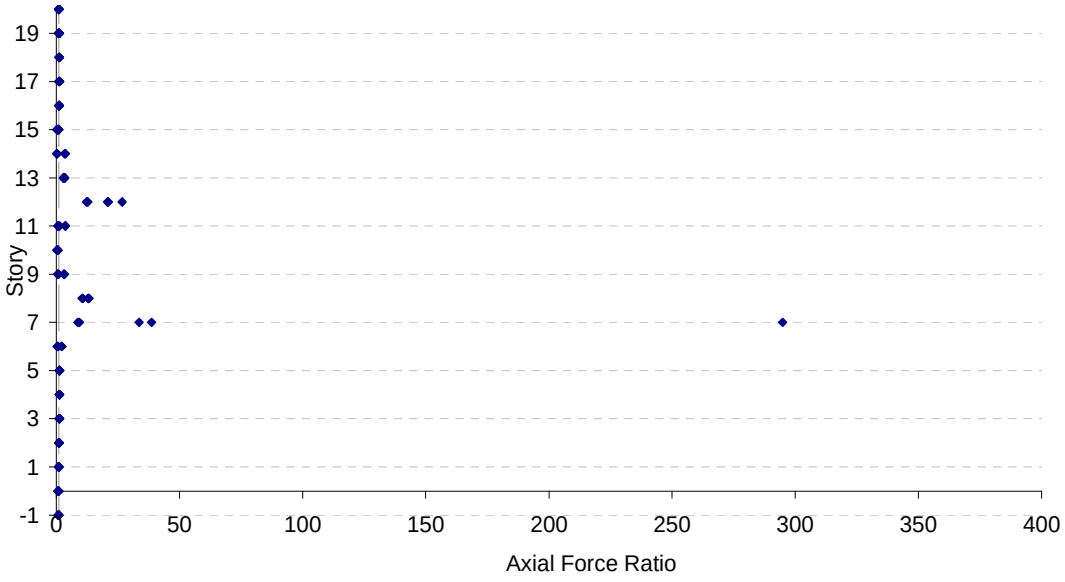

b)

Figure D.36 Axial Force Ratios for $BL\_20-9:13-A-500-0.05-500$ Subjected to Afyon Bay: a) Columns, b) Beams

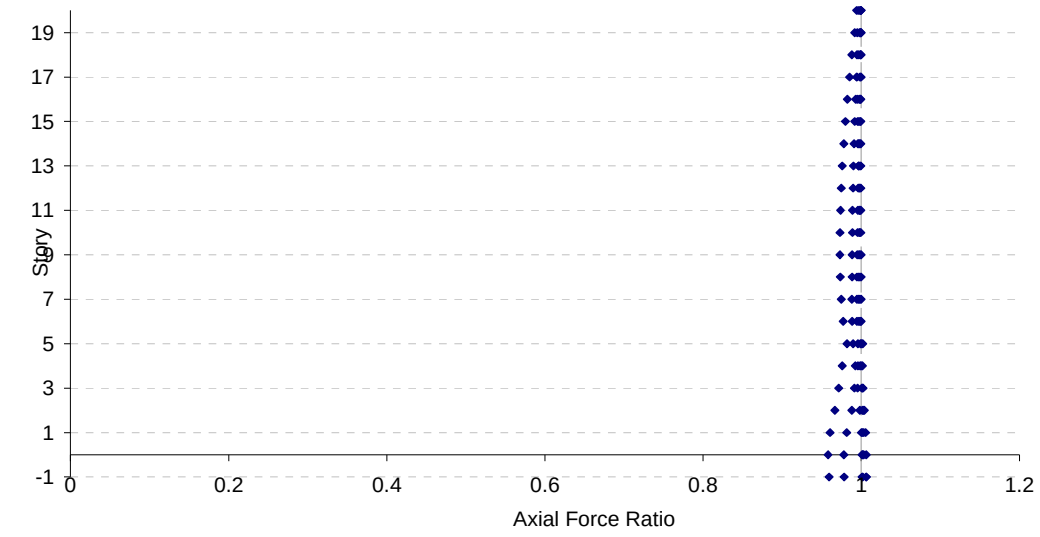

a)

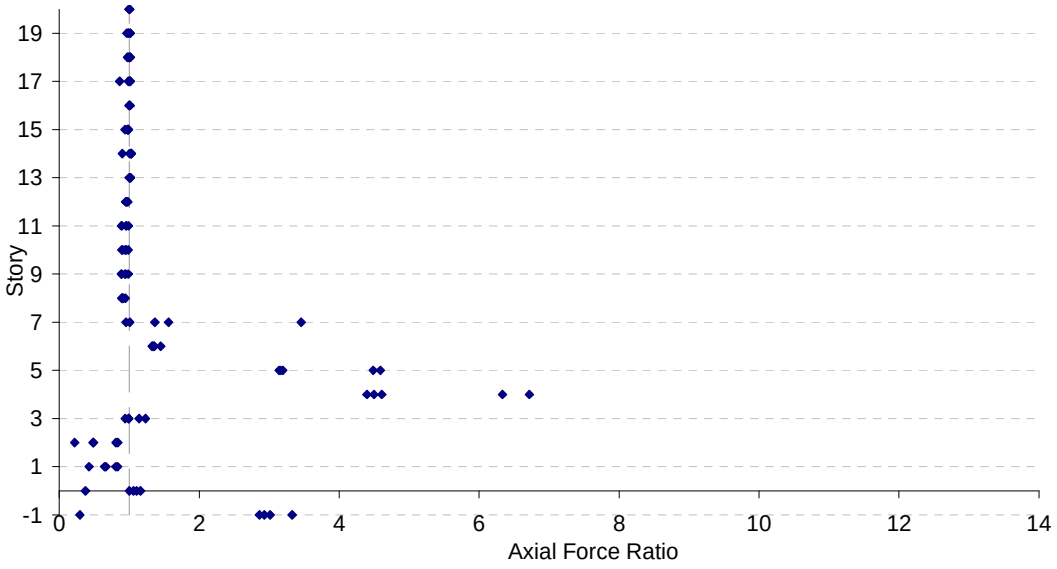

b)

Figure D.37 Axial Force Ratios for $BL\_20-0:5-A-800-0.1-2{,}300$ Subjected to Afyon Bay: a) Columns, b) Beams

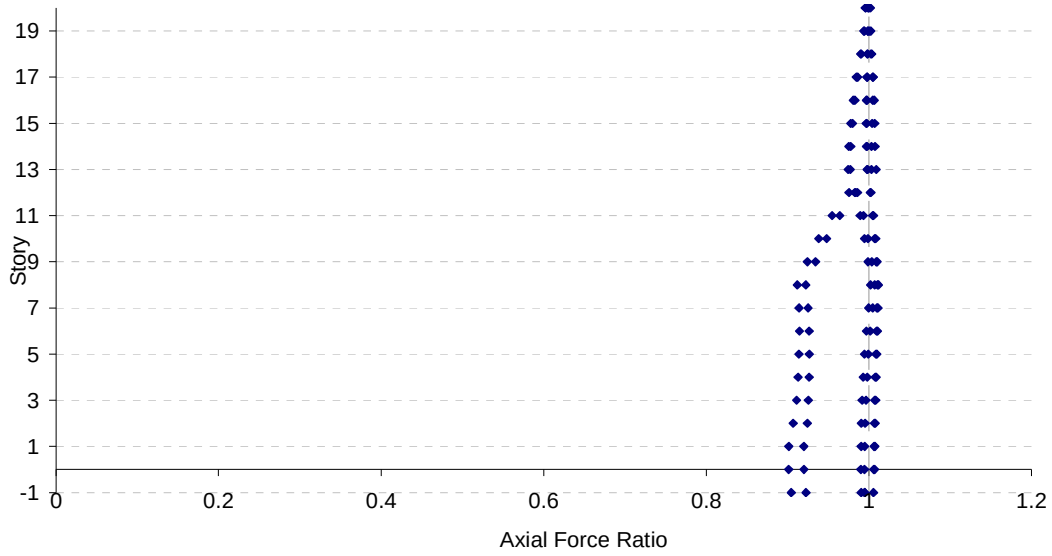

a)

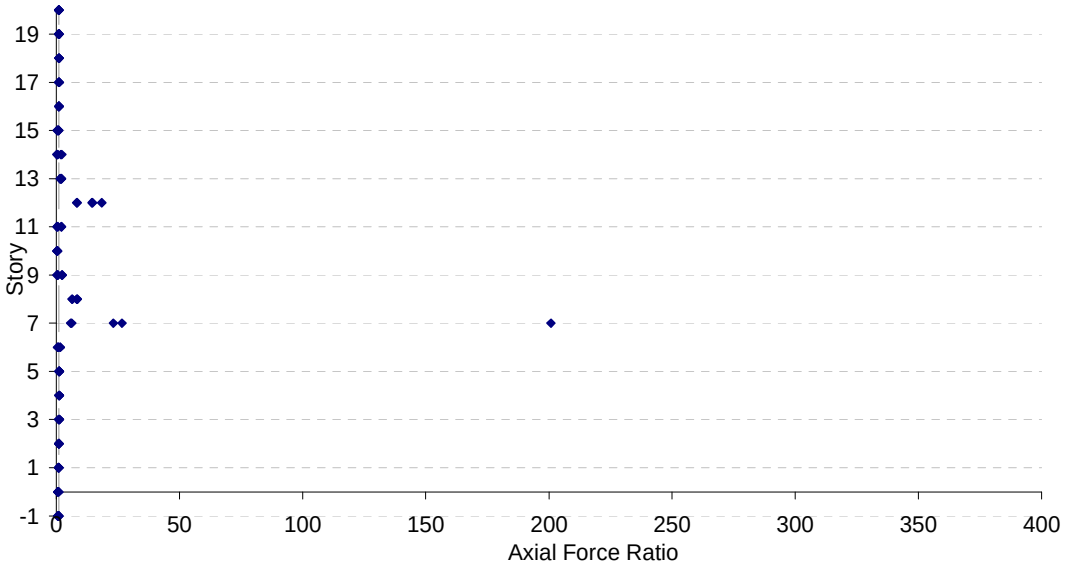

b)

Figure D.38 Axial Force Ratios for $BL\_20-9:13-A-800-0.1-2{,}300$ Subjected to Afyon Bay: a) Columns, b) Beams

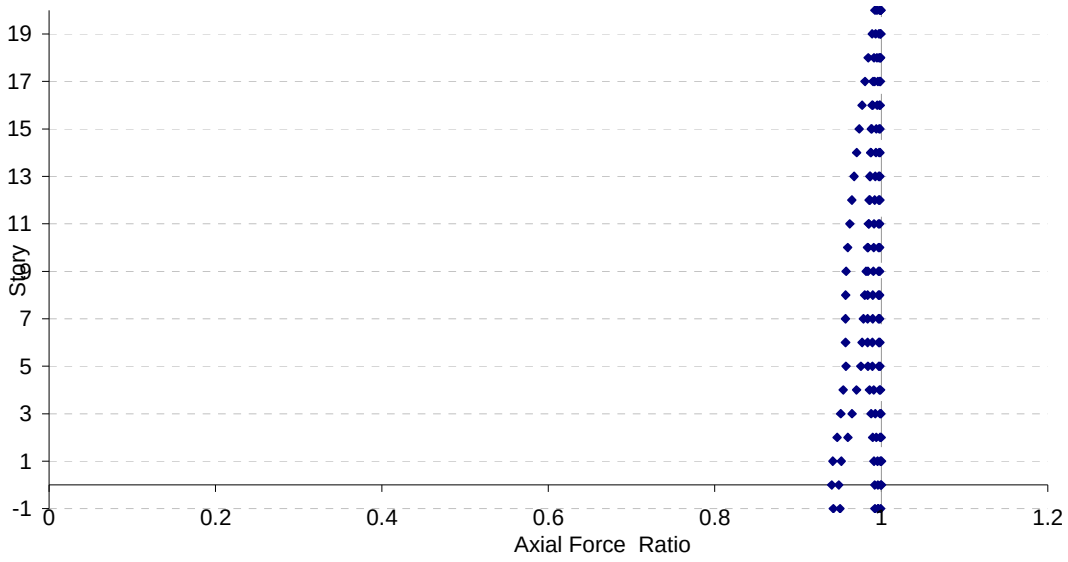

a)

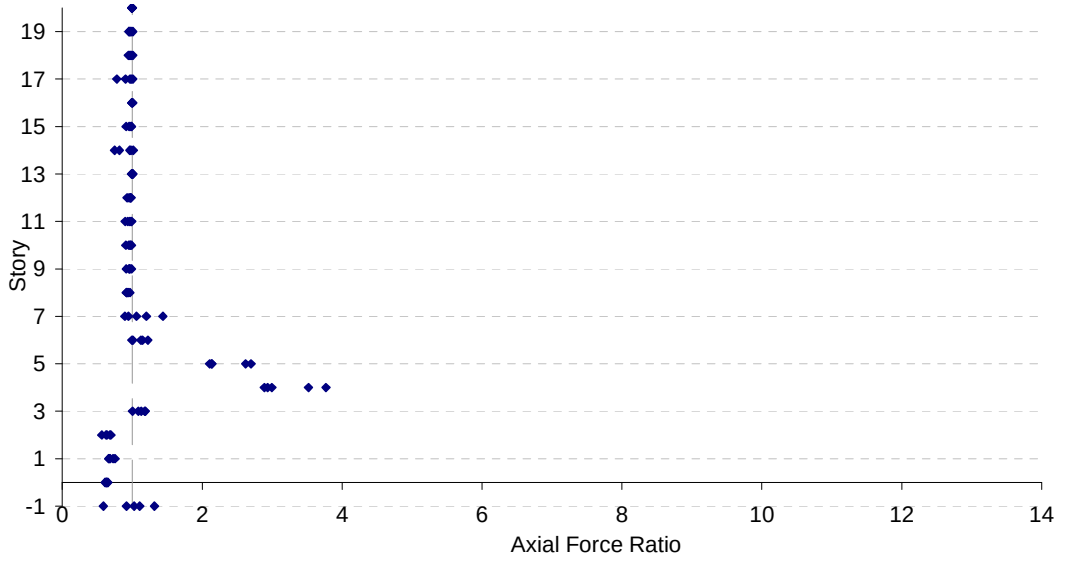

b)

Figure D.39 Axial Force Ratios for $BL\_20-0:5-A-2{,}500-0.05-2{,}000$ Subjected to Afyon Bay: a) Columns, b) Beams

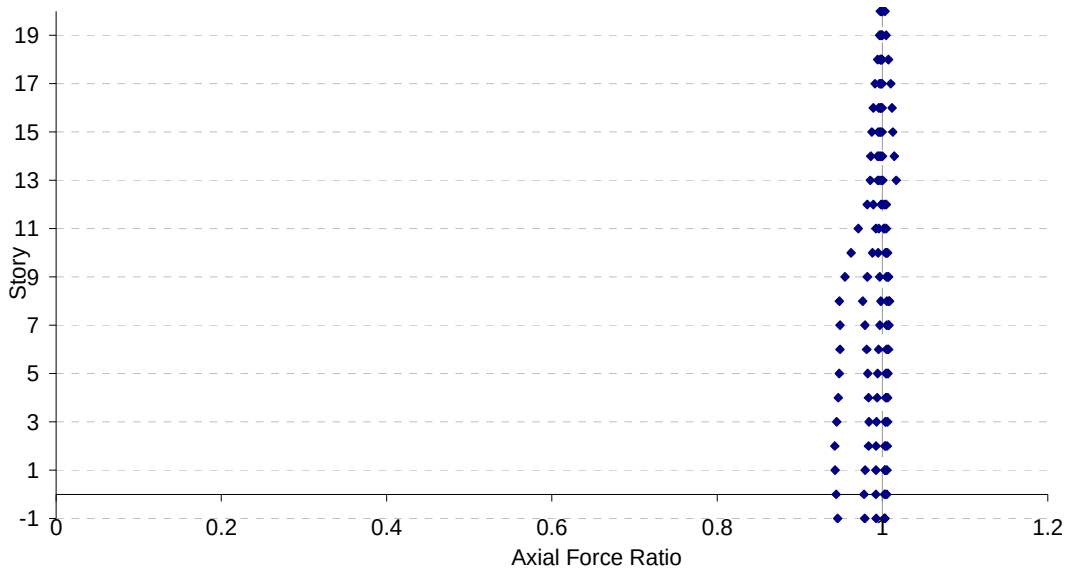

a)

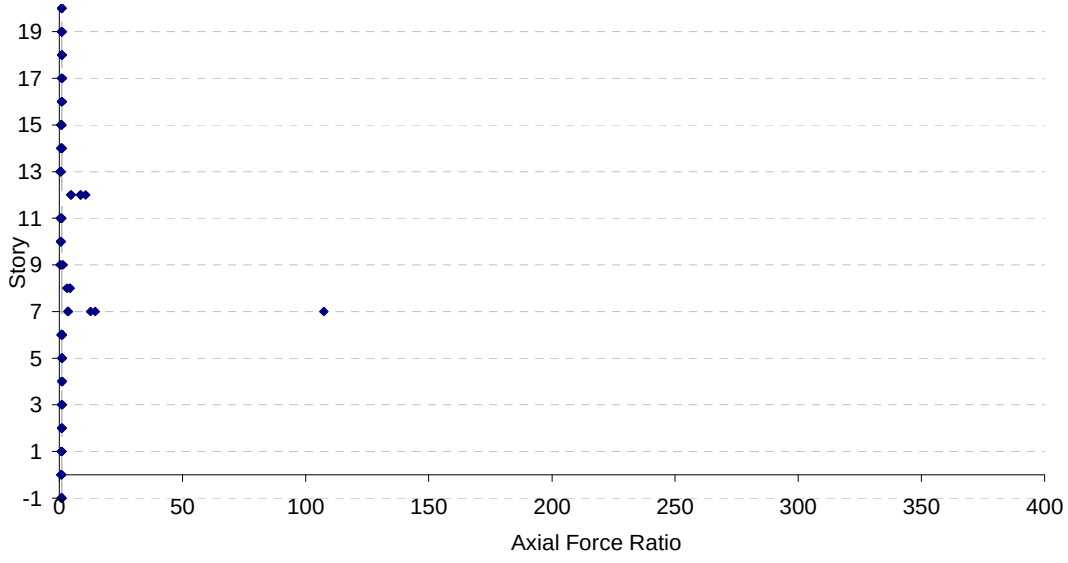

b)

Figure D.40 Axial Force Ratios for $BL\_20-9:13-A-2{,}500-0.05-2{,}000$ Subjected to Afyon Bay: a) Columns, b) Beams

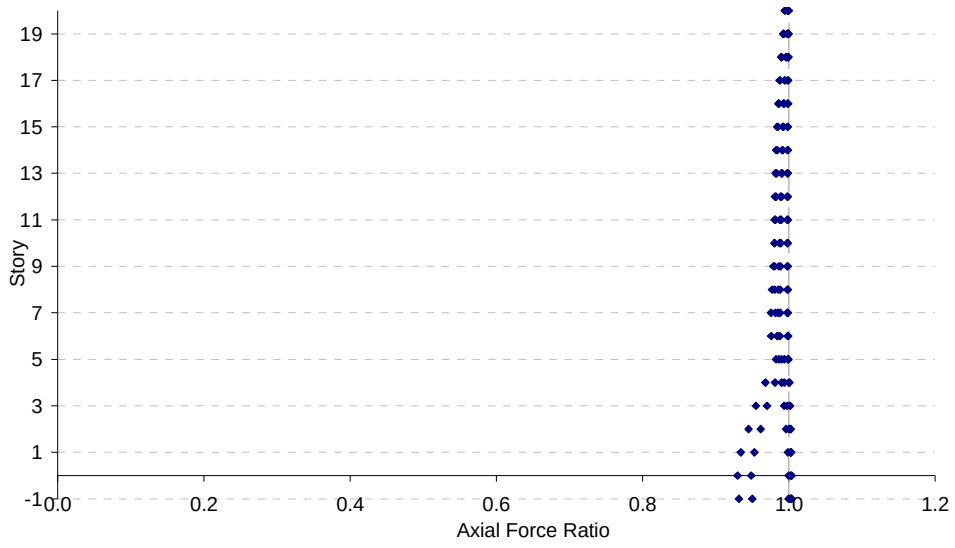

a)

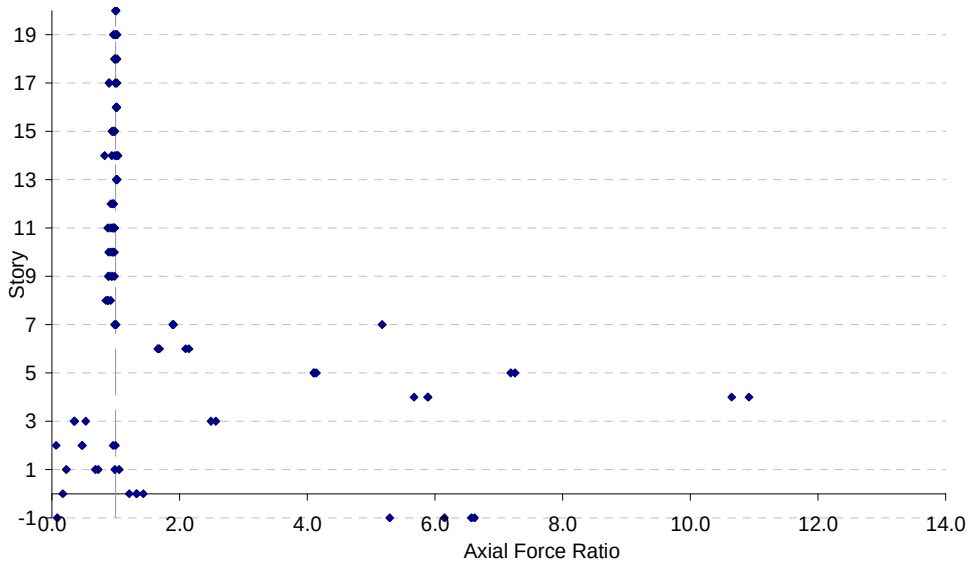

b)

Figure D.41 Axial Force Ratios for $BL\_20-0:5-A-236-0.01-1{,}000$ Subjected to Aydin: a) Columns, b) Beams

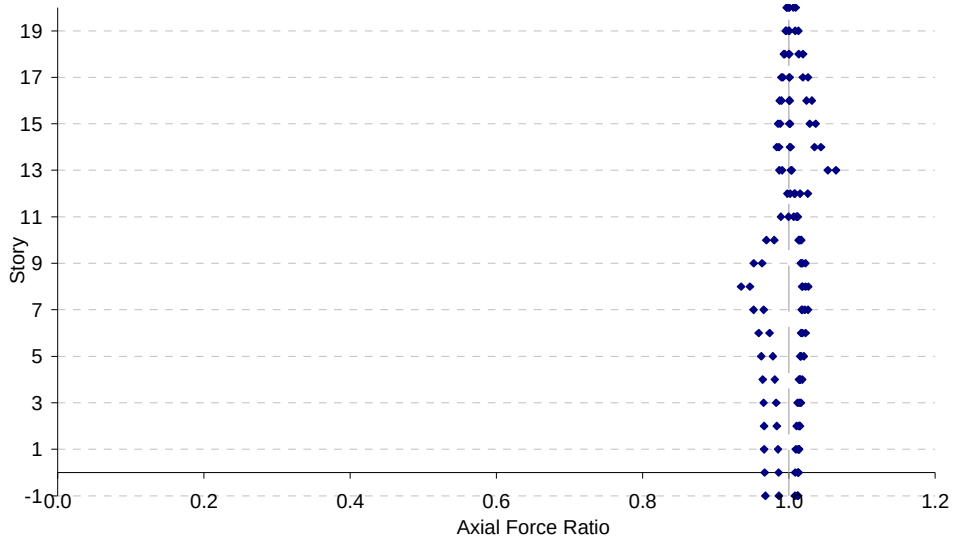

a)

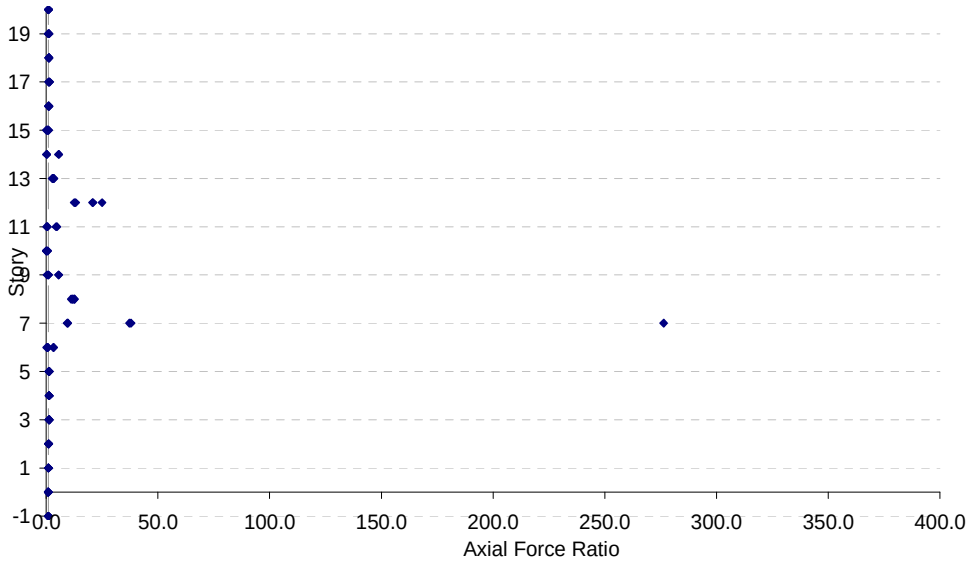

b)

Figure D.42 Axial Force Ratios for $BL\_20-9:13-A-236-0.01-1{,}000$ Subjected to Aydin: a) Columns, b) Beams

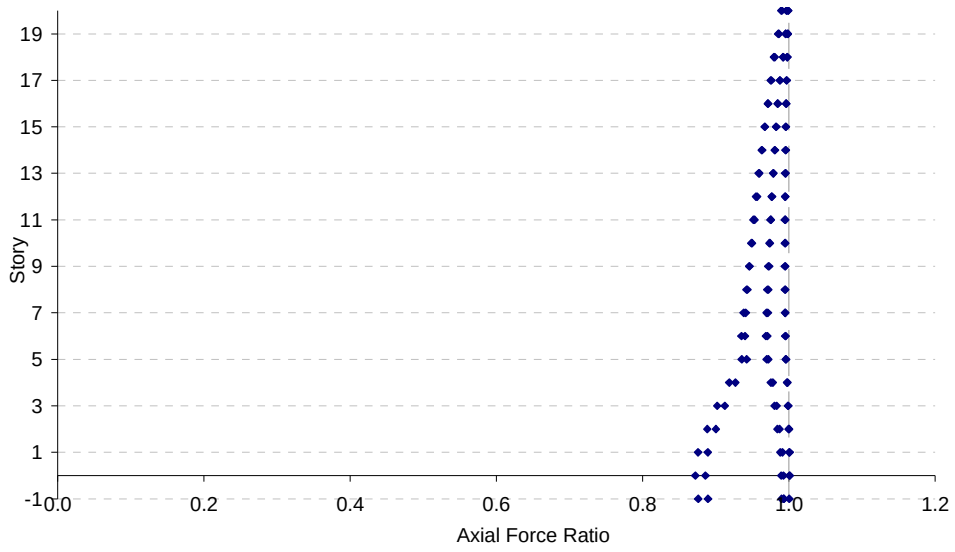

a)

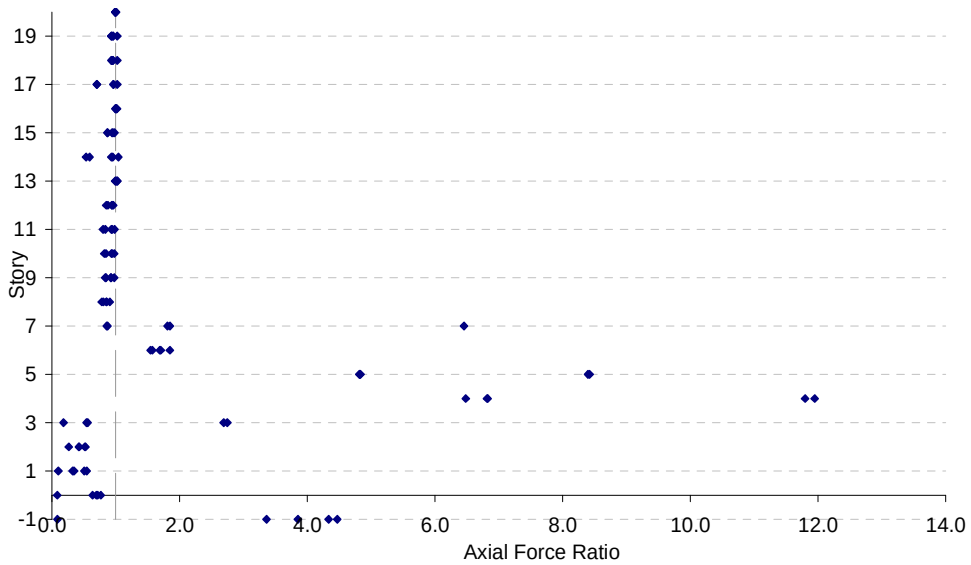

b)

Figure D.43 Axial Force Ratios for $BL\_20-0:5-A-100-0.1-120$ Subjected to Aydin: a) Columns, b) Beams

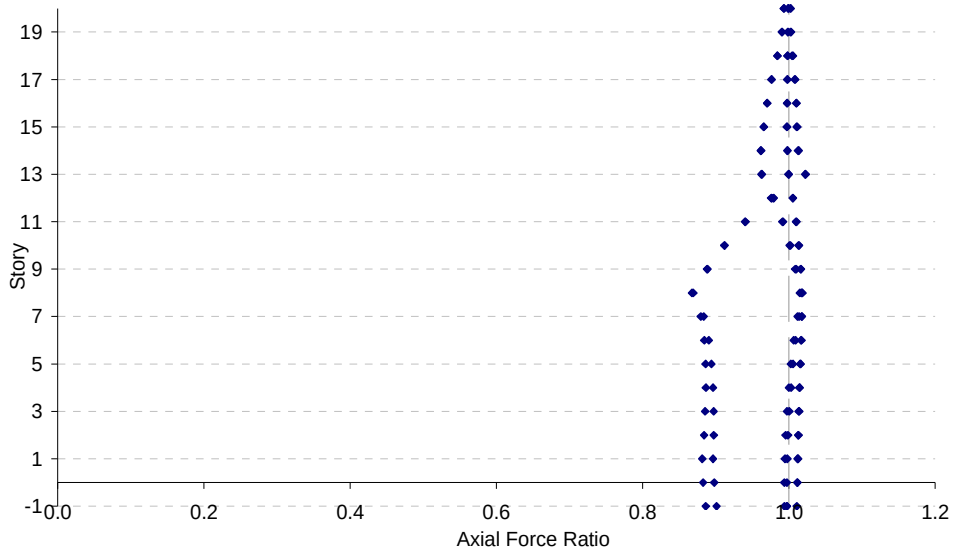

a)

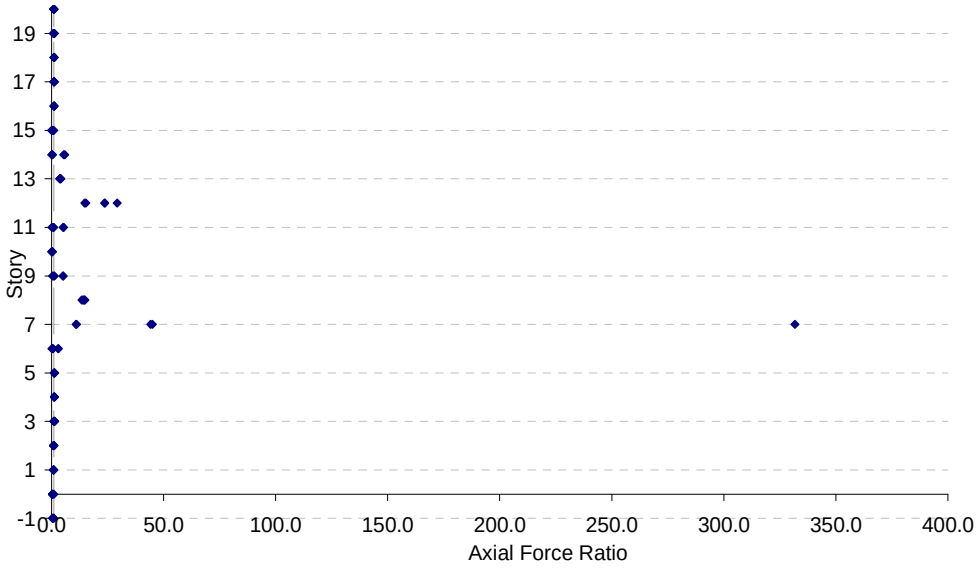

b)

Figure D.44 Axial Force Ratios for $BL\_20-9:13-A-100-0.1-120$ Subjected to Aydin: a) Columns, b) Beams

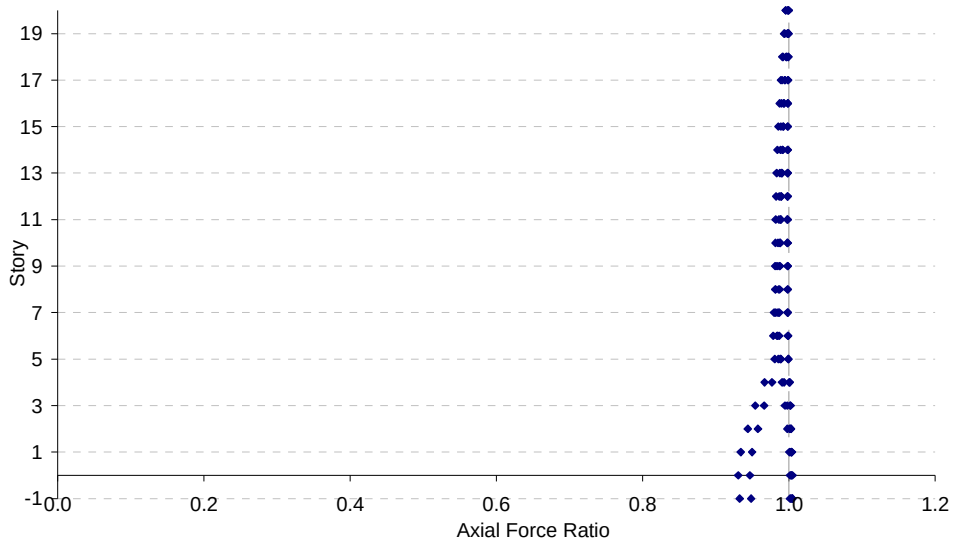

a)

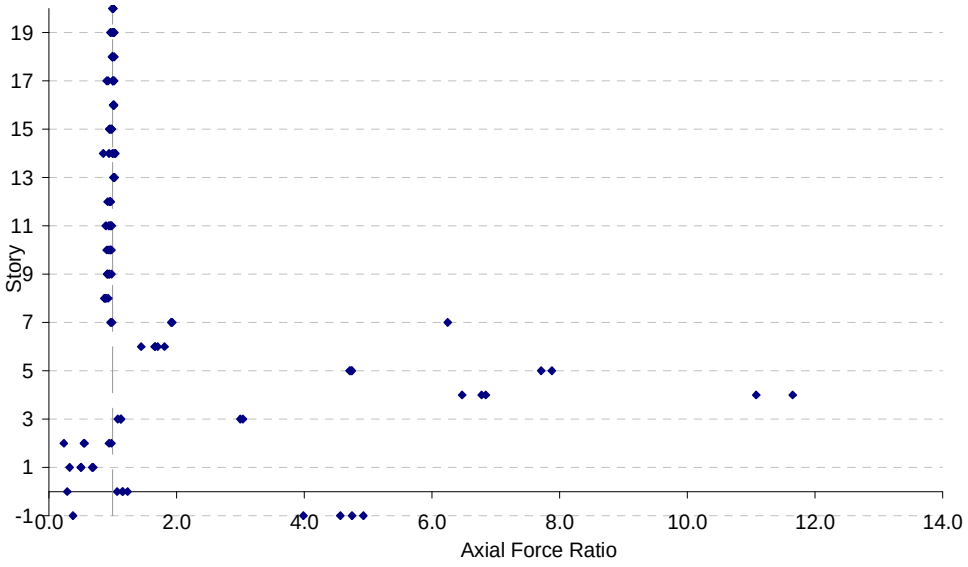

b)

Figure D.45 Axial Force Ratios for $BL\_20-0:5-A-500-0.05-500$ Subjected to Aydin: a) Columns, b) Beams

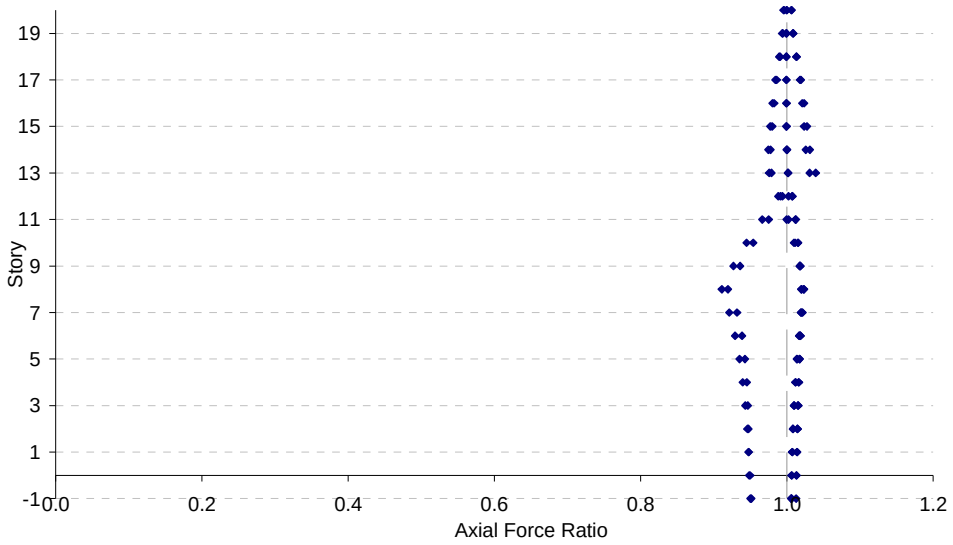

a)

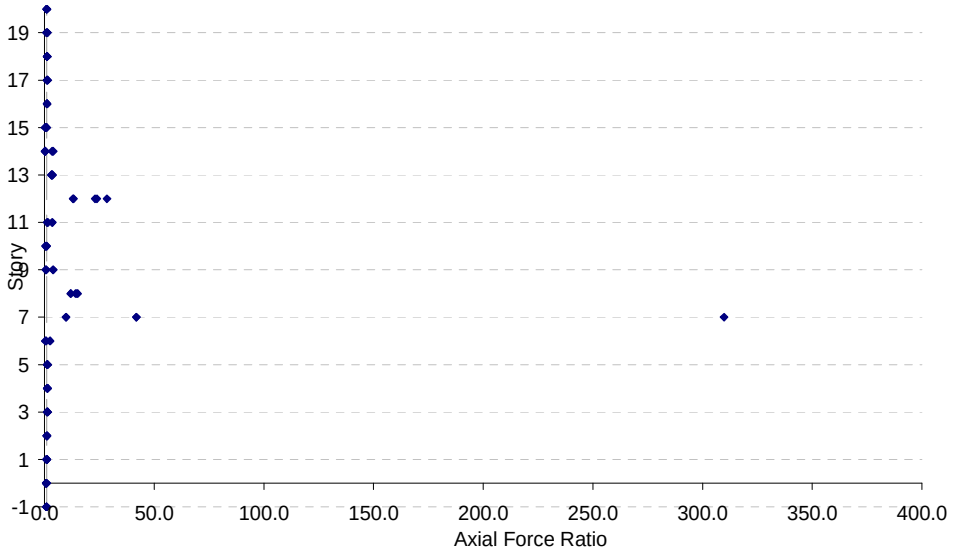

b)

Figure D.46 Axial Force Ratios for $BL\_20-9:13-A-500-0.05-500$ Subjected to Aydin: a) Columns, b) Beams

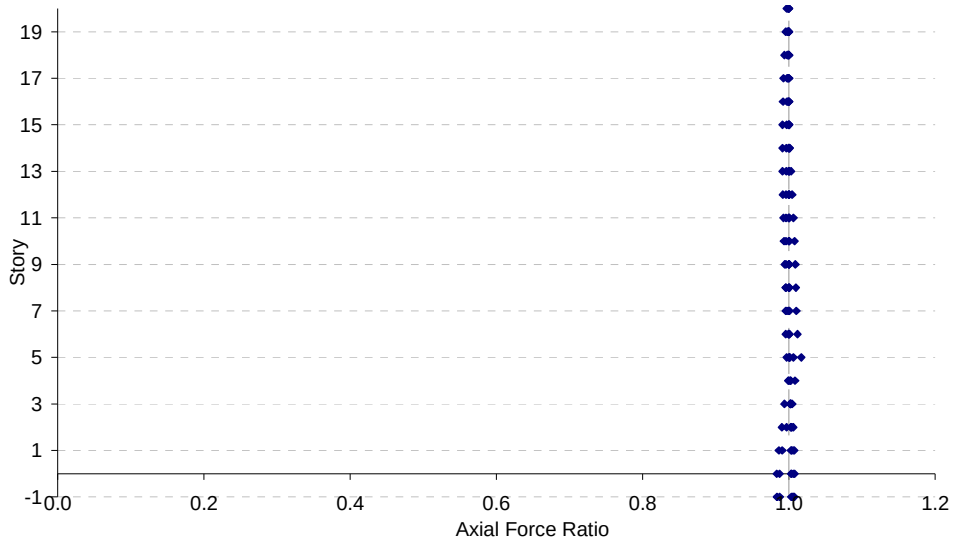

a)

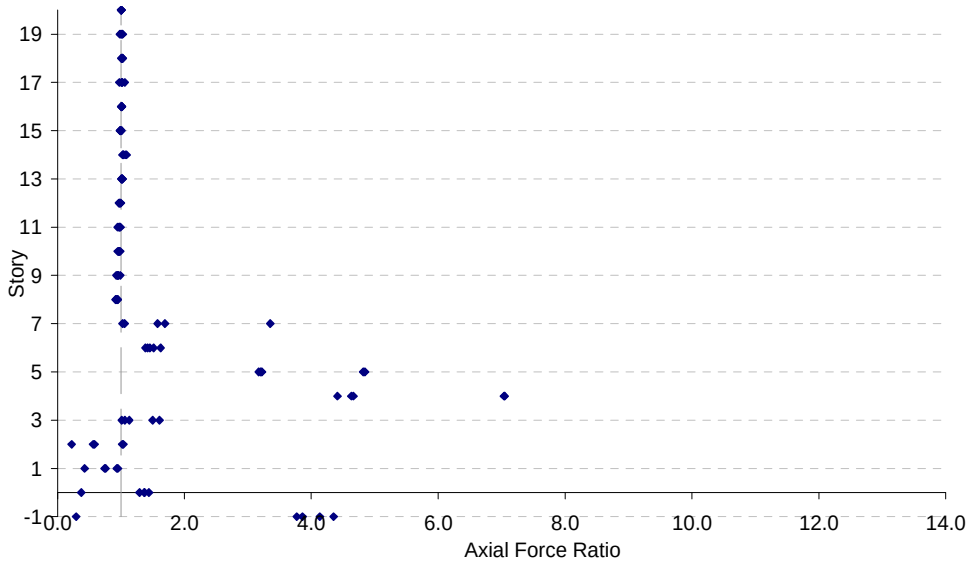

b)

Figure D.47 Axial Force Ratios for $BL\_20-0:5-A-800-0.1-2{,}300$ Subjected to Aydin: a) Columns, b) Beams

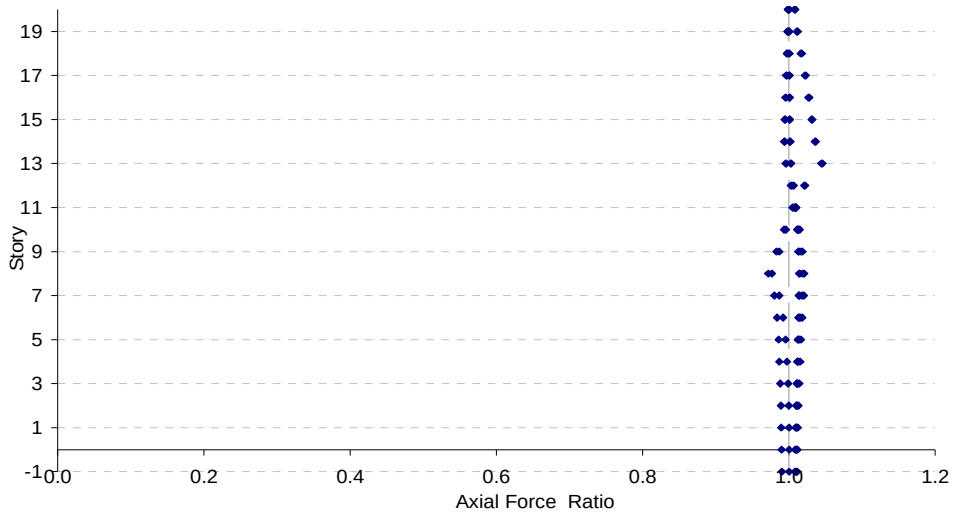

a)

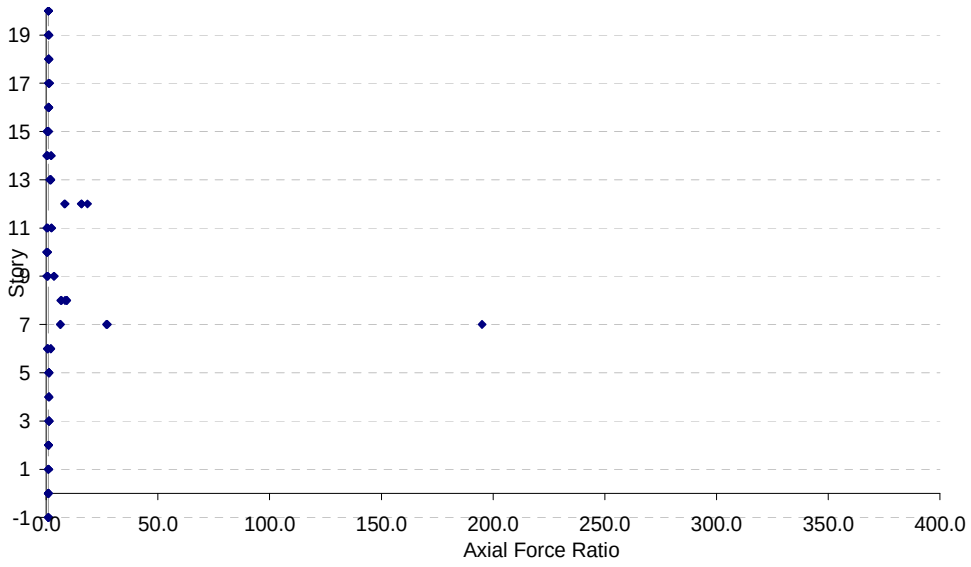

b)

Figure D.48 Axial Force Ratios for $BL\_20-9:13-A-800-0.1-2{,}300$ Subjected to Aydin: a) Columns, b) Beams

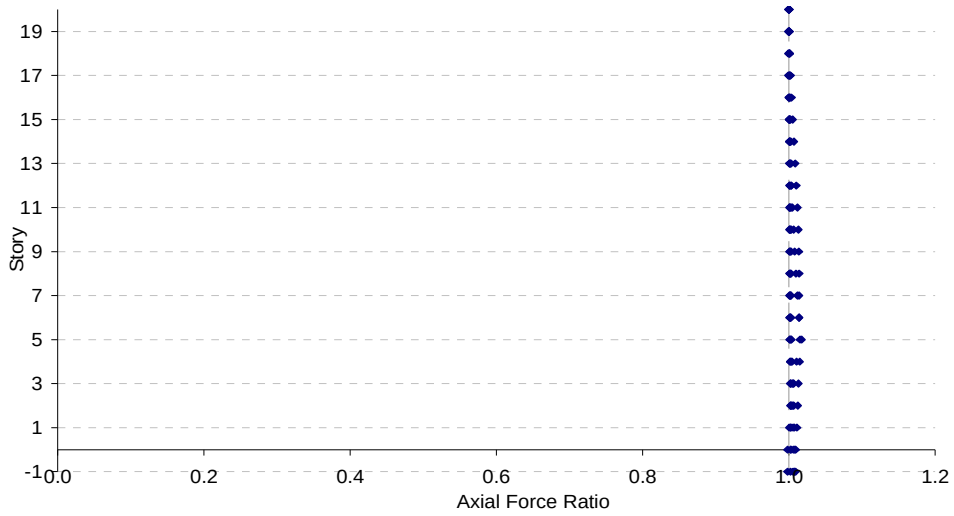

a)

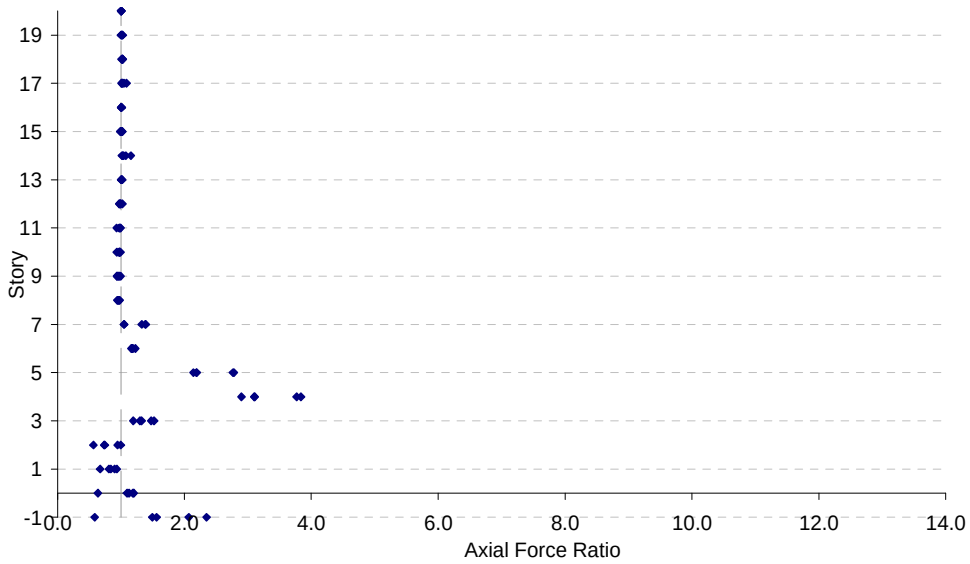

b)

Figure D.49 Axial Force Ratios for $BL\_20-0:5-A-2{,}500-0.05-2{,}000$ Subjected to Aydin: a) Columns, b) Beams

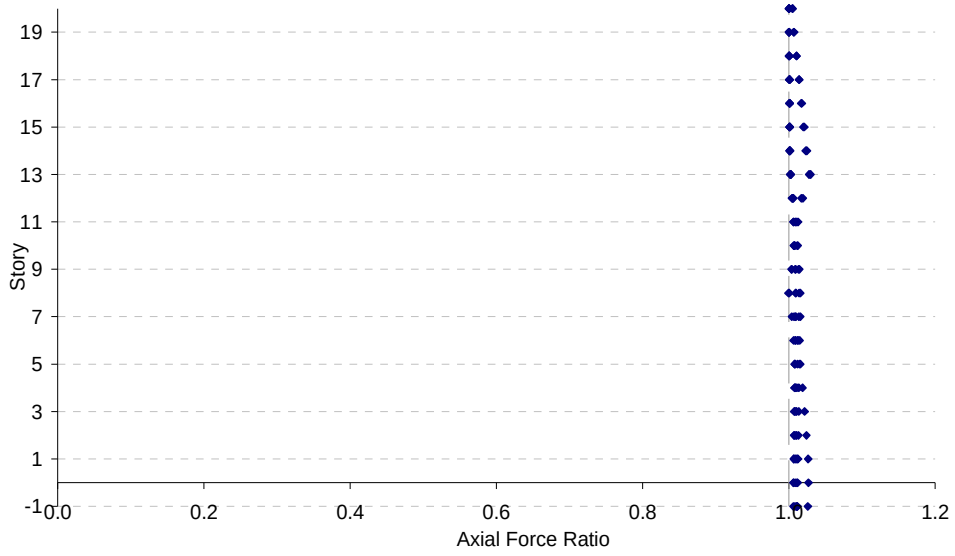

a)

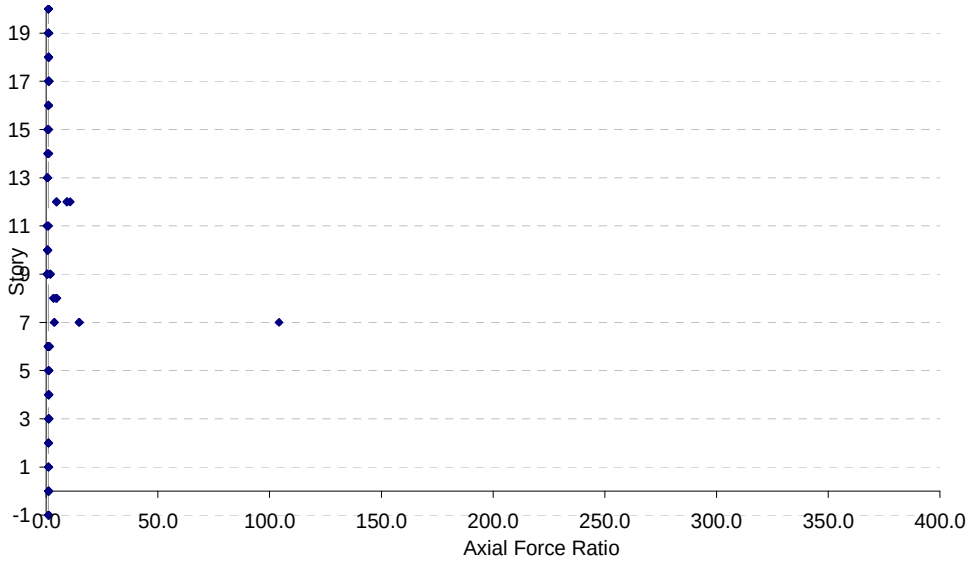

b)

Figure D.50 Axial Force Ratios for $BL\_20-9:13-A-2{,}500-0.05-2{,}000$ Subjected to Aydin: a) Columns, b) Beams

APPENDIX E

AXIAL FORCES FOR SAC FRAME IN EARTHQUAKE ANALYSIS

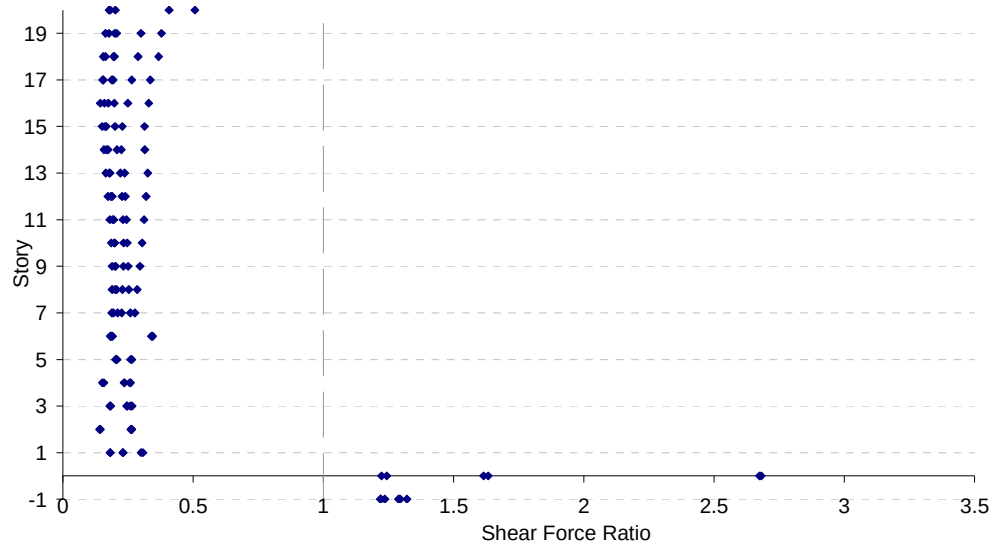

a)

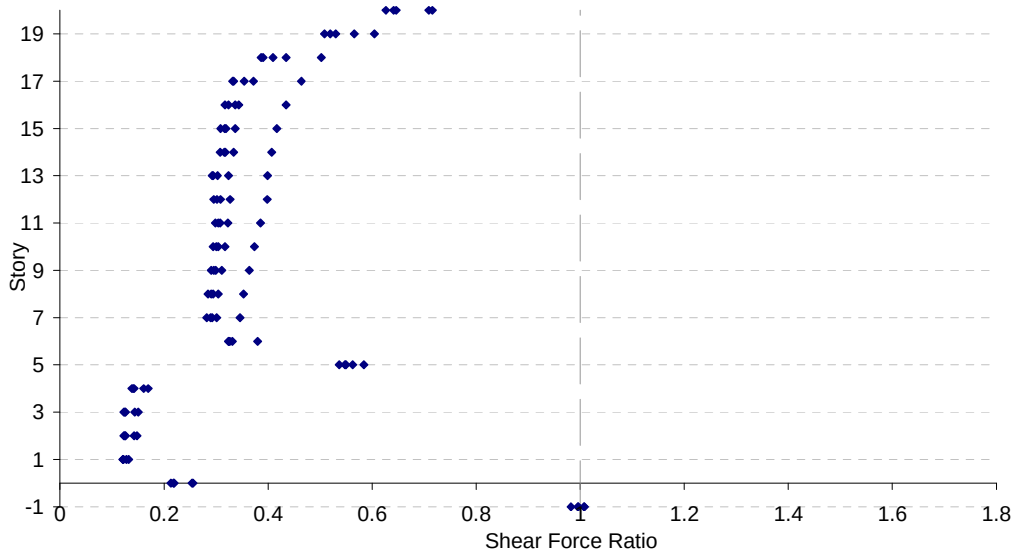

b)

Figure E.1 Shear Force Ratios for $BL\_20-0:5-A-236-0.01-1{,}000$ Subjected to El Centro: a) Columns, b) Beams

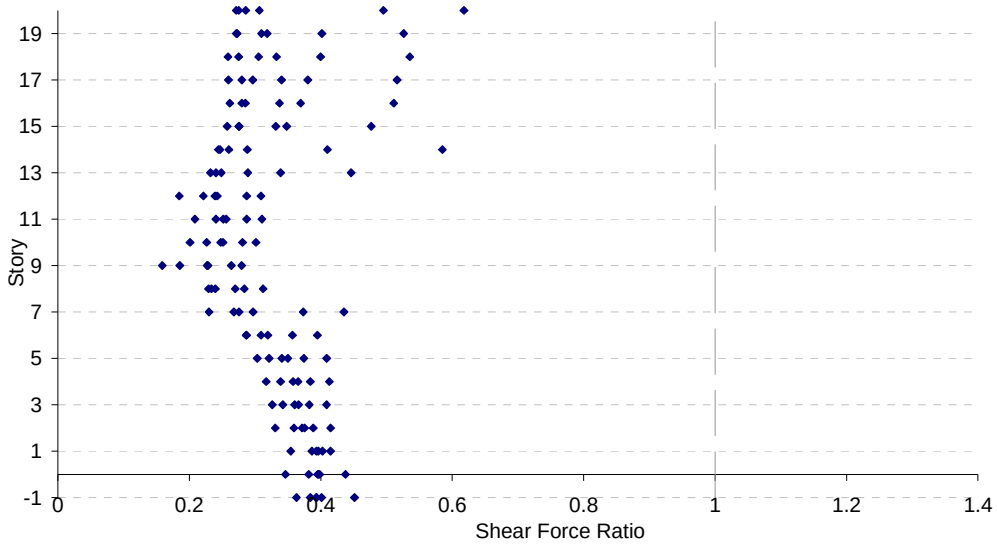

a)

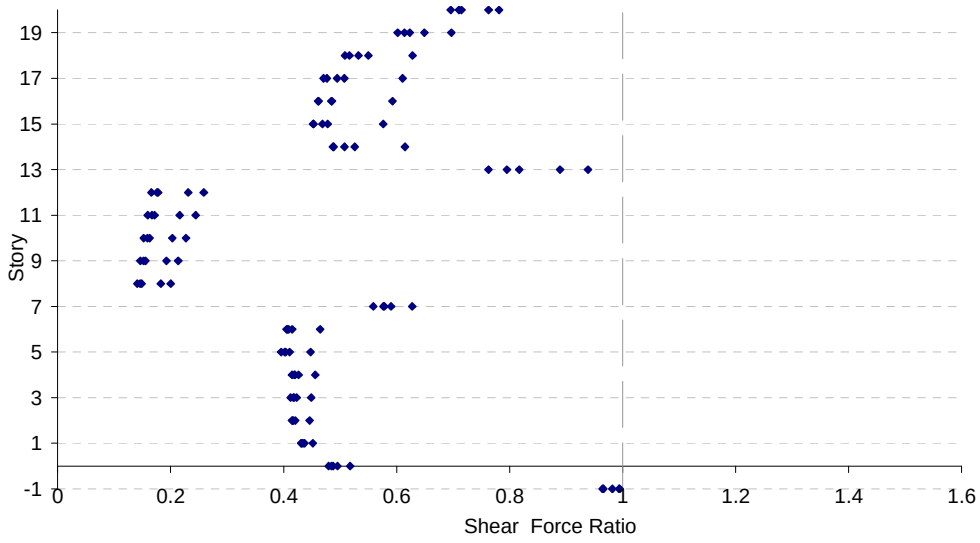

b)

Figure E.2 Shear Force Ratios for $BL\_20-9:13-A-236-0.01-1{,}000$ Subjected to El Centro: a) Columns, b) Beams

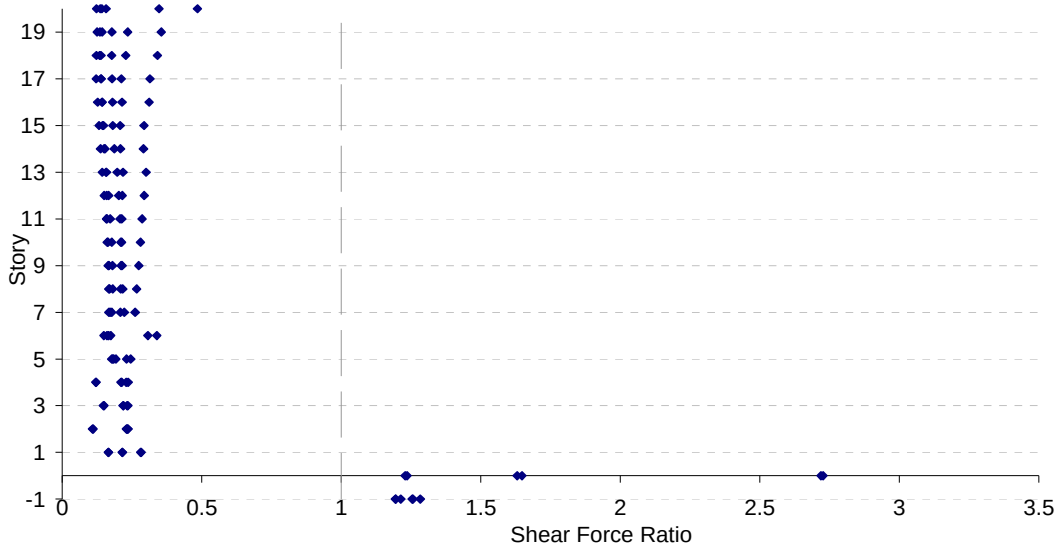

a)

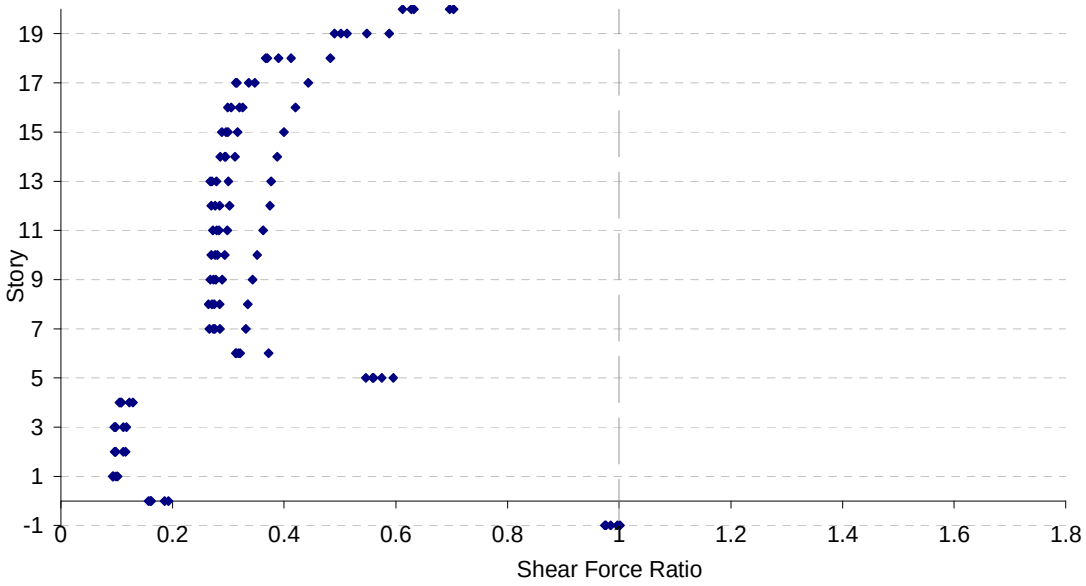

b)

Figure E.3 Shear Force Ratios for $BL\_20-0{:}5-A-100-0.1-120$ Subjected to El Centro: a) Columns, b) Beams

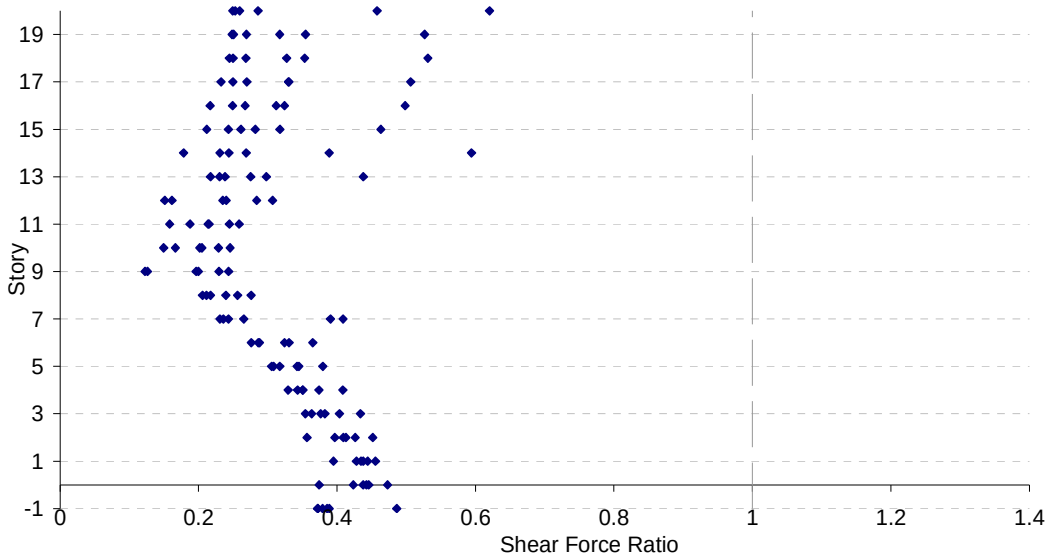

a)

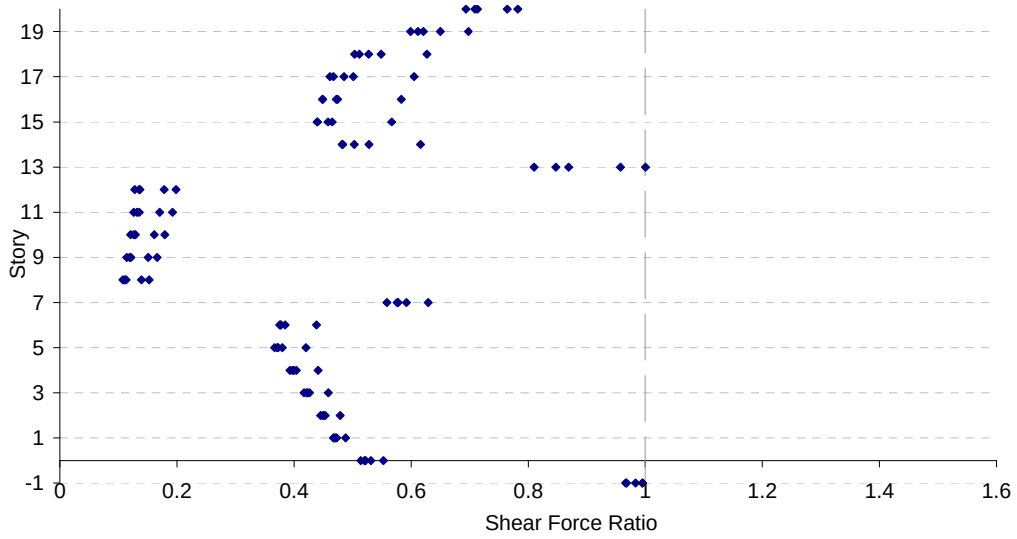

b)

Figure E.4 Shear Force Ratios for $BL\_20-9:13-A-100-0.1-120$ Subjected to El Centro: a) Columns, b) Beams

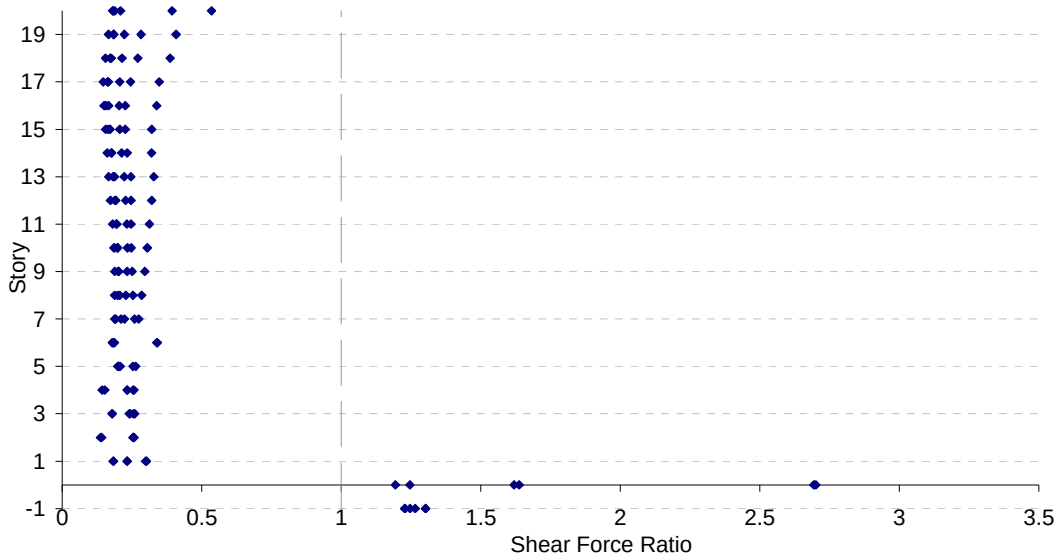

a)

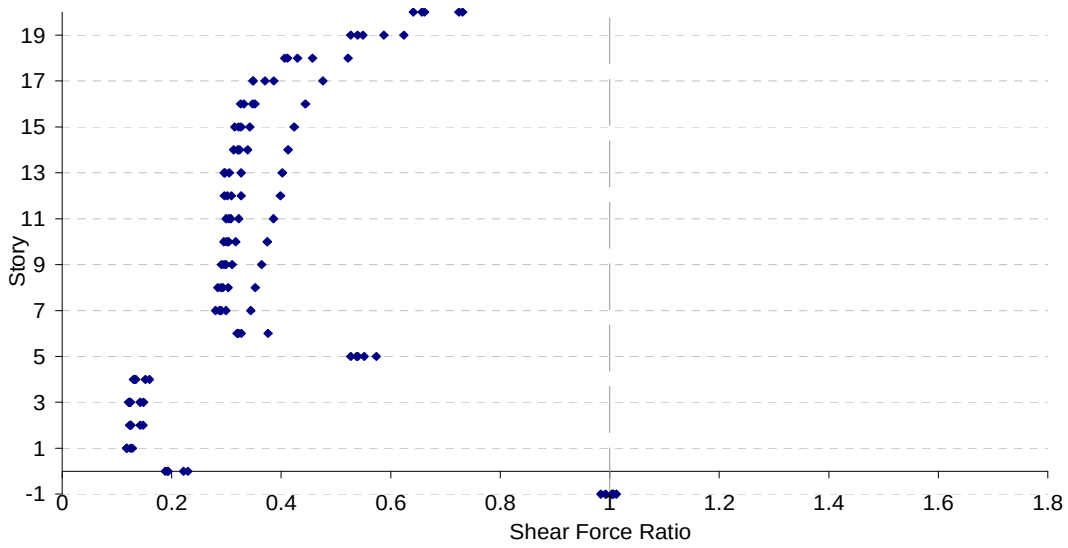

b)

Figure E.5 Shear Force Ratios for $BL\_20-0:5-A-500-0.05-500$ Subjected to El Centro: a) Columns, b) Beams

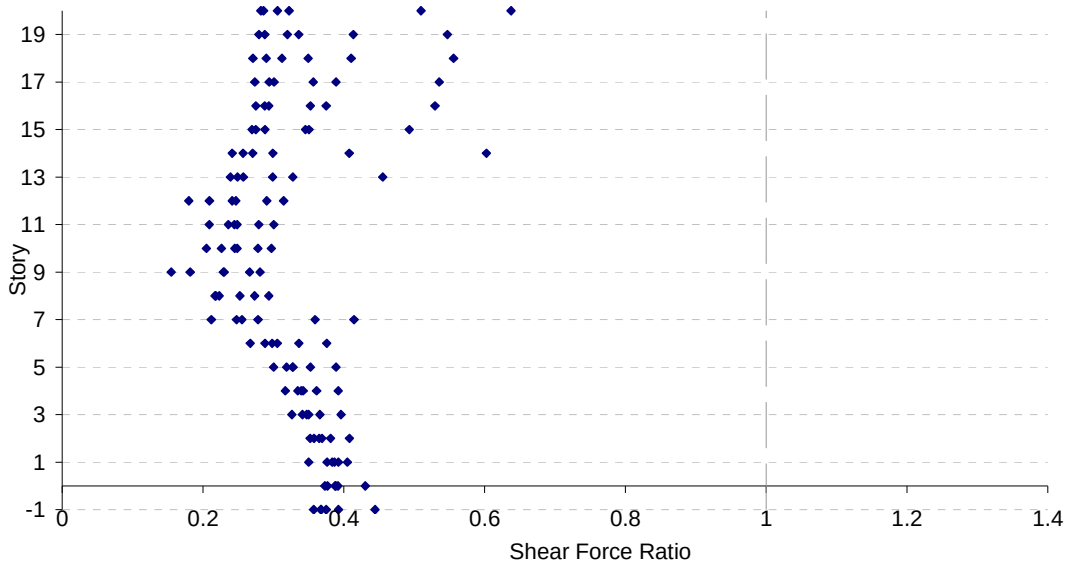

a)

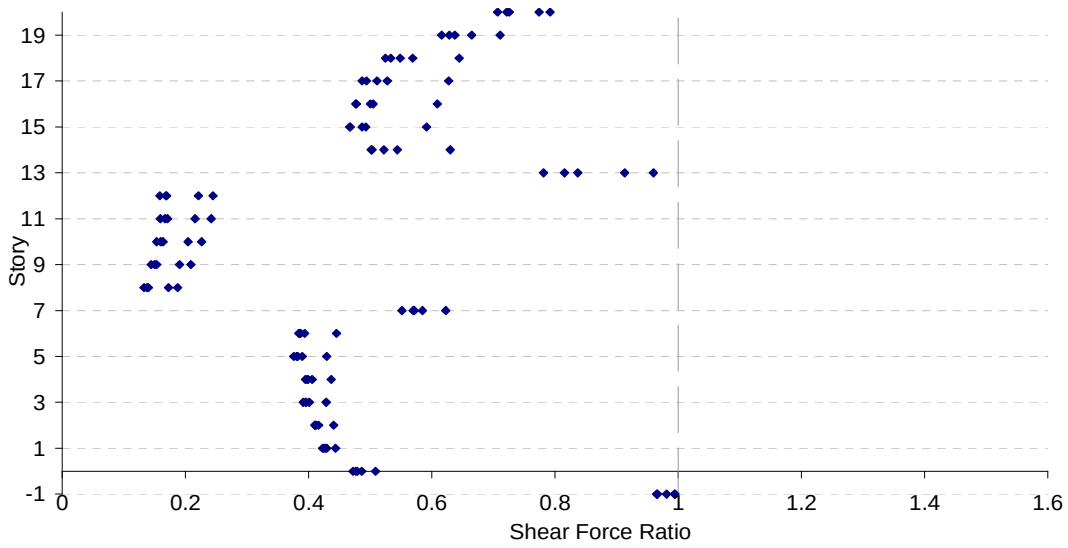

b)

Figure E.6 Shear Force Ratios for $BL\_20-9:13-A-500-0.05-500$ Subjected to El Centro: a) Columns, b) Beams

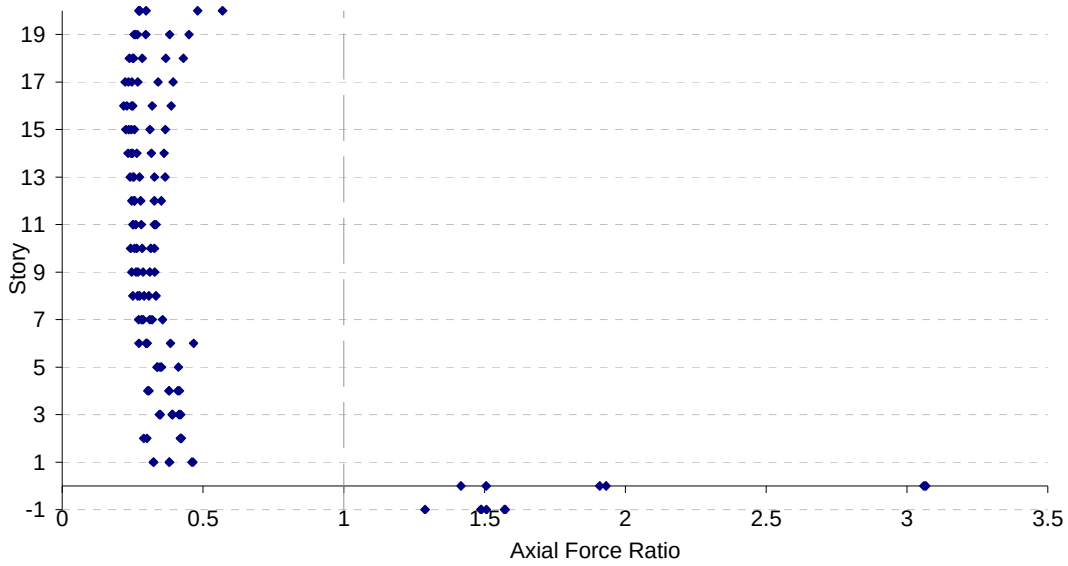

a)

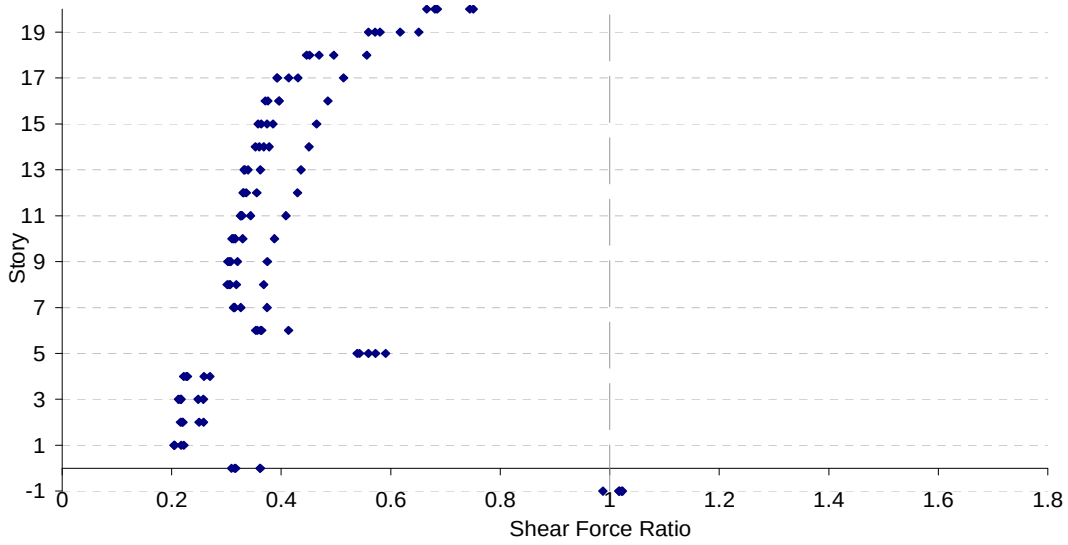

b)

Figure E.7 Shear Force Ratios for $BL\_20-0:5-A-800-0.1-2{,}300$ Subjected to El Centro: a) Columns, b) Beams

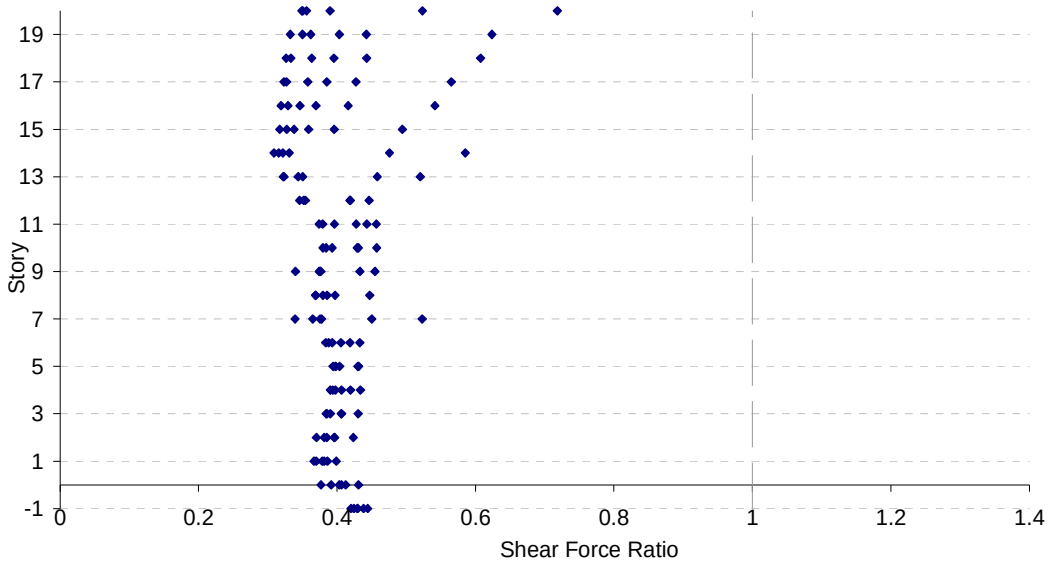

a)

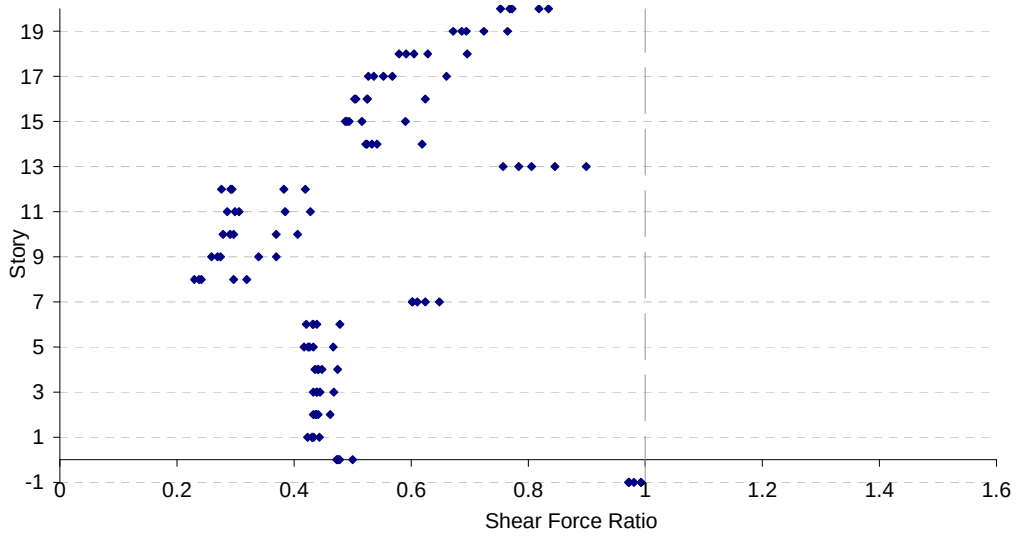

b)

Figure E.8 Shear Force Ratios for $BL\_20-9:13-A-800-0.1-2{,}300$ Subjected to El Centro: a) Columns, b) Beams

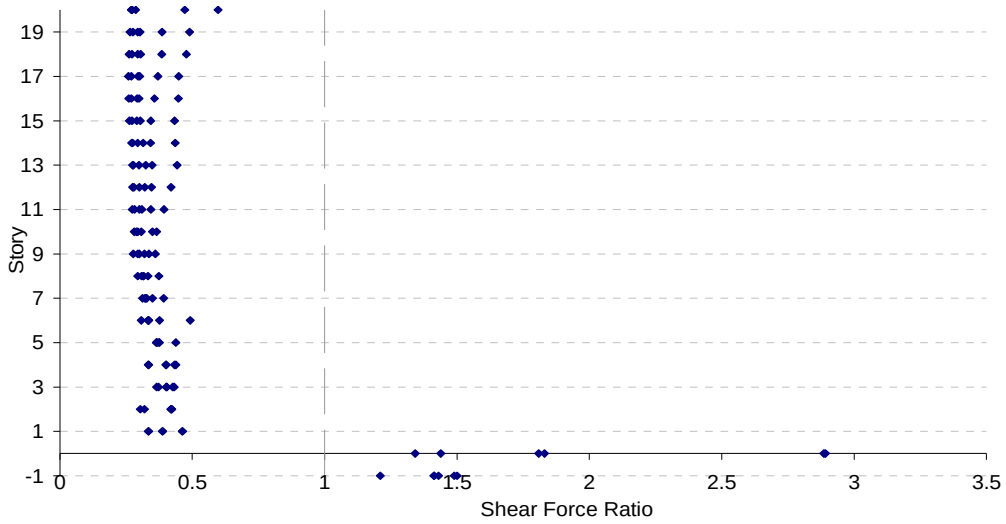

a)

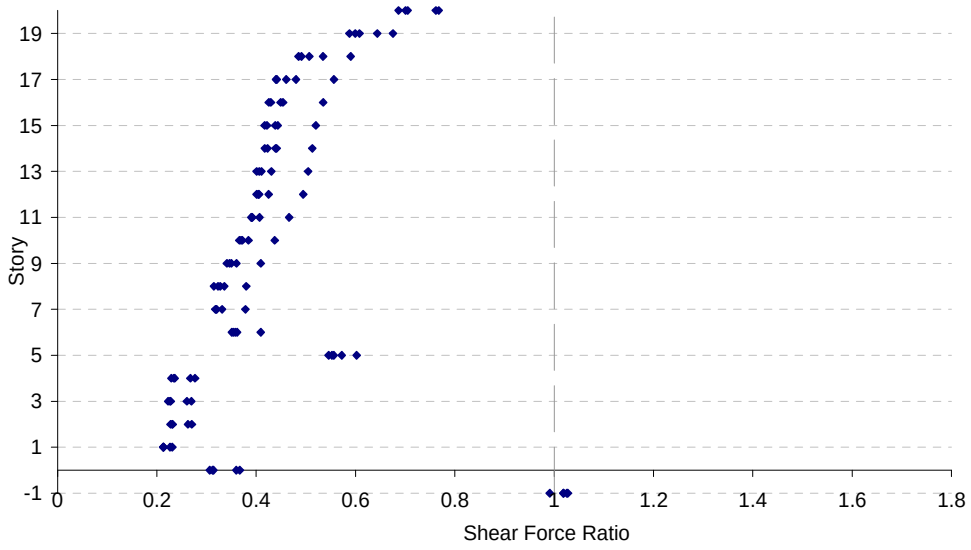

b)

Figure E.9 Shear Force Ratios for $BL\_20-0:5-A-2{,}500-0.05-2{,}000$ Subjected to El Centro: a) Columns, b) Beams

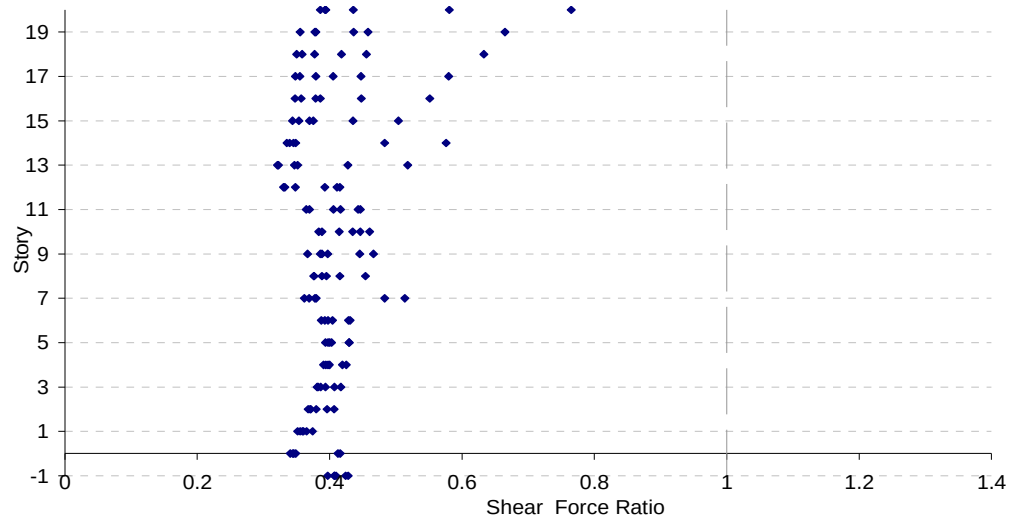

a)

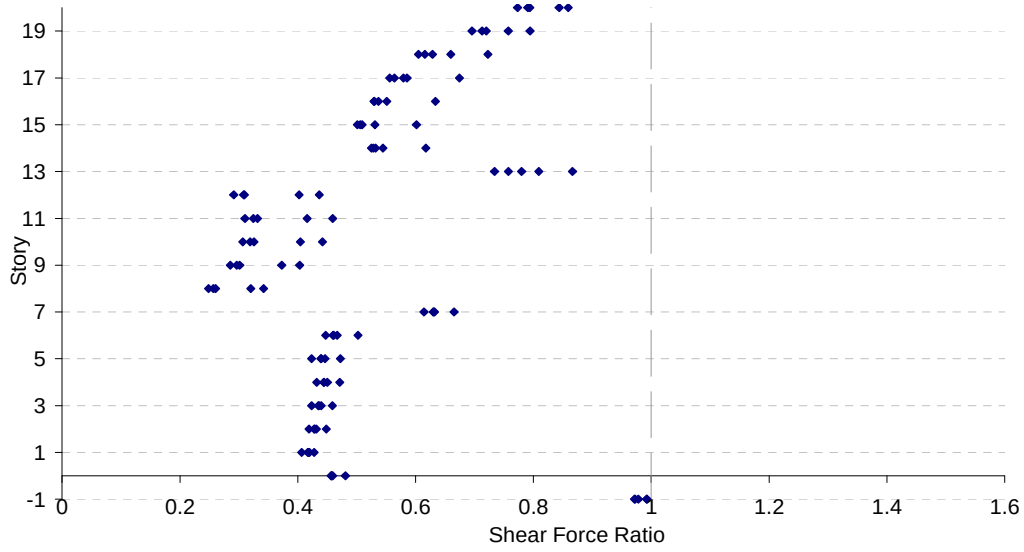

b)

Figure E.10 Shear Force Ratios for $BL\_20-9:13-A-2{,}500-0.05-2{,}000$ Subjected to El Centro: a) Columns, b) Beams

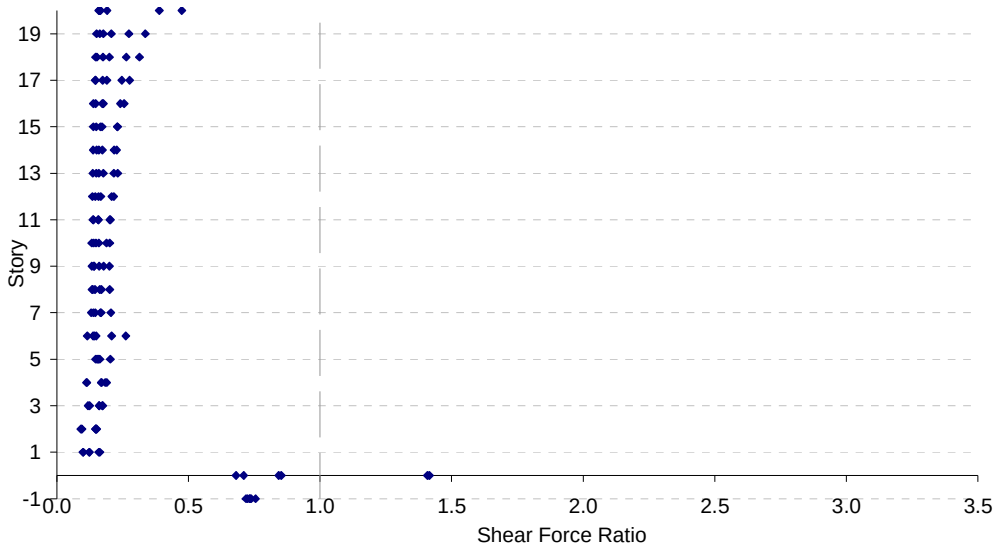

a)

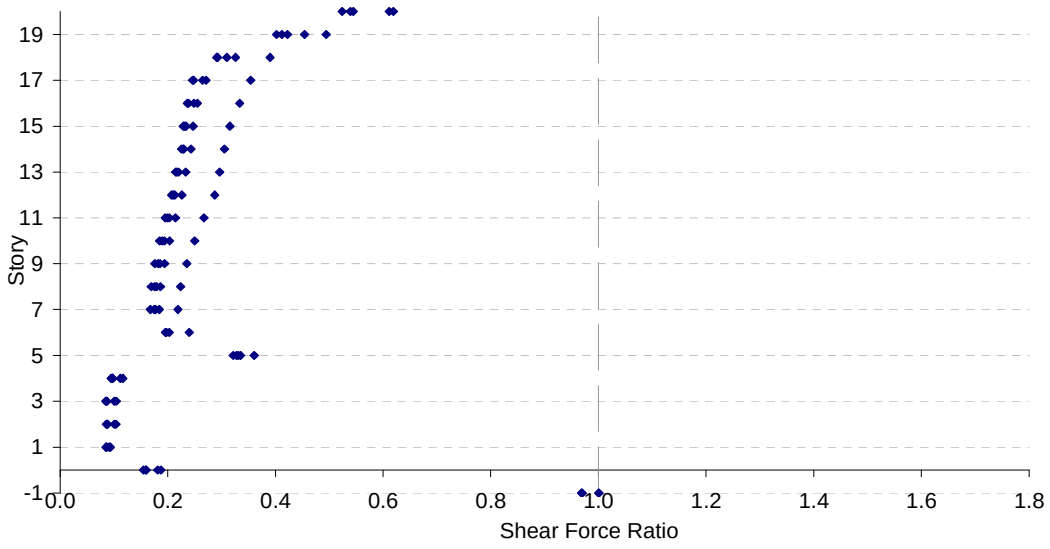

b)

Figure E.11 Shear Force Ratios for $BL\_20-0:5-A-236-0.01-1{,}000$ Subjected to Northridge: a) Columns, b) Beams

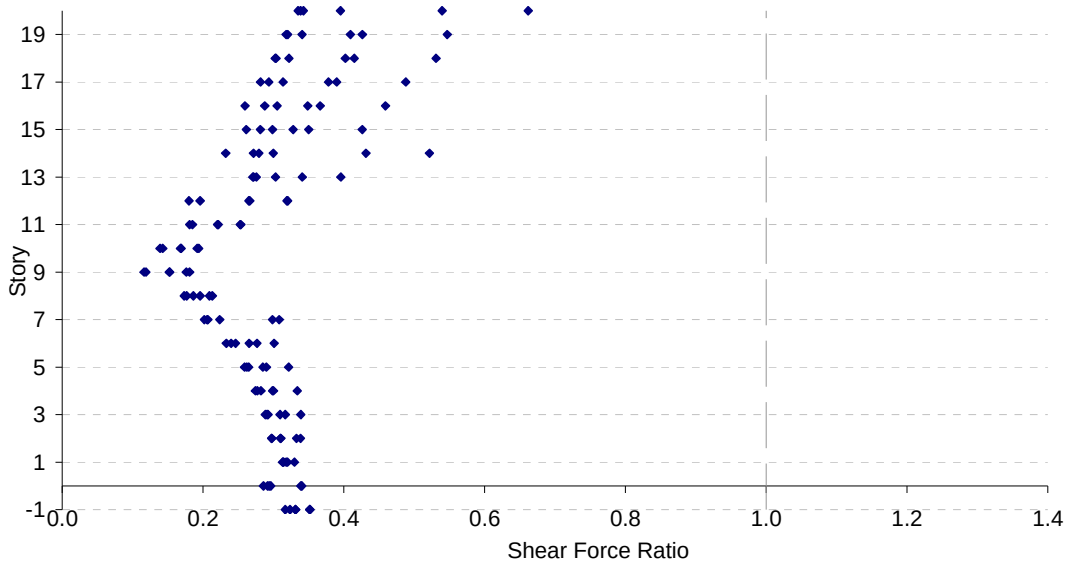

a)

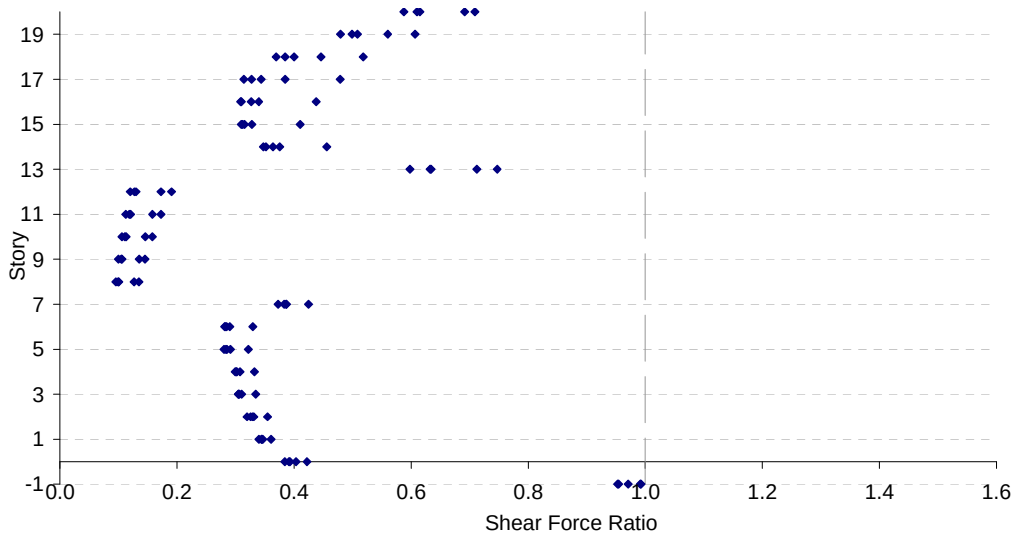

b)

Figure E.12 Shear Force Ratios for $BL\_20-9:13-A-236-0.01-1{,}000$ Subjected to Northridge: a) Columns, b) Beams

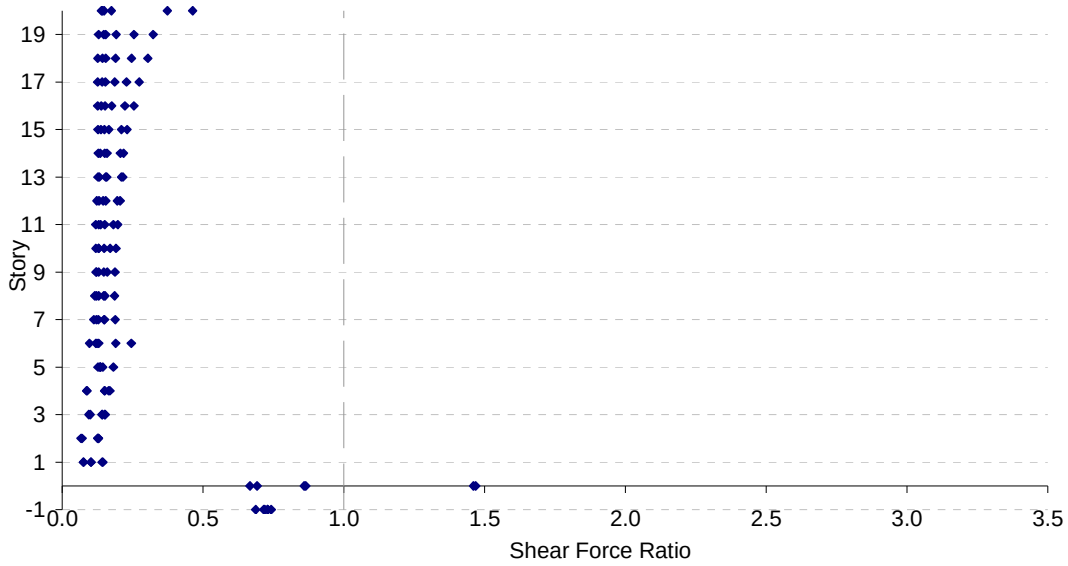

a)

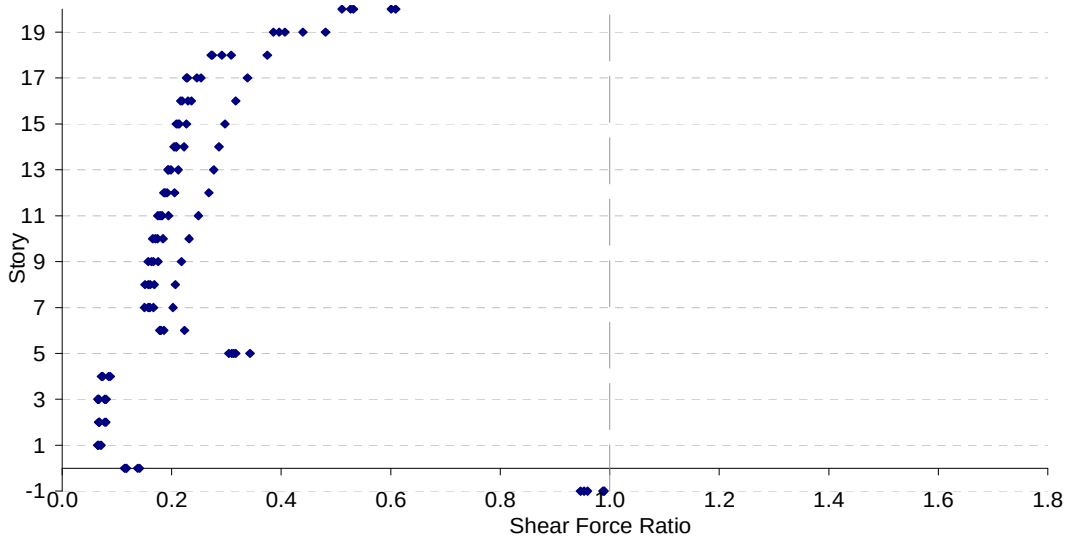

b)

Figure E.13 Shear Force Ratios for $BL\_20-0:5-A-100-0.1-120$ Subjected to Northridge: a) Columns, b) Beams

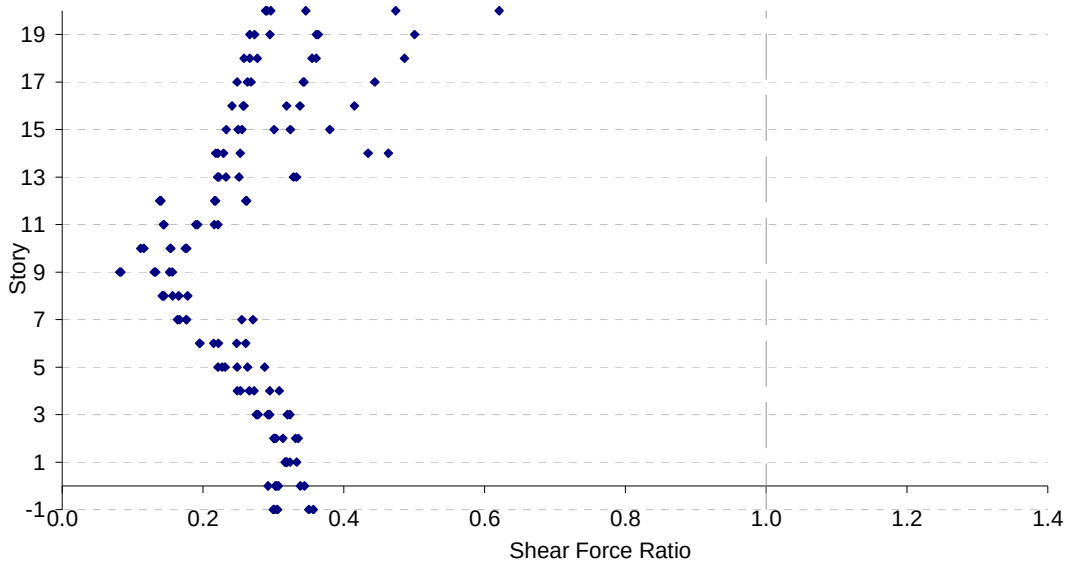

a)

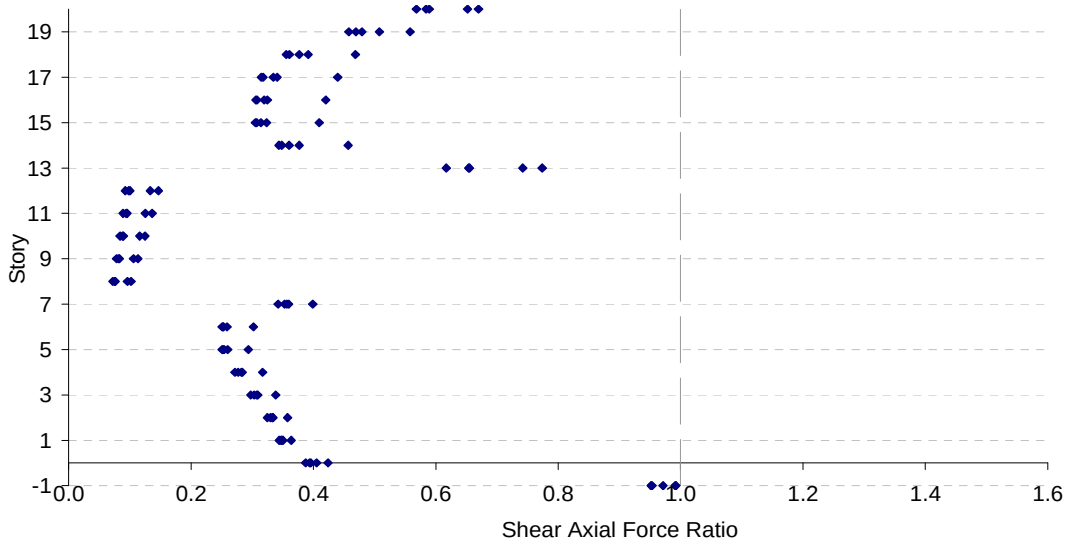

b)

Figure E.14 Shear Force Ratios for $BL\_20-9:13-A-100-0.1-120$ Subjected to Northridge: a) Columns, b) Beams

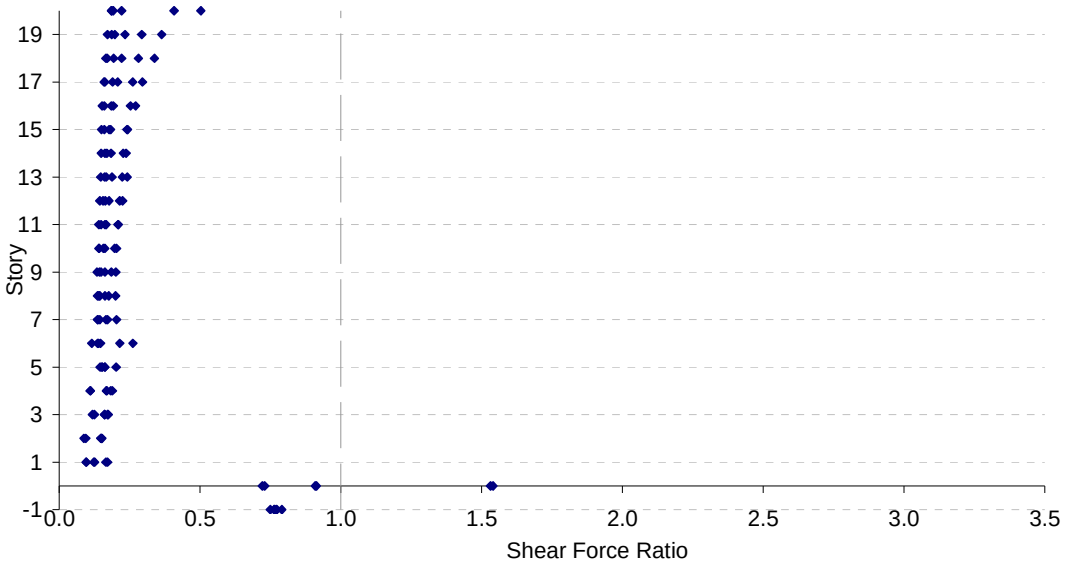

a)

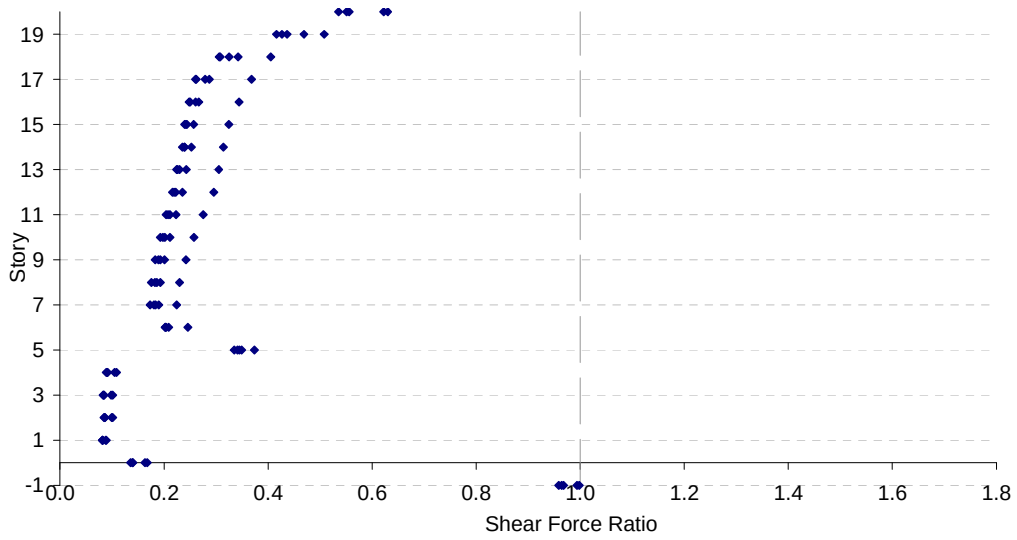

b)

Figure E.15 Shear Force Ratios for $BL\_20-0:5-A-500-0.05-500$ Subjected to Northridge: a) Columns, b) Beams

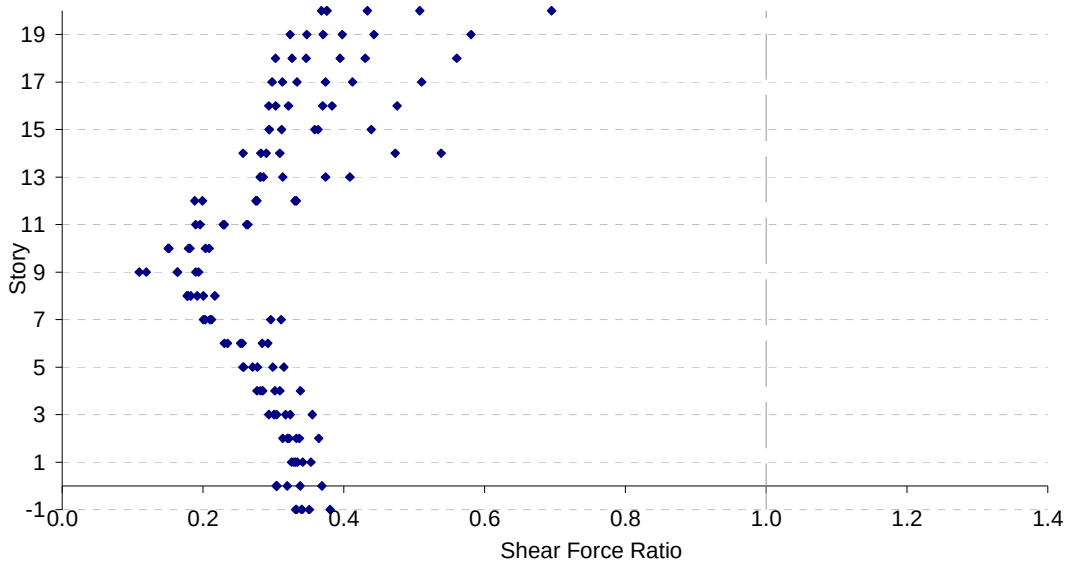

a)

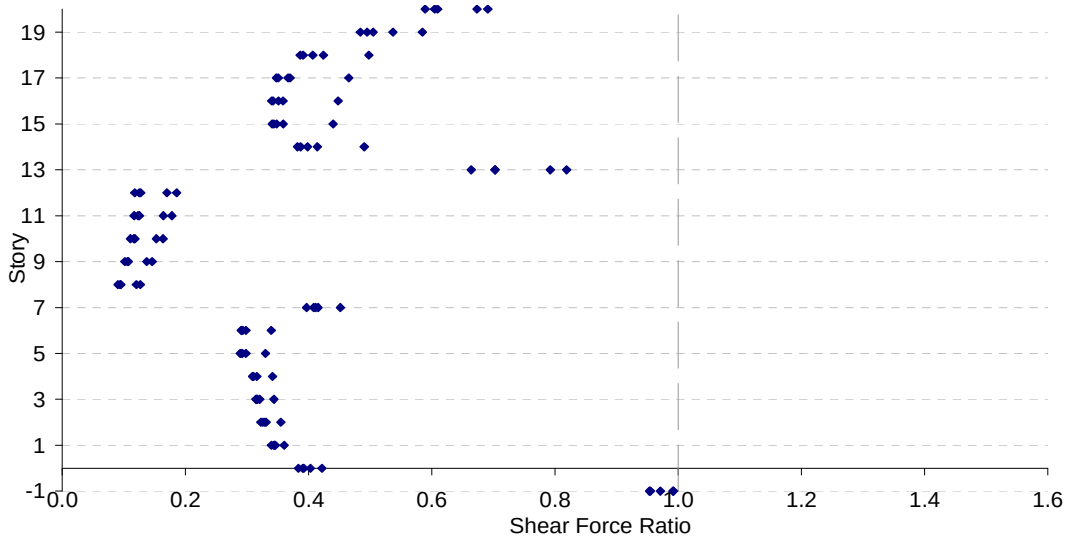

b)

Figure E.16 Shear Force Ratios for $BL\_20-9:13-A-500-0.05-500$ Subjected to Northridge: a) Columns, b) Beams

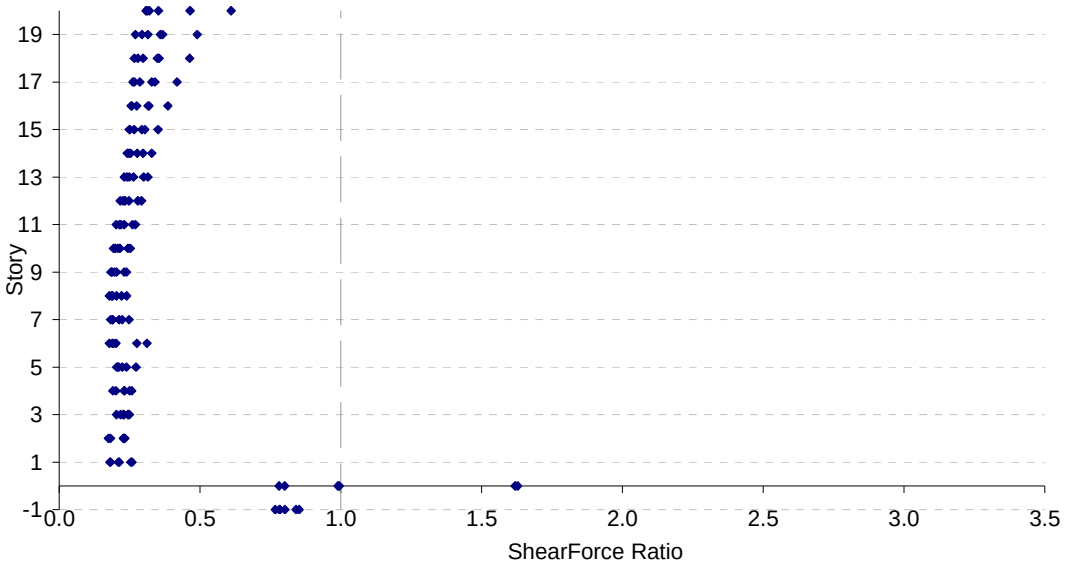

a)

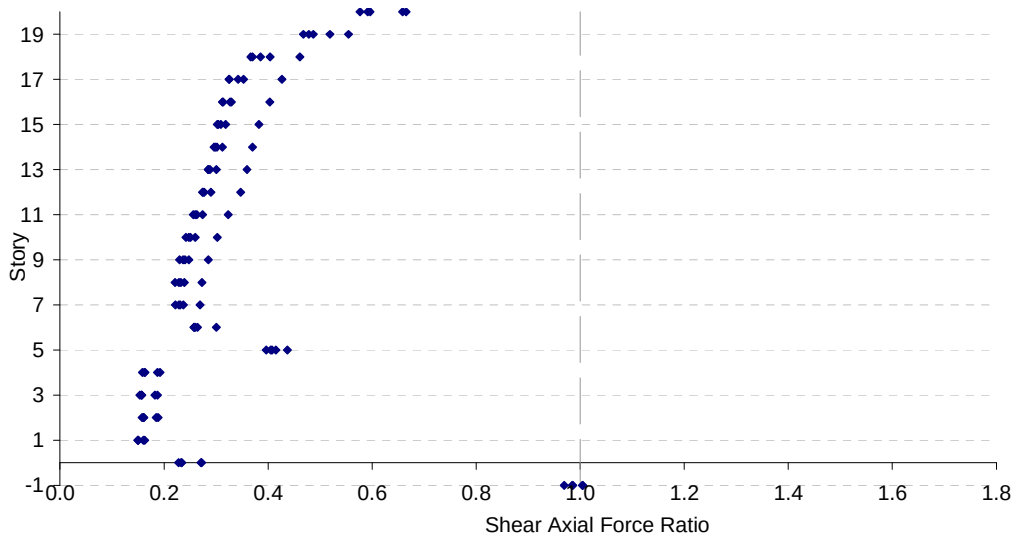

b)

Figure E.17 Shear Force Ratios for $BL\_20-0:5-A-800-0.1-2{,}300$ Subjected to Northridge: a) Columns, b) Beams

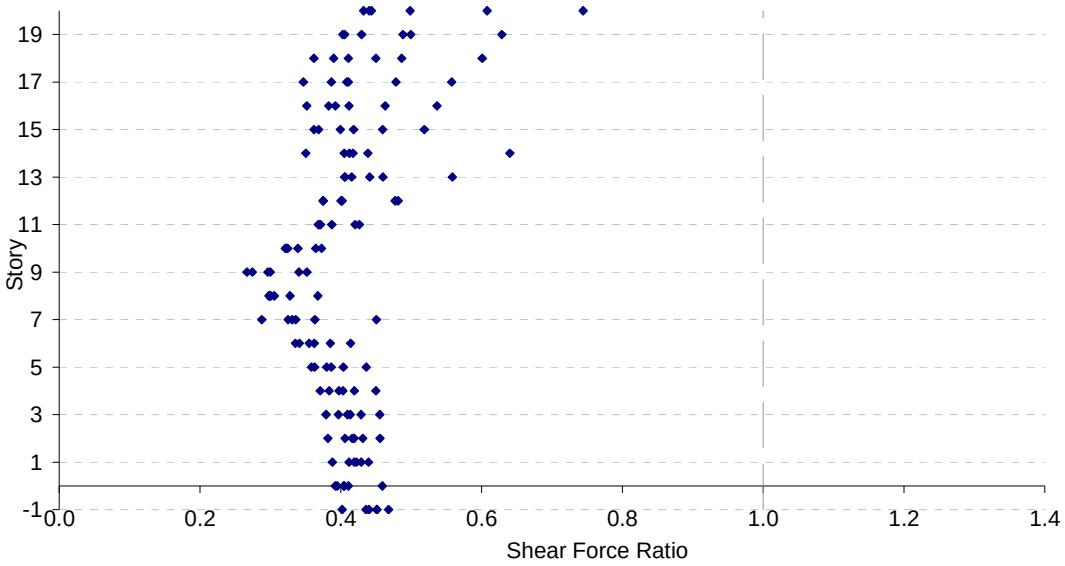

a)

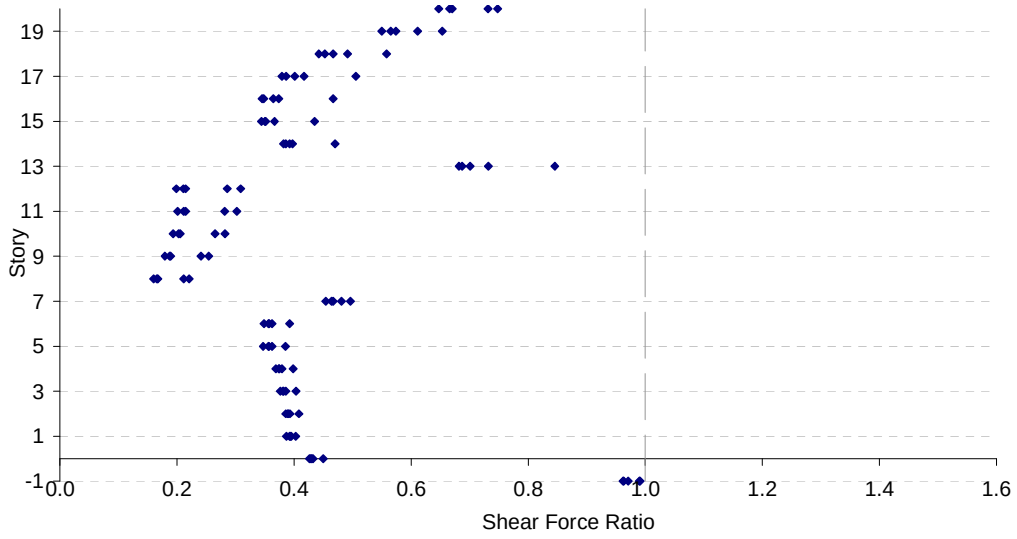

b)

Figure E.18 Shear Force Ratios for $BL\_20-9:13-A-800-0.1-2{,}300$ Subjected to Northridge: a) Columns, b) Beams

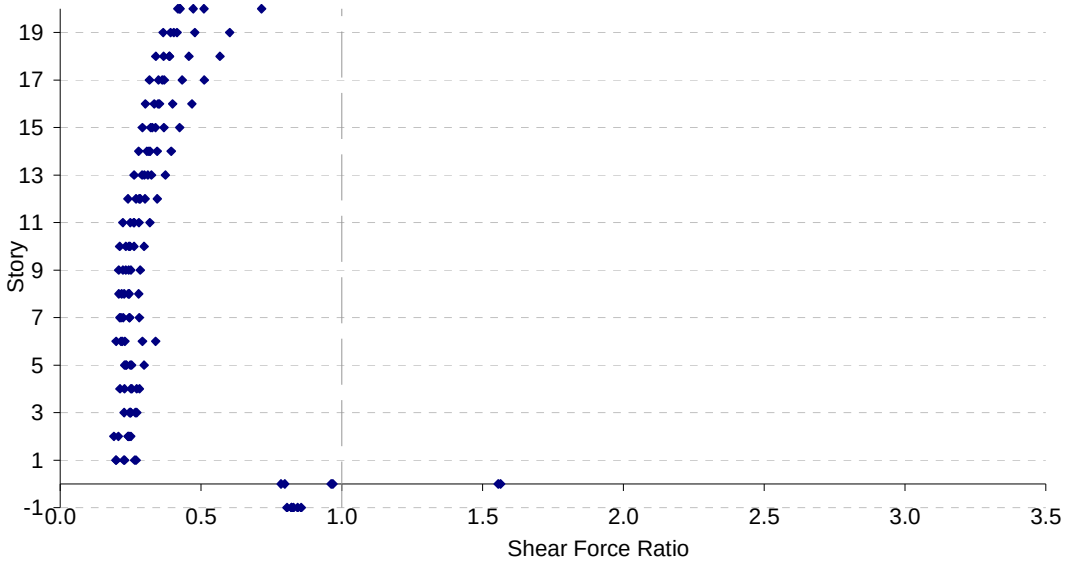

a)

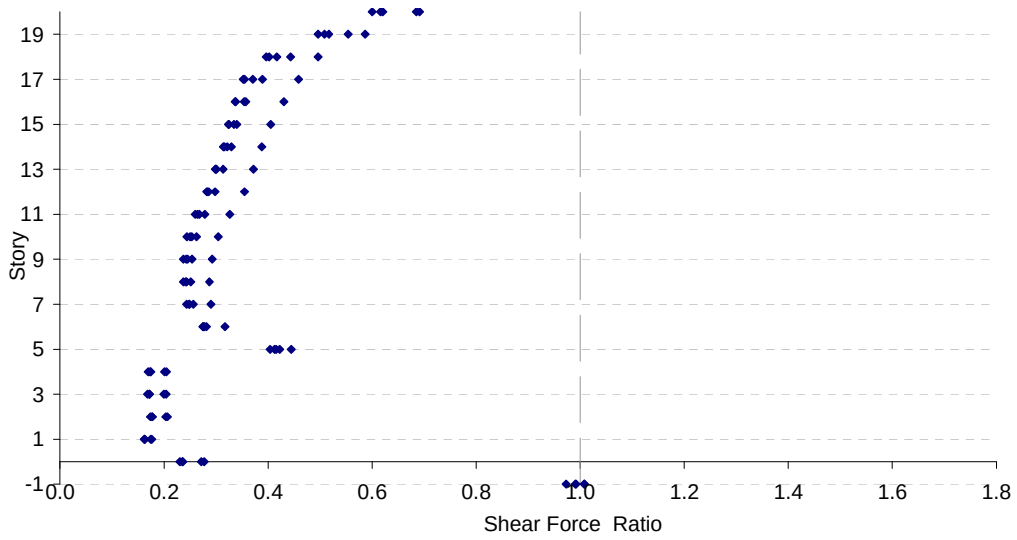

b)

Figure E.19 Shear Force Ratios for $BL\_20-0:5-A-2{,}500-0.05-2{,}000$ Subjected to Northridge: a) Columns, b) Beams

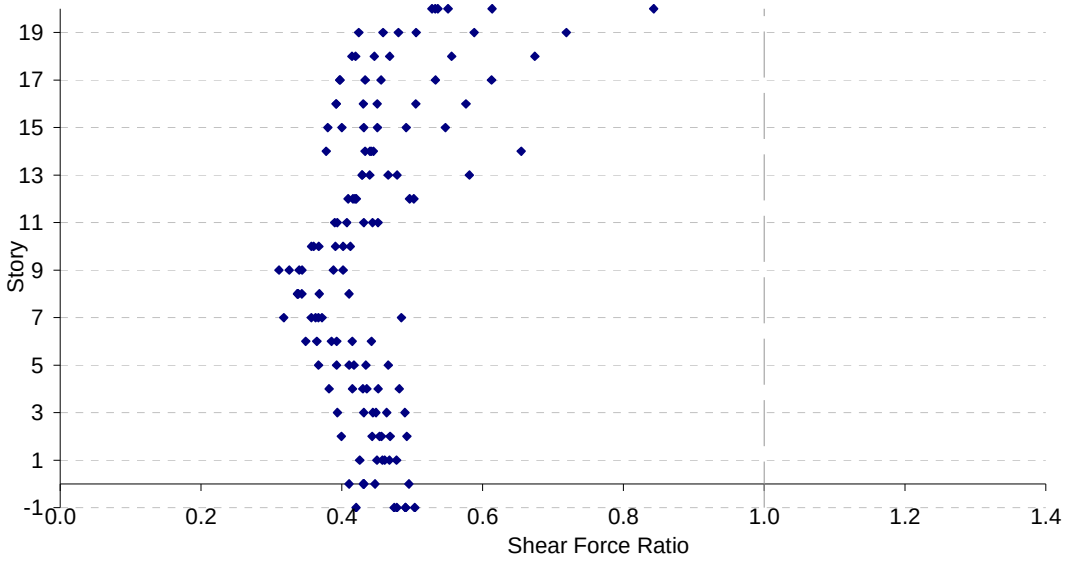

a)

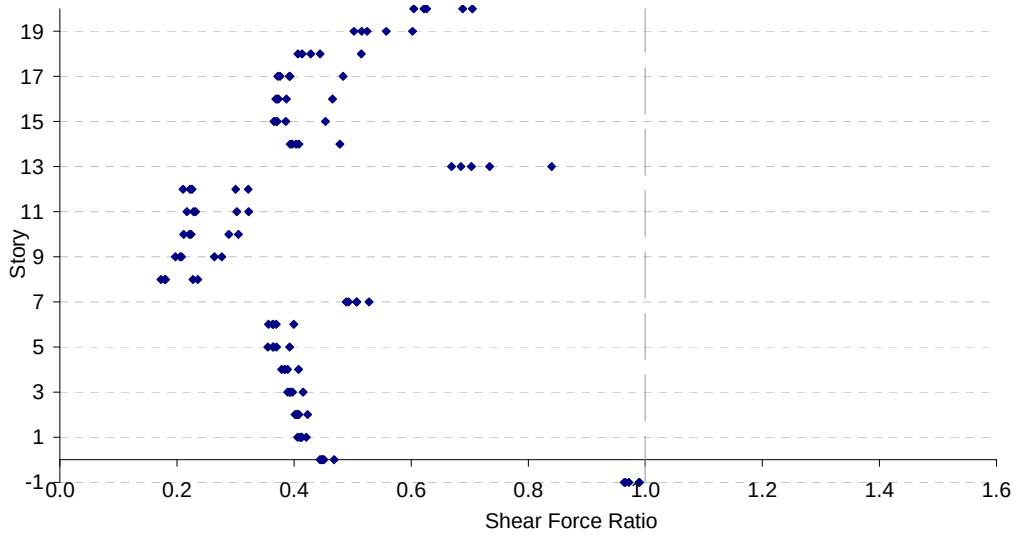

b)

Figure E.20 Shear Force Ratios for $BL\_20-9:13-A-2{,}500-0.05-2{,}000$ Subjected to Northridge: a) Columns, b) Beams

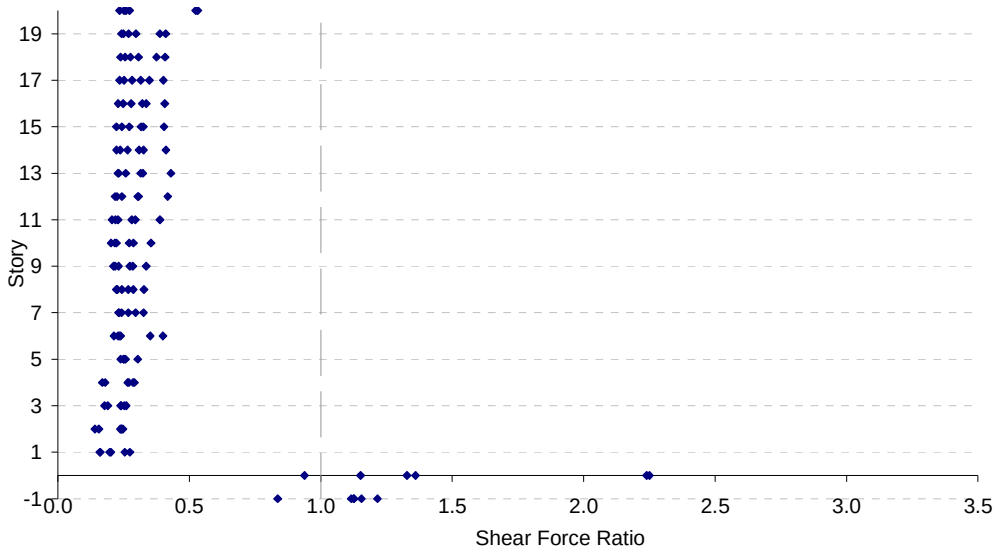

a)

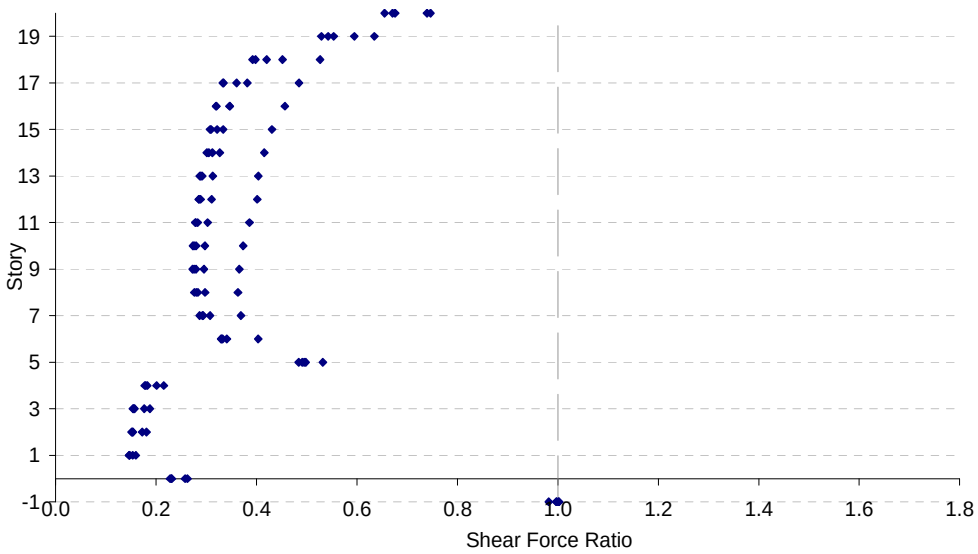

b)

Figure E.21 Shear Force Ratios for $BL\_20-0:5-A-236-0.01-1{,}000$ Subjected to Parkfield: a) Columns, b) Beams

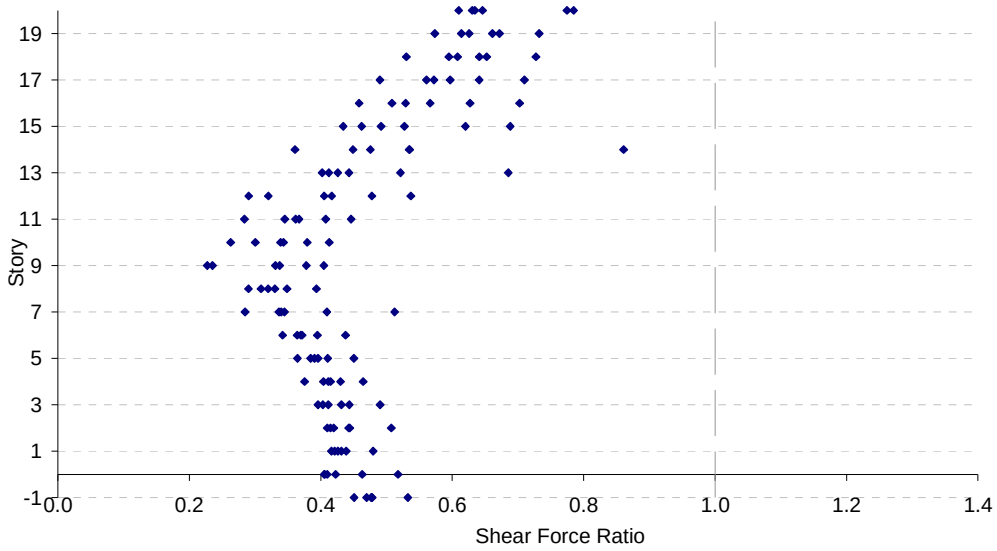

a)

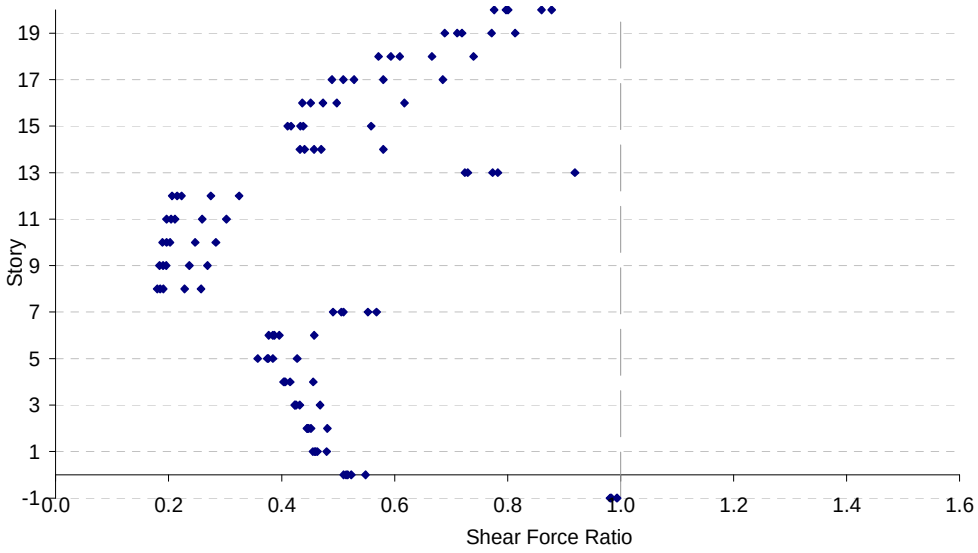

b)

Figure E.22 Shear Force Ratios for $BL\_20-9:13-A-236-0.01-1{,}000$ Subjected to Parkfield: a) Columns, b) Beams

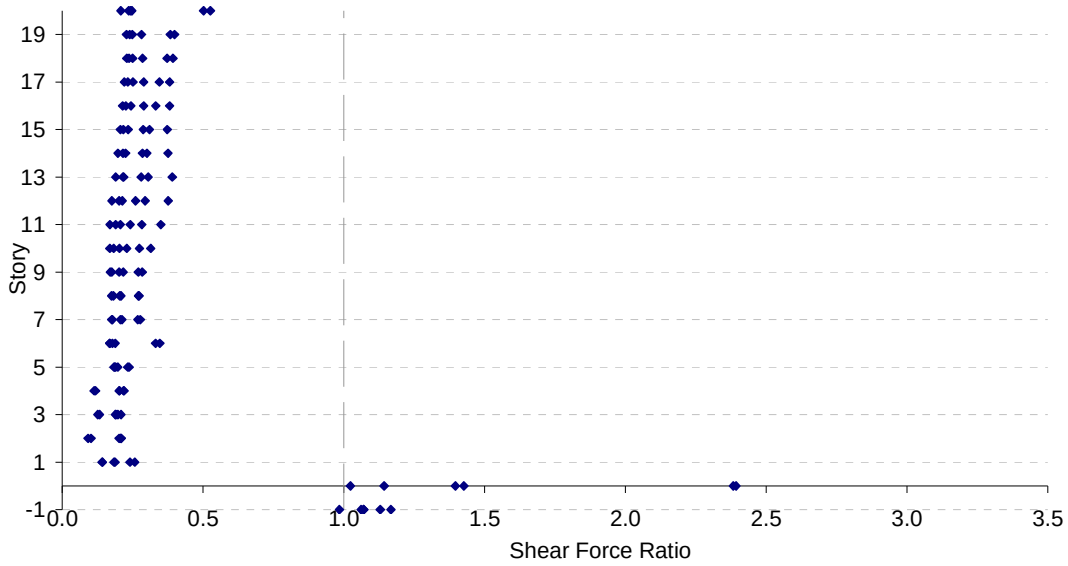

a)

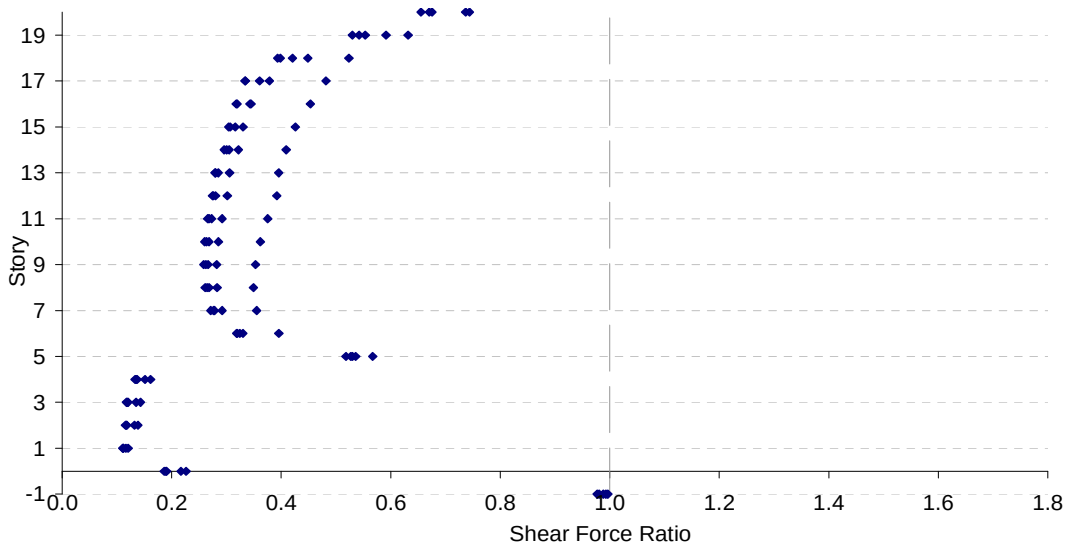

b)

Figure E.23 Shear Force Ratios for $BL\_20-0:5-A-100-0.1-120$ Subjected to Parkfield: a) Columns, b) Beams

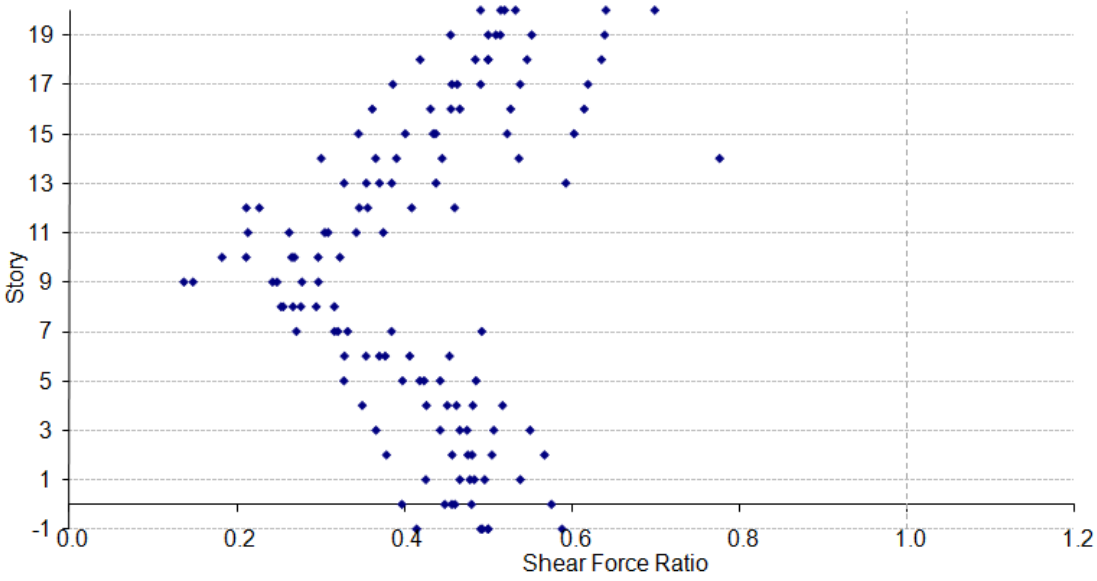

a)

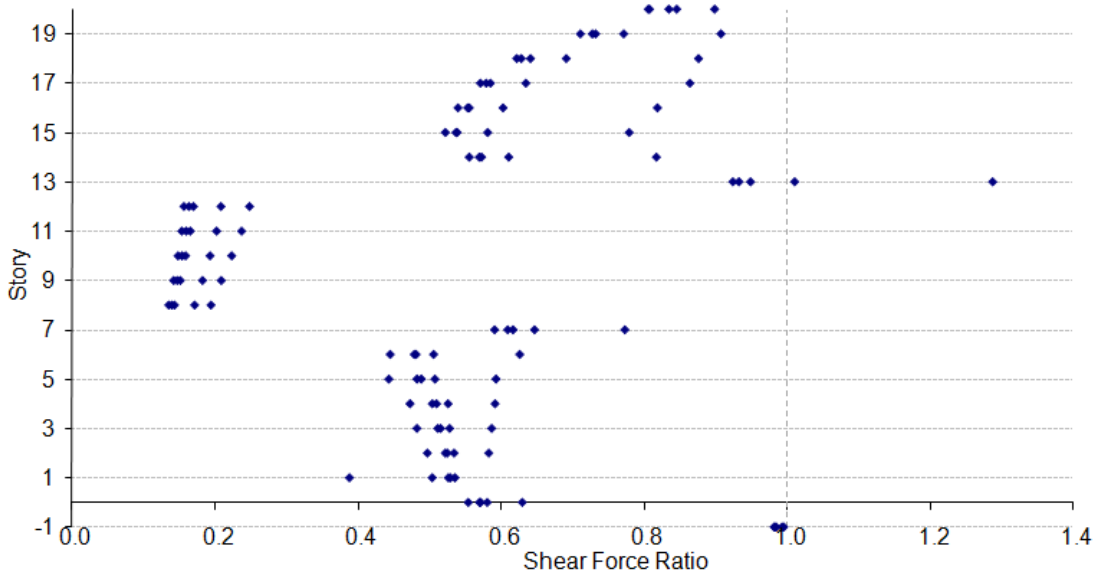

b)

Figure E.24 Shear Force Ratios for $BL\_20-9:13-A-100-0.1-120$ Subjected to Parkfield: a) Columns, b) Beams

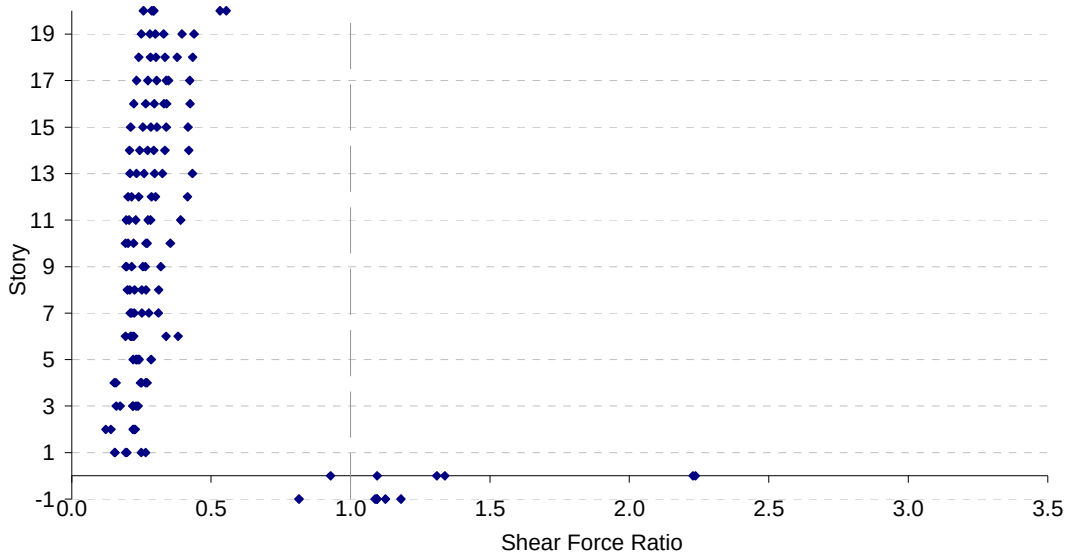

a)

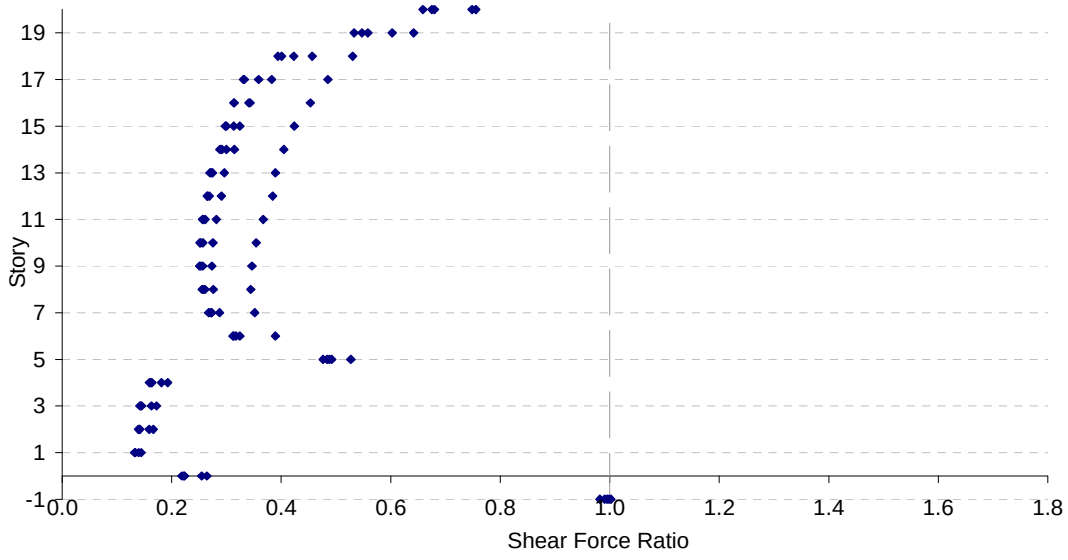

b)

Figure E.25 Shear Force Ratios for $BL\_20-0:5-A-500-0.05-500$ Subjected to Parkfield: a) Columns, b) Beams

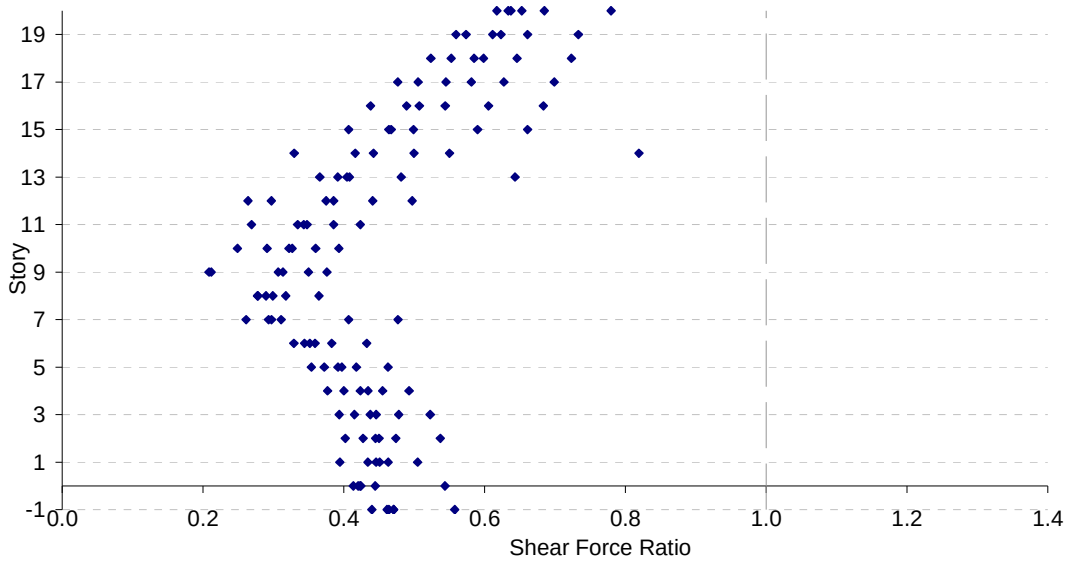

a)

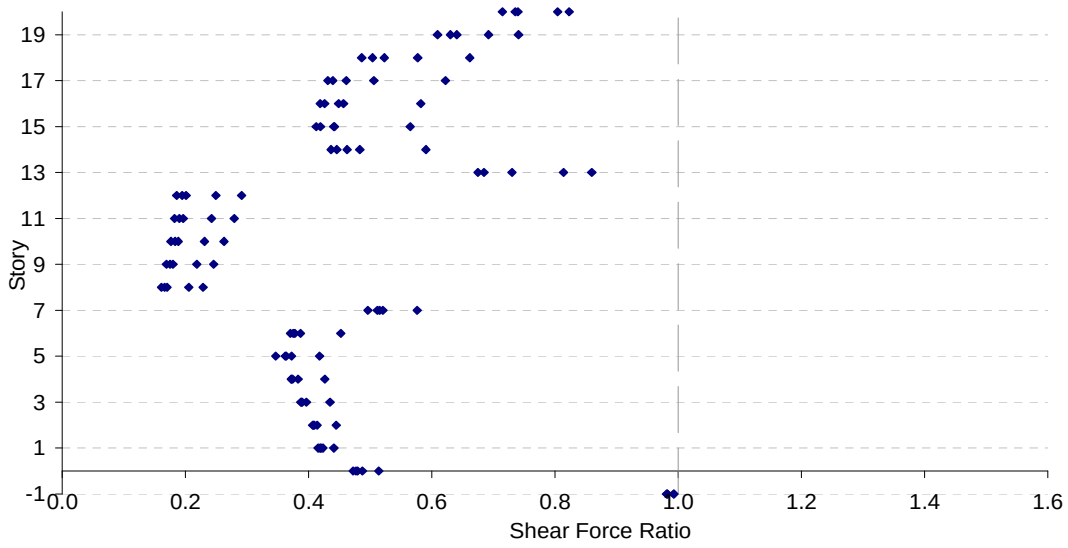

b)

Figure E.26 Shear Force Ratios for $BL\_20-9:13-A-500-0.05-500$ Subjected to Parkfield: a) Columns, b) Beams

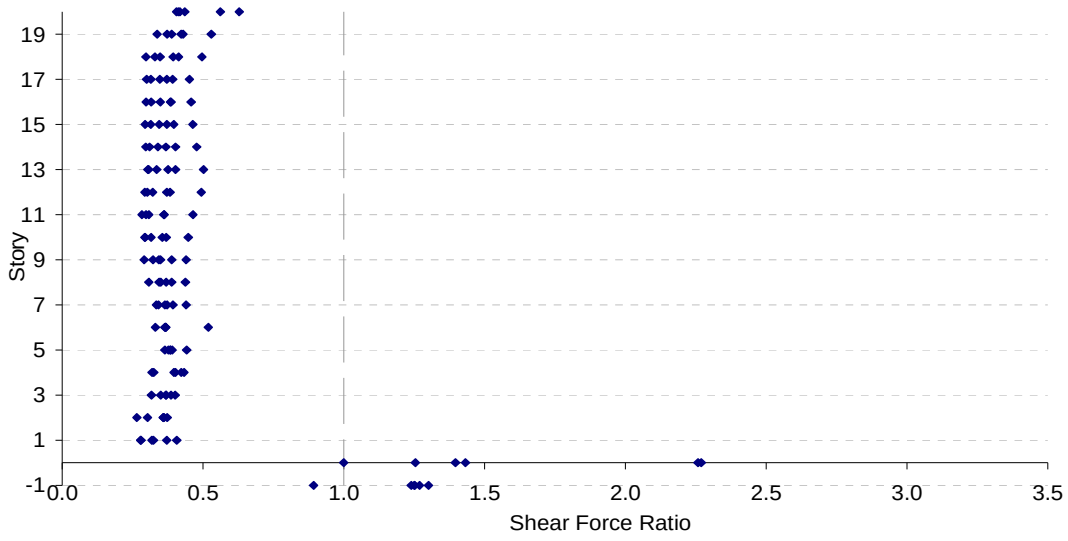

a)

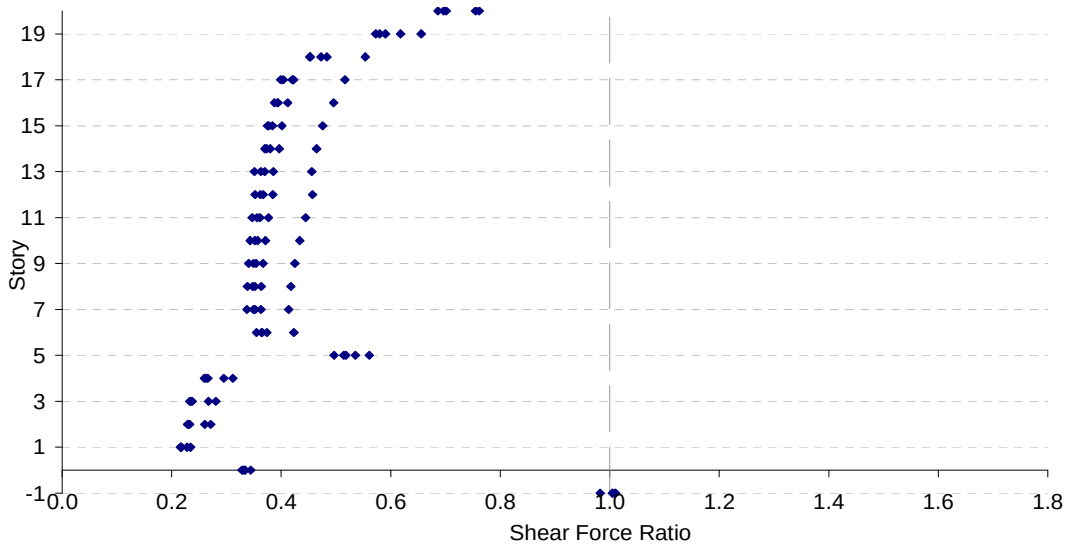

b)

Figure E.27 Shear Force Ratios for $BL\_20-0:5-A-800-0.1-2{,}300$ Subjected to Parkfield: a) Columns, b) Beams

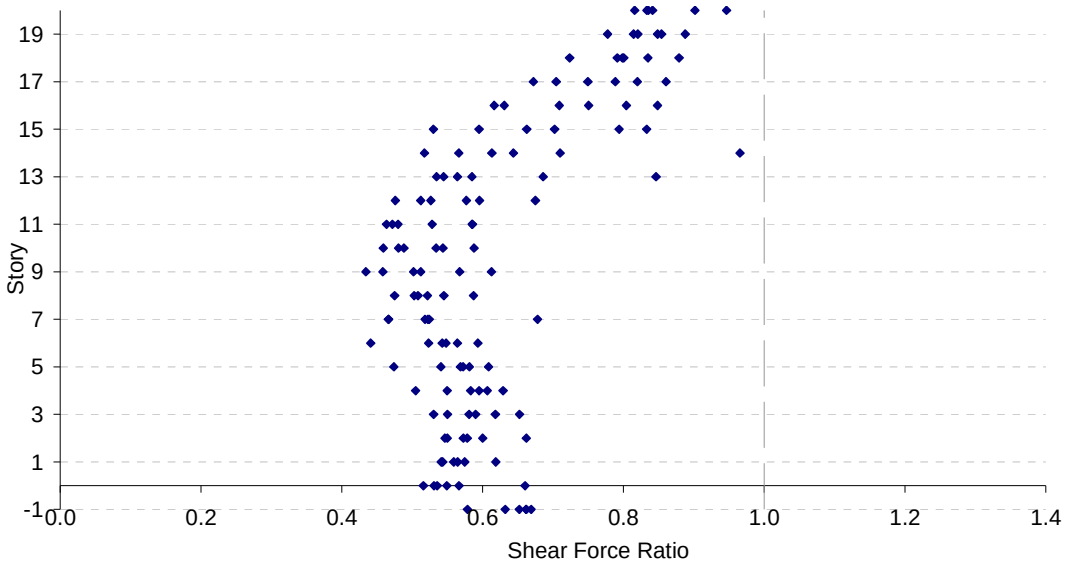

a)

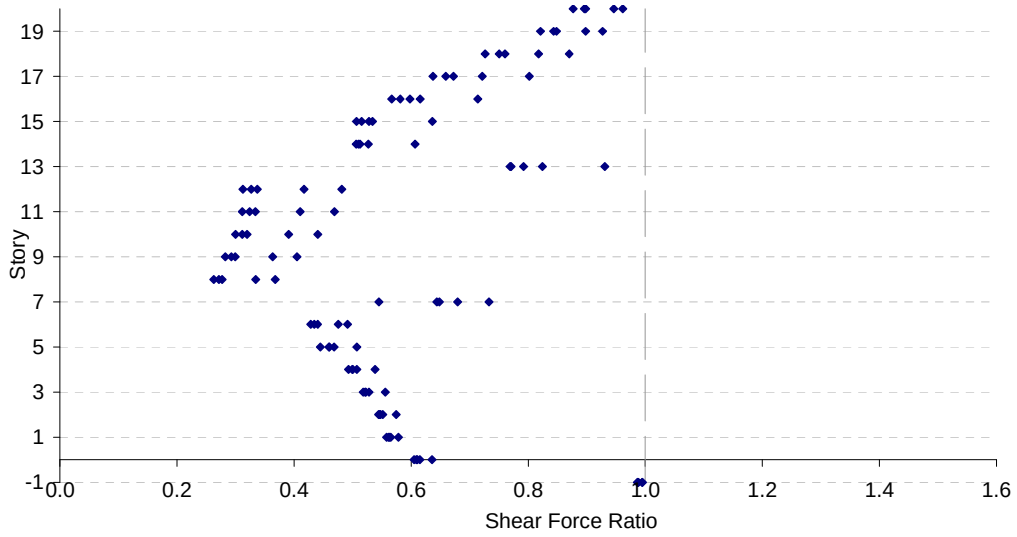

b)

Figure E.28 Shear Force Ratios for $BL\_20-9:13-A-800-0.1-2{,}300$ Subjected to Parkfield: a) Columns, b) Beams

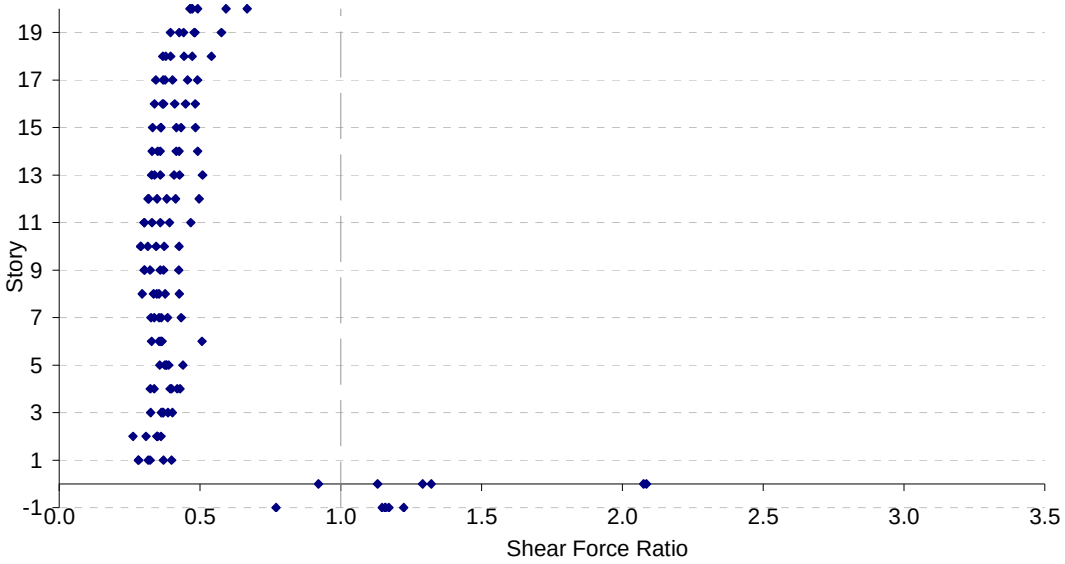

a)

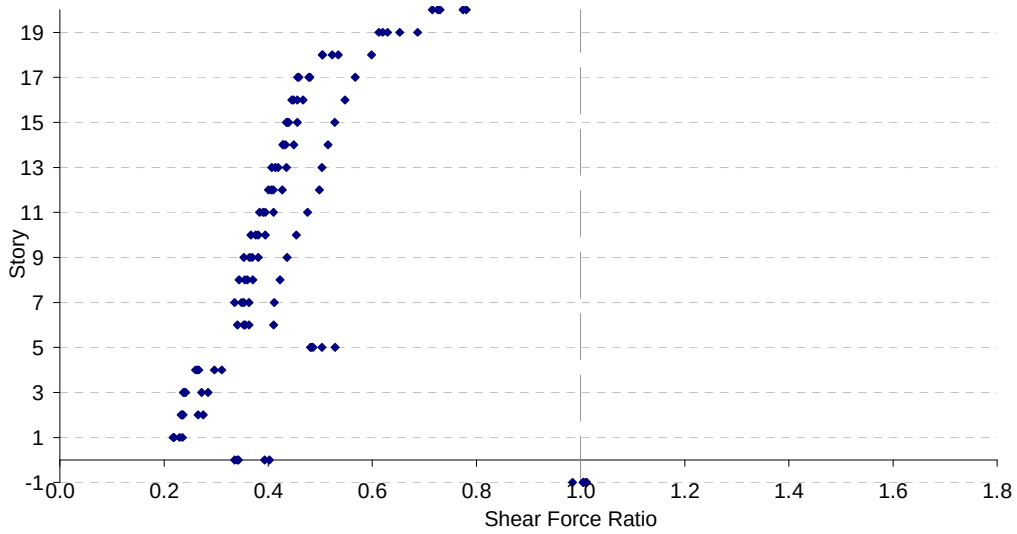

b)

Figure E.29 Shear Force Ratios for $BL\_20-0:5-A-2{,}500-0.05-2{,}000$ Subjected to Parkfield: a) Columns, b) Beams

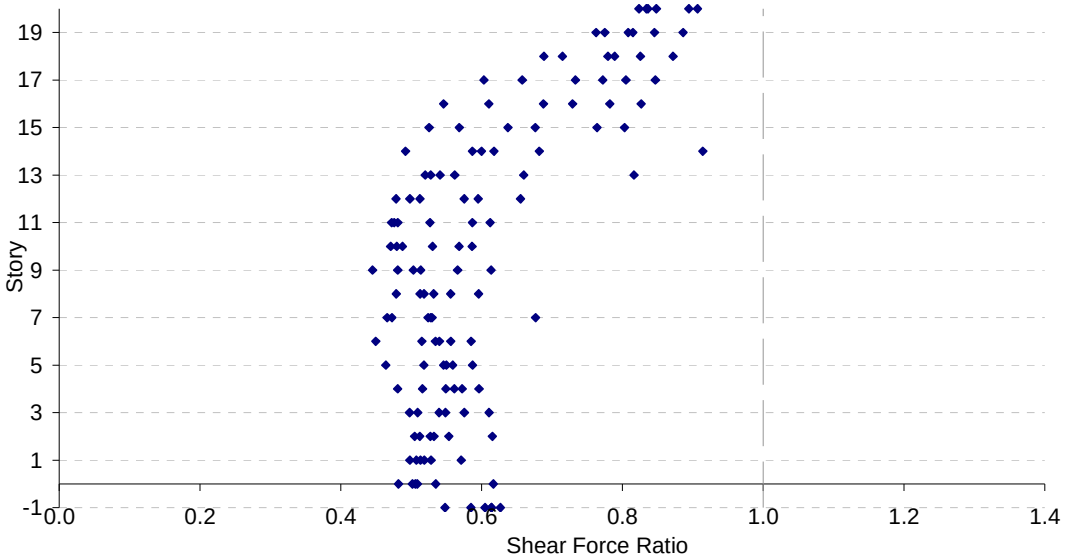

a)

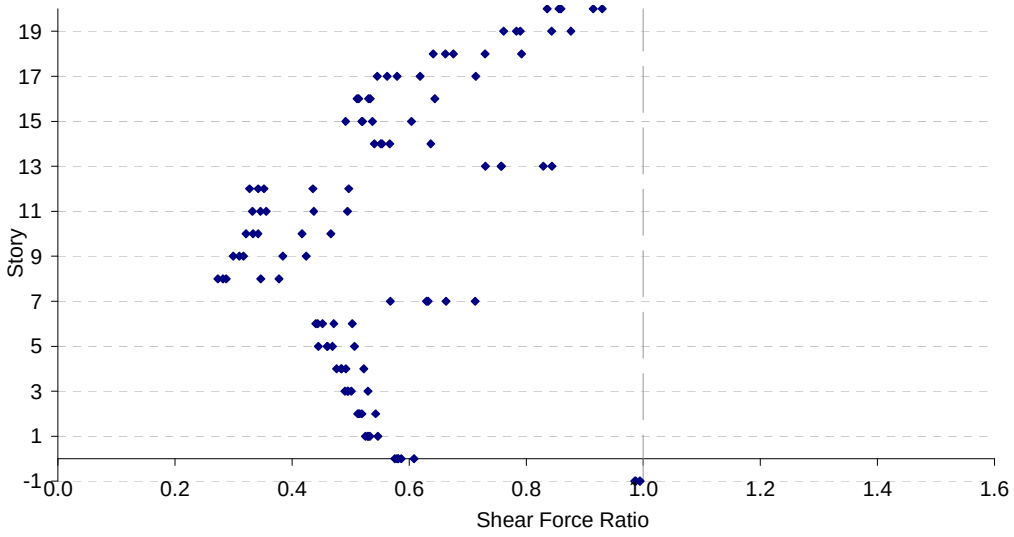

b)

Figure E.30 Shear Force Ratios for $BL\_20-9:13-A-2{,}500-0.05-2{,}000$ Subjected to Parkfield: a) Columns, b) Beams

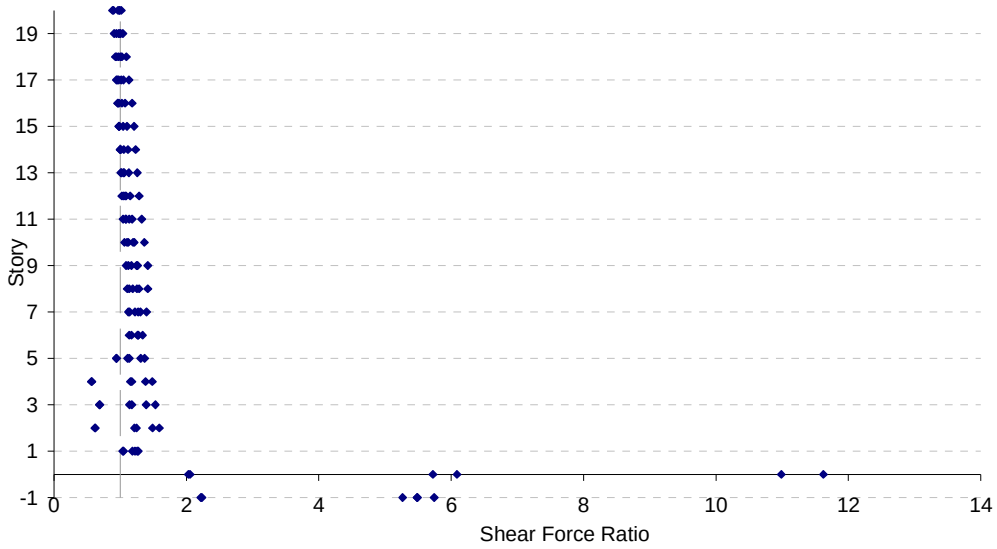

a)

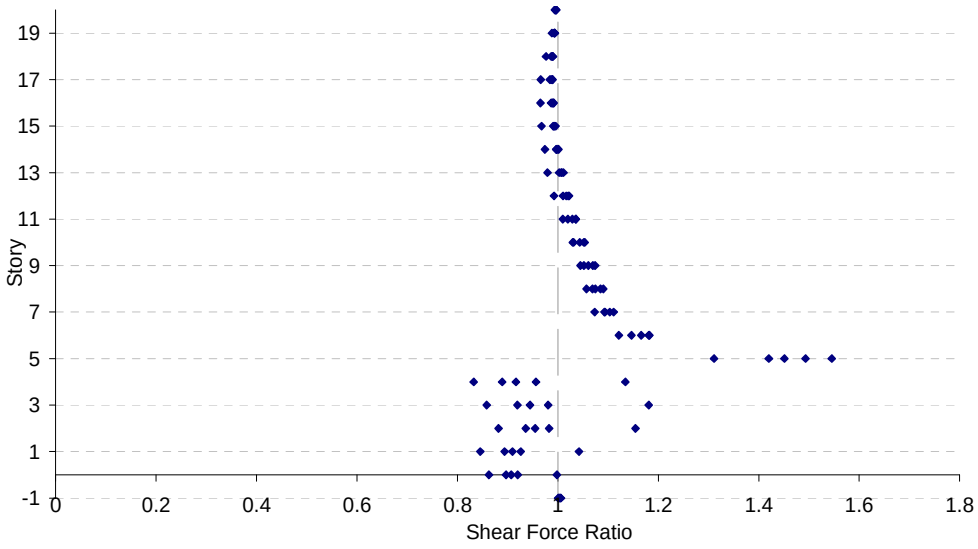

b)

Figure E.31 Shear Force Ratios for $BL\_20-0:5-A-236-0.01-1{,}000$ Subjected to Afyon Bay: a) Columns, b) Beams

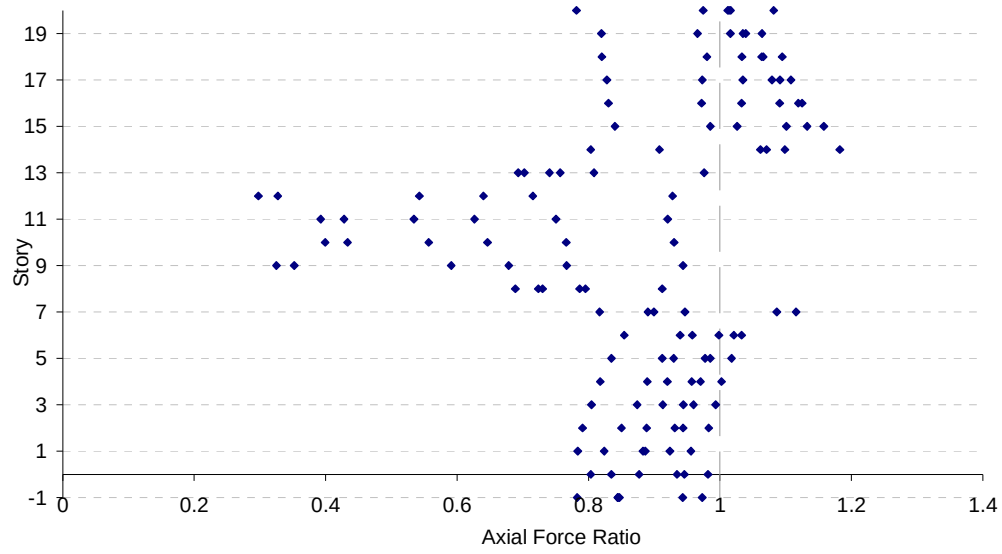

a)

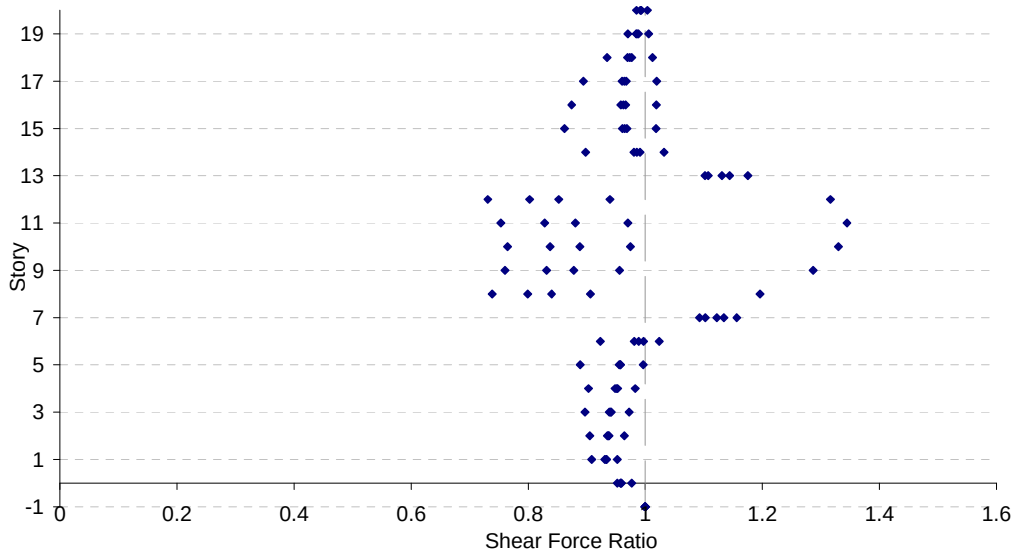

b)

Figure E.32 Shear Force Ratios for $BL\_20-9:13-A-236-0.01-1{,}000$ Subjected to Afyon Bay: a) Columns, b) Beams

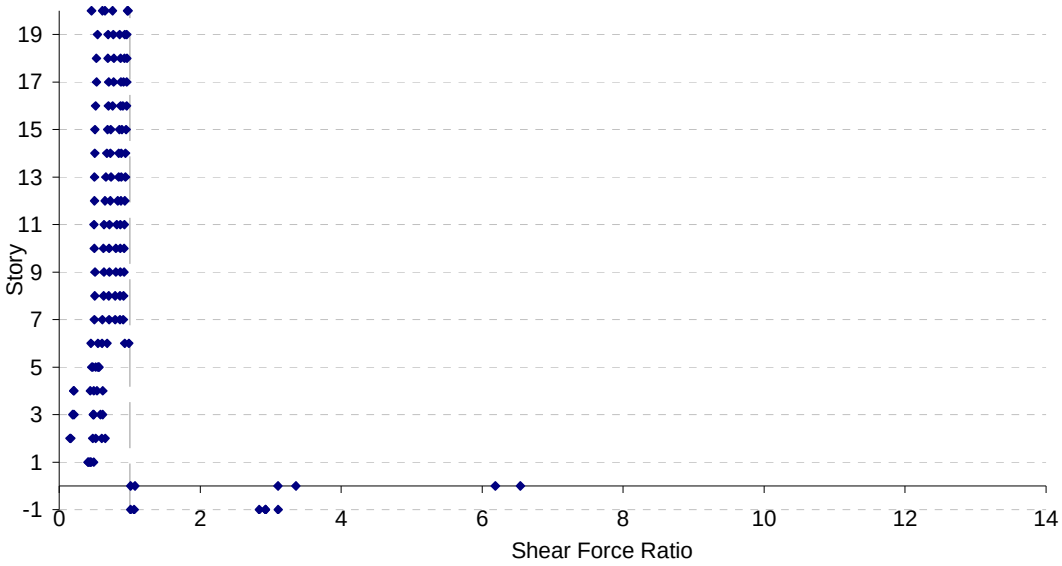

a)

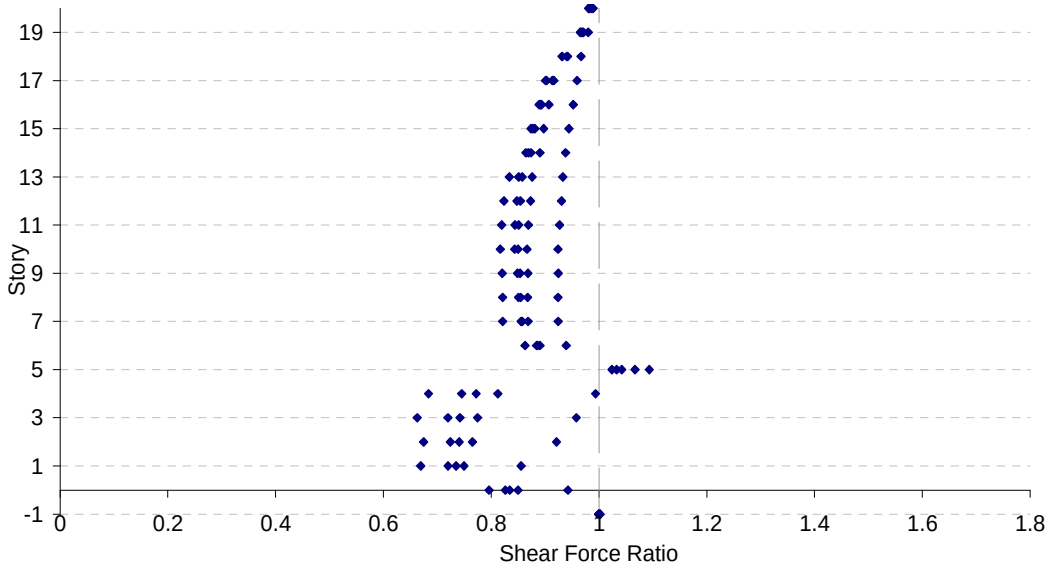

b)

Figure E.33 Shear Force Ratios for $BL\_20-0:5-A-100-0.1-120$ Subjected to Afyon Bay: a) Columns, b) Beams

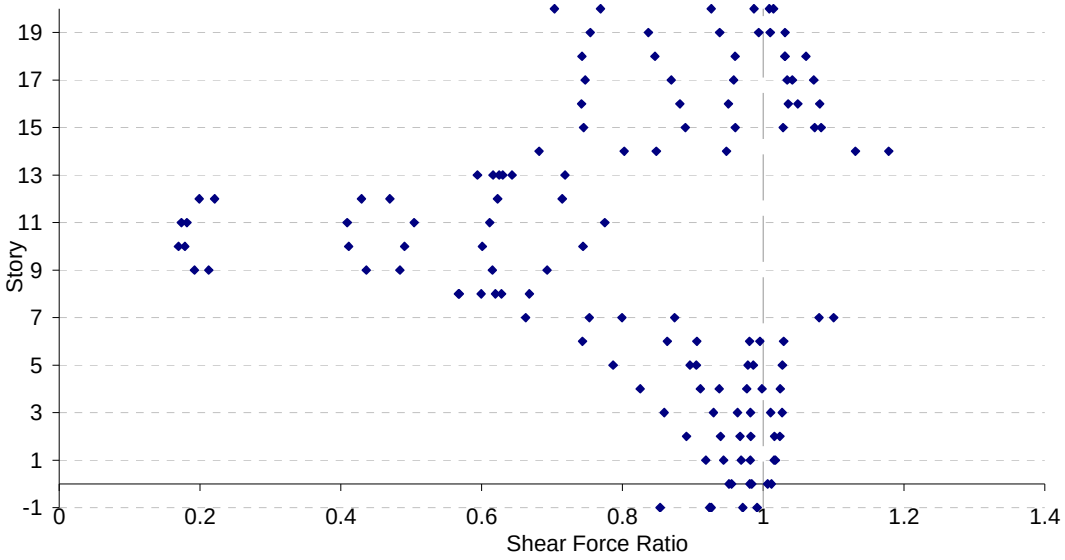

a)

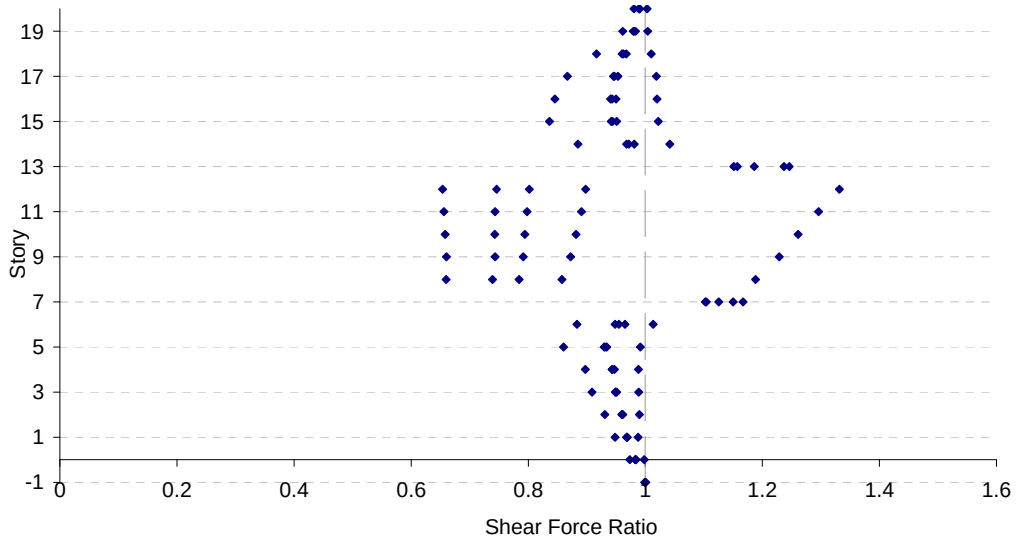

b)

Figure E.34 Shear Force Ratios for $BL\_20-9:13-A-100-0.1-120$ Subjected to Afyon Bay: a) Columns, b) Beams

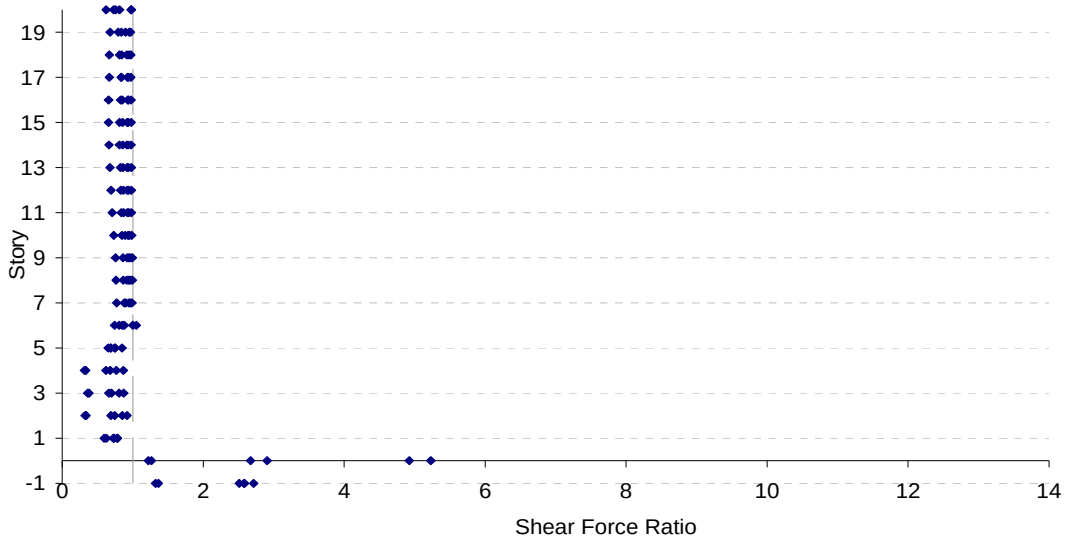

a)

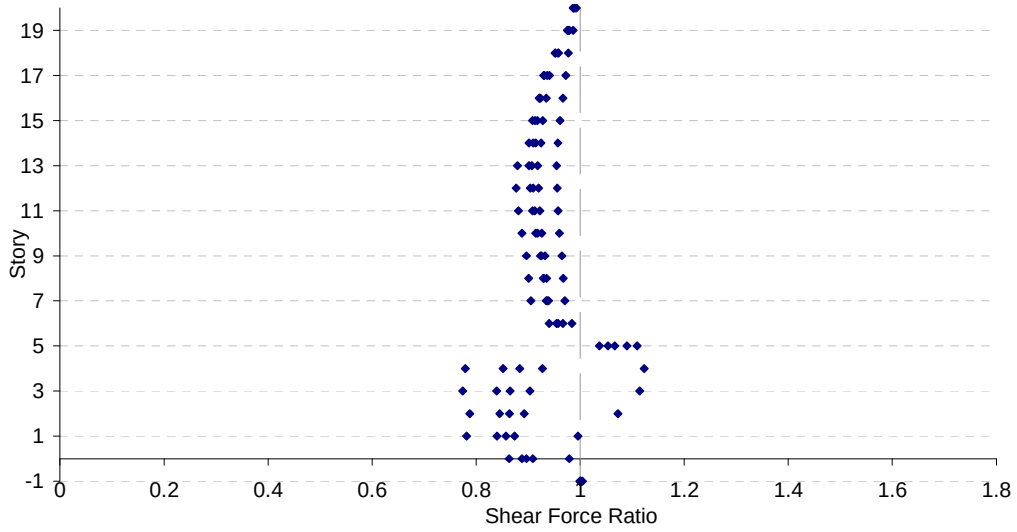

b)

Figure E.35 Shear Force Ratios for $BL\_20-0:5-A-500-0.05-500$ Subjected to Afyon Bay: a) Columns, b) Beams

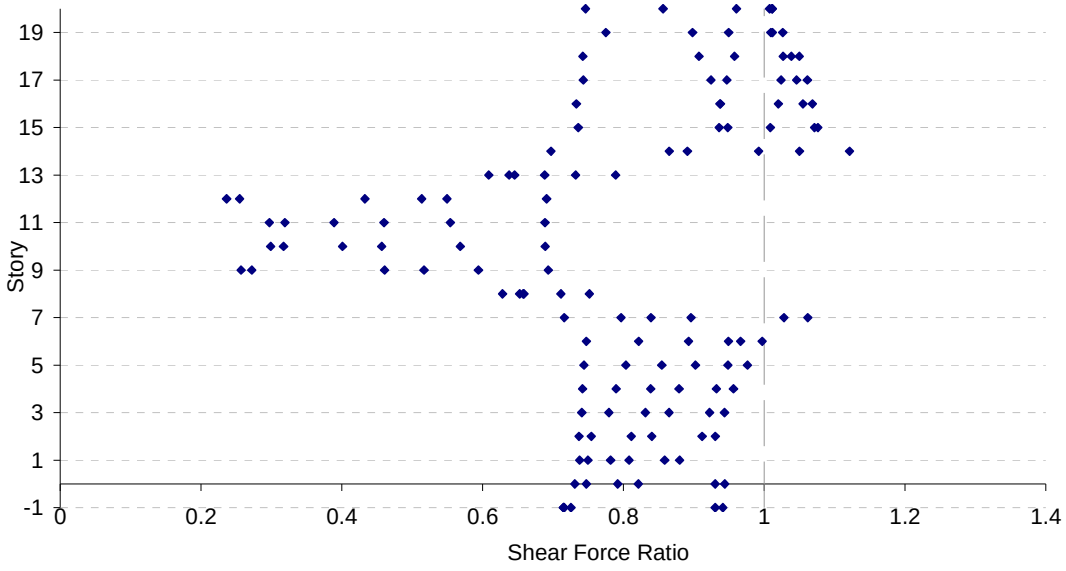

a)

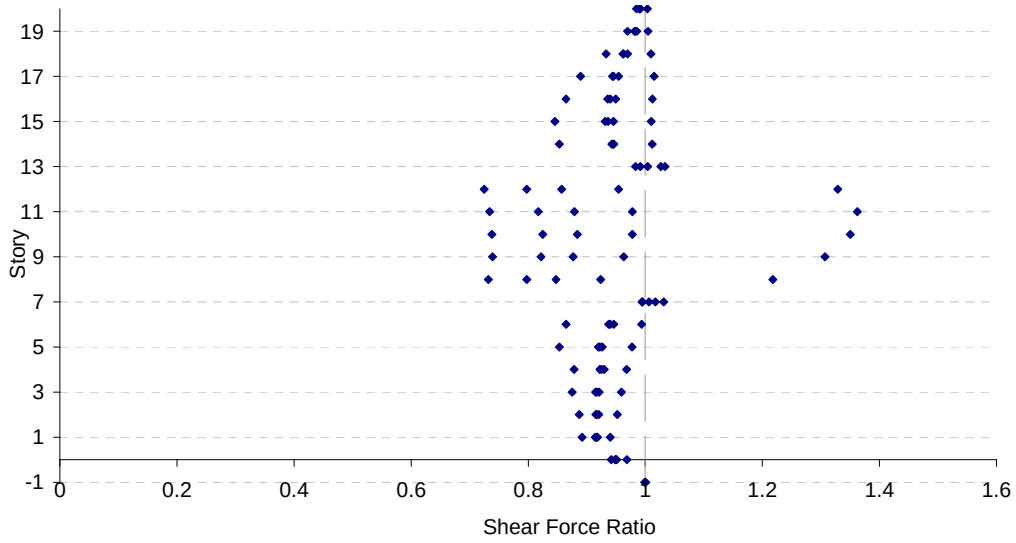

b)

Figure E.36 Shear Force Ratios for $BL\_20-9:13-A-500-0.05-500$ Subjected to Afyon Bay: a) Columns, b) Beams

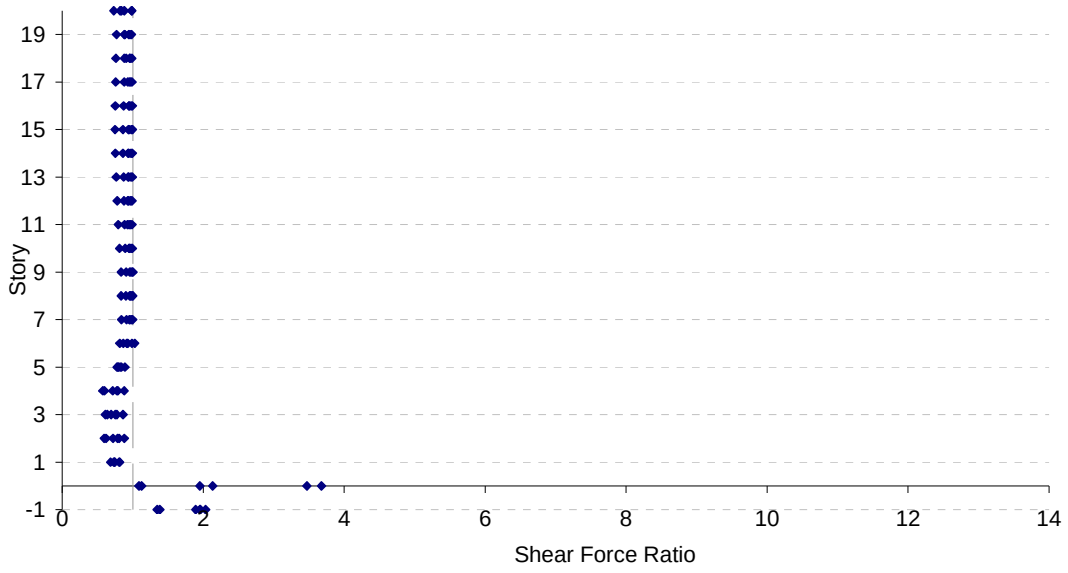

a)

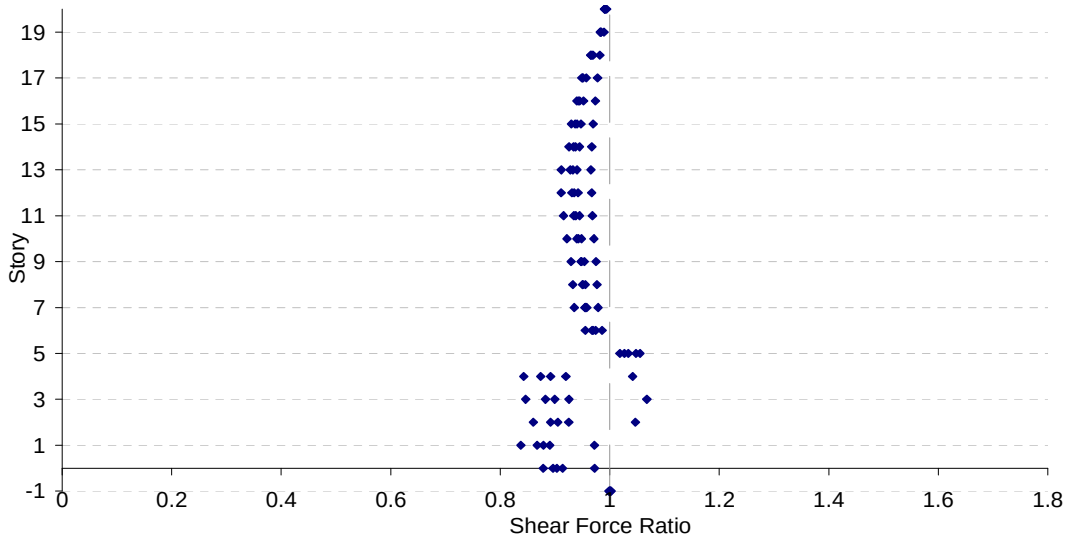

b)

Figure E.37 Shear Force Ratios for $BL\_20-0:5-A-800-0.1-2{,}300$ Subjected to Afyon Bay: a) Columns, b) Beams

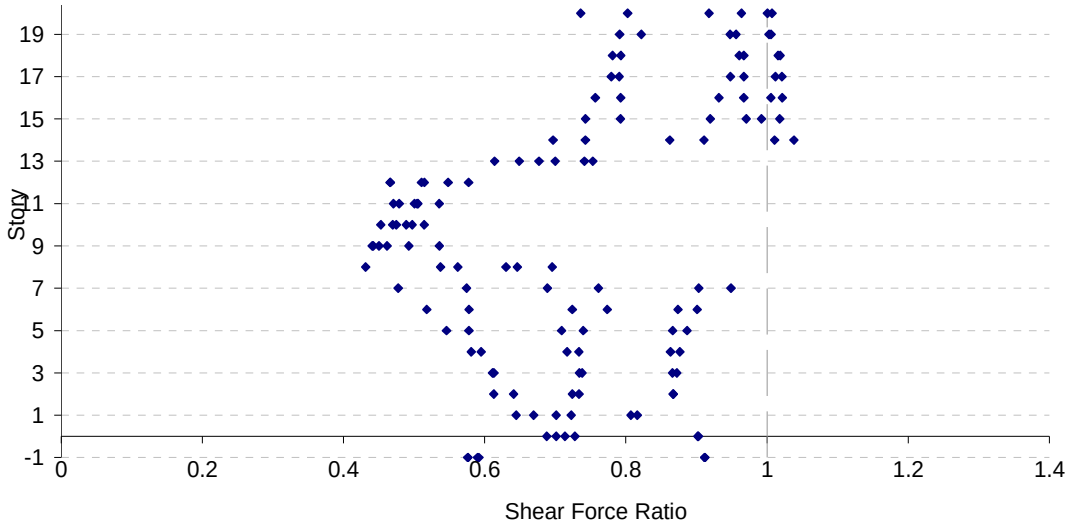

a)

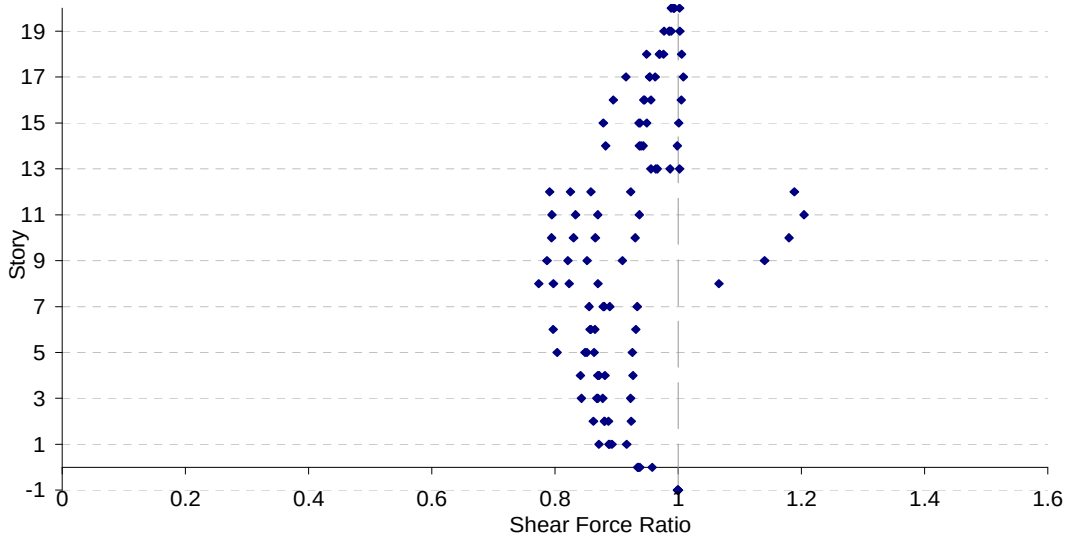

b)

Figure E.38 Shear Force Ratios for $BL\_20-9:13-A-800-0.1-2{,}300$ Subjected to Afyon Bay: a) Columns, b) Beams

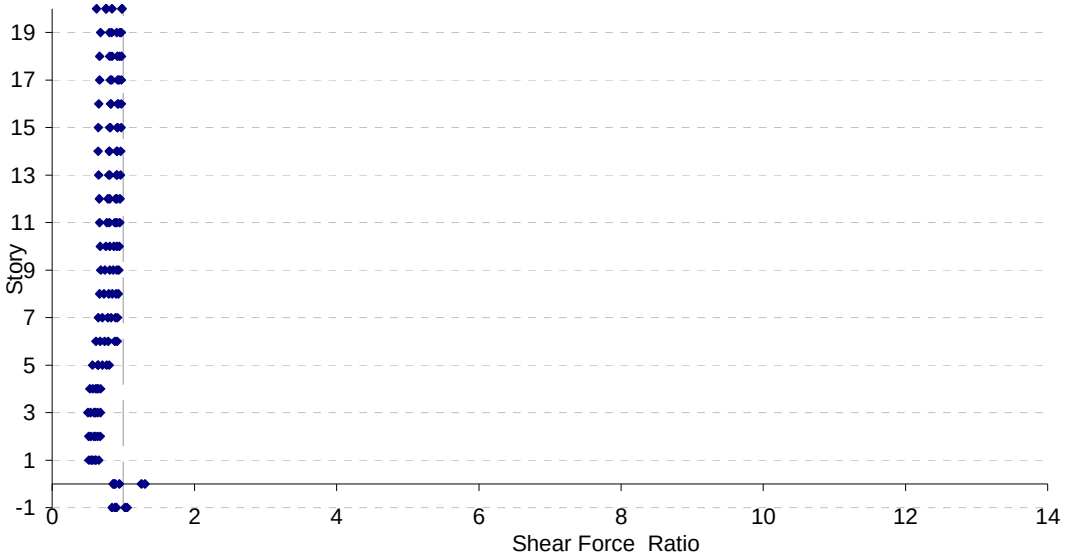

a)

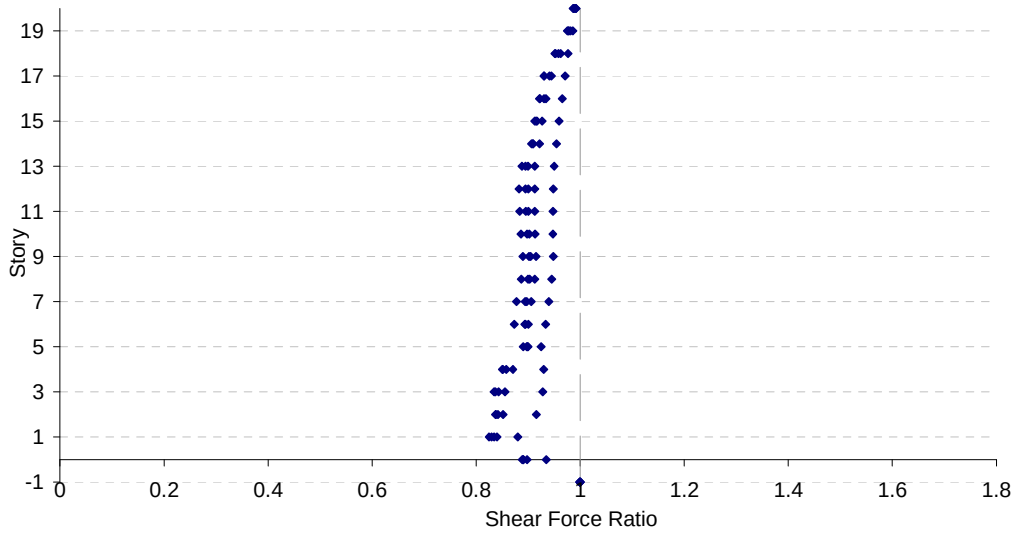

b)

Figure E.39 Shear Force Ratios for $BL\_20-0:5-A-2{,}500-0.05-2{,}000$ Subjected to Afyon Bay: a) Columns, b) Beams

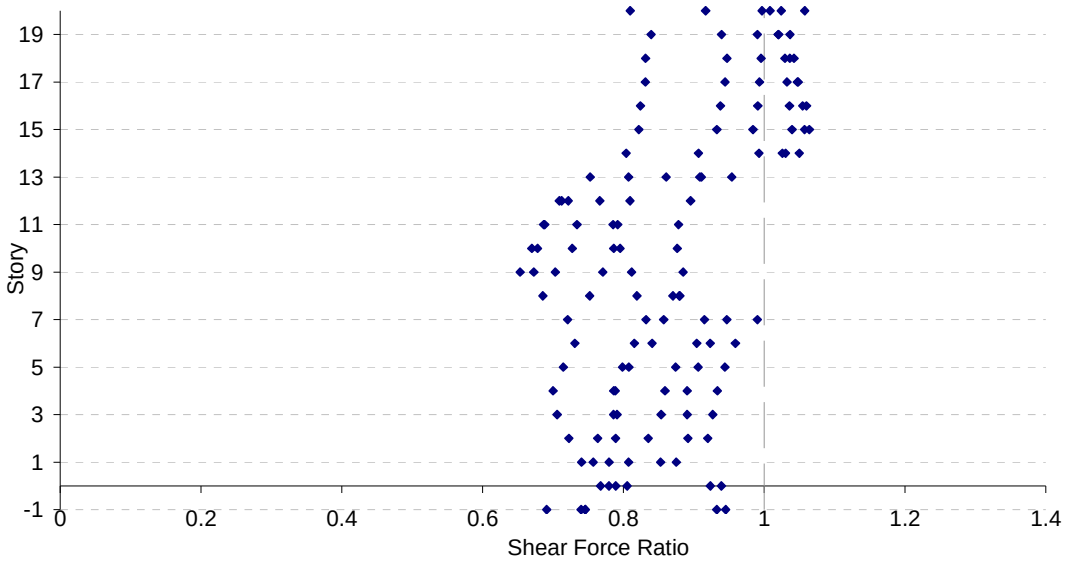

a)

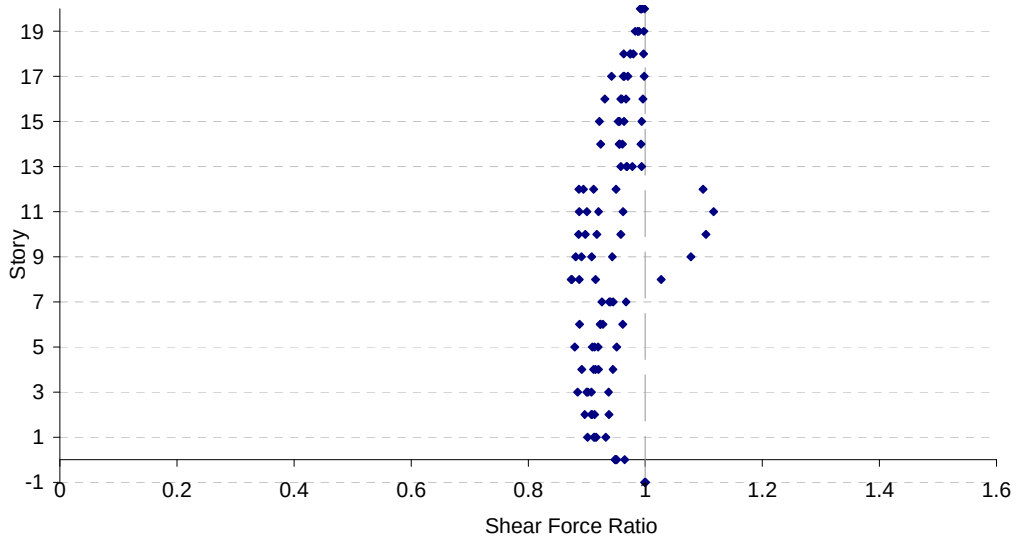

b)

Figure E.40 Shear Force Ratios for $BL\_20-9:13-A-2{,}500-0.05-2{,}000$ Subjected to Afyon Bay: a) Columns, b) Beams

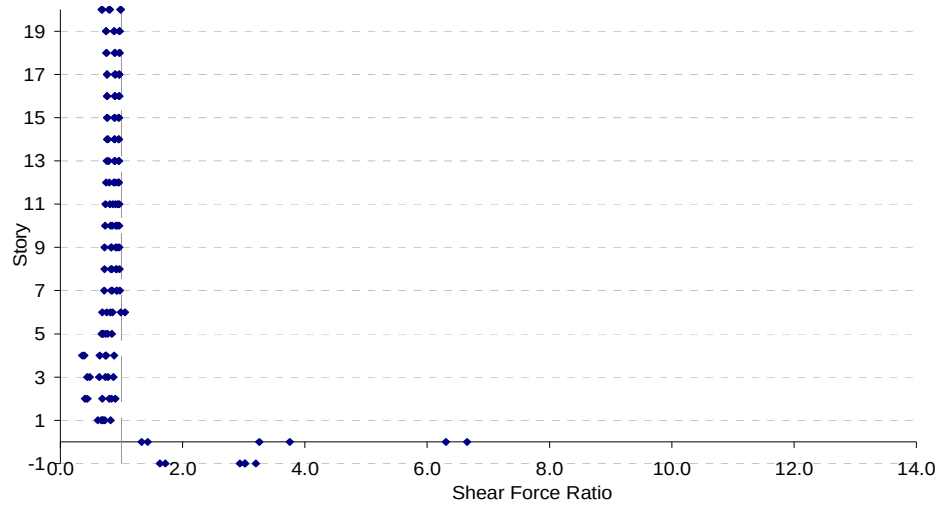

a)

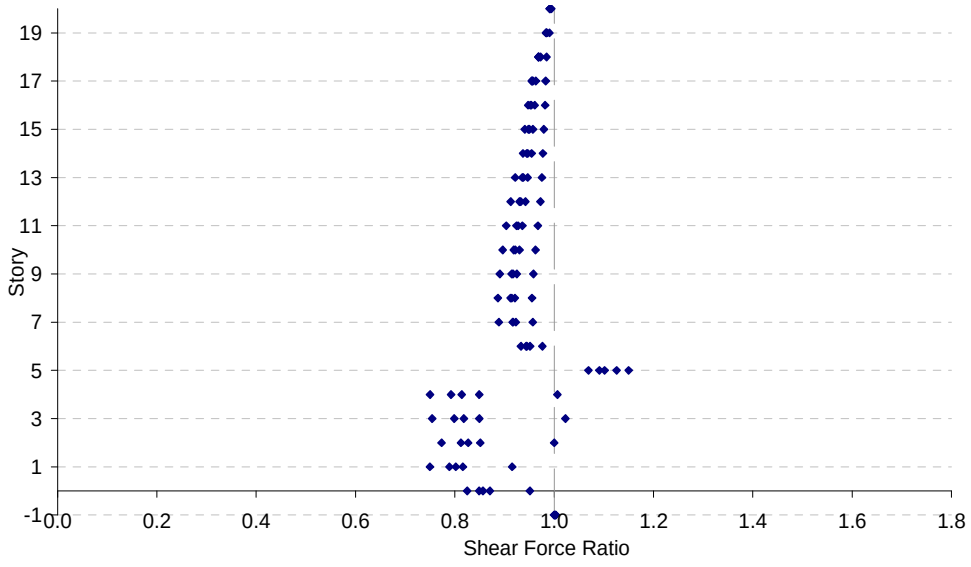

b)

Figure E.41 Shear Force Ratios for $BL\_20-0:5-A-236-0.01-1{,}000$ Subjected to Aydin: a) Columns, b) Beams

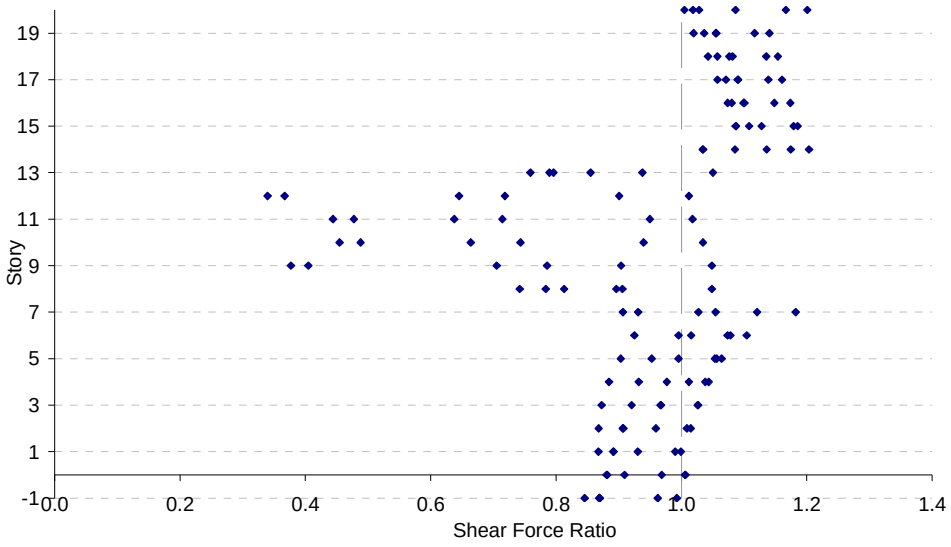

a)

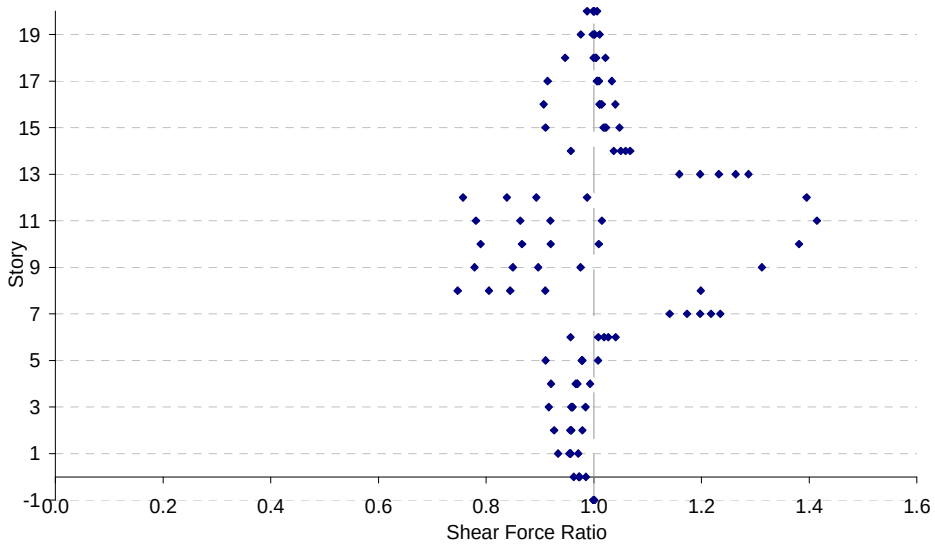

b)

Figure E.42 Shear Force Ratios for $BL\_20-9:13-A-236-0.01-1{,}000$ Subjected to Aydin: a) Columns, b) Beams

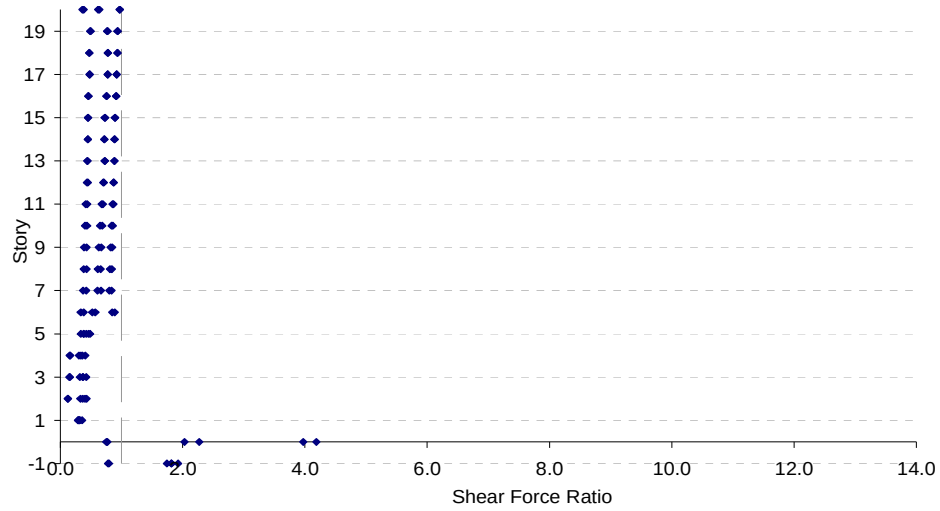

a)

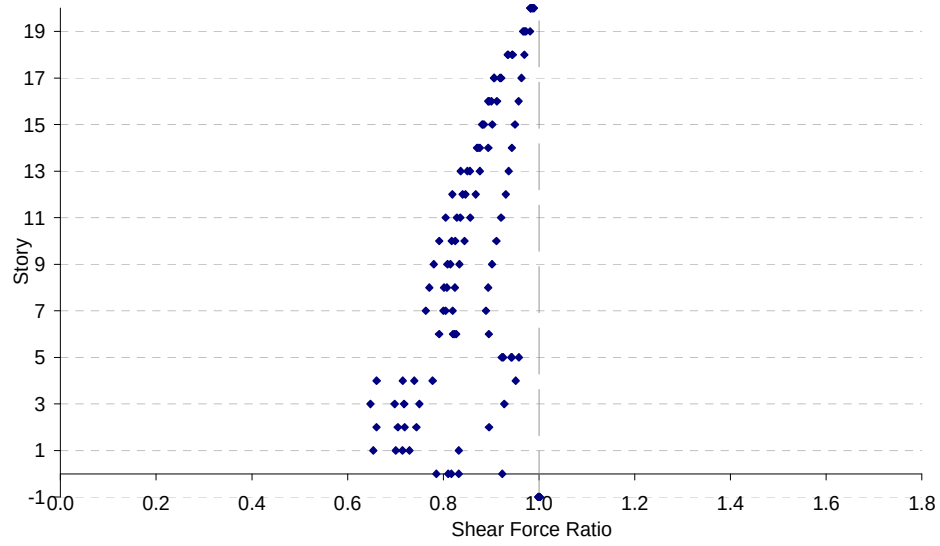

b)

Figure E.43 Shear Force Ratios for $BL\_20-0:5-A-100-0.1-120$ Subjected to Aydin: a) Columns, b) Beams

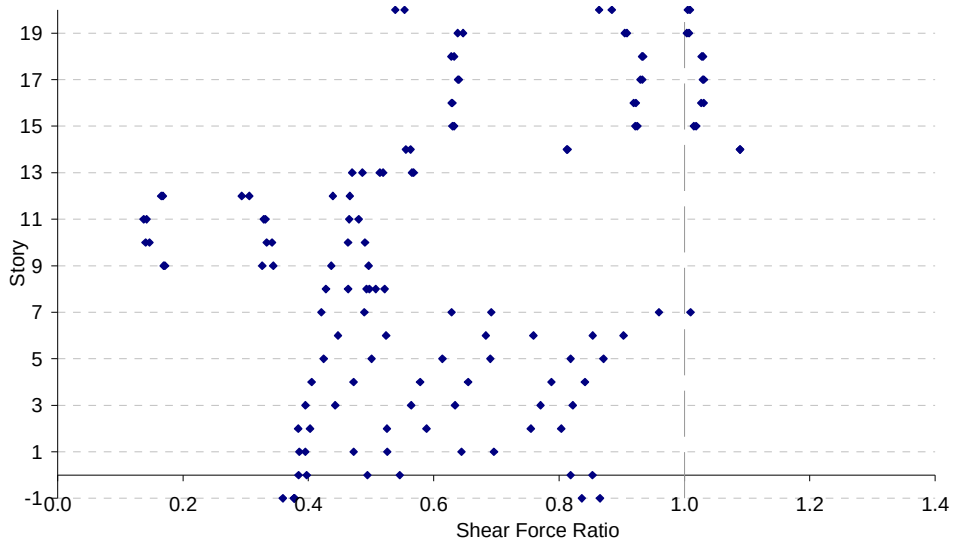

a)

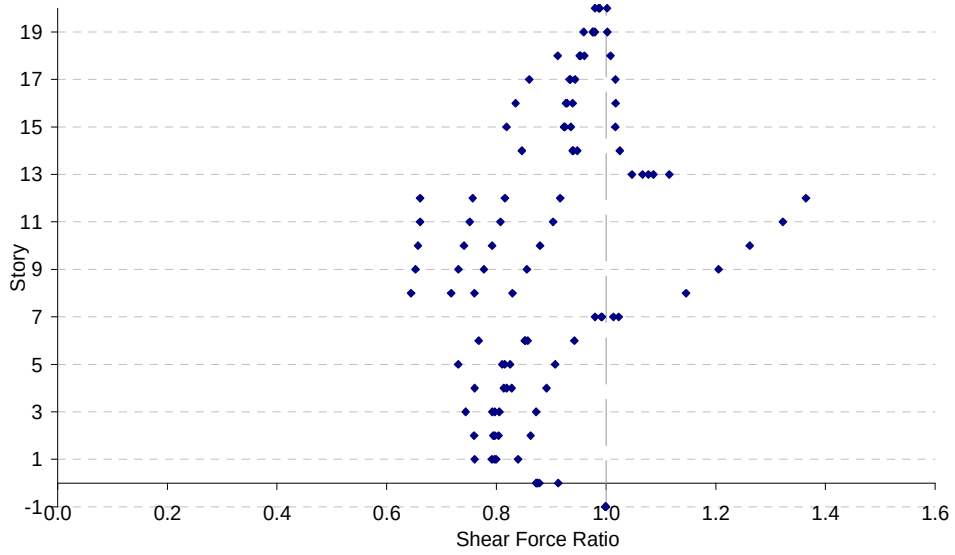

b)

Figure E.44 Shear Force Ratios for $BL\_20-9:13-A-100-0.1-120$ Subjected to Aydin: a) Columns, b) Beams

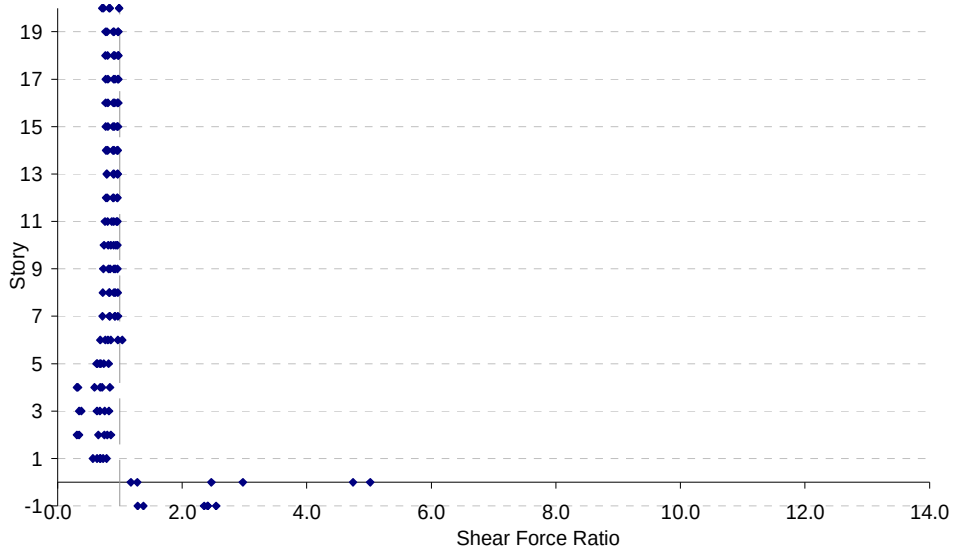

a)

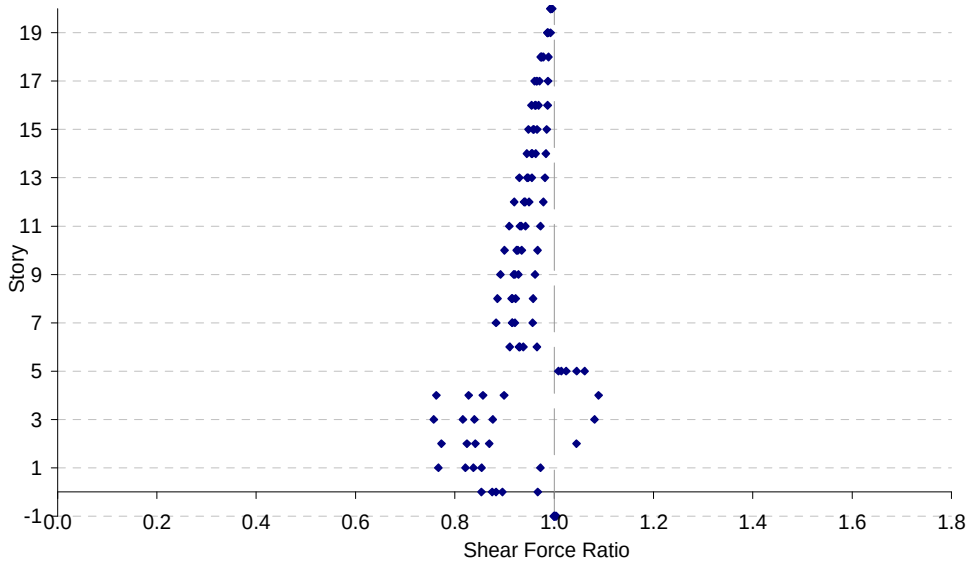

b)

Figure E.45 Shear Force Ratios for $BL\_20-0:5-A-500-0.05-500$ Subjected to Aydin: a) Columns, b) Beams

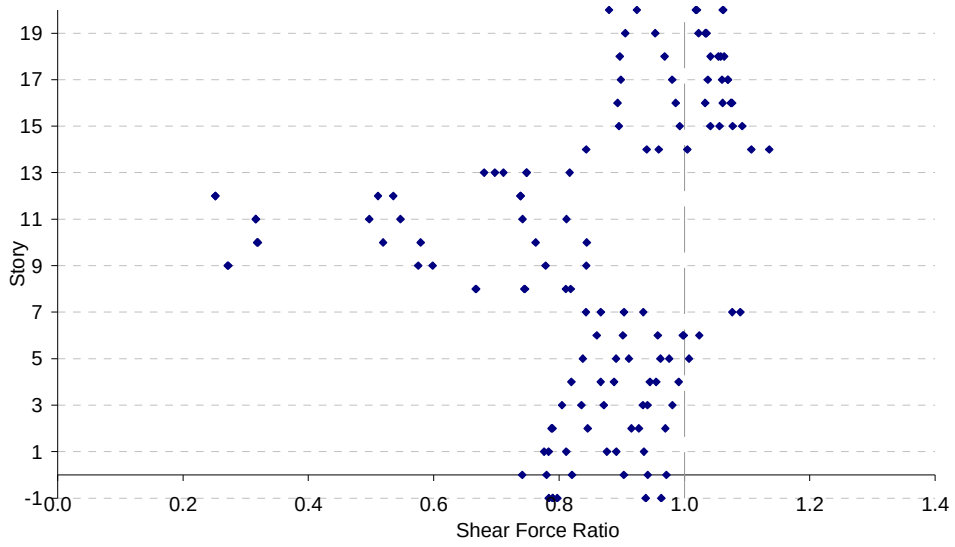

a)

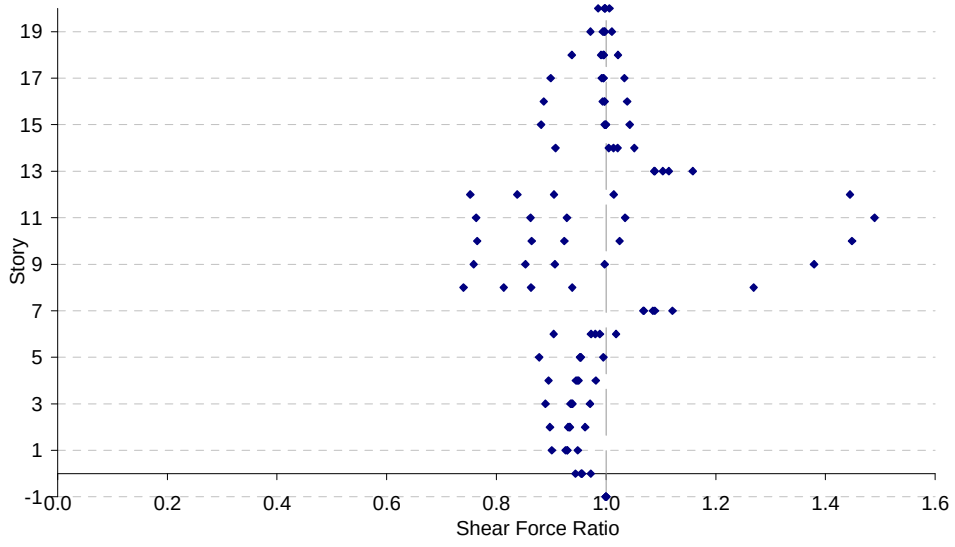

b)

Figure E.46 Shear Force Ratios for $BL\_20-9:13-A-500-0.05-500$ Subjected to Aydin: a) Columns, b) Beams

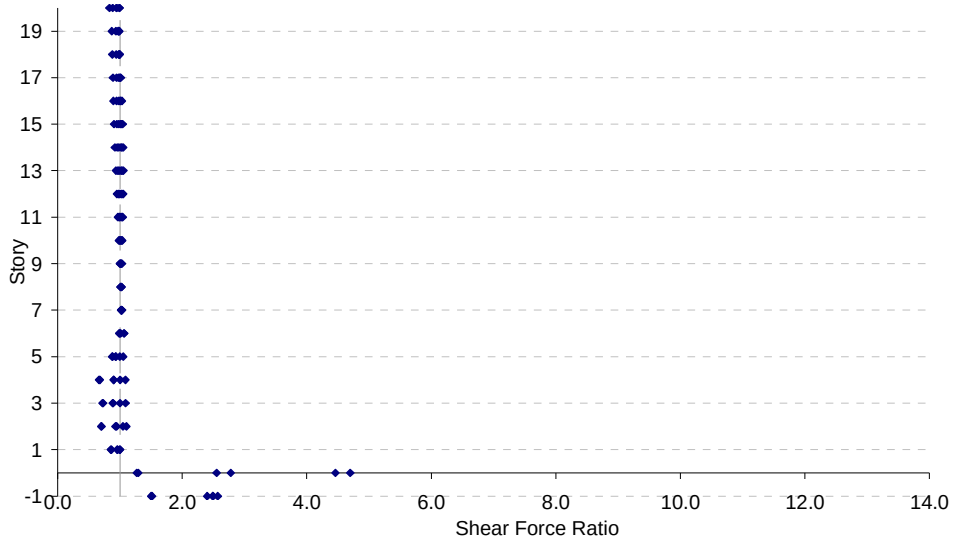

a)

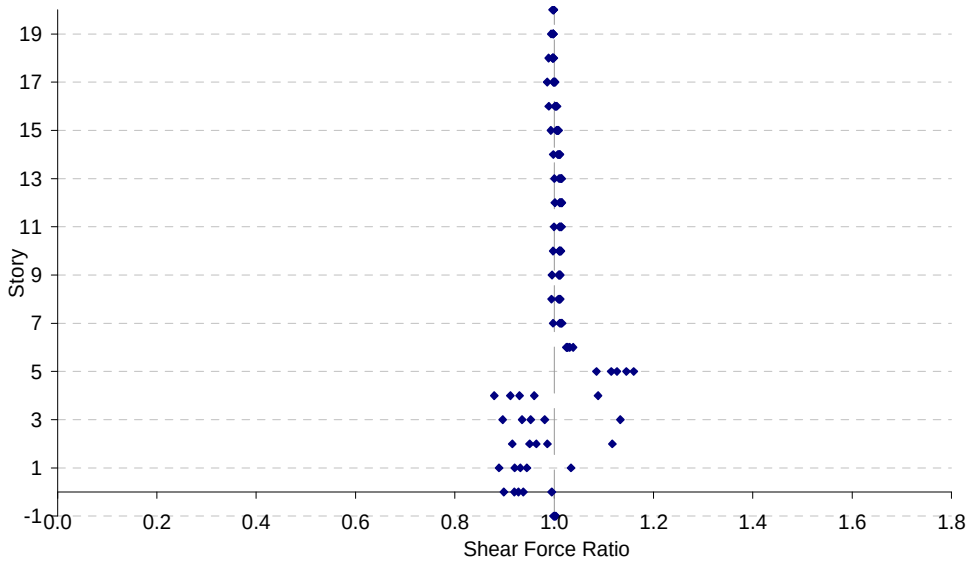

b)

Figure E.47 Shear Force Ratios for $BL\_20-0:5-A-800-0.1-2{,}300$ Subjected to Aydin: a) Columns, b) Beams

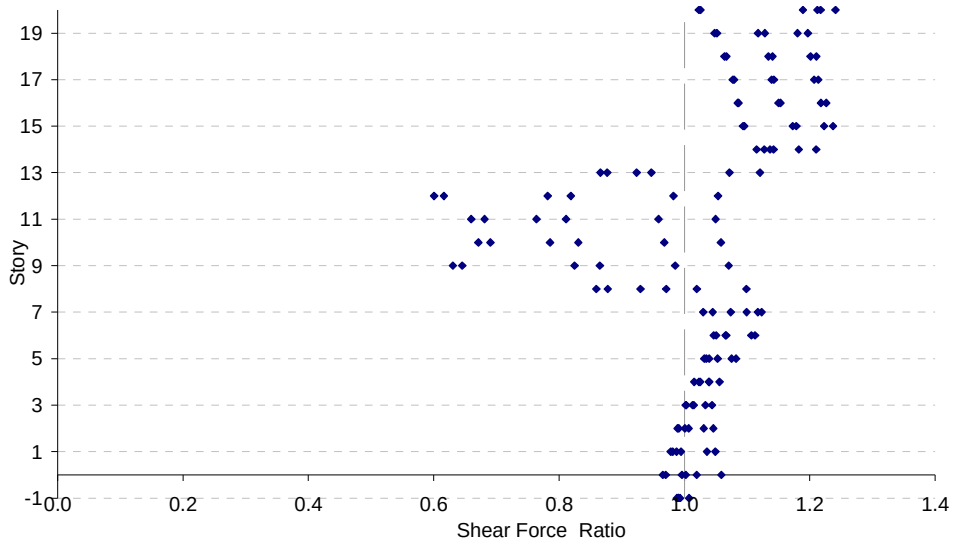

a)

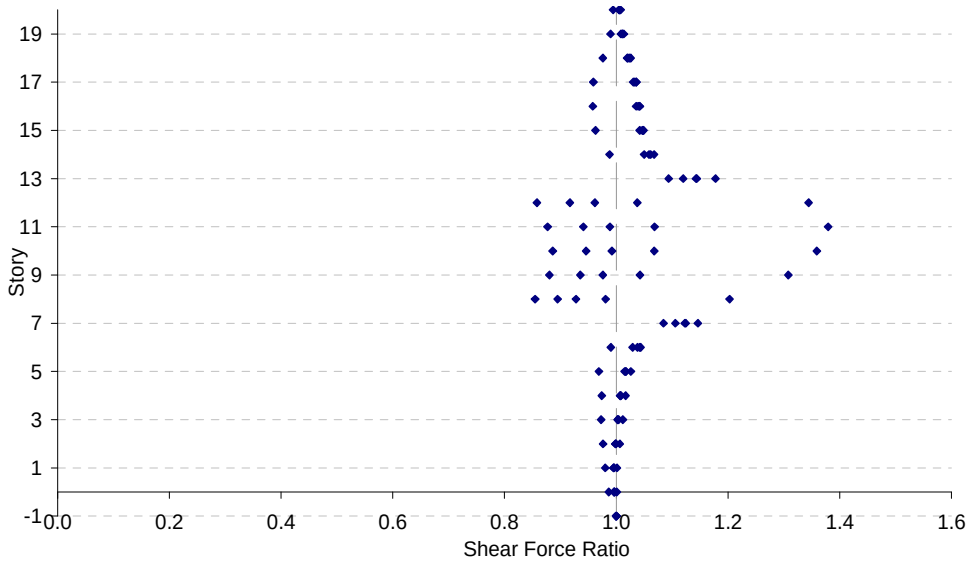

b)

Figure E.48 Shear Force Ratios for $BL\_20-9:13-A-800-0.1-2{,}300$ Subjected to Aydin: a) Columns, b) Beams

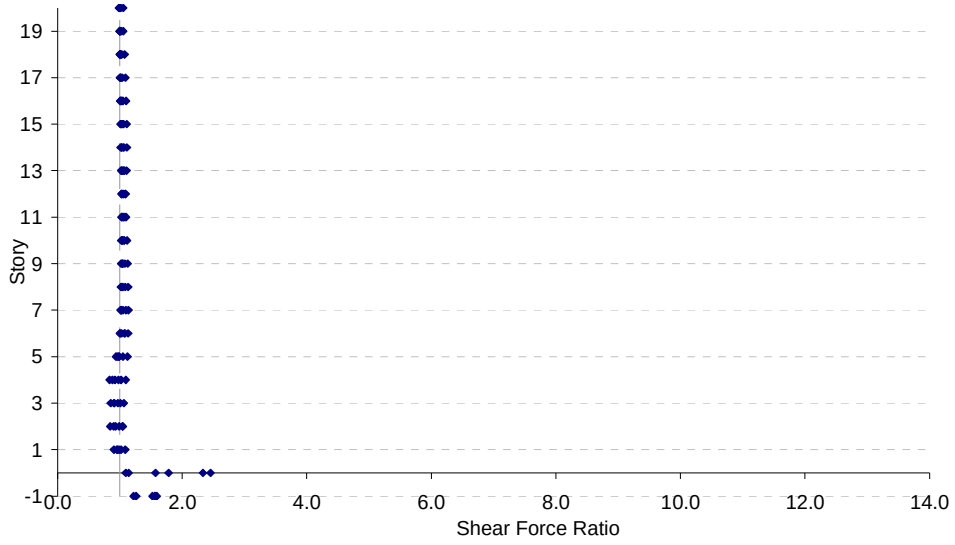

a)

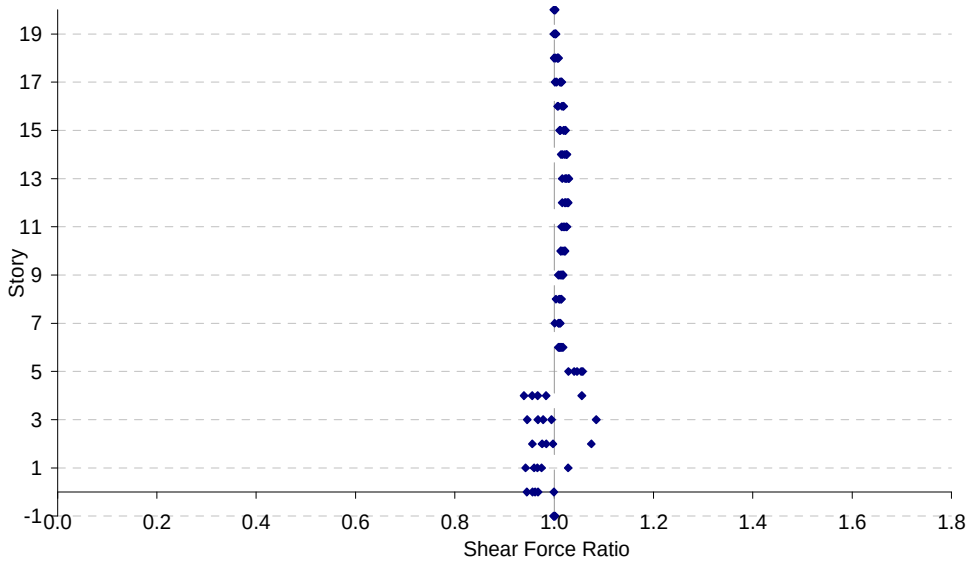

b)

Figure E.49 Shear Force Ratios for $BL\_20-0:5-A-2{,}500-0.05-2{,}000$ Subjected to Aydin: a) Columns, b) Beams

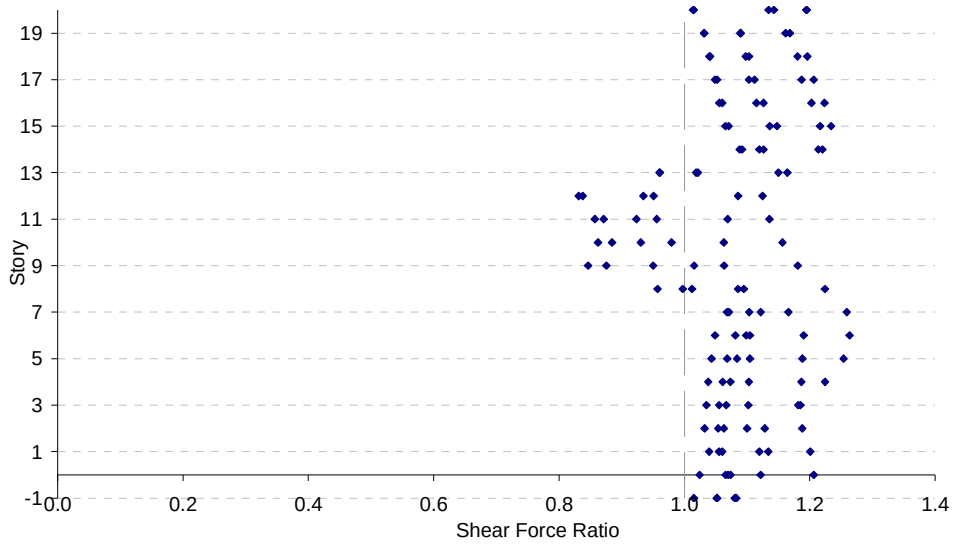

a)

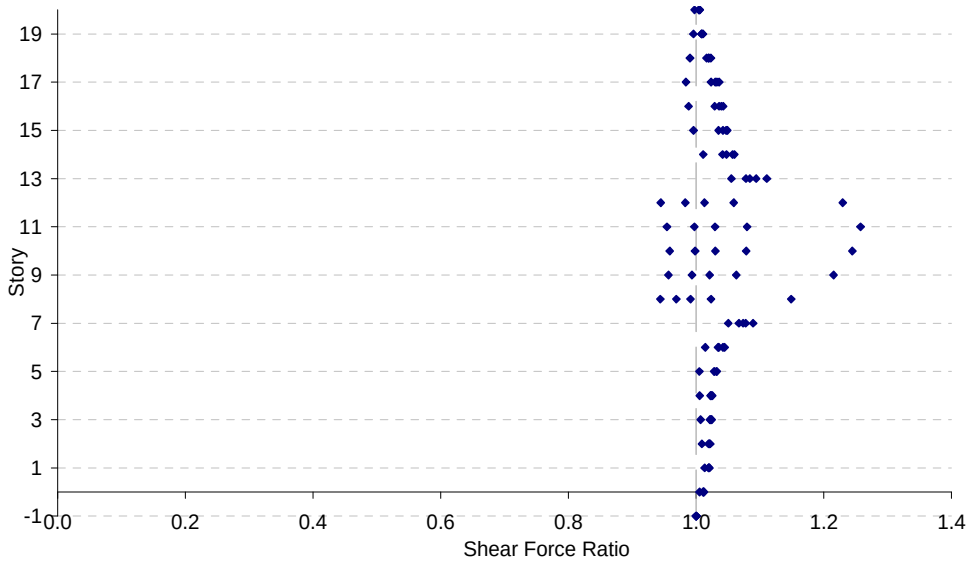

b)

Figure E.50 Shear Force Ratios for $BL\_20-9:13-A-2{,}500-0.05-2{,}000$ Subjected to Aydin: a) Columns, b) Beams

REFERENCES

[1] Bhatti, M. A., Hingtgen, James D., “Effects of Connection Stiffness and Plasticity on the Service Load Behavior of Unbraced Steel Frames.” Engineering Journal First quarter (1995): 21-33.

[2] Chan, S.L., Chui, P.P.T., Non-Linear Static and Cyclic Analysis of Steel Frames With Semi-Rigid Connections, Elsevier, Netherlands, 2000.

[3] Chan, Sui L., Chui, Peret P.T., “A Generalized Design-Based Elastoplastic Analysis of Steel Frames by Section Assemblage Concept.” Engineering Structures Vol. 19, No.8 (1997): 628-636

Abolmaali, Ali, Ardavan Motahari, and Mehdi Ghassemieh. "Energy Dissipation Characteristics of Semi-Rigid Connections." *Journal of Construction Steel Research* (2008).

AISC Manual Committee. *Manual of Steel Construction Load and Resistance Factor Design*. 3rd ed. 1986.

AISC Seismic *Provisions for Structural Steel Buildings*. American Institute of Steel Contruction, 2005.

ATC, 1978, *Tentative Provisions for Development of Seismic Regulations for Buildings*, ATC 3-06, Applied Technology Council, Redwood City, California.

Barsom, John M., and J Jr. V. Pellegrino. "Failure Analysis of Welded Steel Moment-Resisting Frame Connection." *Journal of Materials in Civil Engineering* 1st ser. 14 (2002): 24-34.

Chen, W.F., Lui,, E.M. *Stability Design of Steel Frames*. CRC Press, Boca Raton, FL, 1991.

Chi, Wei M., Gregory G. Deierlein, and Anthony Ingraffea. "Fracture Toughness Demands in Welded Beam-Column Moment Connections." *Journal of Structural Engineering* 1st ser. 126 (2000): 88-97.

Choi, Woo S., K. B. Park, and G. J. Park. "Calculation of Equivalent Static Loads and its Application."*Nuclear Engineering and Design* 235 (2005): 2337-2348.

Chopra, Anil K. *Dynamics of structures theory and applications to earthquake engineering*. Ed. Prentice Hall. 3rd ed. Upper Saddle River, N.J: Pearson/Prentice Hall, 2007.

FEMA-355C, 2000, *State of the Art Report on Systems Performance of Steel Moment Frames Subject to Earthquake Ground Shaking*, prepared by the SAC Joint Venture for the Federal Emergency Management Agency, Washington, DC.

FEMA-355F, 2000, *State of the Art Report on Performance Prediction and Evaluation of Steel Moment-Frame Buildings*, prepared by the SAC Joint Venture for the Federal Emergency Management Agency, Washington, DC.

Hoq, S.M.Ashfaqul, Master's Thesis to be completed in 2010.

Institute, Structural Engineering. *Minimum Design Loads for Buildings And Other Structures SEI/ASCE 7-05 (ASCE Standard No. 7-05) (ASCE Standard)*. New York: American Society of Civil Engineers (ASCE), 2005.

Kasai, K., Maison, B.F., and Mayangarum, A., "Effects of Partially Restrained Connection
Stiffness and Strength on Frame Seismic Performance," *SAC/BD-99/17*, SAC Joint Venture (1999).

King, Won-Sun, and W. F. Chen. "LRFD Analysis of Semi-Rigid Frame Design." *Engineering Journal* 4th ser. 30 (1993): 130-40.

Lee, Kihak, and Douglas A. Foutch. "Performance Evaluation of New Steel Frame Buildings for Seismic Loads." *Earthquake Engineering and Structural Dynamics* 31 (2002): 653-70.

Lee, Kihak, and Douglas M. Foutch. "Seismic Evaluation of Steel Moment Frame Buildings Designed Using Different R-Values." *Journal of Structural Engineering* 9th ser. 132 (2006): 1461-472.

Lee, Kihak, and Douglas A. Foutch. "Seismic Performance Evaluation of Pre-Northridge Steel Frame Buildings with Brittle Connections." *Journal of Structural Engineering* (2002): 546-55.

Lu, Le W., James M. Ricles, Changshi Mao, and John W. Fisher. "Critical Issues in Achieving Ductile Behavior of Welded Moment

Connections." *Journal of Constructional Steel Research* 55 (2000): 325-41.

Maison, B., Rex, C.O., Lindsey, S.D., and Kasai, K., “Performance of PR Moment Frame
Buildings in UBC Seismic Zones 3 and 4,” *ASCE Journal of Structural Engineering*, Vol. 126, No. 1 (2000).

Mao, Changshi, James Ricles, Le W. Lu, and John Fisher. "Effect of Local Details on Ductility of Welded Moment Connections." *Journal of Structural Engineering* 9th ser. 127 (2001): 1036-044.

Miller, Duane K. "Lessons Learned from the Northridge Earthquake." *Engineering Structures* 4-6 20 (1998): 249-60.

Open System for Earthquake Engineering Simulation - Home Page. Web. 1 Feb. 2008. <http://opensees.berkeley.edu/index.php>.

"PEER Strong Motion Database: Introduction." *Welcome to Pacific Earthquake Engineering Research Center - PEER*. Web. 15 Mar. 2008. <http://peer.berkeley.edu/smcat/>.

Popov, Egor P., Tzong S. Yang, and Shih P. Chang. "Design of Steel MRF Connections Before and After 1994 northridge Earthquake." *Engineering Structures* 12th ser. 20 (1998): 1030-1038.

Ricles, James M., Changshi Mao, Le W. Lu, and John W. Fisher. "Inelastic Cyclic Testing of Welded Unreinforced Moment Connections." *Structural Engineering* 4th ser. 128 (2002): 429-40.

"SAC System Performance: Development of Earthquake Ground Motions." *Earthquake Engineering Research Center (EERC): University of California, Berkeley*. Web. 26 Sept. 2008. <http://nisee.berkeley.edu/data/strong_motion/sacsteel/ground_motions.html>.

"SeismoSoft - SeismoSignal." *SeismoSoft - Home*. Web. 27 Aug. 2009. <http://www.seismosoft.com/en/SeismoSignal.aspx>.

Steel Construction Manual, 13th Edition (Book). New York: American Institute of Steel Construction, 2006.

BIOGRAPHICAL INFORMATION

Dobrinka Radulova was born November 18, 1984 in Bourgas, Bulgaria. She received her Bachelor's degree in Civil Engineering from the University of Texas at Arlington in 2007. During this period she worked as an undergraduate research assistant for the Department of Civil Engineering under the guidance of Dr. Ali Abolmaali. In this position, she was exposed to a variety of structural engineering projects such as analysis of box culverts and CCTV camera poles. Meanwhile, Dobrinka's interest in seismic analysis continued to grow as her exposure on this topic was enriched through her coursework. As a result, she perused a Masters degree of Science from the University of Texas at Arlington upon the completion of her undergraduate graduation requirements. During her work as a graduate research assistant, she studied the seismic response of hybrid frames by implementing commonly used semi-rigid connection properties into the analysis. Her work with Dr. Abolmaali on computational non-linear dynamic frame analysis techniques was published by the International Association on Computational Mechanics in 2008.